P-ISSN 2525-2461 • E-ISSN 2615-9937

Vietnam Journal of Science, Technology and Engineering

DECEMBER 2020 • VOLUME 62 NUMBER 4

VIETNAM JOURNAL OF SCIENCE, TECHNOLOGY AND ENGINEERING * DECEMBER 2020 * VOLUME 62 NUMBER 4

Special Issue on ENVIRONMENT AND DEVELOPMENT

vietnamscience.vn

SELECTED PAPERS OF THE WORKSHOP ON ENVIRONMENT AND DEVELOPMENT IN THE 12th SCIENTIFIC CONFERENCE OF VNUHCM - UNIVERSITY OF SCIENCE

Vietnam Journal of Science, Technology and Engineering (VJSTE) **is a quarterly double-blind peer-reviewed academic journal. VJSTE publishes research articles and review articles in all areas of science, technology and engineering with the focus on the life sciences and environmental sciences including the following topics:**

- **Agriculture**
- **Medicine**
- **Pharmacology**
- **Biology**
- **Biotechnology**
- **Ecology**
- **Climatology.**

CLASSIFICATION SCHEME

1. **Mathematics and Computer Science**
   - 1.1. Mathematics
   - 1.2. Computer Science
   - 1.3. Computational Science
2. **Physical Sciences**
   - 2.1. Physics
   - 2.2. Chemistry
   - 2.3. Engineering
3. **Life Sciences**
   - 3.1. Agriculture
   - 3.2. Medicine
   - 3.3. Pharmacology
   - 3.4. Biology
   - 3.5. Biotechnology
4. **Geosciences**
   - 4.1. Geography
   - 4.2. Geology
   - 4.3. Geophysics
   - 4.4. Oceanography
5. **Environmental Sciences**
   - 5.1. Ecology
   - 5.2. Climatology

CONTENTS

DECEMBER 2020 • VOLUME 62 NUMBER 4

9

24

CONTENTS

DECEMBER 2020 • VOLUME 62 NUMBER 4

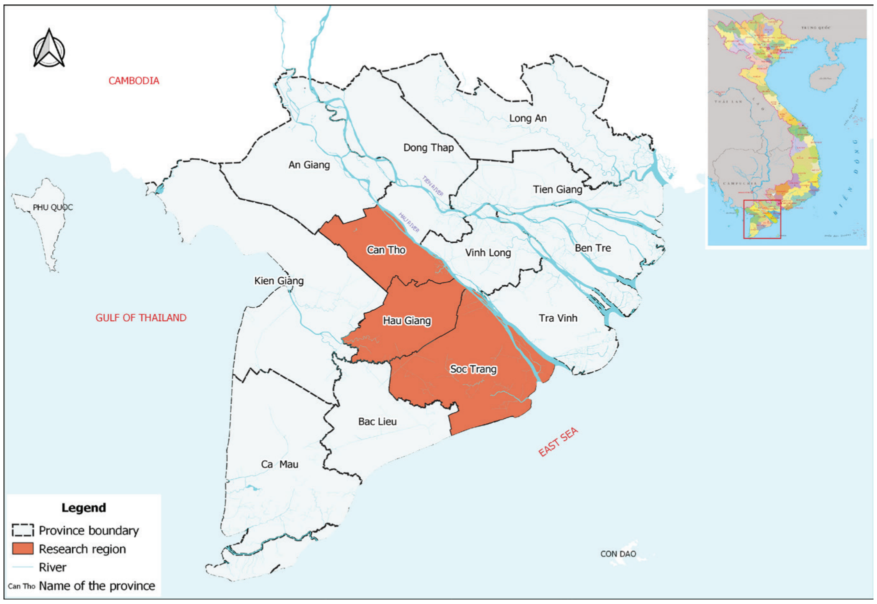

66

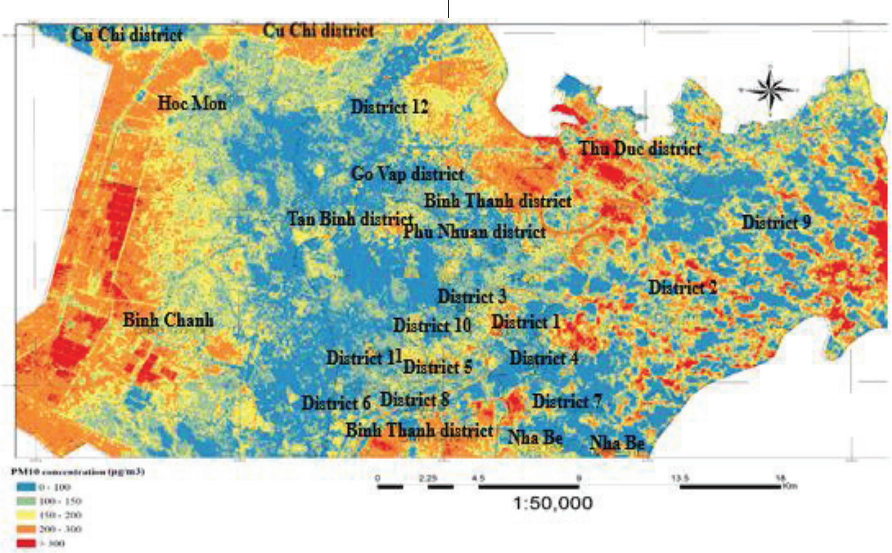

92

Diversity of zooplankton and benthic macroinvertebrates of estuarine coastal waters in Tien Giang province, southern Vietnam

Thuy Lan Chi Nguyen[1], Thi Thu Huong Dinh[1], Thi Cam Tu Dang[1], Anh Duc Pham[1*], Thanh Tam Nguyen[2], Thi Tu Quyen Huynh[2], Nhat Phuong Tran[3]

[1]Ton Duc Thang University
[2]Division of Environmental Management, Tien Giang Department of Natural Resources and Environment
[3]Faculty of Medicine, Van Lang University

Received 6 August 2020; accepted 8 October 2020

Abstract:

The Tien Giang province is located in the tropical climate zone of the Mekong delta. In this study, the diversity of zooplankton and benthic macroinvertebrates were investigated in the estuarine coastal waters of the Tien Giang province of southern Vietnam. 10 sites were observed over six time periods from 2019 (March, May, September, and November) and 2020 (March and May). The taxonomic richness, abundance, and diversity index were applied to this biodiversity assessment of the zooplankton and benthic macroinvertebrates. The results of the assessment showed that 30 species of zooplankton and 18 species of benthic macroinvertebrates were found in the study area. The density of zooplankton at each site ranged from 6 to 93 individuals/sample, while the density of benthic macroinvertebrates at each site fluctuated from 3 to 12 individuals/sample. The Shannon-Wiener diversity index of zooplankton fluctuated from 1.02 to 1.58 and that of the benthic macroinvertebrates ranged between 0.91 and 1.33. Besides, statistical analysis showed that the species richness of the zooplankton and benthic macroinvertebrates positively correlated with their density (r=0.2283-0.6423). This study contributes to the diversity information of zooplankton and benthic macroinvertebrates, which can be used to position the sustainable management of natural resources and evaluate the natural feed sources for aquaculture in this estuarine area.

Keywords: **benthic macroinvertebrates, biodiversity assessment, estuarine area, zooplankton.**

Classification number: **5.1**

*Corresponding author: Email: phamanhduc@tdtu.edu.vn

Introduction

The Tien Giang province is located on the left bank of the Tien river and it borders the East Sea. The part of the Tien river that goes through the province is 103 km long [1]. It has a flat terrain with a slope below 1.0% and the altitude varies from 0 to 1.6 m from sea level. The whole province lies in the lower section of the Mekong river. This region has a tropical monsoon climate that divides the year into two seasons: the rainy season from May to November and the dry season from December to April of the following year [1]. In recent years, the Tien Giang estuarine area has received various types of wastewater from agriculture, aquaculture, industrial, and domestic activities. Specifically, environmental pollution is most evidenced in the area near the Vam Lang sea, where the seawater has turned black and has a foul odour. Besides this, waste is also scattered on the shore or floating in the water. In the areas where boats are anchored, grease and waste accumulate into floating patches on the water surface that further pollute the environment [2].

Being an integral part of river ecosystems, the zooplankton community is closely linked to other components of the aquatic ecosystem [3]. Zooplankton are the main food source for many other secondary consumers such as shrimp. Besides, they are frequently used as bioindicators for the trophic state of the water environment [4]. On the other hand, benthic macroinvertebrates such as molluscs live at the bottom of water bodies during their entire biological cycle. Among the communities that are considered as bioindicators of water quality, those most commonly used are benthic macroinvertebrates because they have several characteristics that make them easy to study. For example, benthic macroinvertebrates show clear responses to environmental conditions. The structure of the benthic communities in an aquatic ecosystem reflects ecological conditions including habitat heterogeneity [5]. In

Europe and North America, the application of invertebrate communities to water quality assessment was developed in the first half of the twentieth century. European scientists developed an indicator species to monitor the water quality, while North American researchers applied biological indicators combined with ecological balance theory to evaluate the ecological health of water bodies [6]. In the 1970s and 1980s, Asian countries such as China, Korea, and Japan began to apply these methods to assess their water quality [7]. In 1996, Thailand was one of the first countries to build a monitoring system using macroinvertebrates in the Ping river. To match the conditions of north Thailand, Mustow (1997) modified the scoring system based on macroinvertebrates where he revised the BMWP^{England} score system and called it the BMWP^{Thai} [6, 8]. Only recently have aquatic biodiversity studies been conducted by scientists in Vietnam and, until now very few studies have evaluated the diversity of zooplankton and benthic invertebrates in the coastal areas of the Mekong delta.

In reports published by the MRC from 2004 to 2007, biodiversity studies of zooplankton and macroinvertebrates were only conducted in the Ba Lai estuary. The biological criteria for evaluation included taxa richness, abundance, and diversity [8]. X.Q. Ngo, et al. (2016) [9] developed a biomonitoring tool based on nematode communities in the Mekong estuaries concentrated in Ba Lai. Because studies of the effects of fishing and other aquacultural activities on the natural resources of coastal zooplankton and benthic macroinvertebrates in Tien Giang are limited, baseline data of zooplankton and benthic macroinvertebrates is crucial to the complete capture of the impacts of anthropogenic pressures.

This study evaluates the structure and composition of zooplankton and benthic macroinvertebrates in the estuarine coastal waters of the Tien Giang province, Vietnam. To the best of author's knowledge, this is the first account of the biodiversity of zooplankton and benthic macroinvertebrates in Tien Giang's estuary waters ever provided.

Materials and methods

Study area

The study area covers 100 km^2 of estuarine coastal waters along a 32-km coastline. The samples of zooplankton and benthic macroinvertebrates from 10 sampling sites were collected for 6 periods in 2019 (March, May, September, and November) and 2020 (March and May). The allocation of the sampling sites and nearby anthropogenic activities are shown in Fig. 1 and Table 1.

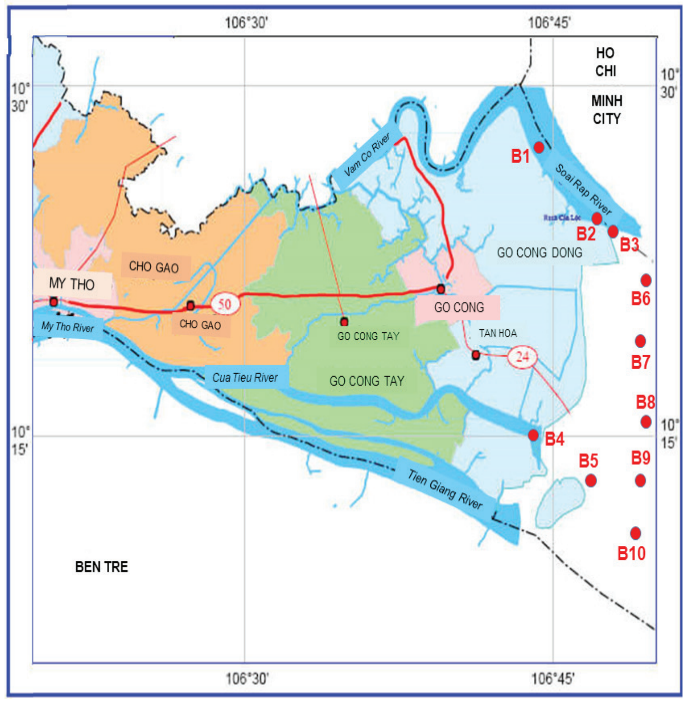

Fig. 1. The estuarine area along the Tien Giang coast with 10 sampling sites (B1-B10).

Table 1. Coordinates and locations of the sampling sites.

Sites	Local names	Describes	Longitude (N)	Latitude (S)
B1	Soai Rap river mouth	Aquaculture, fishing activities	106°46' 32.07"	10°25' 47.50"
B2	Vam Lang fishing port	Trading, fishing activities	106°47' 12.09"	10°24' 30.00"
B3	Vam Lang commune	Aquaculture, fishing activities	106°77' 92.42"	10°26' 78.83"
B4	Den Do fishing port	Aquaculture, fishing activities	106°74' 93.73"	10°26' 78.83"
B5	Phu Dong commune	Aquaculture, fishing activities	106°75' 52.95"	10°25' 11.60"
B6	Kieng Phuoc commune	Aquaculture, fishing activities	106°47' 50.08"	10°21' 43.50"
B7	Tan Dien area	Fishing activities	106°47' 29.06"	10°20' 27.90"
B8	Tan Thanh beach	Beach, aquaculture activities	106°47' 26.08"	10°17' 10.20"
B9	Tieu river mouth	Fishing activities	106°45' 31.05"	10°15' 28.10"
B10	Phu Tan area	Fishing activities	106°48' 13.06"	10°11' 10.50"

Sample collection

Zooplankton: at each site, 10 l of surface water (0-0.5 m deep) were collected in a bucket and filtered slowly through a plankton net with a mesh size of 20 µm. Water was splashed on the outside of the net to wash down any zooplankton adhering on the net [10, 11]. When there was only about 150 ml water volume remaining in the net, the water was transferred into a 250 ml plastic jar. The sample was immediately fixed in the field with formaldehyde to a final concentration of 5% [10, 11].

Benthic macroinvertebrates: at each site, 4 sub-samples were taken with a Petersen grab sampler and pooled into a single sample, which covered a total area of 0.1 m^2. The contents from the grab were removed if the grab did not close properly because material such as wood, aquatic macrophytes, or stones may become trapped in the grab's jaws [10, 12]. Each sample was thoroughly washed with a sieve of mesh size 0.3 mm. The contents of the sieve were placed in jars and fixed with formaldehyde to a final concentration of 5% [10, 12]. The sample jars of zooplankton and benthic macroinvertebrates were labelled with the site name, the site's code, the date, and the sampling position [10-12].

Laboratory analysis

The identification of zooplankton and benthic macroinvertebrates were based on morphology and taxonomic books [13-21]. Zooplankton and benthic macroinvertebrates were identified to the species level. All individuals collected were identified and counted under an Olympus 41 compound microscope (with magnifications of 40-1200x) or a dissecting microscope (16-56x).

Data analysis

The qualitative and quantitative results of the zooplankton and benthic macroinvertebrates were used for the calculation of (i) taxonomic richness (number of taxa); (ii) abundance (numbers of individuals per site); and (iii) the Shannon-Wiener diversity index [22, 23]. The Shannon-Wiener diversity index is given below [24]:

$$H' = -\sum_{i=1}^{s} p_i \log p_i$$

where s is the number of species in a community and p_i is the proportion of each species in the sample.

Linear regression analysis was used to test for statistically significant relationships between the density and species richness and these were measured for all 10 sampling sites.

Results

Species richness

During the six monitoring times, there were 30 species of zooplankton and 18 species of benthic macroinvertebrates found in the study area. Among the zooplankton, hexanauplia was the dominant species composition with 19 species, which corresponds to around 63% of the total (Table 2). On the other hand, the number of polychaeta species of benthic macroinvertebrates was the highest with 9 species in total, which accounted for 50% of the total (Table 2).

Table 2. Communities of zooplankton and benthic macroinvertebrates from estuarine coastal waters in the Tien Giang province during 2019 and 2020.

Classes of zooplankton	Number of species	Proportion to total (%)	Classes of benthic macroinvertebrates	Number of species	Proportion to total (%)
Hydrozoa	1	3.3	Polychaeta	9	50.0
Eurotatoria	1	3.3	Gastropoda	2	11.1
Hexanauplia	19	63.4	Bivalvia	3	16.7
Malacostraca	3	10.0	Ophiurodea	1	5.5
Sagttodea	1	3.3	Malacostraca	3	16.7
Appendicularia	1	3.3			
Larva	4	13.4			
Total species	30	100	Total species	18	100

The zooplankton species of *Paracalanus parvus* and *Acartia clausi* (Hexanauplia) were found at all sampling sites. In addition, the species *Schamckeria speciosa*, *Oithona similis*, and nauplius copepods also occurred widely in the studied areas. Among the benthic macroinvertebrates, the polychaetes *Nereis (Ceratonereis) mirabilis* and the bivalves *Aloidis* sp. were the most species-rich groups and were found at almost all the sites.

The species richness of zooplankton at each site was highly variable and ranged from 2 to 9 species/site. The species richness of benthic macroinvertebrates at each site fluctuated from 2 to 6 species/site. The mean species richness of zooplankton and benthic macroinvertebrates are presented in Figs. 2 and 3.

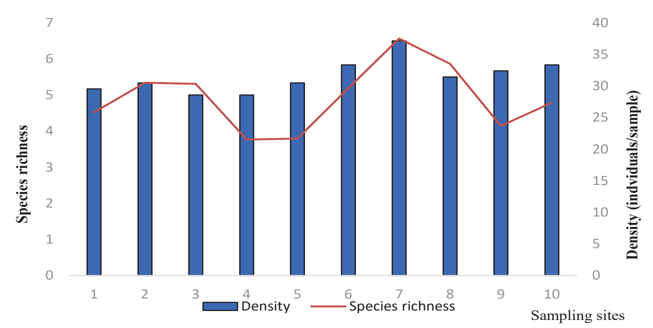

Fig. 2. Average values of density and species richness of zooplankton.

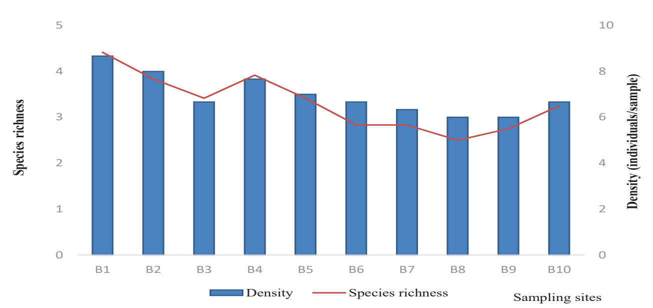

Fig. 3. Average values of density and species richness of benthic macroinvertebrates.

Abundance

The zooplankton abundances at each site were also highly variable and ranged from 6 to 93 individuals/site. The dominant species in the monitoring area were *Schmackeria speciosa, Oithona similis* and nauplius copepods. Among the dominant species, nauplius copepods were prevailing at most of the sampling sites. The benthic macroinvertebrates abundances at each site fluctuated from 3 to 12 individuals/site. The dominant species in the study area were *Nereis (Ceratonereis) mirabilis*, *Scoloplos (Scoloplos) marsupialis*, and *Aloidis* sp. Among the dominant species, *Aloidis* sp. prevailed at most of the sampling sites. The mean density of the zooplankton and benthic macroinvertebrates are presented in Figs. 2 and 3.

Correlation analysis

Statistical analysis showed that the species richness of the benthic macroinvertebrates had a strong positive correlation with the abundance (r=0.6423, p<0.05) (Fig. 4), while the species richness of zooplankton also positively correlated with the abundance (r=0.2283, p<0.05) (Fig. 5).

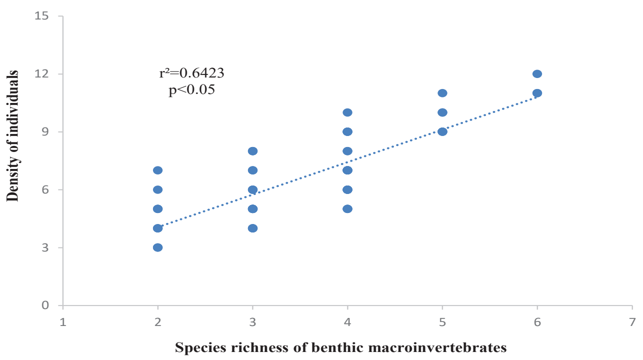

Fig. 4. Correlation between density and species richness of benthic macroinvertebrates.

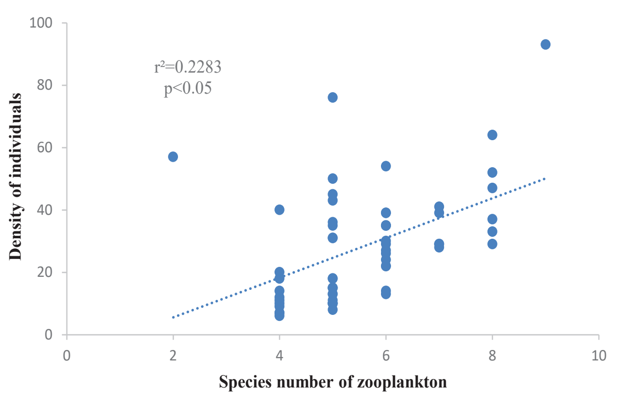

Fig. 5. Correlation of density and species richness of zooplankton.

Diversity index

The values of zooplankton biodiversity during the sampling times in 2019 and 2020 fluctuated between 1.02 and 1.58 while the values of benthic macroinvertebrates fluctuated between 0.91 and 1.33. Generally, the H' values of zooplankton and benthic macroinvertebrates do not differ significantly between sampling sites (Table 3).

Discussion

Pham, et al. (2016) [25] recorded 31 species of zooplankton in April and September 2015 from 5 sampling sites along the Can Giuoc river. The species of the copepods *Schmackeria bulbosa* and *Acartiella sinensis* were dominant in the zooplankton community. Throughout a 26-year sampling/monitoring program from 1989 to 2015 along the Thi Vai river and Cai Mep estuary, 38 benthic macroinvertebrates were reported of which polychaetes were also the dominant species composition [26]. In general, the monitoring results of zooplankton and benthic macroinvertebrates in the estuarine area are more diverse than in the coastal area.

Based on annual biological monitoring in this area, copepods and polychaetes significantly contribute to the species richness of zooplankton and benthic macroinvertebrates. This may be related to the water characteristics of the Tien Giang estuarine coastal waters, which are strongly influenced by seawater from the East Sea. Generally, the mean values of density and species richness of benthic macroinvertebrates collected from the onshore sites were higher than those in the offshore sites because of the softer bottom [27]. The mean values of density and species richness of zooplankton along the coastal bank sites were higher than those from the onshore sites because of lower turbidity [28].

The results of the correlation analysis for zooplankton and benthic macroinvertebrates showed that both organisms have a positive correlation between the species richness and number of individuals. The number of species and density of benthic macroinvertebrates in hard bottom areas may be lower than that in the soft bottom areas [27]. This may also have a similar influence on zooplankton, i.e. when strong sea waves make the bottom hard and force high turbidity, the abundance of this organism can be limited [28].

In general, the values of the biodiversity index (H') of zooplankton and benthic macroinvertebrates during the monitoring

Table 3. The biodiversity index (H') of zooplankton and benthic macroinvertebrates from the estuarine area in Tien Giang province during 2019 and 2020.

H'	B1	B2	B3	B4	B5	B6	B7	B8	B9	B10
Zooplankton	1.32-1.33	1.31-1.37	1.31-1.32	1.12-1.23	1.28-1.45	1.35-1.45	1.53-1.58	1.04-1.22	1.21-1.49	1.18-1.36
Benthic macroinvertebrates	1.21-1.28	1.04-1.23	1.01-1.27	1.09-1.33	0.95-1.24	1.01-1.07	0.95-0.98	0.91-1.01	1.04-1.21	0.95-0.97

times were quite low. The H' values of zooplankton did not differ much between sampling sites, while the H' values of benthic macroinvertebrates seemed to be higher at sites near the river mouth. These results could be related to the hard bottom found in coastal areas in comparison with those near the river mouth. The recorded values of the biodiversity index for both zooplankton and benthic macroinvertebrates in this study were lower than previous research results from the Can Giuoc river, the Thi Vai river, and the Cai Mep estuary.

Conclusions

Throughout the 6 monitoring periods, the authors found 30 species of zooplankton and 18 species of benthic macroinvertebrates in the study area. Among the zooplankton, the number of species of hexanauplia dominated the species composition with 19 species in total, while the species polychaetes was the most prominent of the benthic macroinvertebrates with 9 species in total.

The density of zooplankton ranged from 6 to 93 individuals/sample. The dominant species in the monitoring area were *Schamckeria speciosa*, *Oithona similis*, and nauplius copepods. The densities of benthic macroinvertebrates fluctuated from 3 to 12 individuals/sample. The species of *Nereis (Ceratonereis) mirabilis*, *Scoloplos (Scoloplos) marsupialis*, and *Aloidis* sp. were dominant.

In general, the biodiversity of both zooplankton and benthic macroinvertebrates in the study area was low. This conclusion should be used to orient the sustainable management of natural resources and evaluate the natural feed sources of aquaculture in Tien Giang and the surrounding areas.

ACKNOWLEDGEMENTS

The authors thanks the Tien Giang Centre for Natural Resources and Environmental Monitoring for funding this research.

COMPETING INTERESTS

The authors declare that there is no conflict of interest regarding the publication of this article.

REFERENCES

[1] http://en.tiengiang.gov.vn/.

[2] Minh Thanh (2017), "Pollution problem at Vam Lang fishing port", *Ap Bac Newspaper* (in Vietnamese).

[3] O.Y. Derevenskaya, R.M. Umyarova (2016), "Zooplankton as an indicator of river ecological condition", *International Journal of Pharmacy and Technology*, **8(2)**, pp.14567-14574.

[4] A. Zaghloul, M. Saber, S. Gadow, F. Awad (2020), "Biological indicators for pollution detection in terrestrial and aquatic ecosystems", *Bulletin of the National Research Centre*, **44(127)**, pp.1-11.

[5] A. Oliveira, M. Callisto (2010), "Benthic macroinvertebrates as bioindicators of water quality in an Atlantic forest fragment", *Iheringia, Sér. Zool.*, **100(4)**, pp.1-10.

[6] D.M. Rosenberg, V.H. Resh (1993), *Freshwater Biomonitoring and Benthic Macroinvertebrates*, Springer US, 488pp.

[7] J.C. Morse, Y.J. Bae, G. Munkhjargal, N. Sangpradub, K. Tanida, T.S. Vshivkova, B. Wang, L. Yang, C.M. Yule (2007), "Freshwater biomonitoring with Macroinvertebrates in East Asia", *Frontiers in Ecology and the Environment*, **5(1)**, pp.33-42.

[8] Mekong River Commission (2008), "Biomonitoring of the lower Mekong river and selected tributaries 2004-2007", *MRC Technical Paper No. 20*, Vientiane, 77pp.

[9] X.Q. Ngo, et al. (2016), "The strong link of intertidal nematode communities with sediment features in the Mekong estuaries provides a useful tool for biomonitoring", *Environmental Monitoring and Assessment*, **188(2)**, pp.1-16.

[10] MRC (2010), *Biomonitoring Methods for the Lower Mekong Basin*, Mekong River Commission, Vientiane, 63pp.

[11] T.M.L. Nguyen (2007), *Changes of Zooplankton in Saigon River and Its Tributaries*, University of Natural Science, Ho Chi Minh city, 94pp.

[12] A.D. Pham (2014), *Study on the Water Quality Assessment Using Benthic Macroinvertebrates for the Lower Dongnai River Biomonitoring, Vietnam*, Ph.D. Dissertation, Institute for Environment and Resources, Vietnam National University, Ho Chi Minh city, 159pp.

[13] N.T Dang, T.B. Thai, V.M. Pham (1980), *Classification of Freshwater Invertebrate Zoology in North Viet Nam*, Science and Technology Publisher, Hanoi.

[14] T. Mizuno, E. Takahashi (1993), *An Illustrated Guide to Freshwater Zooplankton in Japan*, Tokai University Press, Japan, 556pp.

[15] J.H. Day (1967), *Monograph on the Polychaeta of Southern Africa*, Part 2: Sedentaria, Trustees of the British Museum (Natural History), London, 878pp.

[16] Y. Dejian, S. Ruping (1988), *Polychaetous Annelids Commonly Seen from the Chinese Waters*, China Agriculture Publisher, 352pp.

[17] Fauchald, Kristian (1977), "The polychaeta worms, definitions and keys to the orders, families and genera", *Natural History Museum of Los Angeles County, Science Series*, **28**, pp.1-188.

[18] P. Fauvel (1953), *The Fauna of India Including Pakistan, Ceylon, Burma and Malaya. Annelida Polychaeta*, Indian Press, 507pp.

[19] P.V. Usakov (1955), *URRS Fauna - Polychaeta*, URRS Academy Publisher, Moscow, 448pp.

[20] R.A.M. Brandt (1974), *The Non - Marine Aquatic Mollusca of Thailand*, Waldeman Kramer Publisher, 423pp.

[21] E.F. Gurianova (1951), *Amphipoda of URRS Sea and Neighboring Waters (Amphipoda - Gammaridea)*, URRS Academy Publisher, Moscow, 1029pp.

[22] D. Chapman (1996), *Water Quality Assessments: a Guide to the Use of Biota, Sediments and Water in Environmental Monitoring*, Great Britain at the University Press, Cambridge, 651pp.

[23] P. Stiling (2002), *Ecology: Theories and Applications,* Prentice Hall, 403pp.

[24] C.J. Krebs, et al. (1989), *Ecological Methodology*, Harper Collins Publishers, New York, 620pp.

[25] A.D. Pham, T.M.L. Nguyen, M.T. Dang, V.M. Pham (2016), "Zooplankton from Can Giuoc river in southern Vietnam", *GeoScience Engineering*, **62(3)**, pp.27-33, DOI: 10.1515/gse-2016-0022.

[26] T.T.H. Nguyen, A.D. Pham, V.M. Pham (2017), "Changes of benthic macroinvertebrates in Thi Vai river and Cai Mep estuaries under polluted conditions with industrial conditions", *GeoScience Engineering*, **63(2)**, pp.19-25, DOI: 10.1515/gse-2017-0008.

[27] J. Xue, J. Yang, Q. Wang, R.B. Aronson, H. Wu (2019), "Community structure of benthic macroinvertebrates in reclaimed and natural tidal flats of the Yangtze river estuary", *Aquaculture and Fisheries*, **4(5)**, pp.205-213.

[28] S.A.R. Balqis, F.M Yusoff, J. Nishikawa, D. Lindsay, S. Nishida (2019), "Influence of environmental parameters on habitat preference of gelatinous zooplakton in various coastal ecosystems, the straits of Malacca", *Regional Studies in Marine Science*, **30**, pp.1-9, DOI: 10.1016/j.rsma.2019.100712.

DOI: 10.31276/VJSTE.62(4).08-17

Removal of methylene blue from simulated wastewater by *Carica papaya* wood biosorbent

Thi Nhu Ngoc Nguyen*, Thi Thanh Hang Huynh, Thi Hien To

Faculty of Environment, University of Science, Vietnam National University, Ho Chi Minh city

Received 4 September 2020; accepted 3 December 2020

Abstract:

In this study, batch and continuous-flow sorption experiments were conducted to evaluate the removal of methylene blue (MB) from aqueous solutions by *Carica papaya* wood (CPW) biosorbents. The effects of critical factors such as initial pH, particle size of the biosorbent, biosorbent dosage, initial dye concentration, contact time, and salt ionic strength were studied in batch experiments. The equilibrium data fit well to the Langmuir isotherm model with the highest monolayer adsorption capacity of 63.29 mg/g at an initial dye concentration of 50 mg/l, pH of 10, and contact time of 60 min. Batch desorption and regeneration studies using 0.1 M HCl as the desorbing agent indicated that the removal efficiency of MB lasted up to 5 cycles. Continuous-flow biosorption experiments were investigated to determine the practical applicability of the biosorbent. The dye removal efficiency increased with an increase in absorbent dosage and decreased with an increase in flow rate. The Thomas model was found to be in good agreement with all the experimental data collected from continuous flow sorption. It was concluded that this study presented CPW as a promising biosorbent material for the removal MB from aqueous solutions.

Keywords: **biosorption, *Carica papaya* wood, desorption, methylene blue.**

Classification number: **5.1**

Introduction

Dye application occurs in several industries such as the textile, paper and pulp, paint, printing, rubber, and cosmetics industries. During the dyeing process, 1-15% of the dye is lost in the effluent discharge that generates endless quantities of dye-containing wastewater [1]. Synthetic dyes, characterized by complex aromatic structures, are stable enough to withstand heat and light and are considered non-biodegradable [2, 3]. Discharge of these dyes into effluent may impart toxicity to aquatic life and may be carcinogenic or mutagenic to human beings, which causes serious damage such as dysfunction of the kidneys, reproductive system, liver, brain, and central nervous system [4-6]. Methylene blue (MB) is a cationic dye that is widely used in dyeing cotton, wool, coloured paper, and coatings for paper stocks [7]. Table 1 represents the general characteristics of methylene blue.

Table 1. General characteristics of methylene blue.

Particulars	Methylene blue
Molecular structure	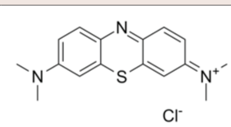
Chemical formula	$C_{16}H_{18}N_3SCl$
Formula weight (g/mol)	319.85
Class	Cationic thiazine dye
Colour Index number	52015
Colour Index name	Basic Blue 9 (BG 9)
λ_{max} (nm)	664

Among the various techniques of dye removal, adsorption is a preferred procedure that demonstrates good performance as it can be used to remove different types of colour from materials [8-10]. Adsorption has been considered a superior method for water treatment in terms of its flexibility, initial cost, simplicity of design, ease of operation, and insensitivity to toxic substances. In addition,

*Corresponding author: Email: ngtnngoc@hcmus.edu.vn

adsorption does not result in the production of any hazardous pollutants [11]. Activated carbon is the most commonly used adsorbent in industry today, but the running costs are expensive [12]. In recent years, numerous works have been focused on the development of cheaper and more effective adsorbents. Lignocellulosic biomass has been found as a potential alternative material because these materials, including natural substances and agricultural residues, are cheap, abundant, and environmentally friendly.

Fig. 1. *Carica papaya* plant.

Carica papaya, popularly known as pawpaw, is an herbaceous fruiting plant belonging to the Caricaceae family (Fig. 1). The composition of *Carica papaya* wood (CPW) consists of crude fibre (30.11±2.67%), protein (4.96±0.68%), and mineral ash (5.92±1.02%) [13]. CPW is a lignocellulosic biomass that mainly contains cellulose, hemicellulose, and lignin, which includes the active functional groups of carboxyl, hydroxyl, sulfhydryl, aldehydes, and ketones on the surface.

The aim of this study was to identify the biosorption potential of CPW in batch and dynamic flow systems from February to June 2018. Batch experiments were conducted to consider the influence of various operational factors such as pH, biosorbent particle size, biosorbent dosage, initial dye concentration, contact time, and salt ionic strength on the dye biosorption process. Also, the biosorbents were able to be regenerated and recyclable over many cycles. Equilibrium adsorption data were analysed by the Langmuir and Freundlich isotherm models and the constants of the isotherm equations were calculated. The continuous-flow experiments were investigated to study the effect of critical factors such as feed flow rate and biosorbent dosage. The Thomas model was used to describe the continuous-flow experimental data.

Materials and methods

Preparation of biosorbent

Carica papaya wood biomass was collected from the felled trunk of a matured papaya tree. The barks were removed, cut into small pieces and washed three times with tap water and three times with distilled water to remove dirt. After that, the biomass was dried to a constant weight at 110°C for 24 h. The dried materials were then sieved in particle sizes of 0.25, 0.5, 0.75 and 1 mm. Finally, the biosorbents were kept in airtight plastic bottles to avoid atmospheric moisture. CPW for this study was carried out without any additional pre-treatment [14].

Solutions and reagents

The stock solution of 500 mg/l of MB was prepared by dissolving 500 mg of dye in 1000 ml distilled water. All working solutions, ranging between 10 and 300 mg/l, were prepared from the stock solution by dilution with distilled water. For pH adjustment, NaOH 0.1 M and HCl 0.1 M were used.

Characterization of biosorbent

Characterization of lignocellulosic biomass has been performed by scanning electron microscopy (SEM), Fourier-transform infrared (FTIR) spectroscopy analysis, and Brunauer-Emmett-Teller (BET) analysis.

Determination of pH_{pzc} of the adsorbent

The point of zero charge (pH_{pzc}) of the biosorbent is defined as the pH at which its surface has a net neutral charge. Fifty millilitres of 0.1 M potassium nitrate was put into a series of 250 ml Erlenmeyer flasks. The solution was adjusted to an initial pH (pH_0) range between 2-10 using either 0.1 M HCl or 0.1 M NaOH. Then, 0.1 g of CPW was added to each flask and the final pH (pH_f) of the solution was measured after 24 h under an agitation speed of 150 rpm at room temperature (about 33°C). The difference between the initial pH and final pH values was calculated as $\Delta pH = pH_0 - pH_f$ and ΔpH was plotted as a function of pH_0. The pH_0 value with a ΔpH equal to zero was called the pH_{pzc} of the biosorbent [14].

Batch biosorption studies

Batch biosorption studies were carried out to evaluate the influence of pH of the dye solution (2-12 pH), biosorbent dosage (0.1-0.8 g), particle size of the biosorbent (0.25-1 mm), and salt ionic strength (NaCl concentration 0.01-0.5 mol/l) using 50 ml of initial MB concentration (20-300 mg/l) placed in 250 ml Erlenmeyer flasks and agitated at 150 rpm for a suitable contact time (30-150 min) at room temperature. The samples were then centrifuged and the supernatant was analysed to determine the residual MB concentration. The remaining amount of dye was determined using a UV/VIS spectrophotometer at a wavelength of 664 nm. The amount of dye adsorbed onto the biosorbent (mg dye per g biosorbent) was calculated based on Eq. (1):

$$q_e = \frac{(C_0 - C_e)\ x\ V}{m} \tag{1}$$

where q_e is the amount of dye adsorbed at equilibrium (mg/g); C_0 and C_e are the initial and equilibrium concentrations of the MB solution (mg/l), respectively; V is the volume of solution (l); and m is the amount of biosorbent (g).

The percent removal (%) of MB was calculated using the following equation:

$$Removal = \frac{C_0 - C_e}{C_0}\ x\ 100 \tag{2}$$

Biosorption isotherm studies

The Freundlich and Langmuir isotherms were studied by varying the dye concentration from 50-300 mg/l at a pH of 10 with an adsorbent dosage of 0.2 g, agitation speed of 150 rpm, and contact time of 30 min.

Desorption and regeneration study

Desorption of the dye from the spent adsorbent was carried out to consider its reusability. The MB-loaded CPW, after the sorption process in the optimal experimental conditions, was dried to a constant weight at 110°C for 24 h. Then, the spent adsorbent was put in contact with 50 ml of 0.1 M HCl, used as the desorbing agent, for 2 h with an agitation speed of 150 rpm. The biosorbent was thoroughly washed with distilled water several times to attain a neutral pH and then was dried in the oven. The regenerated adsorbent was reused for further adsorption studies and the sorption-desorption process was repeated for five cycles. The loss in biomass weight was determined and the biomass was then used for resorption experiments.

Continuous-flow sorption experiments

Continuous-flow sorption experiments were conducted in a 10-ml medical syringe. The biosorbent was packed into the syringe to yield the desired mass. The bottom of the syringe was covered with a layer of glass fibre in order to prevent loss of adsorbent. The MB concentration of 50 mg/l at an optimal pH of 10 flowed downward through the column at a flow rate controlled by a valve. The experiments were carried out to evaluate the influence of the feed flow rate (1, 2, 3, 4, 6 ml/min) and biosorbent mass (0.2, 0.4, 0.6, 0.8, 1.0 g). All the experiments were performed at room temperature. Operation of the continuous-flow experiments was stopped when the effluent concentration of the dye exceeded 99.5% of the initial concentration. The Thomas model was used to analyse the continuous-flow biosorption data.

Results and discussion

Characteristics of CPW

SEM analysis: SEM images (Fig. 2) were taken before adsorption at the two different magnifications (1000x and 3000x) to investigate the surface morphology of the adsorbent. SEM analysis revealed that the surface of the CPW biosorbent had a rough, uneven, and compact structure. Such a structural configuration provides attachment sites for the MB molecules.

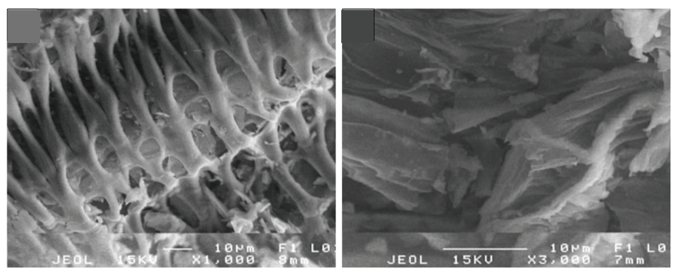

(A) (B)

Fig. 2. SEM images of CPW at two different magnifications of 1000x (A) and 3000x (B).

FTIR analysis: FTIR analysis was used to determine the functional groups of the adsorbent and their responsibility in MB adsorption. The FTIR spectra of CPW (Fig. 3) displayed a number of absorption peaks that indicate the complex nature of the biosorbent. The broad bands at 3390 cm^{-1} represent bonded –OH groups [15]. The peak at 2927.41 cm^{-1} could be assigned to the –CH groups in the lignins of CPW. The peak at 1745.26 cm^{-1} corresponds to C=O functional groups from the lactones and quinones. The functional group –C=O, from the stretching of the amid-I band in the protein peptide bond, is represented at 1610.27 cm^{-1} [16]. The COO− peak located at 1421.28 cm^{-1} represents the carboxylate functional groups. At wave number 1317.14 cm^{-1}, a peak is observed that may be due to the C–N stretching vibrations. The peak at 1238.08 cm^{-1} denotes the bending modes of functional groups O–C–H, C–C–H, and C–O–H. A broad band around 1052.94 cm^{-1} confirmed the presence of the functional group C–O–C from the cellulose and lignin structures of CPW. The peak observed at 638.323 cm^{-1} could be assigned to the stretching of the C–Cl functional groups [17, 18].

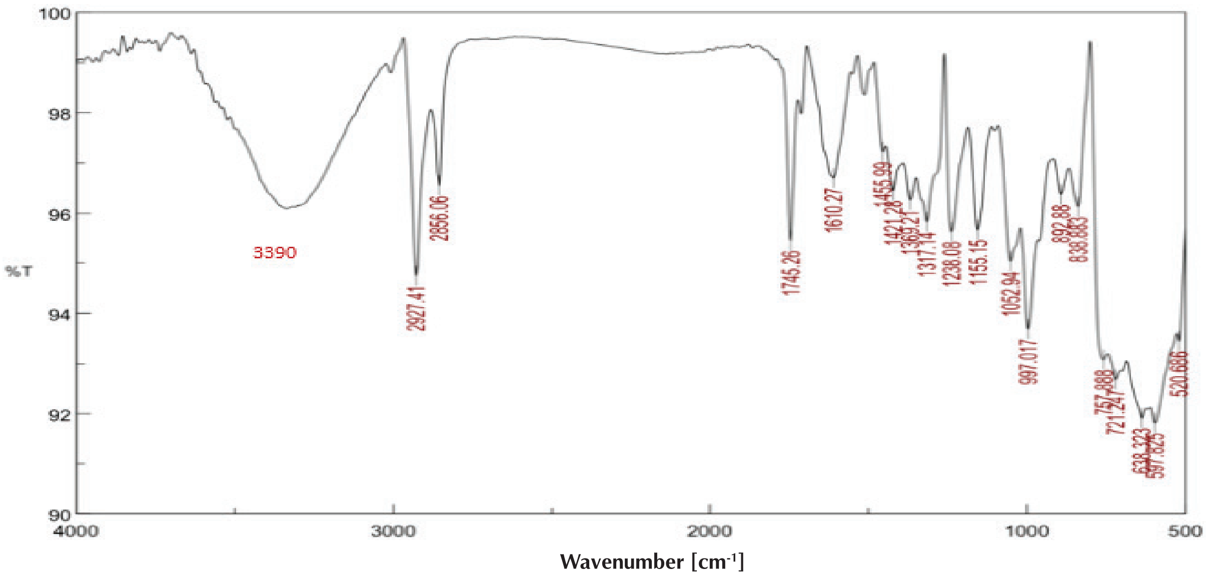

Fig. 3. FTIR spectra of CPW.

BET analysis: the BET surface area of the CPW adsorbent was found to be 0.222 m^2/g. This result indicates that the surface area of the CPW adsorbent was low with a total pore volume of 1.2 cm^3/g. These results were consistent with SEM images that revealed the CPW structure to be without voids. In addition, this examination was similar to previous literature of the BET surface area of lignocellulosic adsorbents that are of agricultural origin [19].

Batch biosorption studies

Determination of pH_{pzc} of the adsorbent: the point of zero charge (pH_{pzc}) is an important parameter that determines the linear range of pH sensitivity and indicates types of surface active centres and the adsorption abilities of surfaces [20]. A plot of ΔpH ($\Delta pH = pH_0 - pH_f$) versus pH_0 for CPW is shown in Fig. 4. The pH_{pzc} of CPW was determined to be approximately 7.3. The pH_{pzc} of material showed that the CPW surface was positively charged at a solution pH<7.3 and negatively charged at a solution pH>7.3. This favours the biosorption of cationic dye-like MB.

Effect of pH: the pH plays an important role in the sorption process as it strongly affects the surface charge of the biosorbent, the degree of ionization of the adsorptive molecule, and the speciation of the biosorbate species. Fig. 5 shows the biosorption of MB by CPW over the pH range of 2 to 12. It was found that the uptake of the dye on CPW was increased with an increase in pH of the dye solution. The biosorption capacity and removal percentage of CPW for the sorption of dye was observed to increase from 7.65 to 23.38 mg/g and 30.61 to 93.51%, respectively, for an initial pH increase from 2 to 12. With a solution pH<6, the dye removal by CPW showed a decrease in performance because the acidic aqueous solution produced more H^+ ions that resulted in protonation of the adsorbent surface. The lower sorption of the dye at lower pH may be because of the effects of electrostatic repulsion and competition for the biosorption sites between the excess H^+ ions and cationic groups on the dye. When the solution pH increases above pH_{pzc}, the surface of CPW becomes negatively charged due to an increase in the number of OH^- while at the same time the number of H^+ decreased. A negatively charged biosorbent

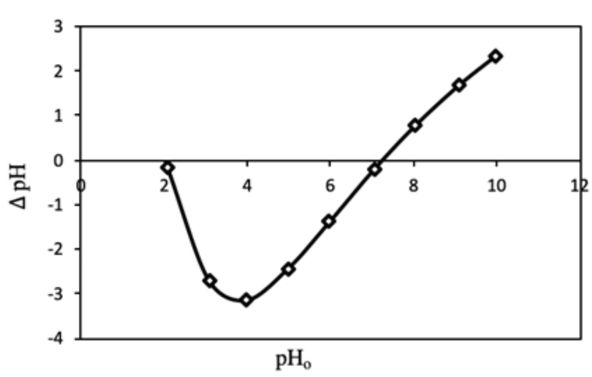

Fig. 4. pH_{PZC} of CPW.

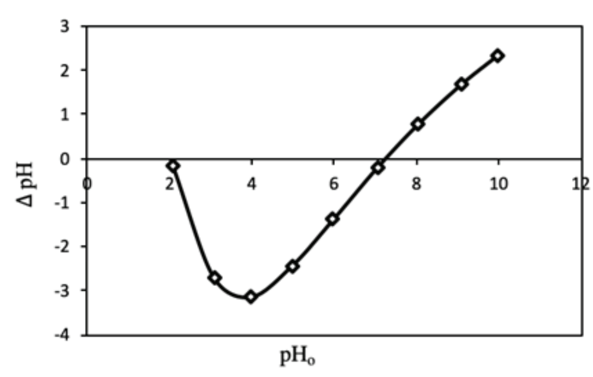

Fig. 5. Effect of initial pH on the adsorption of MB onto CPW.

surface favours the uptake of MB (or any positively charged or cationic dyes) through electrostatic attraction forces [21]. These results are in agreement with the ranges of optimal pH ($pH>pH_{pzc}$) for MB adsorption by CPW. The highest percentage of colour removal was attained at an initial pH of 10. The decrease in the adsorption of dye after a pH of 10 was insignificant. Hence, all further experiments were carried out at pH 10.

Effect of biosorbent particle size: the biosorbent particle size is a critical parameter in the sorption process because it determines the time required for the transport of sorbate within the pore to the adsorbent's active sites. The effect of the absorbent's particle size on the uptake of MB is shown in Fig. 6. When the particle size of the absorbent increased from 0.25 to 0.5 mm, the dye removal efficiency and biosorption capacity were almost unchanged. However, with further increase in particle size, the adsorption percentage and equilibrium sorption capacity decreased sharply. This decrease was attributed to a decrease in the surface area of the adsorbents at larger particle sizes, which provided fewer active sites to be utilized for the sorption of MB molecules [22]. Consequently, further experiments utilized at particle size of 0.5 µm when the effects of other experimental parameters were studied in order to achieve optimum adsorption.

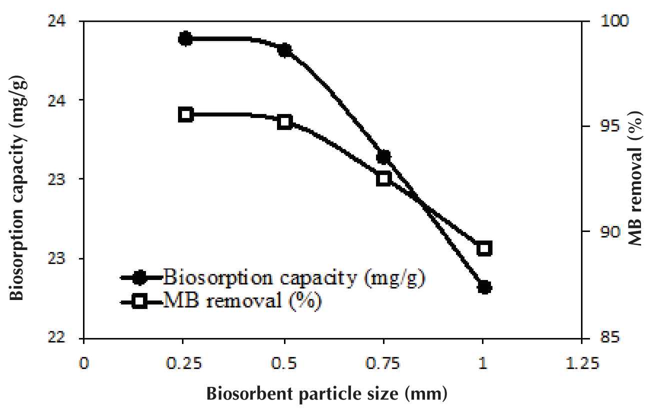

Fig. 6. Effect of biosorbent particle size on the adsorption of MB onto CPW.

Effect of biosorbent dosage: the influence of adsorbent dosage on the uptake of dye was identified by varying the amount of adsorbent from 0.1 to 0.8 g while 50 mg/l initial MB concentration and optimal pH of 10 were kept constant. The equilibrium sorption capacity and the percentage of colour removal for the different adsorbent dosages are depicted in Fig. 7. It was observed that the increase in the biosorbent dosage from 0.1 to 0.2 g resulted in an increase of removal percentage from 92.47 to 94.39%, whereas the sorption capacity of the adsorbent presented a decrease in the effect from 23.12 to 11.8 mg/g. The increase in the biosorption of MB with an increase in the adsorbent dosage was due to the higher surface area of the adsorbent and the greater number of active sites on the adsorbent. When the dose was increased above 0.2 g, the sorption of dye and the biosorption capacity decreased sharply. This can be explained by the fact that at high biosorbent dosages, the fixed number of MB molecules in solution were not enough to completely combine with all the binding sites on the biosorbent, which resulted in a reduction of the adsorption capacity per unit mass of adsorbent. Another reason for the lower percentage of colour removal is interparticle interactions such as aggregation resulting from high biosorbent concentrations. Such aggregation results in a decrease in total surface area of the adsorbent and an increase in the length of diffusion. Hence, 0.2 g of CPW was found to be optimum.

Effect of initial dye concentration: the influence of the initial concentration of dye on the equilibrium biosorption of MB by CPW was evaluated by using 0.2 g adsorbent, a solution pH of 10, and varying MB concentration from 20 to 300 mg/l. As shown in Fig. 8, the equilibrium sorption capacity increased from 4.81 to 53.08 mg/g with increased initial MB concentration. This was a result of an increase in the driving force from the concentration gradient. In addition, the binding sites of the adsorbent are surrounded by much more MB ions at high concentration of dye, which supports the accessibility for biosorption [23]. In addition, at lower MB concentrations

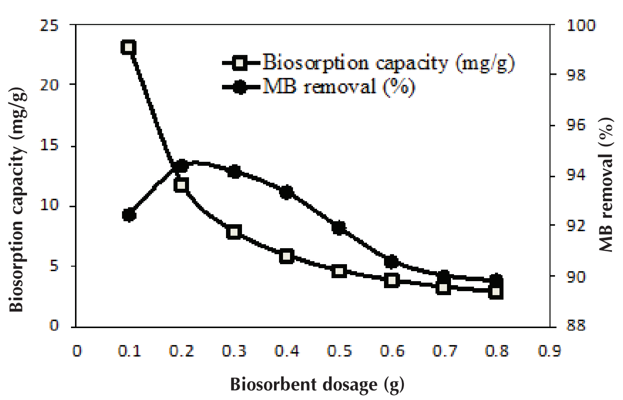

Fig. 7. Effect of biosorbent dosage on the adsorption of MB onto CPW.

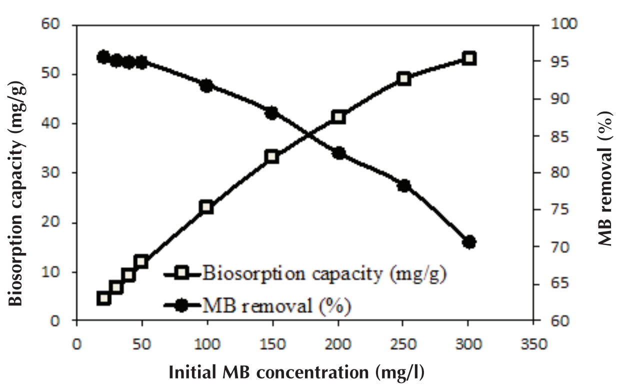

Fig. 8. Effect of initial dye concentration on the adsorption of MB onto CPW.

(20-50 mg/l), all the dye molecules are able to interact with the large number of binding sites, hence, a higher percentage of dye removal. An increase in the MB concentration (>50 mg/l) occurred from the decrease in the biosorption of dye due to the saturation of active sites [24]. Fig. 8 showed that a high removal efficiency was attained at an initial MB concentration of 50 mg/l.

Effect of contact time: the results of changing contact time is represented in Fig. 9. It can be seen that the uptake of dyes was rapid in the initial adsorption period (in the first 60 min). The fast biosorption rate at this initial stage indicates the instantaneous adsorption or external surface adsorption of MB onto CPW [25]. In addition, the higher uptake rate in the initial period may be because of the greater number of binding sites available on the biosorbent and because of the strong attractive forces between the biosorbent and dye molecules. At longer contact times (after 60 min) the rate of biosorption decreased and tended to slow down. After 90 min, the curve plateaued, which showed no considerable adsorption of dye. It can be explained that the number of active sites available for sorption decreased. However, the percentage of MB removal increased slightly from 95.22 to 97.25% for a contact time increase from 30 to 60 min. Therefore, the optimal time for the sorption of the dye was 30 min with 95.22% MB removal efficiency.

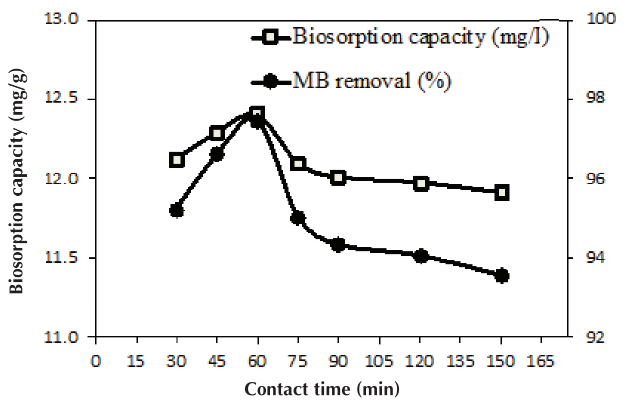

Fig. 9. Effect of contact time on the adsorption of MB onto CPW.

Effect of salt ionic strength on the dyes biosorption: textile industries consume large amounts of salt during the dying process, so the influence of salts on biosorption was evaluated in this study. The variation of the salt concentration depends on the source and type of the industrial effluents [26]. Sodium chloride (NaCl) is known as a stimulator in the dying process, which can affect electrostatic interactions of the dye molecules. To examine how salt concentration affects the biosorption of MB onto CPW, the experiment was carried out with varying NaCl concentrations from 0.01-0.5 M in the dye solution. The results are illustrated in Fig. 10. It was found that the sorption of dye decreased from 85.70 to 41.72% for the increase in the NaCl concentration from 0.01 to 0.5 M. The uptake of dye was significantly affected by the presence of high NaCl concentrations. The decrease in the percentage of dye removal was due to the competition between MB and Na^+ cation for the adsorption of active sites on the biosorbent. Thus, the increase in ionic strength led to a decrease in the adsorption potential of CPW for MB removal. Previous literature also reported that MB adsorption declined considerably with the presence of NaCl in aqueous solutions [27].

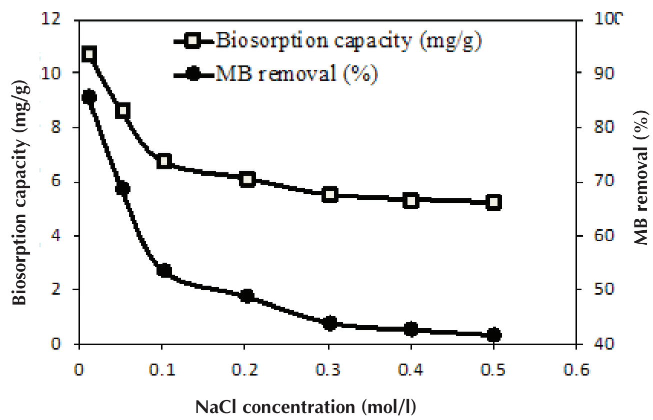

Fig. 10. Effect of NaCl concentrations on the adsorption of MB onto CPW.

Adsorption isotherm: analysis of the adsorption isotherm is of fundamental importance to the evaluation of the interaction of adsorbate molecules with the adsorbent surface. Isotherm studies also calculate the maximum biosorption capacity and equilibrium constants, which express the affinity of the biosorbent. The Freundlich and Langmuir isotherm models were applied to describe the equilibrium biosorption data (Fig. 11).

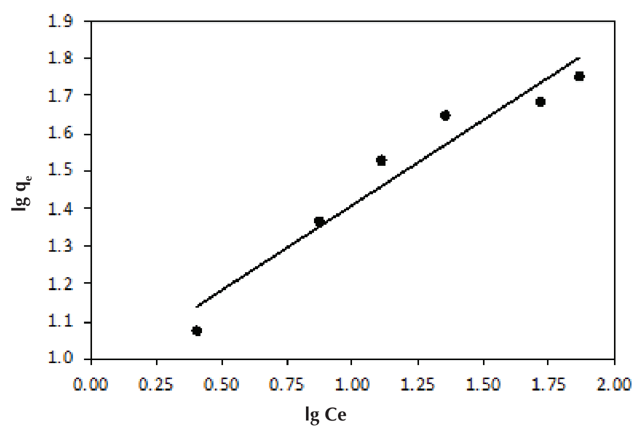

Fig. 11. Freundlich isotherm plots for MB biosorption onto CPW.

The Freundlich model: the Freundlich model is an empirical equation that can be applied to multilayer sorption with a non-uniform distribution of sorption heat and affinity over the heterogeneous surface. The Freundlich equation is given as:

$$q_e = K_F C_e^{1/n} \quad (3)$$

where K_F is Freundlich constant, which is an indicator for adsorption capacity, and 1/n is the adsorption intensity. A value of 0<1/n<1 shows adsorption surface homogeneity. As the value gets closer to 0, the adsorption process is heterogeneous [28]. A value for 1/n<1 shows a normal Langmuir isotherm while 1/n>1 indicates cooperative adsorption [29]. The linear form of the Freundlich equation is given as:

$$lgq_e = lgK_F + \left(\frac{1}{n}\right) lgC_e \quad (4)$$

The values of K_F and n are listed in Table 2. Both the values are calculated from the intercept and slope of the plot of lgq_e versus lgC_e. The value of 1/n is 0.45, from a range between 0 and 1, which showed that the dye uptake by CPW is favourable for sorption. Moreover, the K_F constant of 9.1 l/g indicated a high dye uptake capacity.

The Langmuir model: the Langmuir adsorption model assumes that the adsorbent surface is homogeneous in character and the formation of a monolayer takes place on the surface of the adsorbent. The Langmuir model is given by the following equation:

$$q_e = \frac{Q_0 K_L C_e}{1 + K_L C_e} \quad (5)$$

where Q_0 is the maximum amount of the adsorbed dye per unit mass of adsorbent to form a complete monolayer on the surface bound at concentration C_e (mg/g) and K_L (l/mg) is the Langmuir constant related to the affinity of the binding sites. The Langmuir model can be represented in linear form as:

$$\frac{C_e}{q_e} = \frac{1}{Q_0 K_L} + \frac{C_e}{Q_0} \quad (6)$$

The essential characteristics of the Langmuir isotherm can be expressed in terms of the separation factor R_L, which is a dimensionless constant in Eq. (7):

$$R_L = \frac{1}{(1 + K_L C_0)} \quad (7)$$

A favourable biosorption takes place if $0<R_L<1$, whereas $R_L>1$ shows unfavourable biosorption, $R_L=1$ shows linear biosorption conditions, and $R_L=0$ shows irreversible biosorption conditions [30].

The linear plot of Langmuir isotherm and the plot of the separation factor as a function of initial concentration of MB are shown in Figs. 12 and 13, respectively. The parameters obtained from the Langmuir and Freundlich isotherm plots are listed in Table 2. Analysis of the R values suggests that the Langmuir isotherm model provided a better fitting compared to the Freundlich isotherm models. This implies monolayer coverage of MB molecules onto the CPW surface. This suggestion is consistent with the results of FTIR and SEM shown in Figs. 2 and 3. In essence, the CPW biosorbent has a compact structure without voids, so the adsorption process occurs mainly on the surface of CPW. MB molecules were kept by chemical functional groups such as –OH, C=O, and COO– inside the CPW structure as seen in the FTIR spectrum of Fig. 3. The values of the separation factor, R_L, are between 0 and 1 indicating that the dye uptake by CPW are favourable.

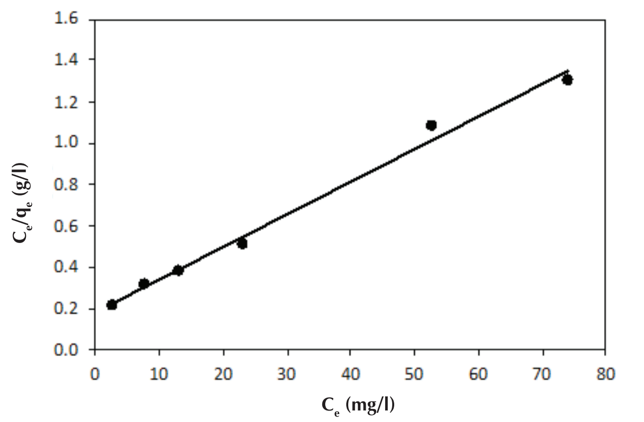

Fig. 12. Langmuir isotherm plots for MB biosorption onto CPW.

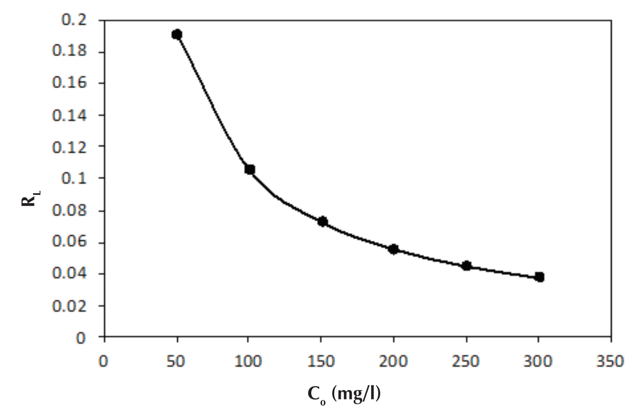

Fig. 13. Effect of initial dye concentration on separation factor.

Table 2. Biosorption isotherm constants for the biosorption of MB onto CPW at room temperature.

Langmuir constants			Freundlich constants		
Q_0 (mg/g)	K_L (l/mg)	R^2	K_F (l/g)	1/n	R^2
63.29	0.085	0.9914	9.1	0.45	0.936

Table 3 summarizes the maximum MB sorption capacity of various low-cost sorbent materials. It can be seen that CPW has high biosorption capacity of MB compare to many of the other reported biosorbents. Differences in the sorption of dye can be explained by the different characteristics of adsorbent materials such as structure, functional groups, and surface area. CPW is an abundant and low-cost material, which makes it a potential biosorbent for the removal of MB from aqueous solutions.

Table 3. Comparison of MB biosorption capacity of CPW with others reported low-cost sorbents.

Adsorbent	Maximum sorption capacity (mg/g)	References
Rice bran	54.99	[31]
Wheat bran	54.79	[31]
Unmodified biomass of barker's yeast	51.5	[11]
Parthenium hysterophorus unwanted weed	39.68	[32]
Coir pith carbon	5.87	[33]
Coconut coir dust	19.61	[34]
Tartaric acid modified bagasse	69.93	[30]
Cereal chaff	20.30	[35]
Carica papaya wood	32.25	[14]
Carica papaya wood	63.29	This study

Desorption and regeneration study: the adsorption capacity of the regenerated biosorbent was carried out over five repeated cycles using 50 ml HCl 0.1 M as the desorbing eluent. The desorption and resorption of MB on the CPW biosorbent is shown in Table 4. The eluent was able to maintain an elution efficiency of more than 90% over the first three cycles, then the efficiency decreased slightly for the next two cycles. However, the final results of the regeneration of MB maintained more than 80% of the sorption of the dye over 5 cycles. Furthermore, a significant biosorbent weight loss was observed during the 4th and 5th regeneration cycles. It is known that the slightly acidic nature of the desorbing agent and the damage in physical-chemical structure of the biosorbent have caused biomass weight loss in subsequent cycles [36]. In addition, the sorption decrease in subsequent cycles may be due to the blockage of the active sites of the biosorbent. The desorption and resorption experiments showed that the CPW has great potential for recycling performance.

Table 4. Desorption and resorption of MB on CPW biosorbent.

Cycle no.	MB removal (%)	Weight loss (%)
1	94.68	7.5
2	94.09	15
3	93.27	26
4	88.48	41.25
5	85.25	48.75

Continuous-flow sorption study

Effect of flow rate: the flow rate is a significant characteristic of the sorption process in the continuous treatment of wastewater on an industrial scale [37]. In this study, the influence of flow rate on MB removal by CPW was performed by varying the flow rate in the range of 1-5 ml/min, maintaining an initial MB concentration of 50 mg/l, solution pH of 10, and absorbent dose of 0.2 g optimized in batch studies. The effect of flow rate on the percentage of dye removal with the above operating conditions is depicted in Fig. 14. It was observed that the uptake of dye was higher at a lower flow rate. At a lower flow rate, there is an increased contact time with the MB solution and therefore the dye had more time to bind with the active sites in the adsorbent [38]. The MB molecules also have more time to diffuse into the pores of the biosorbent through intraparticle diffusion. As the flow rate is increased, the residence time of the MB solution in the column decreases. Then, the residence time of the solute in the column is not large enough for the dye molecules to diffuse into the pores of the adsorbent and capture the active sites on the biosorbent surface leaving the column before equilibrium occurs [39]. Considering the percentage of dye removal and economic efficiency, further experiments were carried out at a flow rate of 2 ml/min.

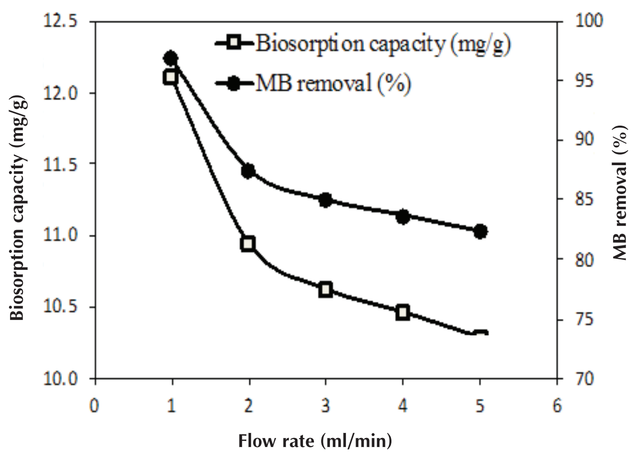

Fig. 14. Effect of flow rate on MB removal in continuous-flow biosorption study.

Effect of absorbent dosage: the experiments were conducted at adsorbent dosages of 0.2 to 1.0 g at a constant flow rate of 2 ml/min and feed concentration of 50 mg/l. The effect of the biosorbent dosage on MB removal in the continuous-flow experiments is represented in Fig. 15. As the absorbent dose is increased by a factor of 2 from 0.2 to 0.4 g, the MB removal efficiency sharply increased from 87.55 to 95.54%. Then, the removal efficiency showed no significant change as the biosorbent dosage was increased, which demonstrated that 0.4 g should be chosen as the optimal biosorbent dosage for the remaining experiments.

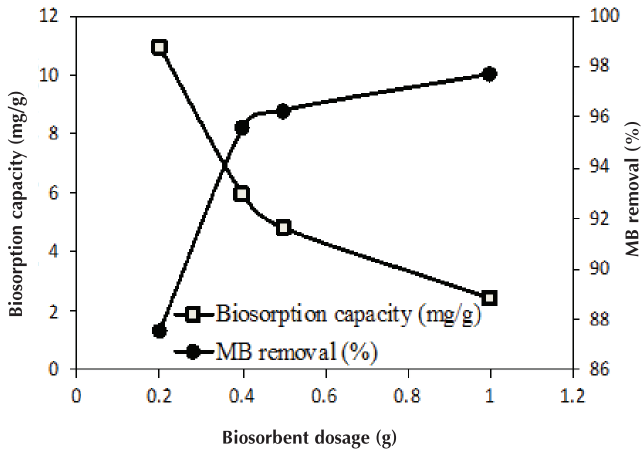

Fig. 15. Effect of biosorbent dosage on MB removal in continuous-flow biosorption study.

Application of Thomas model: the Thomas model is one of the most common and widely used models to estimate the adsorption in column performance theory. The model is based on the assumption that the process follows second-order reversible reaction kinetics and the Langmuir isotherm [40]. The linearized form of the Thomas model can be expressed as follows:

$$\ln\left(\frac{C_0}{C_t}-1\right)=\frac{k_{Th}q_0 w}{Q}-k_{Th}C_0 t$$

where k_{Th} (ml/min/mg) is the Thomas rate constant; q_o (mg/g) is the equilibrium MB uptake per g of the adsorbent; C_o (mg/l) is the influent dye concentration; C_t (mg/l) is the effluent dye concentration at time t; w (g) is the mass of adsorbent in the column, and Q (ml/min) is the flow rate. A linear plot of $\ln(C_0/C_t$-1) versus time (t) is depicted in Fig. 16. The values of k_{Th} and q_o are determined from the intercept and slope of the plot. The values of k_{Th} and q_o, calculated from Eq. (8), were 2.6×10^{-4} (ml/mg/min) and 80.47 mg/g, respectively. The relatively high R^2 (R^2=0.9747) value suggests that the Thomas model was suitable to describe the column data of MB by CPW. The calculated q_e values (q_o=81.82 mg/l) show good agreement with the experimental q_e values (q_e=79.4 mg/l), which further confirms the suitability of the Thomas model for column design and analysis.

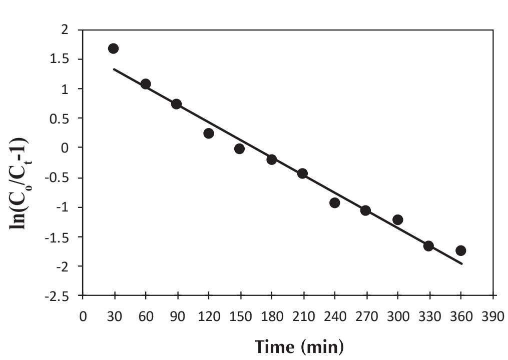

Fig. 16. Thomas model plots for the biosorption of MB onto CPW.

Conclusions

The present study on the adsorption of MB using CPW suggested the following conclusions:

- The results showed that equilibrium was attained within 30 min and the maximum adsorption capacity of MB onto CPW was obtained after contact with 0.2 g of biosorbent, a biosorbent particle size of 0.5 mm, initial solution pH of 10.0, and dye concentration of 50 mg/l. The experimental data showed an excellent fit to the Langmuir isotherm equation, which provided a 63.29 mg/g monolayer biosorption capacity of MB onto CPW.

- Continuous-flow biosorption experiments indicated that the adsorbent dosage and flow rate affected the biosorption characteristics of CPW with a biosorbent dosage of 0.4 g and a flow rate of 2 ml/min resulting in optimal MB removal. The Thomas model adequately described the biosorption of MB onto CPW by a continuous-flow mode.

- The biomass from *Carica papaya* wood has been shown to be highly effective in removing MB from an aqueous solution. The study revealed that this new biosorbent is a very prospective adsorbent for the removal MB from industrial wastewater.

COMPETING INTERESTS

The authors declare that there is no conflict of interest regarding the publication of this article.

REFERENCES

[1] S. Manna, D. Roy, P. Saha, D. Gopakumar, S. Thomas (2017), "Rapid methylene blue adsorption using modified lignocellulosic materials", *Safety and Environment Protection*, **107**, pp.346-356.

[2] J. Song, W. Zou, Y. Bian, F. Su, R. Han (2011), "Adsorption characteristics of methylene blue by peanut husk in batch and column modes", *Desalination*, **265**, pp.119-125.

[3] V. Vimonses, S. Lei, B. Jin, C.W.K. Chow, C. Saint (2009), "Kinetic study and equilibrium isotherm analysis of Congo Red adsorption by clay materials", *Chemical Engineering Journal*, **148**, pp.354-364.

[4] K. Kadirvelu, M. Kavipriya, C. Karthika, M. Radhika, N. Vennilamani, S. Pattabhi (2003), "Utilization of various agricultural wastes for activated carbon preparation and application for the removal of dyes and metal ions from aqueous solutions", *Bioresource Technology*, **87**, pp.129-132.

[5] A.R. Dincer, Y. Günes, N. Karakaya, E. Günes (2007), "Comparison of activated carbon and bottom ash for removal of reactive dye from aqueous solution", *Bioresource Technology*, **98**, pp.834-839.

[6] D. Shen, J. Fan, W. Zhou, B. Gao, Q. Yue, Q. Kang (2009), "Adsorption kinetic sand isotherm of anionic dyes onto organo - bentonite from single and multisolute systems", *Journal of Hazardous Materials*, **172**, pp.99-107.

[7] M.T. Uddin, M.A. Islam, S. Mahmud, M. Rukanuzzaman (2009), "Adsorptive removal of methylene blue by tea waste", *Journal of Hazardous Materials*, **164**, pp.53-60.

[8] A.K. Jain, V.K. Gupta, A. Bhatnagar, Suhas (2003), "Utilization of industrial waste products as adsorbents for the removal of dyes", *Journal of Hazardous Materials*, **B101**, pp.31-42.

[9] Y.S. Ho, G. McKay (2003), "Sorption of dyes and copper ions onto biosorbents", *Process Biochemistry*, **38**, pp.1047-1061.

[10] F. Derbyshire, M. Jagtoyen, R. Andrews, A. Rao, I. Martin-Gullon, E. Grulke (2001), "Carbon materials in environmental applications", *Chemistry and Physics of Carbon*, **27**, pp.1-66.

[11] M. Rafatullah, O. Sulaiman, R. Hashim, A. Ahmad (2010), "Adsorption of methylene blue on low-cost adsorbents: a review", *Journal of Hazardous Materials*, **177**, pp.70-80.

[12] S. Wang, Z.H. Zhu, A. Coomes, F. Haghseresht, G.Q. Lu (2005), "The physical and surface chemical characteristics of activated carbons and the adsorption of methylene blue from wastewater", *Journal of Colloid and Interface Science*, **284**, pp.440-446.

[13] S. Basha, Z.V.P. Murthy, B. Jha (2009), "Sorption of Hg(II) onto Carica papaya: experimental studies and design of batch sorber", *Chemical Engineering Journal*, **147**, pp.226-234.

[14] S. Rangabhashiyam, S. Lata, P. Balasubramanian (2018), "Biosorption characteristics of methylene blue and malachite green from simulated wastewater onto *Carica papaya* wood biosorbent", *Surfaces and Interfaces*, **10**, pp.197-215.

[15] S. Rangabhashiyam, N. Selvaraju (2015), "Adsorptive remediation of hexavalent chromium from synthetic wastewater by a natural and $ZnCl_2$ activated Sterculia guttata shell", *Journal of Molecular Liquids*, **207**, pp.39-49.

[16] T. Akar, B. Anilan, A. Gorgulu, S.T. Akar (2009), "Assessment of cationic dye biosorption characteristics of untreated and non-conventional biomass: Pyracantha coccinea berries", *Journal of Hazardous Materials*, **168**, pp.1302-1309.

[17] R. Han, L. Zhang, C. Song, M. Zhang, H. Zhu, L. Zhang (2010), "Characterization of modified wheat straw, kinetic and equilibrium study about copper ion and methylene blue adsorption in batch mode", *Carbohydrate Polymers*, **79**, pp.1140-1149.

[18] M.C.S. Reddy, L. Sivaramakrishna, A.V. Reddy (2012), "The use of an agricultural waste material, Jujuba seeds for the removal of anionic dye (congo red) from aqueous medium", *Journal of Hazardous Materials*, **203-204**, pp.118-127.

[19] E.D. Asuquo, A.D. Martin, P. Nzerem (2018), "Evaluation of Cd(II) ion removal from aqueous solution by a low-cost adsorbent prepared from white yam (*Dioscorea rotundata*) waste using batch sorption", *Chemical Engineering*, **2**, DOI: 10.3390/chemengineering2030035.

[20] A.A. Poghossian (1997), "Determination of the pHpzc of insulators surface from capacitance - voltage characteristics of MIS and EIS structures", *Sensors and Actuator B: Chemical*, **44**, pp.551-553.

[21] P.S. Kumar, S. Ramalingam, C. Senthamarai, M. Niranjanaa, P. Vijayalakshmi, S. Sivanesan (2010), "Adsorption of dye from aqueous solution by cashew nut shell: studies on equilibrium isotherm, kinetics and thermodynamics of interactions", *Desalination*, **261**, pp.52-60.

[22] K.K. Wong, C.K. Lee, K.S. Low, M.J. Haron (2003), "Removal of Cu and Pb by tartaric acid modified rice husk from aqueous solutions", *Chemosphere*, **50**, pp.23-28.

[23] R. Han, J. Zhang, P. Han, Y. Wang, Z. Zhao, M. Tang (2009), "Study of equilibrium, kinetic and thermodynamic parameters about methylene blue adsorption onto natural zeolite", *Chemical Engineering Journal*, **145**, pp.496-504.

[24] S. Chowdhury, R. Mishra, P. Saha, P. Kushwaha (2011), "Adsorption thermodynamics, kinetics and isosteric heat of adsorption of malachite green onto chemically modified rice husk", *Desalination*, **265**, pp.159-168.

[25] P. Saha, S. Chowdhury, S. Gupta, I. Kumar (2010), "Insight into adsorption equilibrium, kinetics and thermodynamics of malachite green onto clayey soil of Indian origin", *Chemical Engineering Journal*, **165**, pp.874-882.

[26] D. Mitrogiannis, G. Markou, A. Celekli, H. Bozkurt (2015), "Biosorption of methylene blue onto Arthrospira platensis biomass: kinetic, equilibrium and thermodynamic studies", *Journal of Environmental Chemical Engineering*, **3**, pp.670-680.

[27] G. Jian-Zhong, L. Bing, L. Li, L. Kangle (2014), "Removal of methylene blue from aqueous solutions by chemically modified bamboo", *Chemosphere*, **111**, pp.225-231.

[28] B.H. Hameed, D.K. Mahmoud, A.L. Ahmad (2008), "Sorption equilibrium and kinetics of basic dye from aqueous solution using banana stalk waste", *Journal of Hazardous Materials*, **158**, pp.499-506.

[29] K. Fytianos, E. Voudrias, E. Kokkalis (2000), "Sorption desorption behavior of 2,4-dichlorophenol by marine sediments", *Chemosphere*, **40**, pp.3-6.

[30] L.W. Low, T.T. Teng, M. Rafatullah, N. Morad, B. Azahari (2013), "Adsorption studies of Methylene blue and Malachite green from aqueous solutions by pretreated lignocellulosic materials", *Separation Science and Technology*, **48**, pp.1688-1698.

[31] X.S. Wang, Y. Zhou, Y. Jiang, C. Sun (2008), "The removal of basic dyes from aqueous solutions using agricultural by-products", *Journal of Hazardous Materials*, **157**, pp.374-385.

[32] H. Lata, V.V. Garg, R.K. Gupta (2007), "Removal of a basic dye from aqueous solution by adsorption using Parthenium hysterophorus: an agricultural waste", *Dyes and Pigments*, **74**, pp.653-658.

[33] D. Kavitha, C. Namasivayam (2007), "Experimental and kinetic studies on methylene blue adsorption by coir pith carbon", *Bioresource Technology*, **98**, pp.14-21.

[34] K.G. Bhattacharyya, A. Sharma (2005), "Kinetics and thermodynamics of methylene blue adsorption on neem (azadirachta indica) leaf powder", *Dyes and Pigments*, **65**, pp.51-59.

[35] H. Runping, W. Yuanfeng, H. Pan, S. Jie, Y. Jian, L. Yongsen (2006), "Removal of methylene blue from aqueous solution by chaff in batch mode", *Journal of Hazardous Materials*, **137**, pp.550-557.

[36] K. Vijayaraghavan, J. Jegan, K. Palanivelu, M. Velan (2005), "Biosorption of Cobalt (II) and Nickel (II) by seaweeds: batch and column studies", *Separation and Purification Technology*, **44**, pp.53-59.

[37] P.D. Saha, S. Chowdhury, M. Mondal, K. Sinha (2012), "Biosorption of direct red 28 (congo red) from aqueous solutions by eggshells: batch and column studies", *Separation Science and Technology*, **47**, pp.112-113.

[38] A.A. Ahmad, B.H. Hameed (2020), "Fixed-bed adsorption of reactive azo dye onto granular activated carbon prepared from waste", *Journal of Hazardous Materials*, **175**, pp.298-303.

[39] V. Vinodini, N. Das (2010), "Packed bed column studies on Cr(VI) removal from tannery wastewater by neem sawdust", *Desalination*, **264**, pp.9-14.

[40] P.D. Saha, S. Chakraborty, S. Chowdhury (2012), "Batch and continuous (fixed-bed column) biosorption of crystal violet by *Artocarpus heterophyllus* (jackfruit) leaf powder", *Colloids and Surfaces B: Biointerfaces*, **92**, pp.262-270.

DOI: 10.31276/VJSTE.62(4).18-22

Pectin bioplastic films regenerated from dragon fruit peels

Thi Cam Trang Truong[1*], Takaomi Kobayashi[2]

[1]*Faculty of Environmental Sciences, University of Science, Vietnam National University, Ho Chi Minh city, Vietnam*
[2]*Department of Science of Technology Innovation, Nagaoka University of Technology, Japan*

Received 17 August 2020; accepted 10 November 2020

Abstract:

Pectin extracted from dragon fruit peels was used to prepare pectin-based membranes by mixing with the plasticized agent polyethylene glycol (PEG) at pectin to PEG ratios of 5:1, 3:1, and 1:1. SEM images showed the resulting bioplastic films had a transparent yellowish surface without pores or cracks. The water content of the bioplastic films was 29.17, 48.61, and 59.72% for the 5:1, 3:1, and 1:1 ratios, respectively. This showed that the increase in PEG concentration made the bioplastic films weaker and more hydrophilic. The tensile strength of films was 5.0, 4.9, and 2.5 N/mm^2 and the value of optical transmittance was 18, 19, and 24%, for the 5:1, 3:1, and 1:1 ratios, respectively. The significant decrease in tensile strength is attributed to the high concentration of PEG, which lead to the clustering in the material's structure. Therefore, these bioplastic films are applicable to the highly suitable and stable operations of packing materials in the food and medical industries.

Keywords: **bioplastic film, dragon fruit, pectin, polyethylene glycol.**

Classification number: **5.1**

Introduction

Over the past 20 years, the large-scale production and utilization of plastic all over the world has increased dramatically, which entails the issue of waste disposal [1]. In this sense, research on biodegradable films prepared from polysaccharides has been on the rise, which establishes these biopolymers as potential candidates for biodegradable film production [2].

According to the organization European Bioplastics, bioplastics are defined as materials based on renewable resources or those that are biodegradable or compostable [3]. Bio-based plastics are made from polysaccharides such as starches, cellulose, chitin, pectin, proteins like wheat gluten, wool, silk, gelatin, lipids (animal fats), vegetable oils, and products of microorganisms. Pectin is a natural material that appears in a great proportion of fruits and vegetables such as berries, apples, and oranges. Pectin is a mandatory polymer and its use in industry has diverse applications that continues to grow [2]. Pectin is a necessary component in plant cell structure and it consists of α-(1, 4)-linked D-galacturonic acid residues in which a part of the galacturonic acid is esterified or an acetylated methyl or both [4]. Depending on the degree of esterification (DE), pectin is divided into high-methoxyl (HM) pectin (DE>50%) and low-methoxyl (LM) pectin (DE<50%) [5]. Pectin extraction is typically performed by way of solvent extraction from raw materials where all extraction conditions, such as extraction temperature, extraction time, pH, and type of extraction solvent can affect the yield and quality of extracted pectin [4]. Normally, solvents with strong hydrogen bonding capacity are good for polysaccharides [6], which could promote carbohydrate chain spreading. Pectin molecules with a completely extended structure in a good solvent have better steric impediment, which stands in the way of intermolecular flocculation. Pectin has attracted a lot thanks to its exceptional properties; they are able to freeze in the presence of acids and sugars, have a high viscosity, are

*Corresponding author: Email: ttctrang@hcmus.edu.vn

an aqueous-absorbent gel, and easily soluble in water but insoluble in ethanol. Due to the features mentioned, pectin represents a potential polymer for the development of bio-based membranes in the food packaging field [7].

Recently, dragon fruit or pitaya has become a popular fruit due to its attractive appearance and nutrition. It can be processed into a variety of food products such as juice, jam, ice cream, or yogurt. Dragon fruit peel, with up to 39% pectin, instantly becomes a convenient and attractive choice for pectin extraction. In addition, previous research has shown that dragon fruit peel can be used as a raw material for pectin extraction [4]. Like most of the polysaccharides, pectin is glassy in its normal condition, so shrinkage due to water evaporation or swift drying causes defects such as cracks or curling in the films. These films are often brittle and stiff because of extensive interactions between polymer molecules, so the addition of the corresponding plasticizers is required. Plasticizers act by interposing themselves between macromolecular polymeric chains, which reduces cohesion within the film and enhances the free volume inside the film structure [7]. With reference to other reports of polysaccharide-based films, it has been shown that PEG of lower molecular weight exhibits an improved plasticizing effect. PEG is non-toxic, odorless, neutral, slippery, non-volatile, and completely soluble in water, but the solubility decreases with increasing polymer molecular weight. PEG is a non-toxic compound and can be used in pharmaceuticals and food additives (Fig. 1).

Materials and methods

Materials

Fresh dragon fruit peel was collected from solid waste in the Ninh Thuan province, Vietnam. The peels were cut into small pieces and dried at 60°C for 36 h. Chemicals used in the extraction of pectin and preparation of bioplastic membrane such as hydrochloric acid (HCl) and ethanol were supplied by Xilong Chemical Reagent Co., Ltd, China while PEG (400 g/mol) was purchased from LAXOPEG Co., Ltd, India.

Pectin extraction

Pectin from dragon fruit peel was extracted using a method modified from [4]. Specifically, 30 g of the dried dragon fruit peel was added to a mixture of 0.1 M hydrochloric acid in 250 ml of distilled water where the pH was adjusted to 3. The extraction process was carried out at 70°C for 30 min while stirring constantly. The final product was obtained by precipitation with a solvent of 2:1 ethanol-to-pectin. Finally, the precipitate was washed with 45% aqueous ethanol solution and dried in an oven at 50°C for 6 h.

Bioplastic film synthesis

The films were made by mixing pectin from the previous work with PEG at various ratios (5:1, 3:1, and 1:1) while stirring continuously for 30 min [8]. After that, the obtained solution was poured into a petri dish (100x15 mm) and

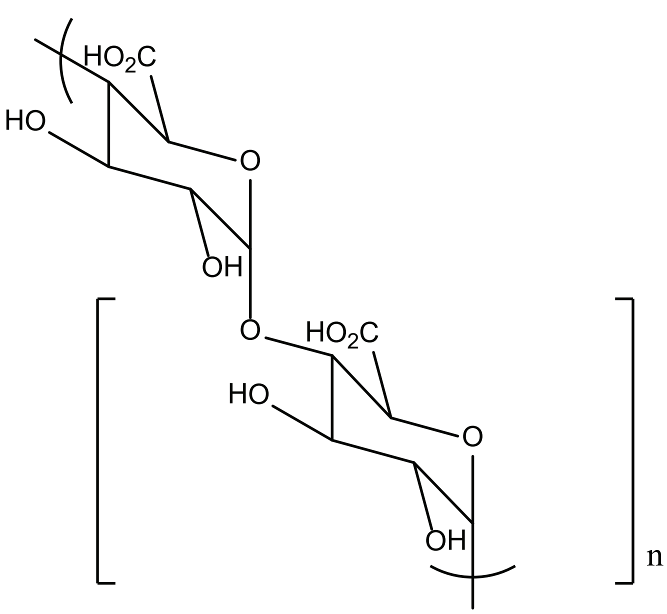

(A)

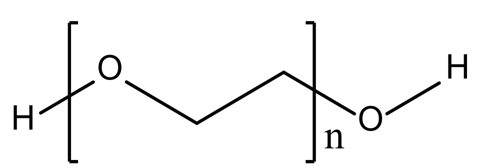

(B)

Fig. 1. Chemical structure of (A) pectin and (B) PEG.

dried at 50°C in 72 h. The film's formation is primarily established between the hydrogen bonds of pectin and PEG with carbonyl groups (C-O), methyl ester ($COOCH_3$), and oxygen atoms from PEG. By adding PEG to the pectin solution, the intermolecular forces in the polymer chain of pectin is reduced owing to an increase in their flexibility and scalability [7].

Characteristics of extracted pectin and pectin-based bioplastic materials

Fourier-transform infrared spectroscopy (FT-IR): FT-IR spectra was used to determine the unknown material, the quality and consistency of the sample, and to quantify the composition of the mixture. The spectra were recorded in the central infrared region (4000 to 400 cm^{-1}) with a resolution of 4 cm^{-1} in absorption mode for 8 to 128 scans at room temperature [9]. After the bioplastic films were made, the FT-IR spectra were measured at the Laboratory of Bio Sustainable and Environmental Materials Engineering, Faculty of Materials Science and Engineering, Nagaoka University of Technology, Japan.

Scanning electron microscopy (SEM): scanning electron microscopy was used to study the morphology of the surface and the cross section of the samples. In the measurement, the samples were fractured in liquid nitrogen and the fractured part was coated with a conductive layer of sputtered gold. The surface and cross section of the samples were investigated using a JSM-5300LV (JEOL, Japan) at the Laboratory of Bio Sustainable and Environmental Materials Engineering, Faculty of Materials Science and Engineering, Nagaoka University of Technology, Japan.

Equilibrium water content (EWC): EWC was measured at room temperature by comparing the initial weight of the dried material to that after immersion in distilled water in continuous intervals of 1 to 6 h and after 12 h. The EWC value was calculated by the following equation: $EWC=(m_2-m_1)/m_1 x100$, where m_1 is the initial weight and m_2 is the weight after immersion in distilled water for a particular time.

Water permeability: water permeability indicates the ability to allow water to pass through the material, which was investigated by placing a sample with 9 cm diameter on the outer edge of a 7.5 cm diameter beaker. Then, certain amounts of distilled water were dripped onto the surface of the sample and the quantity of water passing through the other side was measured after 12 h. The dehumidification ability was carried out by drying the material and weighing it until the mass was constant.

Optical transmittance: the optical transmittance (T) is defined as the ratio of the proportion of light that passes through a sample (P) to the amount of light illuminated on the sample (incident light, P_0). This is an important criterion to determine the quality of a bioplastic membrane, especially one used for food packaging. The greater the transmittance is, the faster food decays. The transmittance was measured by cutting the membrane in such a way that it fit a cuvette filled with distilled water. The conducting photometric measurement at 660 nm by UV-Vis spectrophotometer was calculated by the following formula: $A=-\log T=-\log P/P_0$.

Tensile strength: tensile strength of bioplastic films was carried out by a QC-528M1F device, Ometech, at the Ho Chi Minh City Department of Standards Metrology and Quality. Cross-sectional area of samples of known width (10 mm) and thickness (0.1 mm) were used in the calculations. The value of the tensile strength was calculated by using the following equation:

$$\text{Tensile strength} = \frac{\text{maximum load}}{\text{cross-section area}}\ (N/mm^2)$$

Results and discussion

Pectin extracted from dragon fruit peel has a light pink and yellowish color simply because the betacyanin pigment of dragon fruit was not completely removed (Fig. 2A). The efficiency of this process was 18% and the pectin obtained from it was a low methoxyl pectin with a degree of esterification of 36%. When this is compared with pectin extracted from citrus peel (21.85%) [10] and custard apple peel (8.93%) [11], it is clearly seen that pectin from the dragon fruit peel is an alternative available source that has potential for practical production and application. The productivity of the material preparation process was 116%. The newly molded bioplastic film had a light pink, yellowish hue due to incomplete removal of the betacyanin pigment. Nonetheless, after drying at 50°C for 72 h (Fig. 2B), the film slightly yellowed, which can be explained by the fact that the betacyanin pigment partially decomposed during

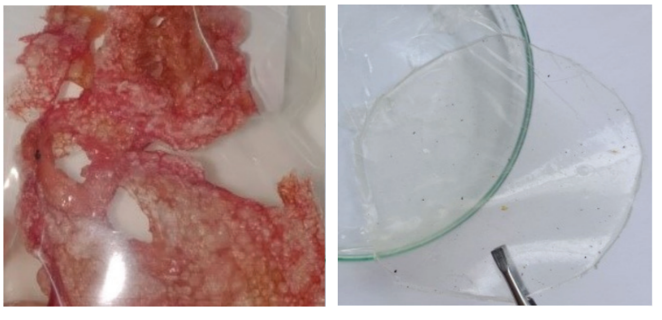

(A) (B)

Fig. 2. (A) Extracted pectin and (B) the pectin-based film.

the heating process. The resulting films were transparent, flexible, and glossy.

Two functional groups were extracted from pectin: the carbonyl group (CO) at 1600 cm^{-1} and the hydroxyl group (OH) at 3200-3600 cm^{-1}. In addition, the carboxyl group (COOH) appeared between 1740-1760 cm^{-1}. Similarities between the functional groups found in the FT-IR spectra of the pectin extracted from dragon fruit peel and that of commercial pectin prove that pectin was successfully extracted [12]. Fig. 3 shows the FT-IR spectra of the bioplastic materials. Specifically, strong absorption bands occurred at 2111 and 1647 cm^{-1}, which refer to carbonyl ester groups (-$COOCH_3$) and the asymmetric prolonged vibration of carboxylate ions (COO^-), respectively. The peaks observed at 1457, 1251, and 1096 cm^{-1} represent the symmetrical elongation fluctuations of C-O-C, C-OH, and C-C links from the structure of pectin, respectively. The observed peaks in the bioplastic film spectra can be attributed to the interaction between pectin and PEG through the formation of hydrogen bonds established between the carbonyl (CO), methyl ester ($COOCH_3$) groups, and oxygen from PEG [7].

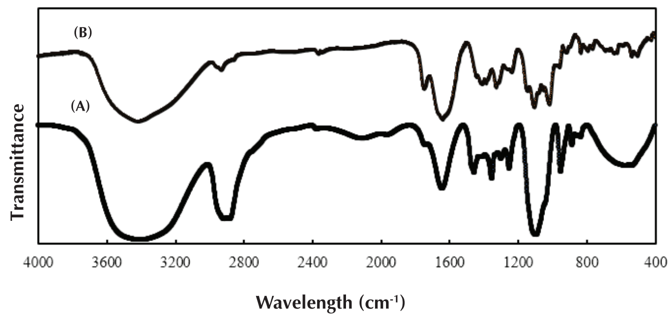

Fig. 3. FT-IR spectra of (A) extracted pectin and (B) bioplastic membrane.

From Fig. 4A, it was obvious that the surface of the bioplastic material was near homogeneous and without pores or cracks. However, there were some signs of fragmentation as seen in Fig. 4B, which were thought to be poorly mixed pectin and PEG, however, this did not affect the structure or morphology of the material. The surface image showed that the bioplastic had a dense structure on the surface.

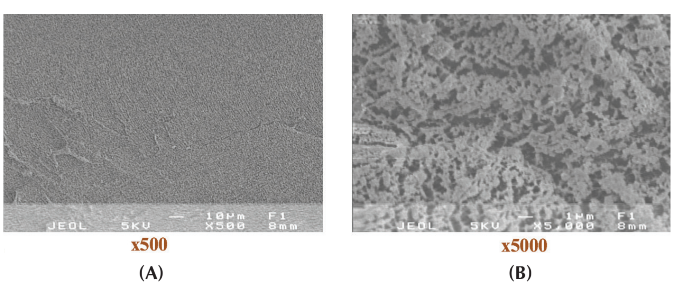

Fig. 4. SEM picture of the surface bioplastic (5:1) at (A) magnification ×500 and (B) magnification ×5000.

The EWC of the films increased gradually by the time of immersion. In terms of the 5:1 and 3:1 ratio films, after 5 h of saturation, their efficiency was 29.17 and 48.61%, respectively. Meanwhile, the 1:1-ratio film reached equilibrium after 6 h and its efficiency reached 59.72%. It was also noticed that the concentration of PEG increased, which lead to an increase in water uptake capacity. This can be explained by the fact that PEG is slightly hygroscopic [7]. It is well documented that the 5:1-ratio film had the least water retention compared to the others. In other words, the mechanical strength of the films was quite good. Thus, according to the results presented in Table 1, the expansion of the film reached a maximum value of 8.33% within 3 h for the 5:1-ratio film and the diameter of the film increased slightly. For the 3:1-ratio film, the swelling level reached its peak of 10% after 3 h. Similarly, the swelling degree of the 1:1-ratio film was 13.33% after 4 h of hydration. On the other hand, data from the permeability test showed that all of the bioplastic films completely dissolved after 1 h with mechanical agitation. The permeability test outcome illustrated that no phenomenon of water passed from the top to the bottom of the bioplastic films after 12 h for all 3 ratios.

Table 1. The characteristics of pectin-based membranes at different ratios.

	Tensile strength (N/mm^2)	Moisture value (%)	Optical transmittance (%)	Water content (%)	Elongation (%)
1:1	2.5	18.18	24	29.17	8.33
3:1	4.9	9.1	19	48.61	10.00
5:1	5	4.5	18	59.72	13.33

Optical transmittance is one of the most important parameters to evaluate material quality for food packaging. In addition, UV rays can cause lipid oxidation and 660 nm wavelength light can create an environment for microorganisms to grow and cause food spoilage. The results showed that the optical transmittance of all 3 films were quite small; 18, 19 and 24% for the 5:1, 3:1, and 1:1, respectively. The 5:1-ratio film had the smallest value (18%), which is very suitable for packaging and preserving food. In contrast, the film with 1:1 ratio had the largest optical transmittance (24%) because of the slight water absorption property. Based on Table 1, it can easily be seen that after 12 h in atmosphere, the bioplastic films were slightly hygroscopic. When the PEG concentration increased, the hygroscopic moisture of the bioplastic films also increased. This can be explained by the fact that PEG is slightly hygroscopic. The film with the 5:1 ratio of pectin to PEG had the lowest value of hygroscopic property (4.5%). On the other hand, the tensile strength of the bioplastic films was 5 N/mm^2, 4.9 N/mm^2, 2.5 N/mm^2 for the 5:1, 3:1, and 1:1 ratios, respectively. The significant decrease in tensile strength was due to the high concentration of PEG, which lead to clustering in the material's structure. Therefore, the bioplastic films in this study are applicable and highly suitable for packing materials in the food and medical industries [3, 13].

In the present work, pectin-based bioplastic films regenerated from dragon fruit peel showed the most stability and beneficial properties when the ratio of pectin to PEG was 5:1. The pectin extraction yield from the dragon fruit peel, as well as the mechanical and chemical properties of the bioplastic films in the present work, showed a higher value than that from a similar recent study [14]. This may be due to using PEG as the cross-linking agent instead of ethylene glycol. There exist bioplastic films regenerated from apple peels [7], citrus medica [10], and custard apple [11], and all films showed good thermal stability, tensile strength, etc., as packing materials. Therefore, pectin-based bioplastic films regenerated from dragon fruit peels are promising as novel films for food and medical industry packaging in the near future.

Conclusions

The present work has shown success in the extraction of pectin from dragon fruit peel with the production of long, strong, and high quality threads of pectin during coagulation. The results of this study showed that bioplastic films with a 5:1 ratio of pectin to PEG had the best results: the saturated hydration time was 5 h with an efficiency of 29.17% and 5 N/mm^2 of the maximum tensile strength, futherrmore, the value of optical transmittance was 18 after 12 h showed that the increase in Pectin concentration made the membranes stronger and tended to be more hydrophilic. These results prove the environmentally friendly bioplastic films are beneficial in food and medical packaging applications in the near future.

COMPETING INTERESTS

The authors declare that there is no conflict of interest regarding the publication of this article.

REFERENCES

[1] Maurizio Avella, Jan J. De Vlieger, Maria Emanuela Errico, Sabine Fischer, Paolo Vacca, Maria Grazia Volpe (2005), "Biodegradable starch/clay nanocomposite films for food packaging applications", *Food Chemistry*, **93**, pp.467-474.

[2] Teresa I.A. Gouveia, Krzysztof Biernacki, Maria C.R. Castro, Maria P. Gonçalves, Hiléia K.S. Souza (2019), "A new approach to develop biodegradable films based on thermoplastic pectin", *Food Hydrocolloids*, **97**, pp.105-175.

[3] Nanou Peelman, Peter Ragaert, Bruno De Meulenaer, Dimitri Adons, Roos Peeters, Ludwig Cardon, Filip Van Impe, Frank Devlieghere Trends (2013), "Application of bioplastics for food packaging", *Food Science and Technology*, **32**, pp.128-141.

[4] Nudthabong Tongkham, Boonyawee Juntasalay, Patareeya Lasunon, Nipaporn Sengkhamparn (2017), "Dragon fruit peel pectin: microwave-assisted extraction and fuzzy assessment", *Agricultural and Natural Resourses*, **51(4)**, pp.262-267.

[5] Shahrooz Rahmati, Aminah Abdullah, Oon Lee Kang, Bioact (2019), "Yellow passion fruit rind - a potential source of low-methoxyl pectin", *Carbohydr. Diet. Fibre*, **100**, pp.100-186.

[6] Eleftheria Antoniou, C. Francisco Buitrago, Marina Tsianou, Paschalis Alexandridis (2010), "Solvent effects on polysaccharide conformation", *Carbohydrate Polymers*, **79**, pp.380-390.

[7] Sanja Šešlija, Aleksandra Nešić, Jovana Ružić, Melina Kalagasidis Krušić, Sava Veličković, Roberto Avolio, Gabriella Santagata, Mario Malinconico (2017), "Edible blend films of pectin and poly (ethylene glycol): preparation and physico-chemical evaluation", *Food Hydrocolloids*, **77**, pp.494-501.

[8] Basma Y. Alashwal, Mohamed Saad Bala, Arun Gupta, Swati Sharma, Puranjan Mishra (2019), "Improved properties of keratin-based bioplastic film blended with microcrystalline cellulose: a comparative analysis", *Journal of King Saud University - Science*, **32**, pp.853-857.

[9] Tuspon Thanpitcha, Anuvat Sirivat, Alexander M. Jamieson, Ratana Rujiravanit, J. Nanopart Res (2009), "Polyaniline nanoparticles with controlled sizes using a cross-linked carboxymethyl chitin template", *Journal of Nanoparticle Research*, **11**, pp.1167-1177.

[10] Bahare Pasandide, Faramarz Khodaiyan, Zeinab E. Mousavi, Seyed Saeid Hosseini (2017), "Optimization of aqueous pectin extraction from *Citrus medica* peel", *Carbohydrydrate Polymers*, **178**, pp.27-33.

[11] C.S. Shivamathia, I. Ganesh Moorthya, R. Vinoth Kumarb, Michael Rahul Soosaia, J. Prakash Maranc, R. Shyam Kumara, P. Varalakshmid (2019), "Optimization of ultrasound assisted extraction of pectin from custard apple peel: potential and new source", *Carbohydrate Polymers*, **225**, DOI: 10.1016/j.carbpol.2019.115240.

[12] J.M. Joel, J.T. Barminas, E.Y. Riki, J.M. Yelwa, F. Edeh (2018), "Extraction and characterization of hydrocolloid pectin from Goron Tula (Azanza garckeana) fruit", *World Scientific News*, **101**, pp.157-171.

[13] Azwan Mat Lazim, Farahain Mokhtar, Siti Fairus Mohd Yusof, Ishak Ahmad, Adil Hakam (2013), "Synthesis and characterization of pH sensitive hydrogel using extracted pectin from dragon fruit peel", *Malaysian Journal of Analytical Sciences*, **17**, pp.481-489.

[14] Risnita Vicky Listyarini, Puspita Ratna Susilawatib, Esther Natalia Nukung, Maria Anastasia Toyo Yuaa (2020), "Bioplastic from pectin of dragon fruit (Hylocereus polyrhizus) peel", *Malaysian Journal of Analytical Sciences*, **23(6)**, pp.203-208.

Single and combined effects of Di-2-ethylhexyl phthalate and bisphenol A on life traits of the tropical micro-crustacean *Ceriodaphnia cornuta*

Van-Tai Nguyen[1, 2], Manh-Ha Bui[3], Emilie Strady[4, 5], Thuy-Chung Kieu-Le [1, 2, 4], Ba-Trung Bui[6], Thanh-Son Dao[1, 2*]

[1]Ho Chi Minh city University of Technology (HCMUT), Vietnam
[2]Vietnam National University, Ho Chi Minh city, Vietnam
[3]Saigon University, Ho Chi Minh city, Vietnam
[4]CARE, Ho Chi Minh city University of Technology (HCMUT), Vietnam
[5]Aix-Marseille Univ., Mediterranean Institute of Oceanography, Université de Toulon, France
[6]Institute for Environment and Resources, Ho Chi Minh city, Vietnam

Received 27 August 2020; accepted 19 November 2020

Abstract:

Plastics, plastic additives, and their emission have attracted significant attention and concern both socially and scientifically. Di-2-ethylhexyl phthalate (DEHP) and bisphenol A (BPA) are two of the many plastic additives widely found in aquatic environments, which can have severe impacts on aquatic animals like micro-crustaceans. Therefore, this study assessed the chronic effects of DEHP and BPA, both individually and jointly, at environmental concentrations (e.g. 50 and 500 µg/l) on the survival rate, reproduction, and growth of the tropical micro-crustacean *Ceriodaphnia cornuta*. We found that each of the two plastic additives, and a mixture of the two, had some influence on the survivorship of *C. cornuta*. While DEHP marginally enhanced the reproduction of the animals, BPA strongly inhibited it. Additionally, the mixture of DEHP and BPA caused a synergistic effect on reproduction but an antagonistic effect on the growth of *C. cornuta*. Both DEHP and BPA induced a significantly longer body of *C. cornuta* when exposed to these plastic additives. Our results showed that the tropical micro-crustacean *C. cornuta* is more sensitive to DEHP and BPA than the temperate micro-crustacean *D. magna* in relation to body length development and reproductive characteristics. Our findings enrich the knowledge of DEHP and BPA toxicity to tropical micro-crustaceans. Besides, our results are also of significant value to freshwater monitoring and environmental risk assessments of plastic additives.

Keywords: **energy cost, plastic additives, synergistic effects, tropical micro-crustacean.**

Classification number: **5.1**

Introduction

The global production of plastic has continuously increased over the past few decades as production reached nearly 360 million tons in 2018 [1]. However, only less than 5% of plastic materials have been recovered [2]. Consequently, the accumulation of plastic in the environment, especially in water bodies, has rapidly increased and become a critical concern for the environment, ecosystems, and human health due to the persistence and non-biodegradability of plastic waste [3, 4]. Further, plastics can contain various harmful chemicals like plastic additives (e.g. phthalate, bisphenol A, etc.) that are added to plastic polymers to provide them with specific characteristics like making them harder, more flexible, and/or durable [5, 6]. However, in the environment, these chemicals enter water bodies through pathways like discharge from industrial manufacturing or even by leaching out of the plastic materials themselves during their use and disposal, which can be magnified under natural conditions such as high temperature and UV radiation [7, 8]. Indeed, the potential release of hazardous additives from plastic materials has been demonstrated in several studies performed under laboratory conditions [9-11]. For instance, a BPA concentration of up to 8.3 µg/l was found in drinking water stored in polycarbonate bottles [9]. Similarly, common phthalate derivatives such as DEHP, dibutyl phthalate (DBP), and diisobutyl phthalate were detected in liquid extracts from polymer-coated materials in a study by Bradley, et al. (2007) [10]. Phthalates and BPA are widely used in the manufacture of plastic and frequently

*Corresponding author: Email: dao.son@hcmut.edu.vn

detected in the aquatic environment. For example, phthalates are mainly used in polyvinyl chloride (PVC) manufacturing while BPA is commonly used as a monomer, an antioxidant, and/or a plasticizer for epoxy resins, polycarbonate (PC), PVC, polypropylene (PP), and polyethylene (PE) plastics [7]. The global production of these additives has continuously increased due to an increase in plastic consumption, which has reached approximately 8 million tons per year [12, 13].

Due to their wide application, huge demand, and mismanaged disposal, plastic products containing phthalates and BPA have led to an increase in concentration of these additives in the environment [12-15]. The concentration of BPA can be higher than 90 µg/l in surface water and up to 370 µg/l in wastewater [12, 16]. Besides, DEHP, the most commonly detected phthalate in aquatic environments, can reach 370 µg/l in surface water [13]. Plastic additives such as phthalates and BPA are known as endocrine-disrupting compounds (EDCs) that can cause intracellular disruption and interfere with the functions of hormones in the endocrine systems of living organisms [15, 17, 18]. Previous studies have reported negative impacts of these additives on aquatic organisms such as phytoplankton, zooplankton, and fish [12-15, 19, 20]. For instance, DBP can alter lipid content causing an inhibition of the growth of the green alga *Chlorella vulgaris* [21]. The work of Wang, et al. (2018) [13] indicated that DEHP can strongly influence biochemical and physiological activities of the micro-crustacean *Daphnia magna* by enzymatic inhibition, increasing lipid peroxidation levels, and modulating the transcription of enzyme levels. Moreover, phthalates can inhibit the absorption and catabolism of fatty acids and cause detrimental effects on the development, reproduction, and lifespan of *D. manga* [5]. Similarly, the detrimental effects of BPA on the enzymatic activity, lipid peroxidation level, and reproduction of *D. magna* has been demonstrated in a study by Jemec, et al. (2012) [22]. Further, exposure to BPA can cause DNA damage resulting in a genotoxic effect on *D. magna* [23]. The acute toxicity of BPA has also been reported on the tropical micro-crustaceans *Ceriodaphnia silvestrii* and *Daphnia similis* with a 48 h-EC_{50} value of 14.44 and 12.05 mg/l, respectively [14]. Moreover, numerous studies have shown that phthalates and BPA have inhibitory effects on the reproduction, development, and enzymatic activity of various fish species, as well as cause their malformation [20, 24-26]. Therefore, the presence of these additives is considered a potential risk of biological disorder in animals and ecological imbalance in aquatic environments.

In aquatic ecosystems, zooplankton (e.g. *Daphnia*, *Ceriodaphnia*) play an important role as they are centrally positioned in the food chain and are among the most vulnerable organisms to pollution [27]. These organisms are commonly used in toxicological assessments due to their wide distribution in aquatic ecosystems, high sensitivities to toxins, and ease of culture under laboratory conditions [28-31]. Although previous studies have shown the negative impacts of phthalates and BPA on various aquatic organisms, the chronic effects of these chemicals on zooplankton from tropical regions have not been fully understood. Therefore, the aim of this study is to assess the chronic impacts of DEHP and BPA on the survival, reproduction, and growth of the tropical micro-crustacean *Ceriodaphnia cornuta* isolated from Vietnam.

Materials and methods

The test organism and chemicals for the experiment

The tropical micro-crustacean, *C. cornuta* (Fig. 1), was isolated from the Mekong river in Vietnam and was maintained for over one year under laboratory conditions at a temperature of 25±1°C, light intensity of 600 lux, and photoperiod of 12 h light: 12 h dark [30, 32]. The organism was raised in an artificial medium called M4/4 [30] and fed a mixture of the green alga *Nannochloropsis* sp. and YTC, a rich nutrient mixture [33]. The alga was cultured in Z8 medium [34] under the laboratory conditions mentioned above.

The plastic additives DEHP and BPA, from Aldrich Sigma, were dissolved in acetone (Merck) at concentrations of 1000 and 5000 mg/l, respectively, and used as the mother solutions for the experiments. The mother solutions were stored at a temperature of 4°C prior to the experiment.

(A) (B)

Fig. 1. (A) The neonate and (B) the adult *Ceriodaphnia cornuta*. Scale bars = 200 µm.

Experimental setup

Prior to the experiments, more than 30 healthy mother *C. cornuta* were randomly selected and incubated in 50 ml beakers containing 30 ml M4/4 medium (3 individuals/beaker). The neonates (less than 24 h old) from these beakers were used for chronic experiments. The chronic experiments were conducted according to APHA (2012) with minor modifications [32]. Briefly, the neonates of *C. cornuta* (less than 24 h old) were randomly collected and exposed to DEHP and BPA at concentrations of 50 and 500 µg/l. Another test was conducted in which the animals were exposed to a mixture of DEHP and BPA at a concentration of 50 µg/l (for each chemical). The control was conducted in parallel with the exposures by culturing the organisms in the M4/4 medium without the addition of plastic additives (Table 1). The concentrations of DEHP and BPA in our study are within the range of the chemical concentrations found in the environment [12, 13, 16].

Table 1. Summary of the chronic exposures of *Ceriodaphnia cornuta* to DEHP and BPA.

No.	Abbreviations of the exposures	Concentrations of DEHP (µg/l)	Concentrations of BPA (µg/l)
1	Control	0	0
2	D50	50	0
3	D500	500	0
4	B50	0	50
5	B500	0	500
6	Mix	50	50

For each treatment, the organism was individually incubated in a 15 ml glass tube containing 10 ml M4/4 medium at the test concentration of chemicals (one organism/tube). There were 10 replicates (n=10) in each treatment. The experiments were performed under the laboratory conditions as mentioned above and lasted for 10 d. The organisms were fed daily with a mixture of green alga *Nannochloropsis* sp. and YTC [33]. The medium in each incubation was totally renewed three times per week. During the experimental time, the life-history traits including survivorship and reproduction of *C. cornuta* were recorded daily over a period of 10 d. By the end of the test, the body length of the living organisms in each treatment was measured by using a microscope (Olympus BX 51) coupled with a digital camera (DP71) [31].

Data treatment

Sigma Plot Version 12.0 was used for data analyses. The ANOVA test was applied to calculate the statistically significant difference in the body length of *C. cornuta* between the control and exposures. A gap of more than 20% in the survival proportion of *C. cornuta* in the treatments was considered as a significant difference [32].

Results and discussion

Effects of DEHP and BPA on the survivorship of Ceriodaphnia cornuta

By the end of the test, more than 90% of total organisms in the control treatments were still alive (Fig. 2), which was in line with the requirement for chronic experiments according to APHA (2012) [32]. During the exposure to DEHP, none of *C. cornuta* died until the end of the incubation, while the survival rate of organisms exposed to BPA at the concentration of 50 µg/l (B50) and 500 µg/l (B500) was 80 and 100%, respectively (Fig. 2A, B). Similarly, 80% of the total *C. cornuta* incubated in a mixture of DEHP and BPA (mix) were still alive at the end of the experiment (Fig. 2C). In this study, the difference in the survivorship of the organisms in all the DEHP and BPA exposures compared to the control were not statistically significant according to APHA (2012) [32]. Hence, the exposures to the individual and mixture of DEHP and BPA at the test concentrations during the 10-d period did not negatively influence the survival of the tropical micro-crustacean *C. cornuta*.

Our results were in line with previous studies reporting that DEHP at concentrations from 158-500 µg/l did not impact the survival rate of *D. magna* during 21 d of incubation [35, 36]. Spadoto, et al. (2017) [14] found that no observed effect concentration of BPA on the tropical micro-crustacean *C. silvestrii* was 1380 µg/l upon 8 d of exposure. Additionally, the authors also showed that the hazardous concentration for 50% of *C. silvestrii* was 493 µg BPA/l, which supports our observation of the survival rate of *C. cornuta* treated with BPA (up to 500 µg/l) in the current study. We expect that the toxicity of the mix (50 µg DEHP/l and 50 µg BPA/l) on *C. cornuta* survival would not be stronger than the highest single chemical treatment (either D500 or B500) and this is confirmed in the current study (Fig. 2). Most likely our study confirms that the EDCs DEHP and BPA at the test concentrations had no significant effects on the survival of a single or parent generation of tropical micro-crustaceans [14].

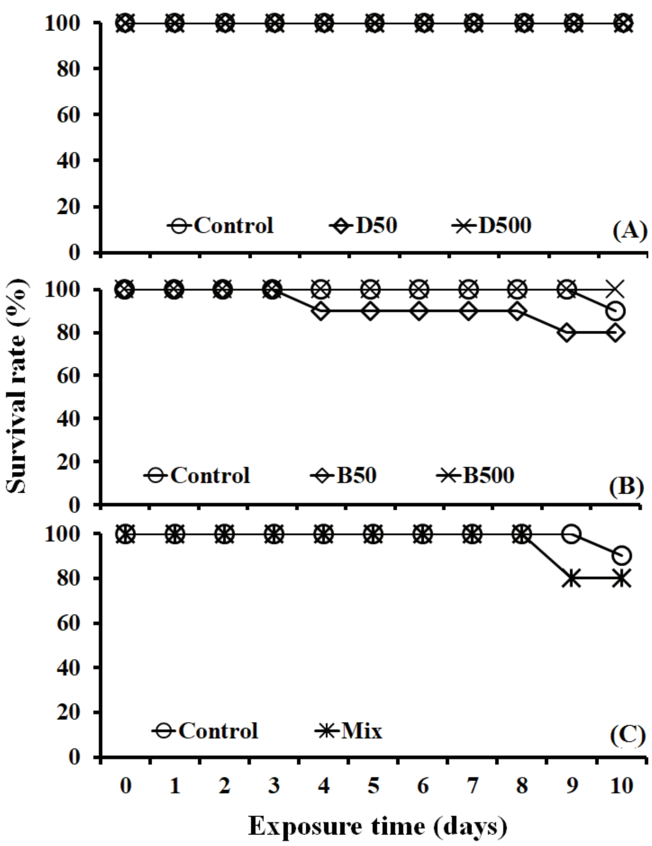

Fig. 2. The survival rate of *Ceriodaphnia cornuta* exposed to (A) DEHP, (B) BPA, and (C) a mixture of DEHP and BPA. D50 and D500 correspond to the medium containing 50 and 500 µg/l of DEHP, respectively, while B50 and B500 correspond to the medium containing 50 and 500 µg/l of BPA, respectively. Mix denotes the medium containing 50 µg DEHP/l and 50 µg BPA/l (Table 1).

Effects of DEHP and BPA on the reproduction of Ceriodaphnia cornuta

After 10 d, the total offspring of *C. cornuta* in the control, D50, and D500 trials were 75, 80, and 86 neonates, respectively. Therefore, the total neonates of D50 and D500 (or reproduction relative) to the control were 107 and 115% (Fig. 3A). On the contrary, in the BPA treatments, the reproduction relative to the control of B50 and B500 were 21 and 22%, respectively (Fig. 3B). The reproductive performance of *C. cornuta* incubated in the mixture of DEHP and BPA was strongly inhibited and gained only 5% compared to the control (Fig. 3C).

Knowles, et al. (1987) [35] and Le, et al. (2019) [36] found that DEHP at concentrations in the range of 50-158 µg/l did not reduce nor enhance the reproduction of *D. magna*. However, a higher DEHP concentration of 390 µg/l resulted in a 1.5-times higher reproduction of *D. magna* compared to the control [15]. The reproduction relative to the control in *C. cornuta* (115%, Fig. 3A) at a DEHP concentration of 500 µg/l was similar to that of *D. magna* (112%) in a previous investigation [36]. This similarity is likely due to both species being micro-crustaceans.

However, the reproduction of *C. cornuta* in the present study was strongly impacted by BPA at both concentrations tested (50 and 500 µg/l, Fig. 3B). This is contrary to the results from a study on another tropical micro-crustacean species *C. silvestrii*, where its fecundity was observed to not be significantly reduced after exposure to 1380 µg BPA/l [14]. Jemec, et al. (2012) [22] found that the no observed effect concentration of BPA on the brood number and total offspring of *D. magna* were 860 and 1730 µg/l, respectively. The brood size of *D. magna* was not impacted by BPA concentrations up to 1380 or even 6900 µg/l [14, 22]. Therefore, it would seem that the reproductive trait of *C. cornuta* from the Mekong river in Vietnam is more sensitive to BPA than that of *C. silvestrii* and *D. magna*. Although DEHP and BPA are both EDCs, they can have opposite effects on the reproduction of micro-crustaceans from the same species, for example, *C. cornuta* in this case. Another study found that BPA at low concentration (e.g. 3 µg/l) could cause DNA damage and significant changes in antioxidant enzyme activities (e.g. catalase) in *D. magna* [23]. The activity of the biotransformation enzyme also significantly increased upon a chronic BPA treatment [22]. Hence the BPA exposures could lead to an energy cost in micro-crustaceans (e.g. *D. magna*). The energy cost, over a chronic treatment, could diminish the reproductive capacity in the exposed animals, which may help to explain the strong reduction in the total neonates of *C. cornuta* in our study. The biochemical responses of *C. cornuta* upon incubation in BPA and DEHP are suggested for further studies.

The relative reproduction of *C. cornuta* in D50, B50, and the mixture to the control (Fig. 3) were 107, 21, and 5%, respectively, which revealed that the mixture of BPA and DEHP resulted in a synergistic effect on the reproduction of the exposed animals. Similarly, Baralic, et al. (2020) [37] reported that a mixture of phthalates (DEHP, DBP) and BPA induced more pronounced effect on a cellular level in mammals than the chemicals individually (DEHP, DBP, BPA). However, to the best of our knowledge, there has been no report on the combined effects of DEHP and BPA on aquatic animals. Apparently, both DEHP and BPA can strongly alter the antioxidant and biotransformation enzyme activities in micro-crustaceans [22, 23, 35] leading to an energy cost over chronic exposures. This would then imbalance the energy distribution that the animals use to maintain their survival, conduct normal activities such as swimming and feeding, and for their growth and reproduction. Specifically, the impairment of the reproduction of *C. cornuta* by BPA was evidenced in this study (Fig. 3B). Hence, an increase in reproductive function impairment would occur upon exposure to BPA and DEHP, however, it is not clear if DEHP impacts other functions or if it just simply causes further energy cost in the animal.

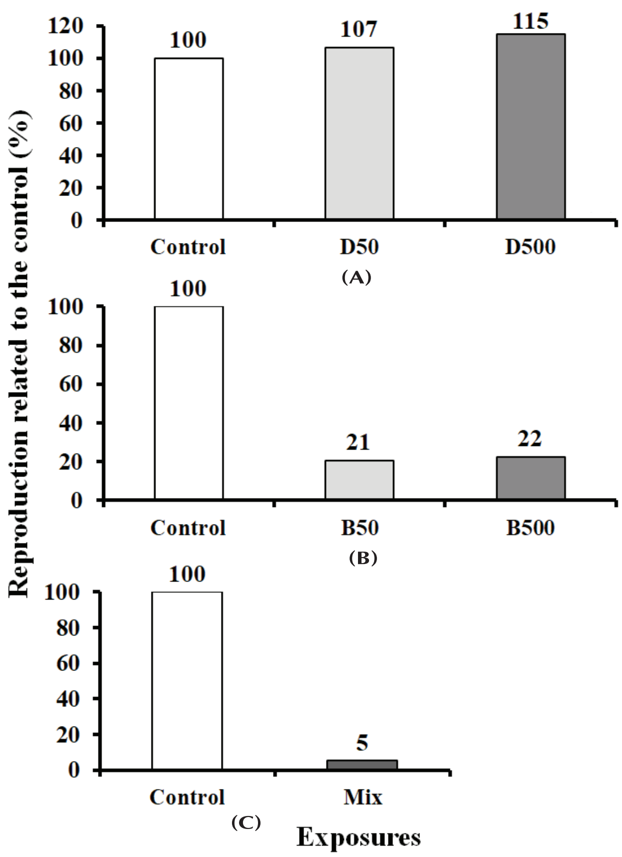

Fig. 3. Total neonates of *Ceriodaphnia cornuta* exposed to (A) DEHP, (B) BPA, and (C) a mixture of DEHP and BPA relative to the control. Abbreviations as in Fig. 2.

Effects of DEHP and BPA on the growth of Ceriodaphnia cornuta

After 10 d, the mean body length of *C. cornuta* in the control was 0.458(±0.024) mm. In the DEHP and BPA treatments, the body lengths of the animals were significantly longer than that of the control. Briefly, the mean body length in D50, D500, B50, and B500 was 0.522(±0.043), 0.532(±0.035), 0.520(±0.045), and 0.532(±0.035) mm, respectively (Fig. 4A, B). Interestingly, the body length of *C. cornuta* in the DEHP and BPA mixture was 0.459(±0.044) mm, which was similar to that of the control (Fig. 4C).

Interestingly, the present results from the DEHP treatments are contrary to previous studies of the micro-crustacean *D. magna* [15, 36] in which DEHP at a concentration of 50 µg/l neither enhanced nor inhibited the body length of *D. magna* at concentrations between 390-500 µg/l. Park & Choi (2009) [23] observed similar body fresh weights of *D. magna* between the control and BPA exposure experiment at a concentration of 30 µg/l. Similarly, Jemec, et al. (2012) [22] did not find any statistically significant change to the body length of *D. magna* exposed to 6900 µg/l BPA. However, in our study, *C. cornuta* growth was stimulated and its body prolonged when exposed to a BPA concentration of 50 µg/l. Therefore, we conclude that the tropical micro-crustacean *C. cornuta* has a much different response to DEHP and is more sensitive to BPA than the temperate micro-crustacean *D. magna* in relation to the body length of the animals.

Differing from the individual exposures to either DEHP or BPA, the mixture of DEHP and BPA in our study did not significantly change the body length of the *C. cornuta*. Hence, these results from the mixture demonstrated antagonistic effects on the body length of the micro-crustacean. It is not completely understood how the mixture of DEHP and BPA prevented body length prolongation compared with the exposure to the individual chemical. However, we can outline some potential causes: 1) a significant increase of energy cost; 2) a potentially competitive binding mechanism; and 3) both energy cost and binding mechanism competition in the animals. As mentioned above, both DEHP and BPA could induce an energy cost and the combined cost of these plastic additives would strongly reduce the energy for not only reproduction but also growth. Considering this, the body length development would be slower than that when exposed to a single plastic additive (DEHP or BPA). Undoubtedly, DEHP or BPA would bind to specific ligand(s) in the micro-crustacean before inducing its effects. For example, the competitive binding mechanism of the metals Cd and Ni to the biotic ligand in *D. magna* was reported by Perez & Hoang (2018) [38] in which the metal Ni (less toxic to *D. magna*) would compete with Cd (more toxic to *D. magna*) to bind to the same biotic ligand. This competition led to a reduction of Cd toxicity to *D. magna*. From this study, one could infer that DEHP and BPA bind to the same biotic ligand in the micro-crustacean *C. cornuta*; one that is closely linked to body length development. However, the latter hypothesis needs further investigations to clarify.

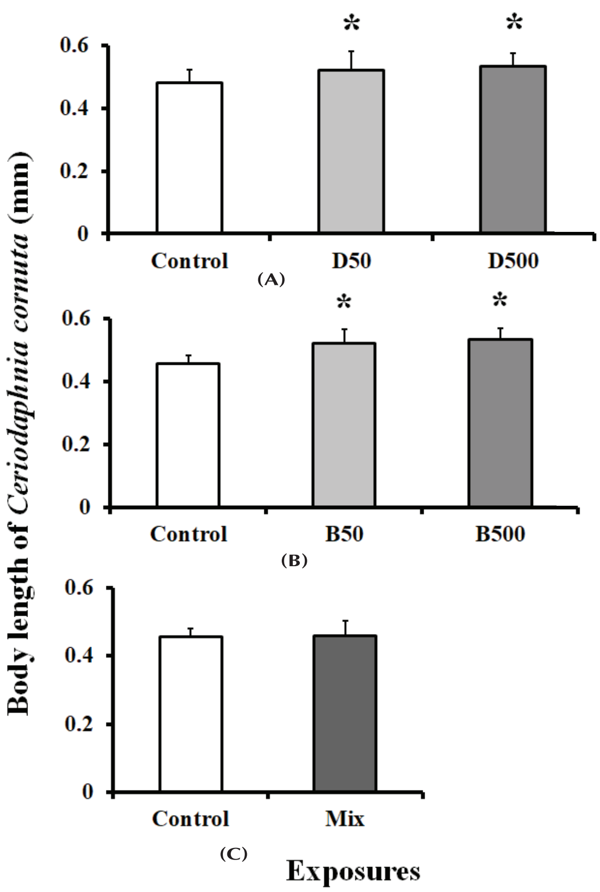

Fig. 4. Body length of *Ceriodaphnia cornuta* exposed to (A) DEHP, (B) BPA, and (C) a mixture of DEHP and BPA. The asterisk indicates a significant difference between the control and exposures ($p<0.05$) by ANOVA followed by Tukey's test. Abbreviations are the same as in Fig. 2.

Conclusions and recommendation

The two plastic additives DEHP and BPA, along with their mixture, did not strongly affect the survival rate of the tropical micro-crustacean *C. cornuta*. While DEHP at the test concentrations only slightly enhanced the reproduction of *C. cornuta*, it significantly boosted their growth. Differently, BPA exposure resulted in faster body length development but inhibited the reproduction of the animals. The mixture of DEHP and BPA had a synergistic effect on the reproductive capacity and an antagonistic effect on the body length development of *C. cornuta*. Energy cost and biotic ligand competition could be the mechanisms behind the observed impairments in the animals exposed to DEHP and BPA. We found that the tropical micro-crustacean *C. cornuta* is more sensitive to DEHP and BPA than the temperate micro-crustacean *D. magna* in relation to body length development and reproductive characteristics. Further investigations of the biochemical responses of *C. cornuta* after exposure to DEHP and BPA are suggested. Our results enrich the knowledge of DEHP and BPA toxicity in tropical micro-crustaceans and are valuable for freshwater monitoring and environmental risk assessments of plastic additives.

ACKNOWLEDGEMENTS

This research is funded by Vietnam National Foundation for Science and Technology Development (NAFOSTED) under grant number 106.99-2019.39, and under the framework of the JEAI PLASTIC project supported by The French National Research Institute for Sustainable Development (IRD).

COMPETING INTERESTS

The authors declare that there is no conflict of interest regarding the publication of this article.

REFERENCES

[1] Plastic Europe (2019), *Plastic - The Facts 2019: An Analysis of European Plastic Production, Demand and Waste Data*, https://www.plasticseurope.org/en/resources/market-data.

[2] H.S. Auta, C.U. Emenike, S.H. Fauziah (2017), "Distribution and importance of microplastics in the marine environment: a review of the sources, fate, effects, and potential solutions", *Environment International*, **102**, pp.165-176.

[3] J.R. Jambeck, R. Geyer, C. Wilcox, T.R. Siegler, M. Perryman, A. Andrady, R. Narayan, K.L. Law (2015), "Plastic waste inputs from land into the ocean", *Science*, **347(6223)**, pp.768-771.

[4] J.C. Anderson, B.J. Park, V.P. Palace (2016), "Microplastics in aquatic environments: implications for Canadian ecosystems", *Environmental Pollution*, **218**, pp.269-280.

[5] G. Latini (2005), "Monitoring phthalate exposure in humans", *Clinica Chimica Acta*, **361(1-2)**, pp.20-29.

[6] J. Im & F.E. Löffler (2016), "Fate of bisphenol A in terrestrial and aquatic environments", *Environmental Science & Technology*, **50(16)**, pp.8403-8416.

[7] L. Hermabessiere, A. Dehaut, I. Paul-Pont, C. Lacroix, R. Jezequel, P. Soudant, G. Duflos (2017), "Occurrence and effects of plastic additives on marine environments and organisms: a review", *Chemosphere*, **182**, pp.781-793.

[8] L.G.A. Barboza, A.D. Vethaak, B.R.B.O. Lavorante, A.K. Lundebye, L. Guilhermino (2018), "Marine microplastic debris: an emerging issue for food security, food safety and human health", *Marine Pollution Bulletin*, **133**, pp.336-348.

[9] U.G. Ugboka, J.N. Ihedioha, N.R. Ekere, F.O. Okechukwu

(2020), "Human health risk assessment of bisphenol A released from polycarbonate drinking water bottles and carbonated drinks exposed to sunlight in Nigeria", *International Journal of Environmental Analytical Chemistry*, DOI: 10.1080/03067319.2020.1759572.

[10] E.L. Bradley, W.A. Read, L. Castle (2007), "Investigation into the migration potential of coating materials from cookware products", *Food Additives & Contaminants*, **24(3)**, pp.326-335.

[11] D. Lithner, I. Nordensvan, G. Dave (2012), "Comparative acute toxicity of leachates from plastic products made of polypropylene, polyethylene, PVC, acrylonitrile-butadiene-styrene, and epoxy to *Daphnia magna*", *Environmental Science and Pollution Research*, **19**, pp.1763-1772.

[12] D. Li, H. Chen, R. Bi, H. Xie, Y. Zhou, Y. Luo, L. Xie (2017), "Individual and binary mixture effects of bisphenol A and lignin-derived bisphenol in *Daphnia magna* under chronic exposure", *Chemosphere*, **191**, pp.779-786.

[13] Y. Wang, T. Wang, Y. Ban, C. Shen, Q. Shen, X. Chai, W. Zhao, J. Wei (2018), "Di-(2-ethylhexyl) Phthalate exposure modulates antioxidant enzyme activity and gene expression in juvenile and adult *Daphnia magna*", *Archives of Environmental Contamination and Toxicity*, **75(1)**, pp.145-156.

[14] M. Spadoto, A.P.E. Sueitt, C.A. Galinaro, T.S. Pinto, C.M.E. Pompei, C.M.R. Botta, E.M. Vieira (2017), "Ecotoxicological effects of bisphenol A and nonylphenol on the freshwater cladocerans *Ceriodaphnia silvestrii* and *Daphnia similis*", *Drug and Chemical Toxicology*, **41(181)**, pp.1-10.

[15] Seyoum & A. Pradhan (2019), "Effect of phthalates on development, reproduction, fat metabolism and lifespan in *Daphnia magna*", *Science of the Total Environment*, **654**, pp.969-977.

[16] Careghini, A.F. Mastorgio, S. Saponaro, E. Sezenna (2015), "Bisphenol A, nonylphenols, benzophenones, and benzotriazoles in soils, groundwater, surface water, sediments, and food: a review", *Environmental Science and Pollution Research*, **22**, pp.5711-5741.

[17] M. Cole, P. Lindeque, C. Halsband, T.S. Galloway (2011), "Microplastics as contaminants in the marine environment: a review", *Marine Pollution Bulletin*, **62**, pp.2588-2597.

[18] M. Giraudo, M. Douville, M. Houde (2015), "Chronic toxicity evaluation of the flame retardant tris (2-butoxyethyl) phosphate (TBOEP) using *Daphnia magna* transcriptomic response", *Chemosphere*, **132**, pp.159-165.

[19] R. Acey, P. Healy, T.F. Unger, C.E. Ford, R.A. Hudson (1987), "Growth and aggregation behavior of representative phytoplankton as affected by the environmental contaminant Di-n-butyl phthalate", *Bulletin of Environmental Contamination and Toxicology*, **39(1)**, pp.1-6.

[20] G. Sun & K. Liu (2017), "Developmental toxicity and cardiac effects of butyl benzyl phthalate in zebrafish embryos", *Aquatic Toxicology*, **192**, pp.165-170.

[21] K. Duan, M. Cui, Y. Wu, X. Huang, A. Xue, X. Deng, L. Luo (2018), "Effect of Dibutyl Phthalate on the tolerance and lipid accumulation in the green microalgae *Chlorella vulgaris*", *Bulletin of Environmental Contamination and Toxicology*, **101**, pp.338-343.

[22] Jemec, T. Tisler, B. Erjavec, A. Pintar (2012), "Antioxidant responses and whole-organism changes in Daphnia magna acutely and chronically exposed to endocrine disruptor bisphenol A", *Ecotoxicology and Environmental Safety*, **86**, pp.213-218.

[23] S.Y. Park & J. Choi (2009), "Genotoxic effects of Nonylphenol and bisphenol A exposure in aquatic biomonitoring species: freshwater crustacean, *Daphnia magna*, and aquatic midge, *Chironomus riparius*", *Bulletin of Environmental Contamination and Toxicology*, **83**, pp.463-468.

[24] V.R.T. Zanotelli, S.C.F. Neuhauss, M.U. Ehrengruber (2010), "Long-term exposure to bis(2-ethylhexyl) phthalate (DEHP) inhibits growth of guppy fish (*Poecilia reticulata*)", *Journal of Applied Toxicology*, **30**, pp.29-33.

[25] X. Zhao, Y. Gao, M. Qi (2014), "Toxicity of phthalate esters exposure to carp (*Cyprinus carpio*) and antioxidant response by biomarker", *Ecotoxicology*, **23**, pp.626-632.

[26] D. Li, Q. Chen, J. Cao, X. Chen, L. Li, N. Cadergreen, H. Xie, L. Xie (2016), "The chronic effects of lignin-derived bisphenol and bisphenol A in Japanese medaka *Oryzias latipes*", *Aquatic Toxicology*, **170**, pp.199-207.

[27] R. Sterner (2009), "Role of zooplankton in aquatic ecosystems", *Encyclopedia of Inland Water*, *Academic Press*, pp.678-688.

[28] D.M.M. Adema (1978), "*Daphnia magna* as a test animal in acute and chronic toxicity tests", *Hydrobiologia*, **59(2)**, pp.125-134.

[29] W. Lampert (2006), "*Daphnia*: model herbivore, predator and prey", *Polish Journal of Ecology*, **54(4)**, pp.607-620.

[30] L.C. Do-Hong, K.B.V. Slooten, J. Tarradellas (2004), "Tropical ecotoxicity testing with *Ceriodaphnia cornuta*", *Environmental Toxicology*, **19(5)**, pp.497-504.

[31] T.S. Dao, L.C. Do-Hong, C. Wiegand (2010), "Chronic effects of cyanobacterial toxins on *Daphnia magna* and their offspring", *Toxicon*, **55**, pp.1244-1254.

[32] American Public Health Association (APHA) (2012), *Standard Methods for the Examination of Water and Wastewater (22nd ed.)*, American Water Works Association, 1496pp.

[33] US Environmental Protection Agency (US. EPA) (2002), *Methods for Measuring the Acute Toxicity of Effluents and Receiving Waters to Freshwater and Marine Organisms (5th ed.)*, 275pp.

[34] J. Kotai (1972), "Introductions for preparation of modified nutrient solution Z8 for Algae", *Norwegian Institute for Water Research*, Oslo, **B-11/69**, pp.1-5.

[35] C.O. Knowles, M.J. McKee, D.U. Palawski (1987), "Chronic effects of Di-2-ethylhexyl phthalate on biochemical composition, survival and reproduction of *Daphnia magna*", *Environmental Toxicology and Chemistry*, **6**, pp.201-208.

[36] T.P.D. Le, V.T. Nguyen, T.M.C. Vo, N.H. Bui, T.S. Dao (2019), "Transgenerational effects of the plasticizer di-2-ethylhexyl phthalate on survival, growth, and reproduction of *Daphnia magna*", *Vietnam Journal of Science, Technology and Engineering*, **61(4)**, pp.64-69.

[37] K. Baralic, A.B. Djordjevic, K. Zivancevic, E. Antonijevic, M. Andelkovic, D. Javorac, M. Curcic, Z. Bulat, B. Antonijevic, D. Dukic-Cosic (2020), "Toxic effects of the mixture of phthalates and bisphenol A - subacute oral toxicity study in wistar rats", *International Journal of Environmental Research and Public Health*, **17**, DOI: 10.3390/ijerph17030746.

[38] E. Perez, T.C. Hoang (2018), "Responses of *Daphnia magna* to chronic exposure of cadmium and nickel mixtures", *Chemosphere,* **208**, pp.991-1001.

DOI: 10.31276/VJSTE.62(4).30-35

Microbiological contamination of indoor air in university classrooms (Case study: University of Science - Vietnam National University, Ho Chi Minh city)

Diep Yen Nga Dang*, **Hong Nhung Vuong, Thi Tam Nguyen, Thi Thanh Thao Phan**

Faculty of Environmental Science, University of Science, Vietnam National University, Ho Chi Minh city

Received 10 August 2020; accepted 9 November 2020

Abstract:

This study was conducted to preliminarily assess microbial contamination of the indoor air inside classrooms at the University of Science - Ho Chi Minh city. At the same time, this study demonstrates the scientific basis of air quality assessment in a school environment and develops long-term direct or indirect solutions to protect the environment and ensure student health. In this project, sampling and quantitative analysis were performed to identify the airborne bacteria and fungi. Samples were collected from classrooms over a period of 4 months (03-06/2019) according to Koch's sedimentation method. The sampling plates were placed 1 m above the floor and the sampling time was 15 min. The colonies were counted after 24-48 h of incubation at 37±1°C for the bacteria and 70-120 h at 25±1°C for moulds. The results showed bacterial and fungal densities ranging from 359.6-2,427.3 CFU/m^3 and 106.1-928.9 CFU/m^3, respectively. The bacterial density was 2-3 times higher than the fungal density for all survey sites likely because the origin of these microorganisms is human activity. In addition, the density of bacteria and fungi in the air were also affected by weather and environmental factors. 5 isolated bacteria were identified as *Bacillus atrophaerus*, *Acinetobacter baumannii*, *Bacillus pumilus*, *Bacillus subtilis*, and *Bacillus cereus*. The fungi isolates included *Aspergillus tamarii*, *Aspergillus niger*, and *Fuligo septica*. They were all related to human and plant diseases.

Keywords: **airborne microorganisms, classroom, indoor air.**

Classification number: **5.1**

Introduction

In recent years, indoor air pollution has been of increasing interest to scientists as well as environmental management authorities as most people are indoors about 80-90% of their time [1, 2]. Hence, indoor air quality is of greater significance to human health due to the greater exposure time of indoor air than outdoor air. An average person inhales around 6-10 l/min and needs 15 m^3 of air per day [3]; thus, it is critical that indoor air be studied and evaluated. According to research by the United States Environmental Protection Agency (USEPA), indoor air pollution is one of the top five public health risks [4] contributing to an increase in the likelihood of cardiovascular diseases, lung diseases, and respiratory diseases [5].

Research by U.S. scientists (Earth and Sciences Division) has shown that the air people normally breathe has 1,800 types of bacteria including non-harmful and harmful ones, both of which affect human health. The human nasal cavity and the oral cavity contain millions of microorganisms that are found in indoor air. Some types of bacteria such as *Streptococcus*, *Mycoplasma*, and *Staphylococcus* cause skin-related diseases, respiratory system diseases, and allergies, which leads to an increase in the proportion of people infected [6, 7]. Human activities, indoor furniture, and equipment are the main factors contributing to the accumulation and spread of microbiological contaminants in indoor air [8, 9]. Human activities such as talking, sneezing, coughing, walking, and washing can produce biological dust in the air. Food, houseplants, house dust, clothing, carpets, wood materials, and furniture can also occasionally release various types of microorganisms into indoor air. Bacteria and fungi also come from outdoor sources such as soil or plants that are transported indoors as dust by wind transport [10, 11].

An increasing amount of research is also being

*Corresponding author: Email: ddynga@hcmus.edu.vn

conducted on indoor air bioaerosols. Series of studies on air microbiology in classrooms, libraries, and lecture halls of several universities have been carried out. Research by D. Guan, et al. [12] in China compared the bacterial density in the classroom between two sampling methods, of which the density was 209-838 CFU/m^3 for the passive sampling method (Natural sedimentation method - NSM) and 353-1,932 CFU/m^3 for the active sampling method (Air planktonic bacteria sampling method). In Poland, B. Ewa, et al. (2018) [13] focused on the viable bacterial concentration in an office, which was found to be in the range of 540-1,360 CFU/m^3. There was a huge difference in bacterial density between the two types of working rooms, specifically, the air-conditioned rooms were found to have a bacterial density 1.5 times higher than non-air-conditioned rooms. In addition, another study in Ethiopia found that the bacterial concentrations in some libraries at Jimma University ranged from 367-2,595 CFU/m^3 [14]. It can be easily recognised that these studies have around a 200-300 CFU/m^3 starting threshold of bacterial density, which is fairly high.

Meanwhile, studies on airborne viable bacteria and fungi from indoor air have not been paid much attention in Vietnam. Over the last decade, there have been several studies on airborne microorganisms in hospitals, food stock, and outdoor air. N.Q. Tuan (2010) [14] performed some sampling for a survey of air microbiology in the recovery and operating rooms of 13 hospitals and found variable microorganism densities ranging between 64.2-1,247.8 CFU/m^3 and higher concentrations obtained at around 200-500 CFU/m^3. The authors referred to the EU clean room classification standards EU GMP 1997, WHO 2002, and Merck's operating room standard (2009) when conducting this study. At that time, the control of air quality and air pollution in the hospitals of Vietnam did not have any standards for the limits of microbiological contamination in recovery and operating rooms. A study of airborne microorganisms in food storage warehouses was conducted by T.N.L. Tuyen, and N.T. Luan (2014) [15] and it showed that the airborne bacteria concentration was greater than the concentration of fungi and then proposed safety measures. In this work, the density of microorganisms in air was found to decrease from morning to afternoon and increased from the dry season to the rainy season. The authors compared the data with the National Technical Regulation on Biosecurity and Poultry Farm Conditions (QCVN 01-15:2010/BNNPTNT) and the Safir standard to assess the aerobic bacteria density in the air because there were no national regulations on limiting the level of microbiological contamination in the air for food storage.

In addition, characteristics of airborne bacteria and fungi in the atmosphere around Ho Chi Minh city from 2014 to 2016 was studied by V.D. Hai, et al. (2019) [16]. There have been remarkable records of the difference in the number of microorganisms between inland and suburban locations. The authors found the average microbial density on weekdays was higher than on the weekends. This study acknowledged that Vietnam did not yet have a set of microbiological standards for the air environment. In addition, the research had found that passive sampling methods often got higher density results than active sampling methods. They also found that the number of airborne microorganisms in the dry season was usually higher than in the rainy season.

Ho Chi Minh city is the most populous city in Vietnam and one of the most important economic centres in the country. This results in a lot of environmental stresses, but, so far, no research on airborne microorganisms has been conducted in the classroom of educational institutions. Most research on the microbiological contamination of indoor and outdoor air are evaluated based on standards and referenced standards of countries around the world. At present, there are not many research papers focusing on environmental pollution by microorganisms in indoor air.

Therefore, this study provides information on the current density of bacteria and fungi at several different classrooms in two campuses of the University of Science, Vietnam National University, Ho Chi Minh city and the impact of environmental factors on the growth of microorganisms in indoor air. The density of microorganisms is one of the most important criteria to be considered for building a healthy and safe space for students and teachers.

Methods and materials

Sampling sites

The air samples of the bacteria and fungi were collected in several classrooms of the University of Science, Vietnam National University, Ho Chi Minh city. The university has 2 campuses, one in the city centre and one in the suburb of the city, which has about 20,000 students enrolled. In this study, the samples were taken from the two campuses at the following locations. From the first campus, three locations including room C32 of ~100 students, room E401 of ~50-80 students, and lecture hall 1 of ~300 students. This campus is near a densely populated area and the main road of the district (Nguyen Van Cu street, district 5). From the second campus, room F106 of ~100 students and lecture hall B of ~300 students. This area is located in the suburbs and covered with many trees around. There is a long distance between the blocks of the classrooms (Linh Trung ward, Thu Duc district).

The different sampling locations provided a variety of microbial densities in the classrooms of each campus. The criteria for selecting the classroom to be surveyed was to represent upper and lower floors, the classroom area, and the number of students in the classroom.

The sample collection time was fixed on the Tuesdays of each week with 2 weeks per period at the 5 locations mentioned. There were 4 sampling periods and at each period samples of bacteria, fungi, and a blank were collected. For each sampling period, the samples were collected twice per day at 9:00 and 14:00 for 4 months from March 2019 to June 2019. Therefore, the total number of expected samples was 5×4 periods×5 locations=100 samples.

Sampling was conducted by a passive method known as the natural sedimentation method (NSM) or Koch's sedimentation method [17]. The sampling height was adjusted to be near the human breathing zone, which was 1 m above the floor. Each dish was exposed to air for 15 min (after conducting a pre-survey to select the appropriate sampling time). During the sampling process, the number of students, temperature, and humidity for each sampled room was also recorded.

Sampling procedure

Bacteria and fungi were collected on Nutrient Agar and Czapek-dox Agar, respectively. After the air exposure, the plates were carefully packed, labelled, and taken to the laboratory for analysis of the total aerobic bacteria and total fungi. The colonies were counted after 24-48 h incubation at 37±1°C for bacteria and 70-120 h incubation at 25±1°C for moulds [18]. The samples were finally subjected to qualitative, quantitative, and microbiological analyses.

Once the colony forming units (CFU) were determined, the CFU/m^3 values were calculated using the following equation described by Omeliansky [19-21]:

$$N = \frac{a \times 100 \times 100}{\pi r^2 \times t \frac{1}{5}}$$

where N is the microbial counts in CFU/m^3 of indoor air, a is the number of colonies per Petri dish, πr^2 is the dish surface area (cm^2), and t is the exposure time (min).

The samples of air-borne microorganisms were then compared to the European Protection Agency's cleanliness classification standards - EUR 14988 EN [22].

This study used protein mass spectrometry (MALDI-TOF) to identify the microorganisms by molecular markers. Any similarities of protein spectra from the target microorganisms were determined from a database of nearly 6,000 different microorganisms. The Maldi biotyper allows the accurate identification of the species of microorganisms including G(+) and G(–) bacteria, anaerobic-aerobic bacteria, yeast, mycobacteria, and mycelium. MALDI-TOF is a fast, simple, and high throughput proteomic technique used to identify many types of bacteria [23].

Results

The indoor air microbial loads of the 5 classrooms were determined by taking 100 samples. The concentration of bacterial and fungi aerosol present in the investigated classrooms are presented in Table 1. The results indicate that the highest bacterial air density in CFU/m^3 were obtained at 14:00 h in room E401 at campus 1, while the lowest bacterial CFU/m^3 air values were obtained at 14:00 h in room F106 at campus 2. The highest fungal air values were recorded at 9:00 h in room E401 at campus 1 with a value of 928.9 CFU/m^3, while the lowest fungal air density was recorded at 9:00 h in lecture hall B on campus 2, which was 106.1±81.3 CFU/m^3.

Table 1. Number of bacteria and fungi in air (CFU/m^3) at 5 points and their sampling time.

Microorganism	Sampling time	Campus 1			Campus 2	
		Lecture hall I (n=4)	*Room C32 (n=4)*	*Room E401 (n=4)*	*Lecture hall B (n=4)*	*Room F106 (n=4)*
Bacteria	9:00	1,077±854.2	1,598.8±1,958.3	2316±1,826.9	484.7±413.4	785.9±188.1
	14:00	1,771.7±776.1	1,625.6±1,285.4	2,427.3±1,906.8	668.1±701.6	359.3±92.4
Fungi	9:00	928.8±398.1	663.5±223.3	928.9±355.3	106.1±81.3	231.5±188.1
	14:00	527.5±54.3	729.8±325.1	746.4±627.9	262.6±276.7	121.7±92.4

The bacterial and fungal densities of the 2 campuses are shown in Fig. 1. The density of microorganisms on campus 1 was higher than that of campus 2 and the bacterial density was higher than the fungal density.

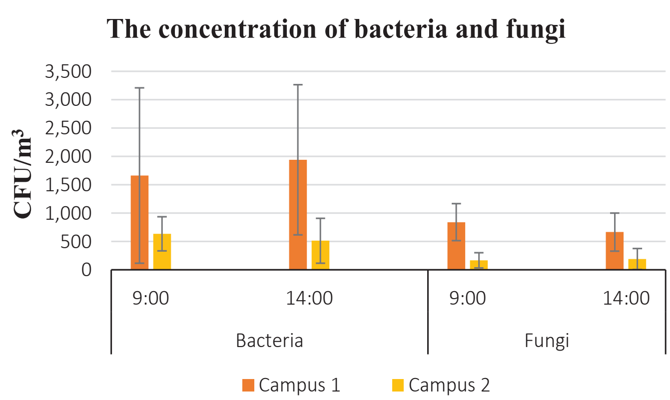

Fig. 1. Microbiological density in campus 1 and 2.

Microbial air quality scenario of classrooms is indicated in Table 2. All survey sites were contaminated with micro-pollutants from low to very high. Room E401 was the most heavily polluted than the rest of the classrooms.

Table 2. Evaluation of microbiological air quality (According to the standards of the European Protection Agency - EUR 14988 EN, 1993 [22]).

Microorganism	Range of values (CFU/m³)	Pollution degree	Campus 1						Campus 2			
			Lecture hall I		*Room C32*		*Room E401*		*Lecture hall B*		*Room F106*	
			9:00	*14:00*	*9:00*	*14:00*	*9:00*	*14:00*	*9:00*	*14:00*	*9:00*	*14:00*
Bacteria	<50	Very low	–	–	–	–	–	–	–	–	–	–
	50-100	Low	–	–	–	–	–	–	–	–	–	–
	100-500	Intermediate	–	–	–	–	–	–	✓	–	–	✓
	500-2,000	High	✓	✓	✓	✓	–	–	–	✓	✓	–
	>2,000	Very high	–	–	–	–	✓	✓	–	–	–	–
Fungi	<25	Very low	–	–	–	–	–	–	–	–	–	–
	25-100	Low	–	–	–	–	–	–	–	–	–	–
	100-500	Intermediate	–	–	–	–	–	–	✓	✓	✓	✓
	500-2,000	High	✓	✓	✓	✓	✓	✓	–	–	–	–
	>2,000	Very high	–	–	–	–	–	–	–	–	–	–

(✓) in the range; (–) not in the range.

As seen in Table 3, the microbial isolates included 5 bacteria and three fungi. *Bacillus pumilus*, *Bacillus subtilis*, and *Bacillus cereus* are common bacteria in the indoor air. They were present across all sampling locations. *Aspergillus tamarii* and *Aspergillus niger* were two common fungi appearing in all classrooms except lecture hall B.

Table 3. The distribution of microorganisms.

Microorganism		Campus 1			Campus 2	
		Lecture hall I	*Room C32*	*Room E401*	*Lecture hall B*	*Room F106*
Bacteria	*Bacillus atrophaerus*	+	–	–	+	+
	Acinetobacter baumannii	–	–	+	+	–
	Bacillus pumilus	+	+	+	+	+
	Bacillus subtilis	+	+	+	+	+
	Bacillus cereus	+	+	+	+	+
Fungi	*Aspergillus tamarii*	+	+	+	+	+
	Aspergillus niger	+	+	+	–	+
	Fuligo septica	–	–	–	+	+

(+) exist; (–) does not exist.

Discussion

Microbiological analysis

The concentration of bacteria in the classrooms of the two campuses ranged from 359.6±92.4 CFU/m^3 to 2,427.3±1,906.8 CFU/m^3 and tended to increase as morning progressed to afternoon. In campus 1, the average bacterial concentration in the room E401 was the highest during the survey and the lowest concentration in lecture hall I with 1,077±854.2 CFU/m^3. Meanwhile in campus 2, the bacterial density in hall B and room F106 tended to be opposite in the morning and afternoon (Table 1). This is mainly explained by the fixed schedule of the week, the same number of students during the sampling period, the area of the classroom and the ventilation, outside air entering the classrooms (temperature, humidity) [24, 25]. Room E401 is small and has poor ventilation but the number of students in class is about 100. The remaining rooms have the same area, which is double the size of the E401 room, so the collected bacterial density was lower. A 2012 study by D. Hospodsky, et al. [26] in the United States also showed that the bacteria present in indoor air were derived primarily from humans. Therefore, the number of occupants in an indoor environment greatly affects the density of the bacteria in the air.

Similar to bacteria, the concentration of fungi at campus 1 was lowest at 527.5±54.3 CFU/m^3 in lecture hall I and the highest concentration was 928.9±355.3 CFU/m^3 in room E401. This was significantly different from the concentration values found at campus 2, which ranged only from 106.1±81.3 CFU/m^3 to 262.6±276.7 CFU/m^3. However, the difference in fungal density among the classrooms in each campus was quite small, only about 200 CFU/m^3 at campus 1 and 120 CFU/m^3 at campus 2 (Table 1). This shows that people are not the main source of fungi in the indoor air. The room's facilities, high humidity, and poor cleanliness of the rooms are conditions that support the strong growth of fungi. Correlation studies of microorganisms inside buildings were conducted by S.A. Wamedo, et al. (2012) [25] and G.S. Graudenz, et al. (2005) [27], which were in agreement with this view. The concentration of fungi in the morning tended to be higher than in the afternoon because the temperature in the morning was around 30^{o}C, which is suitable for fungi growth [28].

From the data in Table 1, the bacterial density was 2-3 times higher than the fungal density at all survey locations. The temperature in Ho Chi Minh city is quite high (32-37^{o}C) during the days, which is more suitable for the growth of bacteria rather than fungi (the optimal temperature range of fungi is 28-30^{o}C) [16]. In summary, the origin of bacteria in the indoor air is mainly from humans while the origin of the fungi is from the condition of the facilities as well as environmental factors. Samples collected in this study were themselves the cause of large density difference between bacteria and fungi concentration [24].

The concentration of microorganisms between 2 campuses

The concentrations of bacteria and fungi were found to be significantly different between the sampling locations of both campuses. Fig. 1 shows that the average density of bacteria at campus 1 in the morning and afternoon was 2-3 times higher than that of campus 2. The bacterial concentration in the afternoon was the highest at 1,941.5 CFU/m^3 while the highest bacterial concentration in campus 2 was only 635.3 CFU/m^3. Similarly, the highest fungal density was 840.4 CFU/m^3 at campus 1, which is 4-5 times higher when compared with campus 2. One explanation for this result is that campus 1 in the city centre where many high-rise buildings are situated nearby. The area of campus 1 is small and the natural ventilation in classrooms (they are without air-conditioners) is not good, which leads to high humidity. The roads in this area are less green and contain a high density of vehicles that generate dust suspended in the air, which easily attaches to the human body. At the same time, the number of students at this facility is quite large, so the air quality in the poorly-ventilated classrooms are worse. campus 2 is located on the outskirts of the city with greener roads and its area is three times larger than campus 1. However, campus 2 is located apart from major road systems and as a result there is less traffic on the roads. The class sizes of campus 2 are much less than the capacity of the classroom, which results in less dust-containing microorganisms. Research by W. Fabian, et al. (2016) [29] also has stated that environmental and outdoor factors (vegetation, urbanization, airborne particulate matter) affect the growth of mould and bacteria in the indoor air.

Assessment of microbiological contamination

This research was conducted based on the European Environmental Protection Agency's standard of microbiological pollution (EUR 14988 EN, 1993 [22] as the standard for assessing the quality of air microbiology in classrooms. In campus 1, lecture hall I and room C32 were infested with bacteria and fungi at a very high level. The bacterial densities were 1,771.7 CFU/m^3 and 1,625.6 CFU/m^3 for lecture hall I and room C32, respectively. The fungal densities were 928.7 CFU/m^3 and 729.8 CFU/m^3 for lecture hall I and room C32, respectively. Meanwhile, a considerable extent of contamination in room E401 was observed for bacteria (2,427.3 CFU/m^3) and fungi (928.9 CFU/m^3) as well. In campus 2, all classrooms had lower levels of microbiological contamination than campus 1 (Table 2). Bacterial pollution ranged from an intermediate to high level while fungi pollution was intermediate. This shows that the microbiological air quality in campus 1 is inferior to campus 2 and this result is completely consistent with the results of a study by H. Shokri, et al. (2010) [30]. Thus, it is necessary to arrange a suitable number of students for each class, design better ventilation systems, and clean classrooms regularly to improve air quality in the classrooms.

Identification of microorganisms

The morphological characteristics of the colonies were selected as a representative of the dominant microorganisms isolated and identified by the MALDI-TOF method. The results showed 5 types of bacteria and 3 types of fungi were predominant over all the sampling sites. The dominant bacteria were *Bacillus atrophaerus*, *Acinetobacter baumannii*, *Bacillus pumilus* (Fig. 2), *Bacillus subtilis*, and *Bacillus cereus*. They were all gram-positive bacteria except for *Acinetobacter baumannii*, which is gram-negative, and aerobic spores. These bacteria are also found in soil, water, and some other habitats. *Bacillus atrophaerus* is a spore-forming bacillus that does not cause disease. This bacterium has been used as biological indicators for disinfection in biological research and method studies as well as in disinfectant studies, disease treatment evaluation, and potential assistance or means for vaccines. The remaining types of bacteria are related to skin diseases, pneumonia, sepsis, incision infection, urinary tract infection, and purulent meningitis after neurosurgery or food poisoning [31, 32]. *Bacillus pumilus*, *Bacillus subtilis*, and *Bacillus cereus* existed at all sampling sites (Table 3) indicating that they are popular bacteria in indoor air.

The dominant fungi included *Aspergillus tamarii*, *Aspergillus niger*, and *Fuligo septica* (Fig. 3). Two common fungi of the genus *Aspergillus* exist mainly in soil and are associated with a number of human diseases such as keratitis, allergies, and rhinitis [33]. They were all present in every classroom except hall B. *Fuligo septica* is the culprit of many types of root, stem, or leaf rot diseases of moistophilic plants, especially vegetables such as kohlrabi, cabbage, and many other fruits and vegetables [34]. *Fuligo septica* only appeared at campus 2 because there are many plants growing on campus (Table 3).

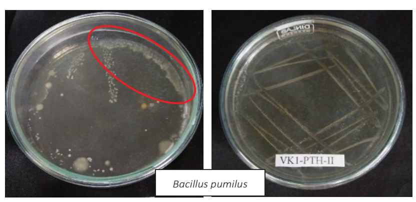

Fig. 2. Bacillus pumilus bacteria before and after isolation.

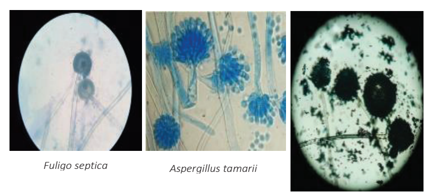

Fig. 3. Types of fungi under microscope.

Conclusions

This study has provided important information on the status of microorganisms in the air and a preliminary evaluation of the microbiological air quality in indoor air at schools. Along with identifying the species, this study helped elucidate the impacts from these microorganisms in the air. The concentrations of bacteria in the air depend on factors such as weather, ventilation, as well as human activities. A limited classroom area with crowded human presence has a strong impact on the density and concentrations of bacteria in the air, which causes them to be high. The fungi concentration depends on environmental factors, the quality of facilities, and sanitation in the classroom. The inferior air quality of campus 1 compared to campus 2 is likely caused by differences of geographical locations. The classrooms at campus 1 have high-to-very high microbiological pollution while campus 2 has an average pollution level. To improve air quality, it is necessary to arrange a suitable number of students for each class, appropriately design ventilation, and to clean the classrooms regularly.

ACKNOWLEDGEMENTS

The authors would like to thank the lecturers of the Faculty of Environment, University of Science - Ho Chi Minh city for their support of facilities, technical expertise and the best conditions for the authors completed this research topic.

COMPETING INTERESTS

The authors declare that there is no conflict of interest regarding the publication of this article.

REFERENCES

[1] A.H. Awad, S.A. Farag (1999), "An indoor bio-contaminants air quality", *International Journal of Environmental Health Research*, **9(4)**, pp.313-319, DOI: 10.1080/09603129973100.

[2] T. Lind, Nilssonmam, T. Bellander, J. Wichmann (2010), "$PM_{2.5}$, soot and NO_2 indoor-outdoor relationships at home, pre-school and schools in Stockholm, Sweden", *Atmospheric Environment*, **44(36)**, pp.4536-4544, DOI: 10.1016/j.atmosenv.2010.08.023.

[3] R.A. Wood, R.A. Burchett, J.T. Orwell, F.R. Torpy (2002), *Plant/Soil Capacities to Remove Harmful Substances from Polluted Indoor Air*, Plants and Environmental Quality Group, Centre for Ecotoxicology, UTS.

[4] H. Gawronska, B. Bakera (2015), "Phytoremediation of particulate matter from indoor air by *Chlorophytum comosum* L. plants", *Air Qual. Atmos. Health*, **8**, pp.265-272, DOI: 10.1007/s11869-014-0285-4.

[5] S.K. Shin, J. Kim, S. Ha, H.S. Oh, J. Chun, J. Sohn, Y. Hana (2015), "Metagenomic insights into the bioaerosols in the indoor and outdoor environments of childcare facilities", *PLOS ONE*, **10(5)**, pp.1-17, DOI: 10.1371/journal.pone.0126960.

[6] P. Treebupachatsakul, S. Tiengrim, V. Thamlikitkul (2006), "Upper respiratory tract infection in Thai adults: prevalence and prediction of bacterial causes and effectiveness of using clinical practice guidelines", *Journal of the Medical Association of Thailand*, **89(8)**, pp.1178-1186.

[7] W. Heping, et al. (2016), "Mycoplasma pneumoniae and streptococcus pneumoniae caused different microbial structure and correlation network in lung microbiota", *Journal of Thoracic Diseaes*, **8(6)**, pp.1316-1322.

[8] J. Qian, D. Hospodsky, N. Yamamoto, W. Nazaroff, J. Peccia (2015), "Size-resolved emission rates of airborne bacteria and outdoor environments of childcare facilities", *PLOS ONE*, **10**, pp.1-17.

[9] M. Taubel, H. Rintala, M. Pitkaranta, L. Paulin, S. Laitinen, J. Pekkannen (2009), "The occupant as a source of house dust bacteria", *J. Allergy Clin. Immunol.*, **124**, pp.834-840.

[10] M.D. Giulio, R. Grande, E.D. Campli (2010), "Indoor air quality in university environments", *Environ. Monit. Assess.*, **170(1-4)**, pp.509-517, DOI: 10.1007/s10661-009-1252-7.

[11] W.W. Nazaroff (2016), "Indoor bioaerosol dynamics", *Indoor Air*, **26**, pp.61-78, DOI: 10.1111/ina.12174.

[12] D. Guan, C. Gou, Y. Li, H. Lv, X. Yu (2015), "Study on the concentration and distribution of the airborne bacteria in indoor air in the lecture threatres at Tianjin Chengjian University, China", *Procedia Engineering*, **121**, pp.33-36, DOI: 10.1016/j.proeng.2015.08.1015.

[13] B. Ewa, B. Izabela, K. Barbara, S.P. Jozef (2018), "Microbiological indoor air quality in an office building in Gliwice, Poland: analysis of the case study", *Air Quality, Atmosphere & Heatlh*, **11**, pp.729-740, DOI: 10.1007/s11869-018-0579-z.

[14] N.Q. Tuan (2010), "Survey of microbiological pollution in the air of operating and recovery rooms in some hospitals in Ho Chi Minh city", *Medical Research*, **14**, pp.173-179.

[15] T.N.L. Tuyen, N.T. Luan (2014), *Study the Situation of Microbiological Pollution in the Air in Food and Food Industry Storage and Propose Safety Measures for Humans and Raw Materials*, Center for the Development of Science and Technology Young, Ho Chi Minh city, pp.4-26.

[16] V.D. Hai, S.M.T. Hoang, N.T.Q. Hung, N.M. Ky, S. Nam, V.B. Quang, T.T.N. Trang, N.D. Duc (2019), "Characteristics of airborne bacteria and fungi in the atmosphere in Ho Chi Minh city, Vietnam - a case study over three years", *International Biodeteioration and Biodegradation*, **145**, DOI: 10.1016/j.ibiod.2019.104819.

[17] P.H. Arthur, C.L. Morris (1939), "The introduction of agar-agar into bacteriology", *Journal of Bacteriol*, **37(5)**, pp.485-493, DOI: 10.1128/JB.37.5.485-493.1939.

[18] P.G. Martin (1997), "Quality assurance in the food control microbiological laboratory", *Manual of Food Quality Control*, Food and Agriculture Organization of the United Nations Rome.

[19] F.H. Samuel, M.M. Abayneh (2014), "Microbiological quality of indoor air in university libraries", *Asian Pac. J. Trop. Biomed.*, **4(1)**, pp.312-317, DOI: 10.12980/APJTB.4.2014C807.

[20] S. Borrego, et al. (2010), "The quality of air at archives and the biodeterioration of photographs", *Int. Biodeterior. Biodegradation*, **64(2)**, pp.139-145, DOI: 10.1016/j.ibiod.2009.12.005.

[21] B. Gutarowska (2010), "Metabolic activity of moulds as factor of building materials biodegradation", *Polish Journal of Microbiology*, **59(2)**, pp.119-124.

[22] http://www.inive.org/medias/ECA/ECA_Report12.pdf.

[23] A.E. Clark, E.J. Kaleta, A. Arora, D.M. Wolk (2013), "Matrix-assisted laser desorption ionization-time of flight mass spectrometry: a fundamental shift in the routine practice of clinical microbiology", *Clin. Microbiol. Rev.*, **26(3)**, pp.547-603, DOI: 10.1128/CMR.00072-12.

[24] J.F. Meadow, et al. (2014), "Indoor airborne bacterial communities are influenced by ventilation, occupancy and outdoor air source", *Indoor Air*, **24(1)**, pp.41-48, DOI: 10.1111/ina.12047.

[25] S.A. Wamedo, P.N. Ede, K. Chuku (2012), "Interaction between building design and indoor airborne microbial load in Nigeria", *Asian J. Biol. Sci.*, **5(4)**, pp.183-191, DOI: 10.3923/ajbs.2012.183.191.

[26] D. Hospodsky, et al. (2012), "Human occupancy as a source of indoor airborne bacteria", *PLOS ONE*, **7(4)**, DOI: 10.1371/journal.pone.0034867.

[27] G.S. Graudenz, C.H. Oliveira, A. Tribess, C. Mendes, M.R. Latorre, J. Kalil (2005), "Association of air-conditioning with respiratory symptoms in office workers in tropical climate", *Indoor Air*, **15(1)**, pp.62-66, DOI: 10.1111/j.1600-0668.2004.00324.x.

[28] A.A. Komlavi (2015), *Fungal Aerosols: Characterization and Immunodetection of Fungal Fragments*, Philosophiae Doctor (PhD) Thesis, Norwegian University of Life Sciences.

[29] W. Fabian, et al. (2016), "Fungal and bacterial communities in indoor dust follow different environmental determinants", *PLOS ONE*, **11(4)**, e0154131pp, DOI: 10.1371/journal.pone.0154131.

[30] H. Shokri, et al. (2010), "Common environmental allergenic fungi causing respiratory allergy in North of Iran", *International Journal of Veterinary Research*, **4(3)**, pp.169-172, DOI: 10.22059/IJVM.2010.21348.

[31] Morbidity and Mortality Weekly Report (2005), *Outbreak of Cutaneous Bacillus Cereus Infection among Cadets in a University Military Program*, Centers for Disease Control and Prevention, Georgia, **54(48)**, pp.1233-1235.

[32] T.L. Pitt, et al. (2007), "Characterisation of Exiguobacterium aurantiacum isolates from blood cultures od six patients", *Clinical Microbiology and Infection*, **13(9)**, pp.946-948, DOI: 10.1111/j.1469-0691.2007.01779.x.

[33] W.T.T. Emily, et al. (2014), "Misidentification of aspergillus nomius and aspergillus tamarii as aspergillus flavus: characterization by internal transcribed spacer, β-tubulin, and calmodulin gene sequencing, metabolic fingerprinting, and matrix-assisted laser desorption ionization-ti", *Journal of Clinical Microbiology*, **52(4)**, pp.1153-1160, DOI: 10.1128/JCM.03258-13.

[34] K. Anna, P. Alzbieta, M. Dominika, P. Przemyslaw (2008), "Sclerotia of the acellular (true) slime mould Fuligo septica as a model to study melanization and anabiosis", *Cellular and Molecular Biology Letters*, **13(1)**, pp.130-143, DOI: 10.2478/s11658-007-0047-5.

DOI: 10.31276/VJSTE.62(4).36-42

Flood inundation mapping using Sentinel-1A in An Giang province in 2019

Thi Hong Diep Nguyen[1*], Trong Can Nguyen[2], Thi Ngoc Tran Nguyen[3], Thien Nhi Doan[3]

[1] *College of Environment and Natural Resources, Can Tho University, Vietnam*
[2] *King Mongkut's University, Thailand*
[3] *Can Tho University, Vietnam*

Received 24 August 2020; accepted 20 November 2020

Abstract:

An Giang is one of the provinces in the Mekong delta that is greatly affected by flood events, which brings damage and devastation to life and property. This study practices the application of Sentinel-1A images to monitor the distribution of flood depths in the An Giang province in 2019 as well as applies regression correlation and thresholding to scattering value analysis. The research results indicated the exponential regression model on the VV polarization images had correlation coefficients (r) in August, September, and October ranging from 0.8398 to 0.9764 and determination coefficients (R^2) ranging from 0.7896 to 0.9533. Results from the map of current flood depth showed that the flood depth ranged from 0-250 cm, which corresponded to four flood levels. The flood area increased from August to October with the largest flooded area being 89,606.82 ha (accounting for 26.15%) mainly on rice lands and in eight urban districts including An Phu, Tinh Bien, Chau Thanh, Chau Phu, Phu Tan, Tri Ton, Chau Doc, and Long Xuyen city. The limit of flood depth determined by using the Sentinel-1A images was below 145 cm. Above this value, the scattering in the image is not significantly different from the actual submerged depth.

Keywords: **An Giang province, backscatter, correlation regression, flood depth, Sentinel-1A.**

Classification number: **5.1**

Introduction

The Mekong delta is located in the low-lying area of the Mekong river basin and has an important role in Vietnamese economy. The Mekong delta is vulnerable to climate change and flood-related disasters. Recently, the Vietnamese part has been severely impacted by an increased frequency of floods and unusually large flooded areas more than any other country in the Mekong river basin. Each year, about half of the delta is flooded by overflow 1 to 3 meters in depth. This area's vulnerability to flooding thus creates a large negative impact on economic development not only in the region, but also in Vietnam as a whole. An Giang is the upstream province of the Mekong river delta thus the water depth and flood duration is higher and longer than in other provinces in the region. Families living in the low-level region of the inland areas in the Mekong river delta, especially in the An Giang province, has suffered the most from the annual flooding [1].

It is necessary to detect flood water levels to determine the magnitude of inundation, water level magnitude, and their variations, which are utilized to monitor the flooding extent. Remote sensing is one of the most promising applications to estimate flood level via satellite altimetry data. Satellite altimetry data includes the ERS-2, ENVISAT, and TOPEX/Poseidon satellites that are used to monitor water levels in rivers, lakes, and floodplains [2-5]. However, the flood water level of the entire flood areas is impossible to examine using this method because satellite altimeters only measure the water level of places due to their orbits. Therefore, another approach applied to calculate flood water levels combines flood area estimation and DEM. According to [6], flood water depths were classified from satellite images and labelled as shallow, medium, and deep using digital elevation data. Combined with these flood depths and physiographic and geological data, flood hazard maps were created. The authors [7, 8] combined DEMs and high-resolution images to measure the water levels of rivers and produced flood inundation maps. The authors [9, 10] performed flood water level calculations using satellite images and identified a simple linear regression to calculate flood depths by a given flood event. Apart from initial studies, several research works have concentrated on improving estimation accuracy [11-14]. Review articles [15, 16] are also available. Since the mid

*Corresponding author: Email: nthdiep@ctu.edu.vn

1990s, with the advantages of synthetic aperture radar (SAR), satellite images have become available and developed for flood monitoring [17], which has continued to improve with launches of very high-resolution SAR satellites over the past decade, particularly, TerraSAR-X by the German Aerospace Center (DLR), Radarsat-2 by the Canadian Space Agency (CSA), and also constellations of COSMO-SkyMed, by the Italian Space Agency (ASI), and Sentinel-1, by the European Space Agency (ESA). Synthetic aperture radar data has the advantage of the ability to create flood mapping through cloud cover and can remain largely unimpacted by adverse weather conditions that often exist during high-impact flood events [18]. This innovation has brought higher reliability to flood mapping and has accelerated flood forecasting progress and flood inundation model development particularly in calibration and validation modelling of the area [19-27] and more recently assimilation [8].

This study aims to develop an estimation method of flood water level for the measurement of water levels on floodplains surveyed through a combination of satellite images and adopted regression models to compute the flood depths of a given flood event. We selected the An Giang province as the study area, which is a flood-prone area with a complex system of canals and rivers. We applied SAR satellite images (i.e. Sentinel-1A data) for the developed method. The results using Sentinel-1A images were verified by comparison with ground observation data and floodplain points in the study area.

Study area and data

Study area (Fig. 1)

The Vietnam Mekong delta (VMD) is the end of the Mekong river. The An Giang province (10°12' N to 10°57' N and 104°46' E to 105°35' E) is the first province of the VMD and it borders with Cambodia in the northwest (104 km long). An Giang's population is over 2.4 million (2019) [28] with a total area around 3,536 km^2 in which 70% of this area is used for agricultural production. There are two distinct seasons in this region that consists of dry and wet (monsoon). The wet season happens between May and November in which high rainfall usually appears in October and November at the end of the wet season. The flooding season occurs nearly at the same time as the rainfall season, leading to the risk of deep inundation. Because of the location's geography, there are two main branches of the Mekong river that flow through the province, namely, the Tien river and Hau river, which bring annual floods to the delta. Thus, An Giang annually faces flooding that is deeper and higher than other provinces. Since the strategy for intensive rice-cultivated production was developed by the Government of Vietnam [29], a full-dykes system that fully encloses the triple rice fields from flood water has been rapidly covering the An Giang province. Consequently, they affect the flood situation over the whole the province as well as in areas downstream [30].

Data used

The SAR sensor onboard the Sentinel satellite uses Terrain Observation with Progressive Scans SAR (TOP-SAR) to acquire images [31]. Level 1 Ground Range Detected (GRD) Sentinel 1A C-band scenes were collected for this study from the Copernicus Open Access Hub (https://scihub.copernicus.eu) on ESA's website. Level 1 GRD products concern SAR data detected, multi-looked, and projected to ground range using an earth Ellipsoid Model with an approximate square pixel resolution [32].

A total number of three GRD SAR scenes, in descending and ascending Interferometry Wide (IW) swath mode with polarization VV and VH, were collected spanning the period from August to

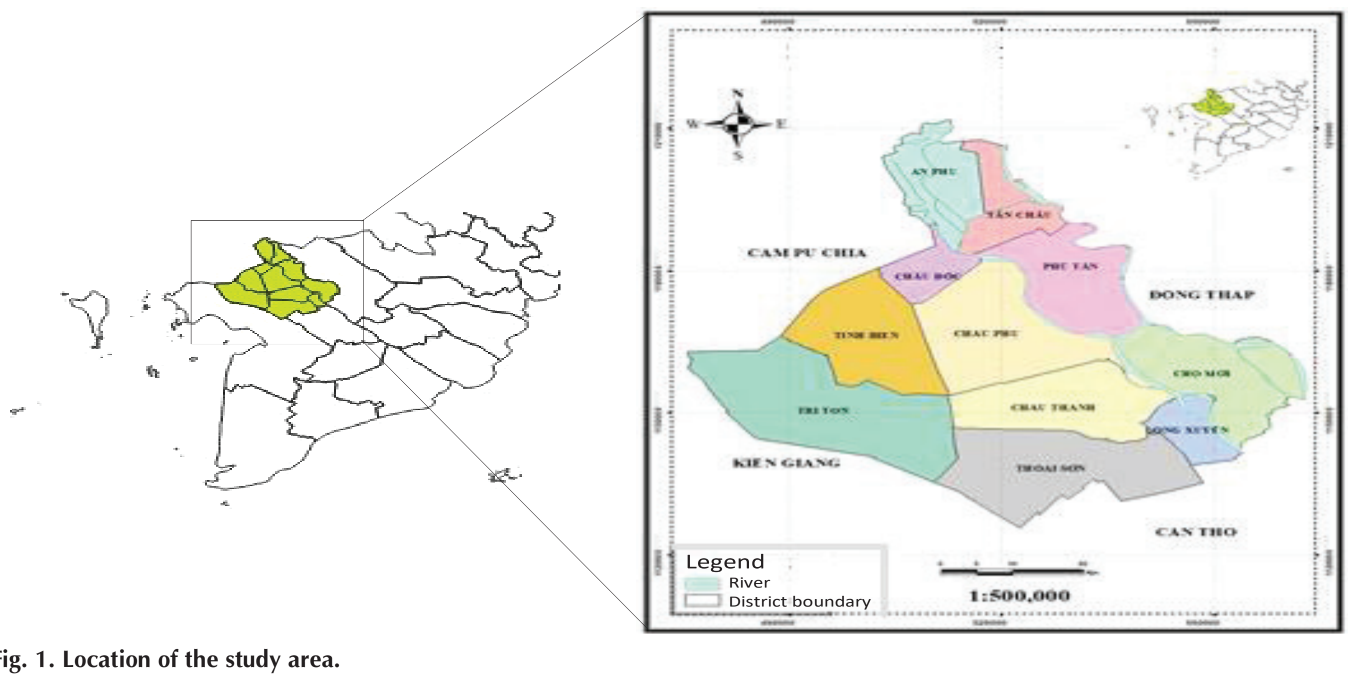

Fig. 1. Location of the study area.

October 2019 (Table 1). These data were processed and analysed to create binary water/non-water products as well as SAR multi-temporal products based on the contrast of the surface variations of land and water showing different back-scattering signatures.

Table 1. Catalogue of Sentinel-1 SAR scenes used.

No.	Scene Name	Date of capture	Resolution	Polarization
1	S1A_IW_GRDH_1SDV_20190806T111128_20190806T111153_028448_033705_9B94	06/08/2019	10 m	VV, VH
2	S1A_IW_GRDH_1SDV_20190911T111130_20190911T111155_028973_034937_F8F8	11/09/2019	10 m	VV, VH
3	S1A_IW_GRDH_1SDV_20191005T111131_20191005T111156_029323_035539_E66C	05/10/2019	10 m	VV, VH

Collection of water depth samples

Water depth samples were collected during the rainy season from August to October 2019, in flood cover in the An Giang province. Photographs were taken at each sample's location, which had coordinates determined using the global positioning system (GPS) and the water depth measurement was made by a depth gauge. The sampling sites selection was conducted with a random sampling technique with 107 total samples with 15 samples in August, 40 samples in September, and 52 samples in October as shown in Fig. 2.

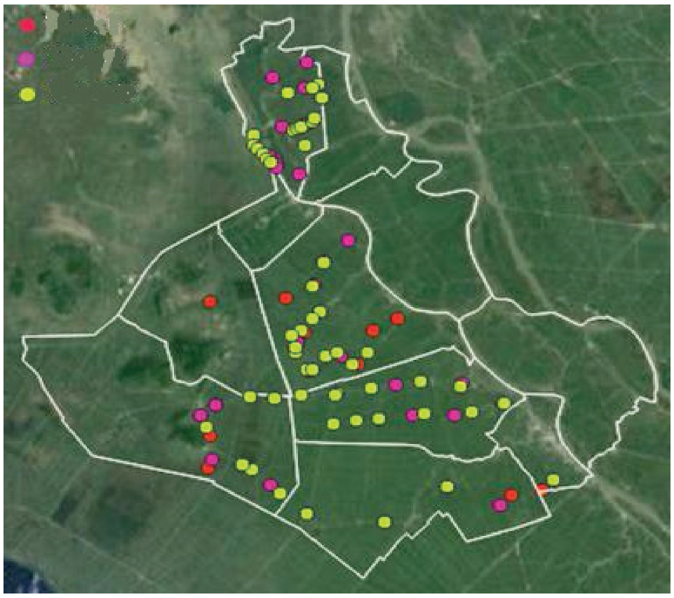

Fig. 2. Location of sampling sites.

Methodology

Data processing

The SAR Sentinel 1 images were processed with the free software SNAP (Sentinel Application Platform) Tool version 7.0.0. [33], which was created by ESA for data classification by Sentinel satellites. In addition, the spatial data validation processing steps are shown in Fig. 3. The image processing steps include: (1) delineating the targeted study area, a subset of the whole image is created by setting the geographic coordinates values of study area; (2) adjusting image resolution, radiometric correction was processed to relate radar backscatter due to pixel values, thus, it is essential for quantitative image calibration to use the SAR data as pixel values to represent the reflecting surface of the true radar backscatter; (3) radiometric correction, this operation is necessary to produce multi-temporal products. With a calibration vector included, Sentinel-1 data allows the conversion of the image's intensity values into sigma naught values (s0). From this step onward, processing is generated for the two polarizations VH and VV that we provide [34, 35]; (4) geometric correction, a correction of geometric distortion caused by topography such as foreshortening and shadows using a digital elevation model correction to the location of each pixel; (5) image filtering, the main problem of SAR data is speckle "noise" caused by the random effect of many small individual reflectors within a given pixel. In order to reduce the speckle in SAR images, different adaptive filters were applied to preserve the radiometric and textural information and to enhance visualization at the same time. After comparison, the Lee filter uses mean and standard deviation with window size determination to assess different factors for smoothing (Fig. 3E). In homogeneous regions of flooded areas, the final pixel value is the linear average of neighbouring pixels [36]. Therefore, this filter uses a priori knowledge of the Probability Density Function (PDF) of the scene when suppressing the speckle of the scene [37, 38]; and (6) conversion of the image intensity values into a sigma naught value, which is a unitless backscatter coefficient that is converted to dB using a logarithmic transformation.

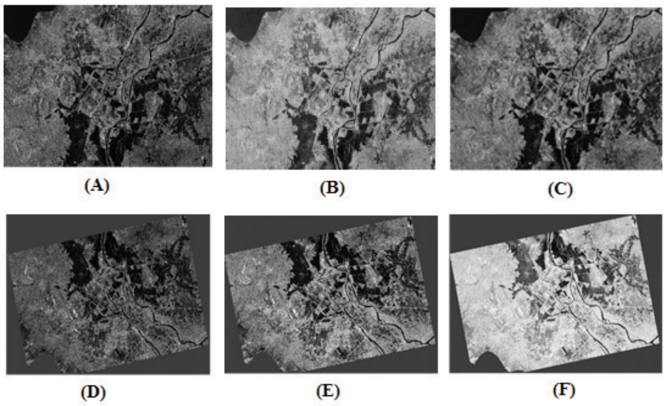

Fig. 3. (A) Delineating the target study area, (B) adjusting image resolution, (C) radiometric correction, (D) geometric correction, (E) image filtering, and (F) sigma naught values (dB).

The last common step in image pre-treatment is to perform a correction of the terrain and ortho-rectification. This mainly eliminates distortions due to changes in the topography and the angle of incidence with the ground with respect to the nadir. The geometric calibration used in this study was range Doppler terrain correction and the digital elevation model (DEM)–SRTM-3Sec to derive precise geolocation information. The map projection type of the output images was expressed in WGS84 geographic coordinates.

The above-mentioned actions are considered as pre-processing steps. In this study, two products were generated based on SAR data: i) binary images showing water and non-water areas over the study area and ii) multi-temporal SAR images combining two or three dates to show spatiotemporal occurrences and a seasonal evolution of the flood event.

For the water/non-water product generation, the image binarization technique was applied. The threshold segmentation algorithm, or histogram thresholding, is a simple, widely used, and effective method to generate a binary image [39]. The first step is to separate water from non-water areas through binarization and selection of a suitable threshold for each image. Low values of the backscatter corresponded to the water, while high values correspond to the non-water areas.

Regression model

Backscatter values at the measurement positions were extracted from the images with VV and VH polarities with the Point Sampling Tool on QGIS. Following the analysis of regression models in Excel, the appropriate form of the fit equation through the correlation between backscattering values on the image and the field depth of inundation was chosen.

Performance assessment

The flood depth performance was assessed and estimated using three statistical metrics parameters, namely, RMSE (Root Mean Square Error), MAE (Mean Absolute Error), and r (correlation coefficient).

$$\mathrm{RMSE} = \sqrt{\frac{1}{n}\sum_{j=1}^{n}(xi - X)^2} \quad (1)$$

$$r = \frac{\sum_{i=1}^{n}(x_i-\bar{x})(y_i-\bar{y})}{\sqrt{\sum_{i=1}^{n}(x_i-\bar{x})^2\sum_{i=1}^{n}(y_i-\bar{y})^2}} \quad (2)$$

where x_i and y_i are the calculated and measured flood depth values the i^{th} sample, respectively; $\bar{x}$ and $\bar{y}$ are the mean values of the EC measurement and the flood depth values prediction, respectively; and n is the total number of samples used.

Results

Data collection

The correlation data and regression analysis/verification were completed from 107 flooding points in An Giang province as shown in Table 2.

Table 2. Data used for correlation and regression analysis.

No.	Date	Total measuring points	Total analysing points	Total regression points	Total inspection points	Excluded points
1	06/08/2019	15	12	07	05	03
2	11/09/2019	40	36	26	10	04
3	05/10/2019	52	48	33	15	04
Total		107	96	66	30	11

Regression models

Two regression models suitable for the study of flood depth including linear regression and exponential regression models were obtained from the results of the regression and correlation analysis (Table 3).

Table 3. The regression model equation used to estimate the flood depth of on each polarized Sentinel-1A image in 2019.

No.	Month	Polarization	Regression Model	r(η)	R^2
1	August	VV	DSN1=-0.9211*VV-1.7404	0.7545	0.5692
2			DSN2=1.6324*$e^{-0.143*VV}$	0.7976	0.6361
3		VH	DSN3=-0.955*VH-8.3268	0.8204	0.673
4			DSN4=0.6974*$e^{-0.138*VH}$	0.8055	0.6488
5	September	VV	**DSN5=-3.9199*VV-28.351**	**0.8826**	**0.779**
6			DSN6=0.4281*$e^{-0.247*VV}$	0.7919	0.6271
7		VH	DSN7=-4.4258*VH-61.815	0.8218	0.6753
8			DSN8=0,0648*$e^{-0.267*VH}$	0.7053	0.4975
9	November	VV	**DSN9=-7.1994*VV-30.918**	**0.7119**	**0.5069**
10			DSN10=1.8742*$e^{-0.21*VV}$	0.8557	0.7322
11		VH	DSN11=-10.492*VH-144.03	0.7457	0.5561
12			DSN12=0.1152*$e^{-0.282*VH}$	0.8275	0.6848

Table 3 shows that all 12 regression model equations have a negative correlation and the correlation and determination coefficients are greater than 0.5. The model with the highest coefficients is the linear regression model on the VV polarization in September with r and R^2 being 0.8826 and 0.779, respectively. In contrast, the model with the lowest r and R^2 coefficients is the linear regression model on the VV polarization in October with 0.7119 and 0.5069, respectively.

Validation flood depth models

The number of inspection points was 5 points in August, 10 points in September and 15 points in October. In the testing results of all regression models shown in Table 3, there was a correlation between the estimated flood depth in image and the field flood depth since the coefficient of determination R^2 is greater than 0.5. The most suitable regression model is the exponential regression model on the VV polarization with correlation coefficients, coefficients of determination, deviations (Bias), and root mean square errors (RMSE) given in Table 4 for August, September and October. The study used an exponential model to establish the maps of current flood depth status in each month in 2019.

Table 4. The relevance of the regression models through testing coefficients and the correlation between estimated flood depth and field flood depth in 2019.

No.	Month	Polarization	Inspected regression model	R	R^2	Bias (cm)	RMSE (cm)
1	August	VV	DSN1=-0.9211*VV-1.7404	0.6384	0.7999	-2.17	2.67
2			**DSN2=1.6324*e$^{-0.143*VV}$**	**0.8886**	**0.7896**	**-2.04**	**2.41**
3		VH	DSN3=-0.955*VH-8.3268	0.8177	0.6687	-1.6	2.11
4			DSN4=0.6974*e$^{-0.138*VH}$	0.8738	0.7636	-1.41	1.84
5	September	VV	DSN5=-3.9199*VV-28.351	0.9456	0.8941	6.78	11.99
6			**DSN6=0.4281*e$^{-0.247*VV}$**	**0.9764**	**0.9533**	**3.06**	**7.55**
7		VH	DSN7=-4.4258*VH-61.815	0.8881	0.7887	2.56	14.06
8			DSN8=0.0648*e$^{-0.267*VH}$	0.9555	0.9129	3.25	10.57
9	October	VV	DSN9=-7.1994*VV-30.918	0.8663	0.7505	-29.69	33.8
10			**DSN10=1.8742*e$^{-0.21*VV}$**	**0.8398**	**0.7052**	**2.29**	**17.93**
11		VH	DSN11=-10.492*VH-144.03	0.5458	0.2979	-12.36	34.79
12			DSN12=0.1152*e$^{-0.282*VH}$	0.6762	0.4573	-5.44	55.55

Flood depth mapping in 2019 in An Giang

Based on the selected regression model, flood depth maps were created in An Giang during three months from August to October in 2019. The maps contain flood depths that are graded according to a colour scheme from light to dark (Fig. 4). In August, the flooding level was low and it was concentrated on the four districts of Thoai Son, Chau Thanh, Chau Phu, and Phu Tan (Fig. 4A). By September, floods began to increase in both surface distribution and depth with a focus on areas without dikes in districts like An Phu, Tinh Bien, Chau Phu, Chau Thanh, Phu Tan, and Chau Doc city (Fig. 4B). Finally, in October, the flood surface continued to expand and the flood depth was at its highest this month. The flood area was distributed outside the dikes and expanded to eight districts including An Phu, Tinh Bien, Chau Thanh, Chau Phu, Phu Tan, Tri Ton, Chau Doc, and Long Xuyen city (Fig. 4C).

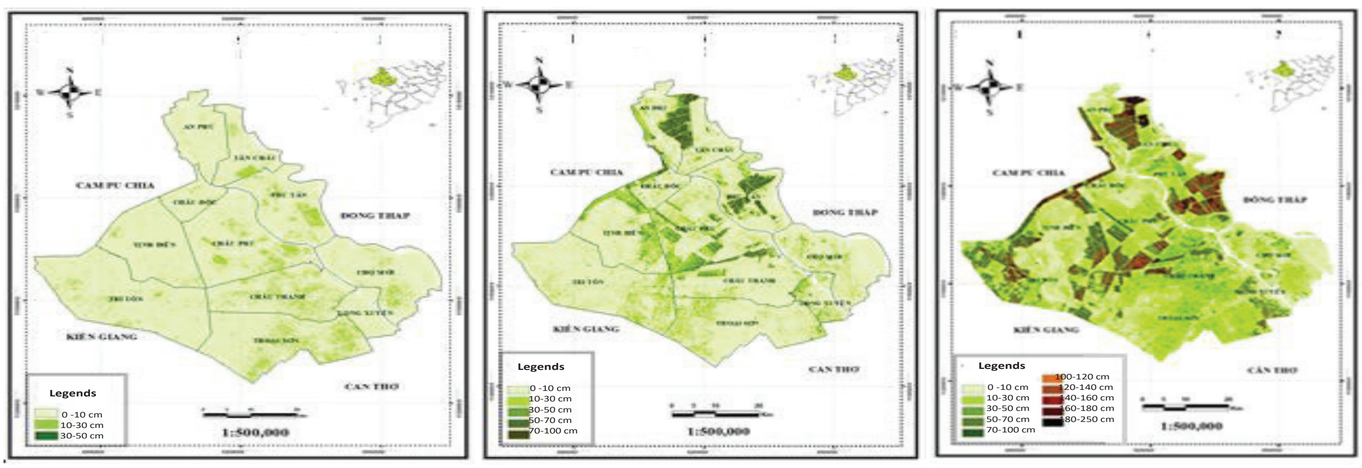

Fig. 4. The flood depth distribution in the An Giang province in 2019 (A) in August, (B) in September, and (C) in October.**Fig. 4. The flood depth distribution in the An Giang province in 2019 (A) in August, (B) in September, and (C) in October.**

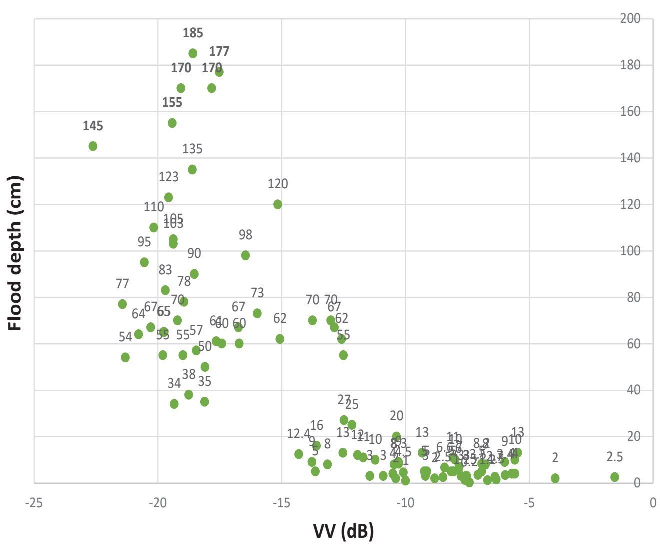

Fig. 5. Threshold diagram of field flood depth and backscattering values on VV polarization.

Estimation flood depth threshold on Sentinel-1A image

According to Fig. 5, the deeper the flood depth is, the lower the backscattering value on the VV polarization becomes and vice versa. However, when the depths range from 140-160 cm, there is a sudden change where the backscattering values decrease at a depth from above 145 cm to -22.6 dB. The data in Fig. 5 shows that the values of flood depth and backscattering are no longer in correlation over the depth of 145 cm, at which the backscattering values begin to go along the opposite direction (forward).

The flooding depths of more than 145 cm were tested to clarify that the thresholding results of the flood depth limit on Sentinel 1A images have eliminated depth value correlations to the backscattering values in each location where field depth values were measured. Fig. 6 shows the flood depth limit using the Sentinel-1A images below 145 cm, the depth values above 145 cm did not have a significant difference due to the backscattering value compared to the actual flood depth.

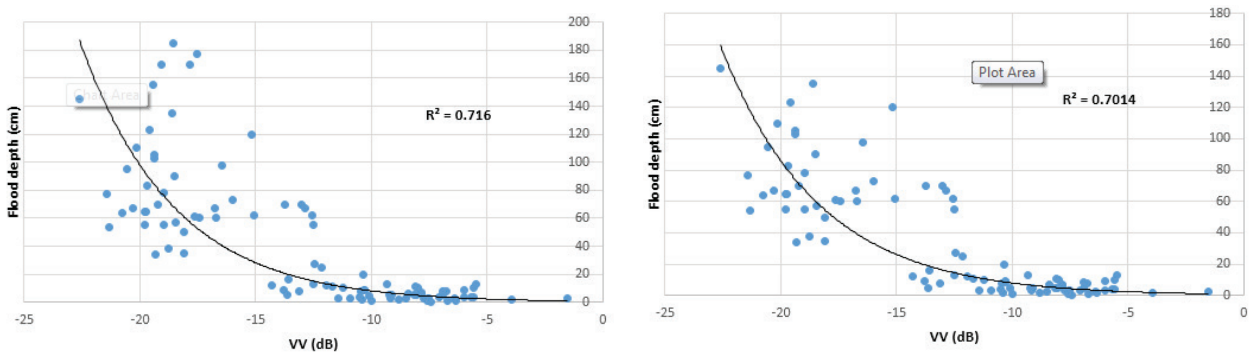

(A) (B)

Fig. 6. Correlation between field flood depth and the backscattering value on VV polarization in 2019: (A) correlation coefficient (96 samples), (B) correlation coefficient (91 eliminated samples).

Flood depth threshold in 2019 in An Giang province

The VV polarization results were used to create thresholds and develop flood depth maps (Table 5). It was shown that there was not much difference between the imagery values (dB) thresholded as a water object during the three months of flooding because the flooding levels were different, thus the backscattering values were not the same. In general, a low backscattering value indicates the presence of water and, in contrast, a high backscattering value does not indicate the presence of water.

Table 5. Correlation between backscattering values and water values on Sentinel 1A images during three months in 2019.

No.	Date	Imagery values (dB)	Water values (dB)
1	06/08/2019	+30,6 to -24,8	-12 to -24,8
2	11/09/2019	+22,4 to -26,2	-14 to -26,2
3	05/10/2019	+14,7 to -25,4	-16 to -25,4

Discussion

This research aimed to detect flood depth using Sentinel-1 data for recording water levels changes from August to October 2019 in the An Giang province, which is an upstream province in the Mekong river delta. Sentinel-1 SAR imagery proved an effective tool for excellent spatiotemporal dynamic of flood depth maps and offers the possibility of processing an entire study area based on the extent of spatial coverage for each image. Mapping development for the variations in water depth levels in the study area before, during, and after the flood event was also feasible with Sentinel-1 imagery. The flood season occurred from May to November in 2019 with the flood extent taking place in October 2019 outside the dyke when floods covered nearly the entire the An Giang province. It was also proved that there was a high correlation between backscatter value and flood depth value during the flood event and limited backscatter values for flood depths on Sentinel 1A images.

Flood depth maps created from Sentinel-1 SAR images complement and validate information that elucidates the spatial and temporal evolution of floods. The results advise the use of Sentinel-1 SAR images to derive flood depth by the calibration and evaluation of hydrological models and as a data source that can be analysed using other methodologies.

Sentinel 1A data was collected from August to October 2019 and, in this research, could not show a series map of flooded areas during rainy season periods. Also, the impact of a drainage system was not mentioned in this research to analyse water withdrawal in an inundated area.

The research must take into consideration that satellite observations allow one to outline a flooded area and estimate the water depth at the specific date and time during the flood events corresponding to a minimum and maximum water depth classification. Future work may consider integrating a DEM filling procedure for water level estimation to indicate an error in the flood map and its corresponding elevation. This would be information that improves the statistics and estimation of the water levels.

Conclusions

This study has determined a correlation between the values of field flood depth and backscattering values from Sentinel-1A image polarizations with high correlation coefficients (r) >0.8 (0.84-0.98) and the coefficients of determination R^2>0.75 (0.79-0.95) for three months (August, September and October) in 2019. At the same time, flood depths were observed to range from 0-250 cm with five water depth levels. In August, the area was the lowest with 21,601.65 ha (accounting for 6.31%) of the total provincial flooded area and was divided into two levels of flood depths ranging from 0-50 cm. In September the flooded area increased to 56,656.75 ha (accounting for 16.54%) and was divided into three levels of flood depth corresponding to depths ranging from 0-100 cm. In October the distribution of flood depth reached its peak with the highest flooded area of 89,606.82 ha (accounting for 26.15%) and was divided into four levels of flooding corresponding to the depth of flood from 10-250 cm. This study determined the threshold of flood depth using Sentinel-1A images below 145 cm. If the depth of flood exceeds this value, the scattering value on the image will not find a difference in the field flood depth.

ACKNOWLEDGEMENTS

The authors thank the Department of Science and Technology in the An Giang province, which has been very helpful in providing valuable materials and supporting us during the survey. We highly appreciate the valuable funding in part by the Technological

Cooperation Project "Building capacity for Can Tho University to be an excellent institution of education, scientific research and technology transfer" of JICA. Our gratitude extends to the Can Tho University Improvement Project VN15-P6 which was funded by a Japanese ODA loan to all those who provided us the possibility to complete this research in ODA-E3 project. Lastly, but of equal importance, we owe a great debt to the project management board and colleagues at the College of Environment and Natural Resources to support us during the accomplishment of this project. We thank the European Space Agency for providing us with the satellite data used in this study.

COMPETING INTERESTS

The authors declare that there is no conflict of interest regarding the publication of this article.

REFERENCES

[1] Ministry of Agriculture and Rural Development (MARD) (2010), *Flood Proofing for Poor Coastal and Inland Households in the Mekong River Delta in Viet Nam - Pilot in An Giang Province*, United Nations Development Program, Project Duration: 11/1-30/9/2007, Program Component: Environment and Energy for Sustainable Development.

[2] F. Frappart, et al. (2006), "Water volume change in the lower Mekong from satellite altimetry and imagery data", *Geophysical Journal International*, **167**, pp.570-584.

[3] S.J. Birkinshaw, et al. (2010), "Using satellite altimetry data to augment flow estimation techniques on the Mekong river", *Hydrological Processes*, **24**, pp.3811-3825.

[4] A.A. Jarihani, et al. (2013), "Evaluation of multiple satellite altimetry data for studying inland water bodies and river floods", *Journal of Hydrology*, **505**, pp.78-90.

[5] F. Baup, F. Frappart, J. Maubant (2014), "Combining high-resolution satellite images and altimetry to estimate the volume of small lakes", *Hydrology and Earth System Sciences*, **18**, DOI: 10.5194/hess-18-2007-2014.

[6] M.M. Islam, and K. Sado (2000), "Development of flood hazard maps of Bangladesh using NOAA-AVHRR images with GIS", *Hydrological Sciences Journal*, **45(3)**, pp.337-355.

[7] D. Raclot (2006), "Remote sensing of water levels on floodplains: a spatial approach guided by hydraulic functioning", *International Journal of Remote Sensing*, **27**, pp.2553-2574.

[8] R. Hostache, X. Lai, J. Monnier, C. Puech (2010), "Assimilation of spatially distributed water levels into a shallow-water flood model. Part II: use of a remote sensing image of Mosel river", *Journal of Hydrology*, **390**, pp.257-268.

[9] P. Matgen, et al. (2007), "Integration of SAR-derived river inundation areas, high-precision topographic data and a river flow model toward near real-time flood management", *International Journal of Applied Earth Observation and Geoinformation*, **9(3)**, pp.247-263.

[10] G. Schumann, et al. (2007), "High-resolution 3-D flood information from radar imagery for flood hazard management", *IEEE Transactions on Geoscience and Remote Sensing*, **45**, pp.1715-1725.

[11] D.C. Mason, et al. (2007), "Improving river flood extent delineation from synthetic aperture radar using airborne laser altimetry", *IEEE Transactions on Geoscience and Remote Sensing*, **45(12)**, pp.3932-3943.

[12] F. Pan, et al. (2013), "Application of the inundation area - lake level rating curves constructed from the SRTM DEM to retrieving lake levels from satellite measured inundation areas", *Computers & Geosciences*, **52**, pp.168-176.

[13] D.C. Mason, et al. (2016), "Improving the tan DEM-X digital elevation model for flood modeling using flood extents from synthetic aperture radar images", *Remote Sensing of Environment*, **173**, pp.15-28.

[14] K. Chen, R.M. Horton, D.A. Bader, C. Lesk, L. Jiang, B. Jones, L. Zhou, X. Chen, J. Bi, P.L. Kinney (2017), "Impact of climate change on heat-related mortality in Jiangsu province, China", *Environ. Pollut.*, **224**, DOI: 10.1016/j.envpol.2017.02.011.

[15] Z.N. Musa, I. Popescu, A. Mynett (2015), "A review of applications of satellite SAR, optical, altimetry and DEM data for surface water modeling, mapping and parameter estimation", *Hydrology and Earth System Sciences*, **19**, pp.3755-3769.

[16] S. Grimaldi, et al. (2016), "Remote sensing-derived water extent and level to constrain hydraulic flood forecasting models: opportunities and challenges", *Surveys in Geophysics*, **37**, pp.977-1034.

[17] G.J.P. Schumann, A. Domeneghetti (2016), "Exploiting the proliferation of current and future satellite observations of rivers", *Hydrol. Process.*, **30**, pp.2891-2896.

[18] G.J.P. Schumann, D.K. Moller (2015), "Microwave remote sensing of flood inundation", *Phys. Chem. Earth Parts A/B/C*, pp.84-95.

[19] P.D. Bates, M.S. Horritt, C.N. Smith, D.C. Mason (1997), "Integrating remote sensing observations of flood hydrology and hydraulic modelling", *Hydrol. Process.*, **11**, pp.1777-1795.

[20] G. Aronica, P.D. Bates, M.S. Horritt (2002), "Assessing the uncertainty in distributed model predictions using observed binary pattern information within GLUE", *Hydrol. Process.*, **16**, pp.2001-2016.

[21] J. Garcia-Pintado, J.C. Neal, D.C. Mason, S.L. Dance, P.D. Bates (2013), "Scheduling satellite-based SAR acquisition for sequential assimilation of water level observations into flood modelling", *Journal of Hydrology*, **495**, pp.252-266.

[22] P. Matgen, M. Montanari, R. Hostache, L. Pfister, L. Hoffmann, D. Plaza, et al. (2010), "Towards the sequential assimilation of SAR-derived water stages into hydraulic models using the particle filter: proof of concept", *Hydrology and Earth System Sciences*, **14(9)**, pp.1773-1785.

[23] P.D. Bates (2012), "Invited commentary: integrating remote sensing data with flood inundation models: how far have we got?", *Hydrol. Process.*, **26**, pp.2515-2521.

[24] G.J.P. Schumann, P.D. Bates, M.S. Horritt, P. Matgen, F. Pappenberger (2009), "Progress in integration of remote sensing derived flood extent and stage data and hydraulic models", *Rev. Geophys.*, **47**, DOI: 10.1029/2008RG000274.

[25] G. Di Baldassarre, G. Schumann, P.D. Bates (2009), "A technique for the calibration of hydraulic models using uncertain satellite observations of flood extent", *Journal of Hydrology*, **367**, pp.276-282.

[26] M.S. Horritt and P.D. Bates (2002), "Evaluation of 1-D and 2-D numerical models for predicting river flood inundation", *Journal of Hydrology*, **268**, pp.87-99.

[27] P.D. Bates, M.S. Horritt, G. Aronica, et al. (2004), "Bayesian updating of flood inundation likelihoods conditioned on flood extent data", *Hydrol. Process.*, **18**, pp.3347-3370.

[28] https://en.wikipedia.org/wiki/An_Giang_Province (accessed on 10 May 2020).

[29] Benedikter (2013), *The Vietnamese Hydrocracy and the Mekong Delta*, ISBN 9793643904379.

[30] V.H.T. Duong, T. Van, F. Nestmann, P. Oberle, N.T. Nam (2014), *Land Use Based Flood Hazards Analysis for Mekong Delta*, Proceedings 19th IAHR Asian and Pacific Regional Division 2014, DOI: 10.13140/2.1.5153.9842

[31] F. De Zan, A. Monti Guarnieri (2006), "Terrain Observation by Progressive Scans, September", *IEEE Transactions on Geoscience and Remote Sensing*, **44(9)**, pp.2352-2360.

[32] https://sentinel.esa.int/web/sentinel (accessed on 8 August 2019).

[33] https://step.esa.int/main/download/snap-download (accessed on 22 December 2019).

[34] B. Tavus, S. Kocaman, C. Gokceoglu, H.A. Nefeslioglu (2018), "Considerations on the use of Sentinel-1 data in flood mapping in urban areas: Ankara (Turkey) 2018 floods", *Int. Arch. Photogram. Remote Sens. Spat. Inf. Sci.*, **XLII-5**, pp.575-581.

[35] H.-J. Ban, Y.-J. Kwon, H. Shin, H.-S. Ryu, S. Hong (2017), "Flood monitoring using satellite-based RGB composite imagery and refractive index retrieval in visible and near-infrared bands", *Remote Sens.*, **9**, DOI: 10.3390/rs9040313.

[36] J.-M. Park, W.J. Song, W.A. Pearlman (1999), "Speckle filtering of SAR images based on adaptive windowing", *IEE Proc. Vis. Image Signal Proces.*, **146**, pp.191-197.

[37] E. Nazry, A. Lopes, R. Touzi (1991), *Detection of Structural and Textural Features for SAR Images Filtering*, Proceedings of IGARSS, **91**, pp.2169-2172.

[38] A. Lopes, E. Nezry, R. Touzi, H. Laur (1993), "Structure detection and statistical adaptive speckle filtering in SAR images", *Int. J. Remote Sens.*, **14(9)**, pp.1735-1758.

[39] L. Pulvirenti, M. Chini, N. Pierdicca, L. Guerriero, P. Ferrazzoli (2011), "Flood monitoring using multitemporal COSMO-SkyMed data: image segmentation and signature interpretation", *Remote Sens. Environ.*, **115(4)**, pp.990-1002.

DOI: 10.31276/VJSTE.62(4).43-48

Nutrients in sediment regulate benthic algal assemblages in the tropical Tri An reservoir of Vietnam

Thi Hoang Yen Tran[1], Thanh Thai Tran[1], Xuan Quang Ngo[1, 2], Thanh-Luu Pham[1, 2*]

[1]Institute of Tropical Biology, Vietnam Academy of Science and Technology
[2]Graduate University of Science and Technology, Vietnam Academy of Science and Technology

Received 10 August 2020; accepted 30 October 2020

Abstract:

Benthic algal assemblages are considered effective indicators of environmental change because they sensitively respond to a variety of environmental conditions. This study aims to investigate the relationship between the benthic algal community and nutrient variables in sediment using Spearman's correlation and linear regression analysis. A total of 27 genera of benthic algae were recorded during the study period where cyanobacteria and diatom were the two dominant groups. Several species belonging to *Achnanthidium, Luticola, Lyngbya, Navicula*, and *Phormidium* sensitively responded to nutrient levels and were used as bioindicators. Multiple stepwise linear regression revealed that ammonium (NH_4^+) and total nitrogen (TN) positively correlated with several indices of the benthic algae assemblage. This preliminary data set demonstrates the use of benthic algae as precise biological indicators for a measure of the ecological integrity of an aquatic ecosystem and contributes to the further study of benthic environments in tropical regions.

Keywords: **benthic diatom, bioindicators, linear regression analysis, nutrient factors, Spearman's correlation analysis.**

Classification number: **5.1**

Introduction

Sediments in lakes and reservoirs are home to a variety of benthic organisms including animals, plants, microorganisms, as well as a sink of pollutants [1]. Benthic algal communities in sediment play a vital role in the biogeochemical cycle of its primary elements and contribute to about 20-25% of global primary production [2, 3]. In addition, benthic algae are primary producers in freshwater ecosystems that consist of lentic (particularly lakes, reservoirs and wetlands) and lotic (including streams and rivers) waters [3]. Because of their taxonomic distinction, abundance, good preservation in sediment, and their rapid response to environmental changes, they have been widely used as environmental indicators in freshwater ecosystems [4].

Among environmental factors, phosphate and nitrate content have been identified as the two most important variables that can account for the distribution of benthic algal assemblages in lentic waters [5-7]. Nitrogen and phosphorus are important for the development of different groups of diatom and cyanobacteria [8]. Benthic diatoms have been used to assess the ecological status of standing waters [9, 10]. Some diatom species such as *Achnanthidium eutrophilu* and *Navicula cryptotenella* are bioindicators of ecological conditions from oligosaprobous to hypereutraphentic, while *A. minutissimum* was reported as tolerant to nutrient loadings [10]. Therefore, a definitive understanding of benthic algal assemblages is essential to assess water quality degradation and nutrient enrichment in inland reservoirs [2, 5, 11].

The Tri An reservoir (TAR), located in the Dinh Quan district, Dong Nai province, Vietnam, is about 70 km northeast of Ho Chi Minh city [12]. It receives water from the Dong Nai and La Nga rivers. The reservoir has had multiple purposes such as a hydroelectric power plant, flood

*Corresponding author: Email: thanhluupham@gmail.com

control, as a domestic and industrial water supply, fisheries, and for the irrigation of agricultural fields [13]. There are a large number of fish cages, as well as a sugar factory, at the inflow of the reservoir by the La Nga river that leads to nutrient enrichment [13, 14]. For this reason, cyanobacterial blooms and their toxins in the TAR have recently been reported [12, 13, 15] and the relationships between several environmental factors and the distribution of cyanobacteria have been investigated [13]. However, little is known about the composition of the benthic algal community and their distribution in the TAR or how they respond to changes in environmental variables. Therefore, the objectives of this study were to describe the benthic algal community's compositions and understand whether nutritional factors in sediment can influence their structure and distribution in the TAR.

Materials and methods

Field sampling and nutrient analyses

Sediment samples were collected monthly from 8 sampling stations from March to May (dry season) and from June to August (rainy season) in 2019 using a stainless-steel hand borer. The samples were stored in plastic boxes kept in an ice box and transferred to the laboratory for analysis. Nutrient concentrations in the sediment were analysed colorimetrically in triplicate with a spectrophotometer (Hach DR/2010) according to the methods described by APHA (2005): nitrate 4500NO_3^- (A); ammonium 4500NH_4^+ (B); total nitrogen Kjeldahl, 4500N (C); phosphate 4500PO_4^{3-} (D); and total phosphorous 4500P (E) [16]. The samples were collected in the TAR at three regions with distinct occupation characteristics: the lower Tri An dam site (DN), the reservoir sites (TA1-TA5), and the upstream sites of Dong Nai (DQ) and La Nga rivers (LN) (Fig. 1).

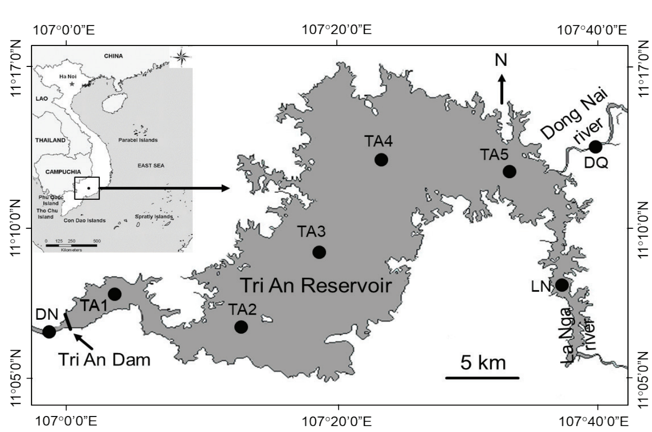

Fig. 1. Map of the Tri An reservoir and the 8 sampling locations.

Diatom sampling and identification

The benthic algae were collected on hard substrates in the field by using a toothbrush to scrape three stones over a surface area of 10 cm^2 [17]. Subsequently, the samples were preserved in plastic bottles and fixed in 4% neutralized formalin and then moved to the laboratory. The subsamples were concentrated to 10 ml and directly used for identification and to count the cyanobacteria. For diatom identification and counting, about 5-10 ml of a subsample was cleaned with concentrated nitric acid and washed with distilled water until it reached a circumneutral pH value. The morphology of the clear samples was observed with a light microscope (Olympus, Tokyo, Japan) at 400× magnification. The cell density was counted using a Sedgewick Rafter counting chamber. A minimum of 400 units were counted in each sample. The valves of the benthic algae were identified to the level of genera by using standard identification guides of several books [18-21].

Data analysis

Statistical calculations were performed using Statgraphic Centurion XV. One-way analysis of variance (ANOVA) was used to test the significance of the differences among the study sites and was based on the nutrient variables and diatom species structure metrics. The analysis was completed using Tukey's Honest Significant Difference (HSD). The correlation between the diatom species' structure metrics and environmental parameters was determined by Spearman's correlation analysis followed by linear regression analysis. All variables were log transformed (log+1) to normalize their distributions before analysis.

The diatom community's structural distribution, the Margalef's species richness index (d), Shannon-Weiner diversity index (H'), Pielou's evenness index (J'), and Simpson's diversity index (D'), which are commonly used in water quality bioassessments, were used to characterize each site [22].

Results and discussion

Nutritional concentration in sedimentary environment

The nutrient content of the sedimentary environment in TAR from the dates March to August in 2019 are illustrated in Fig. 2. During that time, the TN concentration in the rainy season was higher than in dry season and ranged from 0.04-0.19% and 0.04-0.29% in dry and rainy season, respectively. The TN concentration in the reservoir sites (TA1-TA5) were higher than that of the other sites ($p<0.05$). The N-NH_4^+ concentration was not much different in the dry and rainy season, which ranged from 3.6-29.6 mg/100 g and 1.4-22.7 mg/100 g in dry and rainy season, respectively. The N-NO_3^-

content varied from 1.4-5.4 mg/100 g and 0.1-3.2 mg/100 g in the dry and rainy season, respectively. The N-NO_3^- content in the dry season was higher than that of the rainy season, but it was not significantly different among reservoir sites ($p<0.05$). The TP value varied from 0.011-0.11% and from 0.01-0.07% in dry and rainy season, respectively. The TP content in the upstream sites (TA5, LN, DQ) were higher than that of the other sites during both seasons ($p<0.05$). The P-PO_4^{3-} content varied from 0.004-0.065% and 0.004-0.068% in the dry and rainy season, respectively. The concentration of P-PO_4^{3-} had almost the same trend as TP during both seasons.

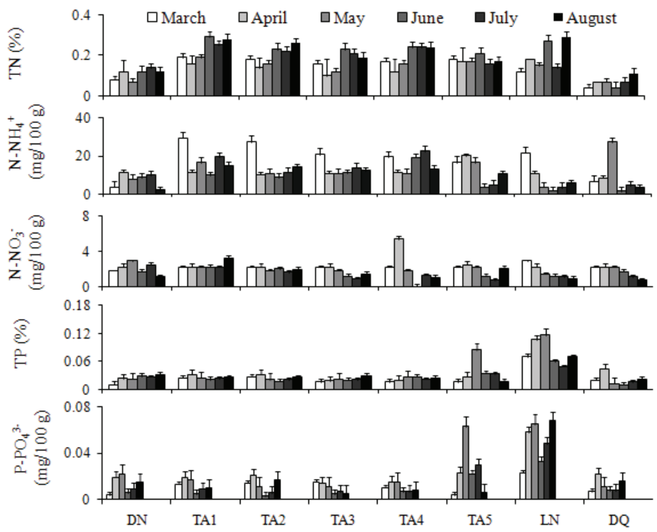

Fig. 2. The content of nutrients in the sedimentary environment.

Sediment in reservoirs, where nitrogen and phosphorus compounds are stored, can operate as a source of nutrient enrichment that could lead to eutrophication [23]. During the survey period, the main reservoir area (reservoir bed) had a higher nutrient content than the rest, particularly in TN and NH_4^+ concentrations. This may affect the sedimentation process and create a high potential for nutrient accumulation. In addition, the high nutrient content of TP and P-PO_4^{3-} at upstream sites such as TA5 and LN, especially in both seasons, may be due to the excessive food and excretion that is dumped directly into the environment from nearby cage fish farming. Many studies have already addressed the negative impact of fish cage culture on benthic organism communities of rivers and lakes. The sediment of organic matter released from the farming process could discharge between 67 to 89% of its nitrogen and phosphorus into the surrounding environment. Over time, the excess accumulation of phosphorus and nitrogen compounds can easily cause benthic algal communities, as well as phytoplankton, to grow in abundance and biomass that can lead to the eutrophication of cyanobacteria and diatom adapted to high concentrations [24, 25].

Benthic algal community composition and abundance

The benthic algal community structure from March to August in 2019 is illustrated in Fig. 3. A total of 27 genera of benthic algae were identified during the study period of which 13 genera belonged to cyanobacteria and 14 genera belonged to diatom. The benthic algal communities at the reservoir sites were more diverse than at the lower and upper sites. *Navicula, Nitzschia, Luticola, Thalassionema, Phormidium, Planktothrix, Plectonema,* and *Lyngbya* were the most common genera. While most of the genera of cyanobacteria were observed to be of the filamentous form, the diatoms were of the genera with order centrales and pennales.

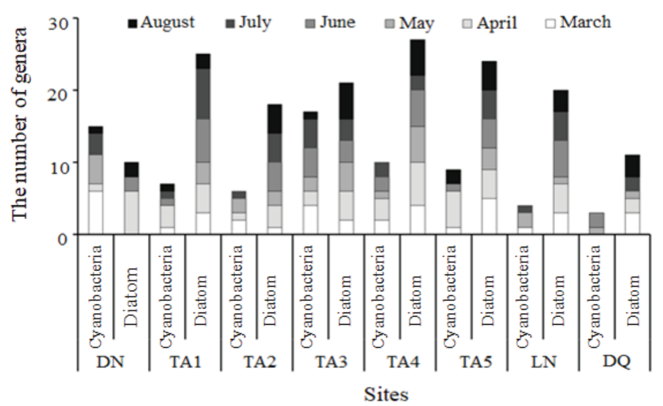

Fig. 3. The number of genera at each survey site.

The abundance ranged from 1000-9600 (cells/cm^2) and from 800-15600 (cells/cm^2) in dry and rainy season, respectively (Fig. 4). Generally, the cell density was higher in the rainy season than in the dry season and the cell density at the reservoir sites were higher than those in the downstream and upstream sites during both seasons. The abundance in August was significantly higher than the other months (10000-15000 cells/cm^2) owing to the dramatically increasing cell density of several diatoms, namely *Luticola, Navicula,* and *Nitzschia.*

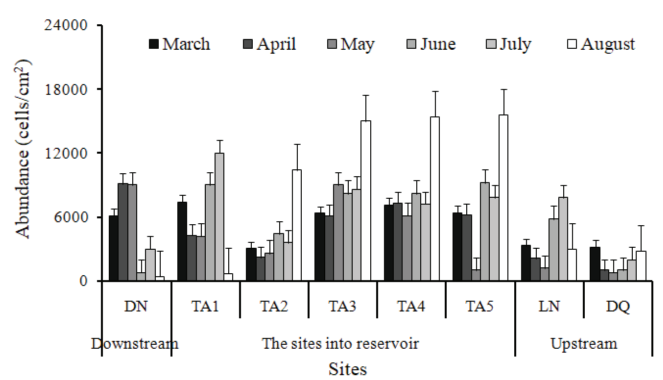

Fig. 4. The abundance of benthic algal communities in Tri An reservoir.

For the cyanobacterial communities in the TAR, the species of *Phormidium* spp. and *Plectonema* spp. were the two most abundant at 18 and 17%, respectively (Fig. 5). In addition, the other species belonging to the *Planktolyngbya*, *Planktothrix*, *Lyngbya*, and *Oscillatoria* genera also commonly found while the species of *Anabaena, Pseudanabaena,* and *Spirulina* were not common. As for the diatom, the species of *Navicula* spp. and *Nitzschia* spp. were dominant and accounted for the largest percentage of the total density, 20 and 13%, respectively, while the other species belonging to the genera of *Synedra*, *Gyrosigma*, *Achnanthidium*, and *Amphora* were rarely recorded (Fig. 5).

Because this study was based on the distribution of benthic microalgae assemblages in the surface sediments of the TAR, the distribution of these dominant species could reflect nutrient levels in the environment. Particularly, diatoms are used as main food sources for many consumers in the food chain because they are rich in protein and fatty acids [26]. At some sites with high nutrient concentrations such as TA1-TA5, some genera such as *Navicula*, *Nitzschia*, *Thalassionema*, *Phormidium*, and *Lyngbya* had a significantly higher percentage of total density (over 70%) while the other stations with low nutrient concentrations, such as the upstream and downstream (DN, DQ, and LN), many species of *Plectonema*, *Achnanthidium*, and *Gomphone* existed. Our results are consistent with previous observations that the species belonging to the *Gomphoneis* and *Achnanthidium* genera are related to low TP content in the sediment whereas the species belonging to the *Luticola* and *Navicula* genera indicate a high TP and nitrogen content [27, 28].

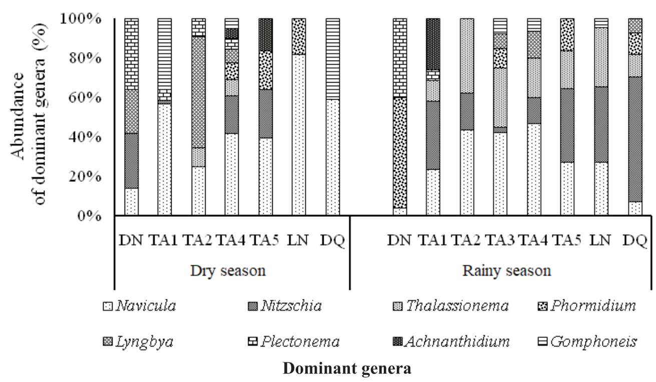

Fig. 5. The distribution of the dominant genera.

Benthic algal assemblage species diversity metrics

Diversity is a composite parameter that integrates the number of species and the distribution of biomass among these species [29]. The temporal and spatial variations of benthic algal metrics are shown in Fig. 6. From this figure, Margalef's diversity (d) ranged from 0.14-0.92 and 0.13-0.75 in the dry and rainy season, respectively (see Fig. 6A). The evenness (J') was also high as all of values surpassed 0.7 with a minimum value of 0.72 (Fig. 6B). The Shannon-Weiner diversity index (H') ranged from 0.88-3.04 and from 0.88-2.79 in the dry and rainy season, respectively (Fig. 6C). Overall, the H' index was relatively low, which indicated a low biodiversity of benthic algae communities and ongoing pollution in the environment while the classification systems of SFT (1997) [30] revealed that the quality of water was indeed polluted. Simpson's diversity index (D') ranged from 0.38-0.87 and from 0.42-0.84 in dry and rainy season, respectively (Fig. 6D). The high value of the dominance index (D) reflected the dominance of the two diatom *Luticola* sp. and *Navicula* sp. at all reservoir sites.

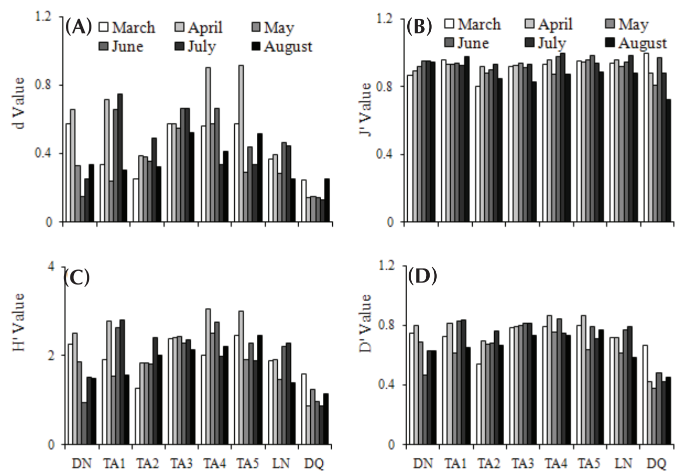

Fig. 6. Benthic algal metrics (d, J′, H′, and D′) in Tri An reservoir.

Relationship between benthic algae distribution and nutrients in sedimentary environment

The correlation between the benthic algae distribution and the nutrient-related variables in sediment are depicted in Fig. 7. The results of Spearman's correlation analysis showed that NH_4^+ and TN correlated with benthic algal metrics in which NH_4^+ was associated with the H' index ($p=0.0352$) while TN was related to a few indices such as H', D, and d ($p=0.0241$, $p=0.0187$, and $p=0.0379$, respectively). The results from the linear regression analysis indicated that there was a strong correlation between the TN value and the H', D, and d indices with $R^2=26.8702\%$ and $p=0.0002$, $R^2=25.3578\%$ and $p=0.0003$, and $R^2=31.8274\%$ and $p<0.001$, respectively. There was little correlation found between the H' index and NH_4^+ concentration with $R^2=15.3685\%$ and $p=0.0093$.

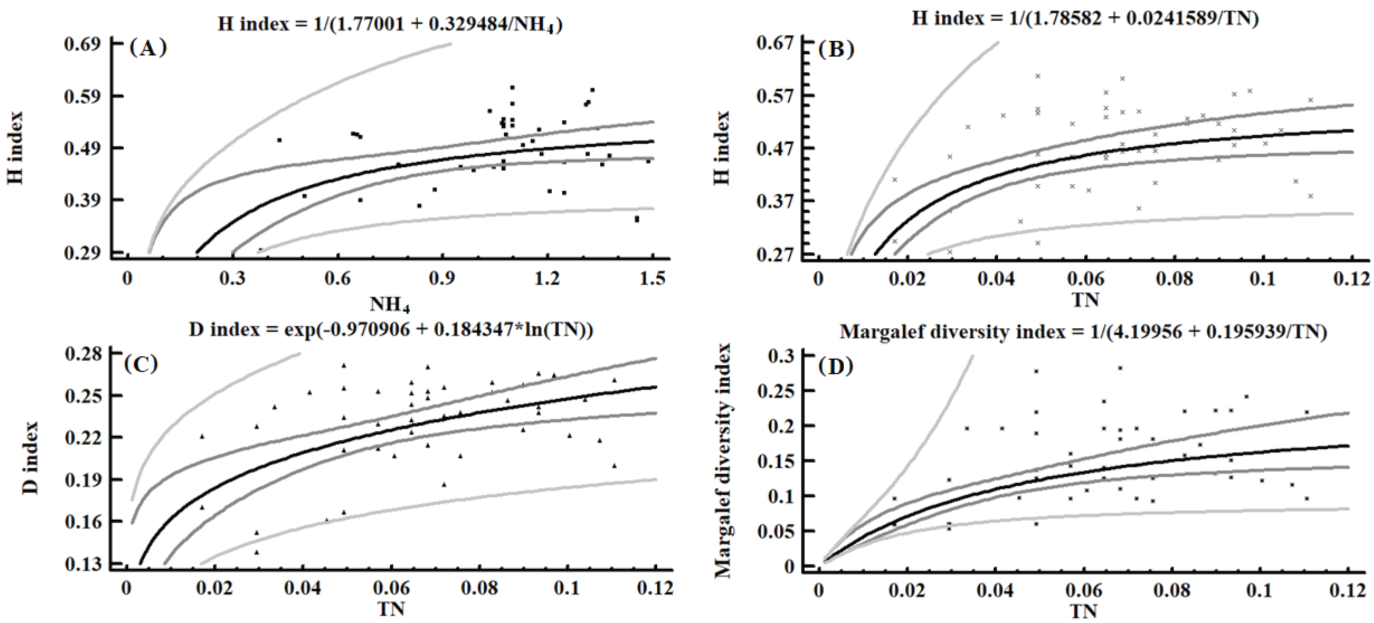

Fig. 7. Model of linear regression analysis: (A) The correlation between NH_4^+ concentration and H′ index; (B), (C), and (D) are the correlations between TN concentration and the H′, D, and d indices, respectively.

Nutrients are a key factor influencing diatom activity and growth rate as well as any variations in nutrients can change the community structure of the diatoms [31]. In this study, NH_4^+ and TN are considered associated with the diversity of benthic algae assemblage. That means, if NH_4^+ and TN values grow by accretion, the diversity indices will increase and vice versa. Previous studies have demonstrated that the benthic microalgae community are strongly influenced by nutrient concentrations [26]. According to Saros, et al. (2011) [32], increases in the two diatom taxa *Asterionella formosa* and *Fragilaria crotonensis* were indicators of N enrichment in an N-limited reservoir and these two species responded positively to moderate N enrichment. The results of Hillebrand, et al. (2000) [29] showed that the nutrient and spring grazing experiment influenced the biomass and species composition of benthic microalgae in which species richness was significantly decreased by grazer presence (ANOVA, $p=0.013$) and increased with nitrogen supply. It is well known that sediments are an important source of nutrients to freshwater ecosystems. For example, nutrient cycling at the sediment-water interface is affected by both dissolved oxygen and by nutrient concentration gradients that result from algal decay [33]. The release of nutrients from the bottom sediment can have a significant impact on water quality and can result in continued eutrophication by excessive input of phosphorus and nitrogen that has become one of the most common damages to surface waters [34]. Thus, our results indicate that the nutrients in sediment may restructure the distribution of several diatom and cyanobacteria in the TAR.

Conclusions

The benthic algae assemblage in the TAR was investigated in this study. The presence of species such as *Navicula, Nitzschia,* and *Phormidium* represented eutrophic environments in reservoir sites whereas *Plectonema* and *Achnanthidium* were indicators of nutrient-poor environments in the upstream and downstream sites. The TN and NH_4^+ concentration were the two main environmental variables that regulated the benthic algae assemblage in the TAR. The present work has provided a first framework on the distribution and diversity of benthic algae in response to the nutrients in this area. Further studies focusing on the impact of benthic algae in response to other components, as well as using them as bioindicators in aquatic ecosystems, should be implemented.

ACKNOWLEDGEMENTS

This research was founded by the Vietnam National Foundation for Science and Technology Development (NAFOSTED) under grant number "106.04-2018.314".

COMPETING INTERESTS

The authors declare that there is no conflict of interest regarding the publication of this article.

REFERENCES

[1] M. Wang, W. Cheng, T. Wan, T. Meng, Z.J. Hao, L.D. Shi (2018), "Effects of water ecological environment on benthic algae in a water source reservoir", *IOP Conference Series: Earth and Environmental Science*, **191(1)**, DOI: 10.1088/1755-1315/191/1/012056.

[2] J. Yang, H. Jiang, W. Liu, B. Wang (2018), "Benthic algal

community structures and their response to geographic distance and environmental variables in the Qinghai-Tibetan lakes with different salinity", *Frontiers in Microbiology*, **9**, DOI: 10.3389/fmicb.2018.00578.

[3] J. Wang, Q. Liu, X. Zhao, A.G. Borthwick, Y. Liu, Q. Chen, J. Ni (2019), "Molecular biogeography of planktonic and benthic diatoms in the Yangtze River", *Microbiome*, **7(153)**, pp.1-15.

[4] S.B. Faustino, L. Fontana, E.C.R. Bartozek, C.E.D.M. Bicudo, D.D.C. Bicudo (2016), "Composition and distribution of diatom assemblages from core and surface sediments of a water supply reservoir in Southeastern Brazil", *Biota Neotropica*, **16(2)**, DOI: 10.1590/1676-0611-BN-2015-0129.

[5] A.I. Negro, C.D. Hoyos (2005), "Relationships between diatoms and the environment in Spanish reservoirs", *Limnetica*, **24(1-2)**, pp.133-144.

[6] S. McGowan, H.V. Gunn, E.J. Whiteford, N.J. Anderson, V.J. Jones, A.C. Law (2018), "Functional attributes of epilithic diatoms for palaeoenvironmental interpretations in South-West Greenland lakes", *Journal of Paleolimnology*, **60(2)**, pp.273-298.

[7] R.V.H. Hansika, S.K. Yatigammana (2019), "Distribution of diatom assemblages in the surface sediments in Sri Lankan reservoirs located in the main climatic regions and potential of using them as environmental predictors", *Tropical Ecology*, **60(3)**, pp.415-425.

[8] B. Sabour, M. Loudiki, V. Vasconcelos (2009), "Growth responses of *Microcystis ichthyoblabe* Kützing and *Anabaena aphanizomenoides* Forti (cyanobacteria) under different nitrogen and phosphorus conditions", *Chemistry and Ecology*, **25(5)**, pp.337-344.

[9] M.H. Novais, S. Blanco, C. Delgado, M. Morais, L. Hoffmann, L. Ector (2012), "Ecological assessment of Portuguese reservoirs based on littoral epilithic diatoms", *Hydrobiologia*, **695(1)**, pp.265-279.

[10] D. Fidlerová, D. Hlúbiková (2016), "Relationships between benthic diatom assemblages structure and selected environmental parameters in Slovak water reservoirs (Slovakia, Europe)", *Knowledge and Management of Aquatic Ecosystems*, **417**, DOI: 10.1051/kmae/2016014.

[11] Y. Pan, et al. (2016), "Variation of benthic algal assemblages among habitats in subalpine Karstic lakes and implications for bioassessment", *Hydrobiologia*, **777(1)**, pp.183-196.

[12] H.Q. Nguyen, N.T. Ha, T.L. Pham (2020), "Inland harmful cyanobacterial bloom prediction in the eutrophic Tri An reservoir using satellite band ratio and machine learning approaches", *Environmental Science and Pollution Research*, **27**, pp.9135-9151.

[13] T.S. Dao, J. Nimptsch, C. Wiegand (2016), "Dynamics of cyanobacteria and cyanobacterial toxins and their correlation with environmental parameters in Tri An reservoir, Vietnam", *Journal of Water and Health*, **14(4)**, pp.699-712.

[14] V.H. Nguyen, V.T. Dinh, D.R. Nguyen, D.L. Le (2013), "Study on the impact of the Tri An reservoir on its downstream groundwater level regime", *Journal of Sciences of the Earth*, **34(4)**, pp.465-476.

[15] T-L. Pham, T.H.Y. Tran, N.S. Hoang, X.Q. Ngo, T.T. Tran (2020), "Co-occurrence of microcystin-and geosmin-producing cyanobacteria in the Tri An reservoir, a drinking water supply in Vietnam", *Fundamental and Applied Limnology*, **193(4)**, DOI: 10.1127/fal/2020/1296.

[16] A.D. Eaton, L.S. Clesceri, E.W. Rice, A.E. Greenberg, M.A.H. Franson (2005), *Standard Methods for the Examination of Water and Wastewater (21st edition)*, American Public Health Association, 1325pp.

[17] J.D. Wehr, G.S. Robert, J.K. Patrick (2003), *Freshwater Algae of North America: Ecology and classification*, Elsevier, 935pp.

[18] U. Rumrich, H. Lange-Bertalot, M. Rumrich (2000), *Diatoms of the Andes: From Venezuela to Patagonia/Tierra del Fuego*, Gustav Fischer, 671pp.

[19] D. Metzeltin, H. Lange-Bertalot (2002), *Diatoms from the "Island Continent" Madagascar*, A.R.G. Gantner Verlag K.G. Koenigstein, 286pp.

[20] D. Metzeltin, H. Lange-Bertalot (2007), *Tropical Diatoms of the South America II*, A.R.G. Gantner Verlag K.G. Koenigstein, 877pp.

[21] J.C. Taylor, J. Prygiel, A. Vosloo, A. Pieter, L. van Rensburg (2007), "Can diatom-based pollution indices be used for biomonitoring in South Africa? a case study of the crocodile west and Marico water management area", *Hydrobiologia*, **592(1)**, pp.455-464.

[22] A. Agrawal, K. Gopal (2013), "Biomonitoring of water and wastewater", *Springer Science Business Media*, DOI: 10.1007/978-81-322-0864-8.

[23] R.G. Wetzel (2001), *Limnology: Lake and River Ecosystems*, Gulf Professional Publishing, 1006pp.

[24] L. Nordvarg, T. Johansson (2002), "The effects of fish farm effluents on the water quality in the Åland archipelago, Baltic Sea", *Aquacultural Engineering*, **25(4)**, pp.253-279.

[25] L. Mwebaza-Ndawula, V. Kiggundu, G. Magezi, J. Naluwayiro, W. Gandhi-Pabire, H. Ocaya (2013), "Effects of cage fish culture on water quality and selected biological communities in northern Lake Victoria, Uganda", *Uganda Journal of Agricultural Sciences*, **14(2)**, pp.61-75.

[26] L.D.N. Silvano Filho, E.J. de França, M.M. de Júnior, A.D.N. Moura (2019), "Interactions between benthic microalgae, nutrients and benthic macroinvertebrates in reservoirs from the semi-arid Neotropical region", *Fundamental and Applied Limnology/Archiv für Hydrobiologie*, **192(3)**, pp.237-254.

[27] M.G. Potapova, D.F. Charles, K.C. Ponader, D.M. Winter (2004), "Quantifying species indicator values for trophic diatom indices: a comparison of approaches", *Hydrobiologia*, **517(1-3)**, pp.25-41.

[28] S.A. Wood, R.G. Young (2012), *Benthic Cyanobacteria and Toxin Production in the Manawatu-Wanganui Region*, Prepared for Horizons Regional Council, Cawthron Report No.1959, 36pp.

[29] H. Hillebrand, B. Worm, H.K. Lotze (2000), "Marine microbenthic community structure regulated by nitrogen loading and grazing pressure", *Marine Ecology Progress Series*, **204**, pp.27-38.

[30] SFT (1997), "Classification of environmental quality in fiords and coastal waters (in Norwegian)", SFT report **97(03)**, *Norwegian Pollution Control Authority, Oslo*.

[31] R. Shen, H. Ren, P. Yu, Q. You, W. Pang, Q. Wang (2018), "Benthic diatoms of the Ying river (Huaihe river basin, China) and their application in water trophic status assessment", *Water*, **10(8)**, DOI: 10.3390/w10081013.

[32] J.E. Saros, D.W. Clow, T. Blett, A.P. Wolfe (2011), "Critical nitrogen deposition loads in high-elevation lakes of the western US inferred from paleolimnological records", *Water, Air & Soil Pollution*, **216(1-4)**, pp.193-202.

[33] M. Zhu, G. Zhu, L. Zhao, X. Yao, Y. Zhang, G. Gao, B. Qin (2013), "Influence of algal bloom degradation on nutrient release at the sediment-water interface in lake Taihu, China", *Environmental Science and Pollution Research*, **20(3)**, pp.1803-1811.

[34] W.H. Nowlin, J.L. Evarts, M.J. Vanni (2005), "Release rates and potential fates of nitrogen and phosphorus from sediments in a eutrophic reservoir", *Freshwater Biology*, **50(2)**, pp.301-322.

Using a numerical model with moving boundary conditions to study the bed change of a Mekong river segment in Tan Chau, An Giang, Vietnam

Kim Tran Thi[1, 2], Huy Nguyen Dam Quoc[1], Phung Nguyen Ky[3], Bay Nguyen Thi[4, 5*]

[1]*Ho Chi Minh city University of Natural Resources and Environment*
[2]*Institute for Environment and Resources, Vietnam National University, Ho Chi Minh city*
[3]*Institute for Computational Science and Technology*
[4]*Ho Chi Minh city University of Technology*
[5]*Vietnam National University, Ho Chi Minh city*

Received 11 August 2020; accepted 5 November 2020

Abstract:

Numerical models that calculate bed change are becoming increasingly popular because of their long-term forecast projections and their ability to identify causes of bed change. However, the reliability of the simulation results depends on the length of the data series and the algorithms in the model, in which the boundary condition method plays a critical role. The aim of this study is to assess the effectiveness of the HYDIST model to update wet and dry fronts as well as recalculate the wet boundaries of the hydraulic model before its input into the sediment transport model. The moving boundary theories (wet and dry fronts) of Zhao (1994) and Sleigh (1998) were applied. The velocity distribution of the wet boundaries was recalculated after every time step, then the outcomes of the hydraulic model were used as input for the sediment transport model. The results showed good agreement between the simulated and measured data in term of discharge, water level, and sediment concentration. At the same time, the HYDIST model can be successfully used to simulate sediment deposition and riverbank movement.

Keywords: **bed change, boundary condition, Mekong, numerical model, sediment transport.**

Classification number: **5.1**

Introduction

Sediment transport affects river environments in many ways via erosion and sediment deposition. The development and degradation of a riverbed significantly influence flow changes and the economic development of the region. Besides, a change in the river profile can threaten channel stability and affect irrigation facilities on both sides of the river. Therefore, the accurate simulation of bed change in a river is of great significance to regional planning and other long-term projects.

Today, with computer engineering and information technology development, researchers have built numerical models that can simulate changes in riverbeds. With the advantage of simulating many scenarios over different periods, identifying the cause of an impact and forecasting the future is possible. However, accurate calculations and long-term forecasts take a significant amount of time to calculate.

Sediments are solid mineral particles that are transported and deposited in the water flow resulting in their accumulation in riverbeds and floodplains. Sediments are usually formed as heterogeneous particles of various sizes with a larger specific gravity than water [1-3]. Based on the laws of motion, sediments are classified into suspended and bottom sediments [1-4]. The evolution of the loading or deposition of bed sediments changes the topography of the river bed and affects changes in river flows [5-7].

To simulate the change of the riverbed, scientists have used many methods such as observations, physical models,

*Corresponding author: Email: ntbay@hcmut.edu.vn

and numerical models. For simple curved channels, both physical models on the laboratory scale and large scale surveys have been used to study sediment transport [8-10]. However, numerical models pose major advantages in simulation and prediction [11-15].

For irregular topography, both positive and negative bed slopes generally exist and lead to cell drying and wetting with moving fronts, which cannot be easily solved by a simple horizontal boundary condition. Therefore, some techniques have been developed for these shallow water equations. Zhao, et al. (1994) [16] and Sleigh, et al. (1998) [17] introduced two similar schemes to track the wetting and drying fronts, in which cells are divided into wet, dry, and partially dry types according to two tolerances [16, 17]. Technology for tracking the wet-dry front has been developed, in combination with the method of Brufau, et al. (2004) [18], to achieve zero mass error by Liu, et al. (2014) [19].

Based on the above analysis, in this paper, we propose improving the HYDIST model initially developed by Bay, et al. (2012, 2019) [20, 21]. This study will focus on developing the boundary conditions in the hydraulic model and sediment transport model of the HYDIST model.

1. First, the moving boundaries problem (wetting and drying fronts), which is based on the work by Zhao, et al. (1994) [16] and Sleigh, et al. (1998) [17], is applied.

2. Secondly, the flow sequence, Q(t), and the velocity distribution on the liquid boundary, u,v(x, y, t), is recalculated according to the formula assuming the roughness coefficient n is constant at the boundary inlet [22], which are each applied to achieve zero error at the positions of the boundaries.

The developed model will be calculated for a segment of the Tien river located in Tan Chau town, and compared with observational data to assess the reliability of the model.

Materials and methods

Study area

Tien river is one of the two major tributaries of the Mekong delta (along with the Hau river) flowing into Vietnam (Fig. 1). After branching in Phnom Penh (Cambodia), the Tien river flows into Vietnam beginning in Tan Chau town, An Giang province. Then, the main flow goes through the provinces of An Giang, Dong Thap, Vinh Long, and Ben Tre [23].

A segment flowing through An Giang has the style of a braided river; the riverbed is wide with coastal sandbars and sand bars in the heart. This part has a complex terrain, is stream folded, and has intense erosion. In recent years, failure banks have increasingly affected the socio-economic development and planning in the local area and construction along the river in the An Giang province [24-27].

The topography was collected at the Department of Investment and Construction Project of the Tan Chau area on October 6, 1999. The features (water level $\varsigma(t)$, discharge Q(t), and total suspended sediment C(t)) at the Tan Chau station were collected from 1999 to 2006 from the Project: "Research to identify causes, mechanisms and propose feasible technical and economical solutions to reduce erosion, sedimentation for the Mekong river system (2017-2020)", code No. KHCN-TNB.DT/14-19/C10 in 2019.

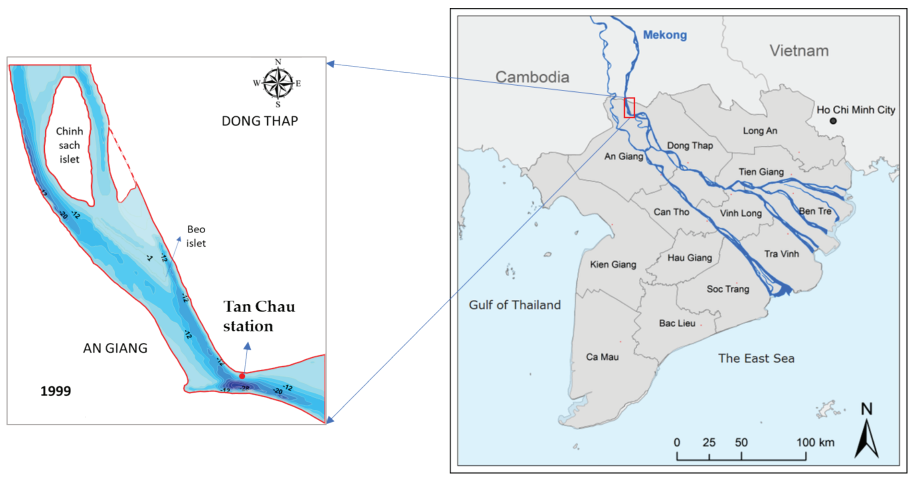

Fig. 1. Study area.

HYDIST model

The adopted model is a 2D surface model where Ox and Oy represent the length and width of the study area as seen in Fig. 2. The model is based on a system of four governing equations: the Reynolds equation in Ox and Oy directions, the continuity equation, the suspended sediment transport equation, and the bedload continuity equation as follows [21, 28].

Reynolds equation in Ox and Oy directions:

$$\frac{\partial u}{\partial t}+u\frac{\partial u}{\partial x}+v\frac{\partial u}{\partial y}=-g\frac{\partial \varsigma}{\partial x}-Ku\frac{\sqrt{u^2+v^2}}{h+\varsigma}+A\nabla^2 u \quad (1)$$

$$\frac{\partial v}{\partial t}+u\frac{\partial v}{\partial x}+v\frac{\partial v}{\partial y}=-g\frac{\partial \varsigma}{\partial y}-Kv\frac{\sqrt{u^2+v^2}}{h+\varsigma}+A\nabla^2 v \quad (2)$$

Continuity equation:

$$\frac{\partial \varsigma}{\partial t}+\frac{\partial}{\partial x}[(h+\varsigma)u]+\frac{\partial}{\partial y}[(h+\varsigma)v]=0 \quad (3)$$

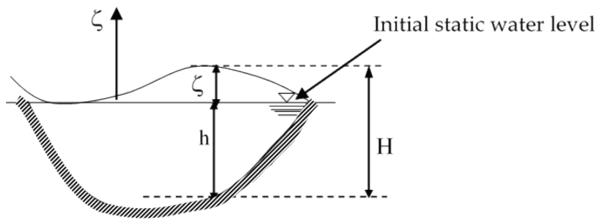

Fig. 2. The illustration of the initial static level.

Suspended sediment transport equation:

$$\frac{\partial C}{\partial t}+\gamma_v\left(u\frac{\partial C}{\partial x}+v\frac{\partial C}{\partial y}\right)=\frac{1}{H}\frac{\partial}{\partial x}\left(HK_x\frac{\partial C}{\partial x}\right)+\frac{1}{H}\frac{\partial}{\partial y}\left(HK_y\frac{\partial C}{\partial y}\right)+\frac{S}{H} \quad (4)$$

Bed load continuity equation:

$$\frac{\partial h}{\partial t}=\frac{1}{1-\varepsilon_p}\left[E+\frac{\partial}{\partial x}\left(HK_x\frac{\partial C}{\partial x}\right)+\frac{\partial}{\partial y}\left(HK_y\frac{\partial C}{\partial y}\right)+\frac{\partial q_{bx}}{\partial x}+\frac{\partial q_{by}}{\partial y}\right] \quad (5)$$

with $q_i=(b_y, b_{ee})$

$$q_b=0.053\left(\left(\frac{\rho_s}{\rho}-1\right)g\right)^{0.5}d_m^{1.5}T^{2.1}D_*^{-0.3}\frac{(u,v)}{\sqrt{u^2+v^2}} \quad (6)$$

Numerical approach

These equations are solved by the Alternating Direction Implicit (ADI) method. The fundamental concept of ADI is to split the finite difference equations into two, one with the x-derivative and the next with the y-derivative, both taken implicitly [29]. The computational grid for the governing system of equations is shown in Fig. 3.

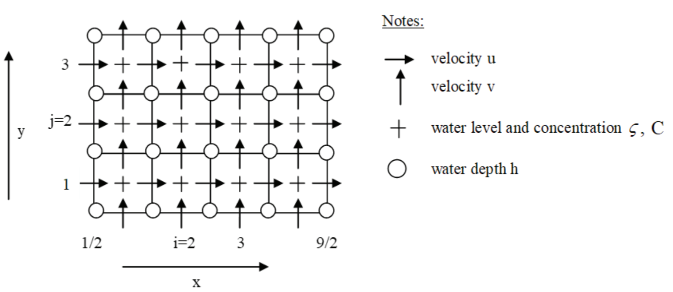

Fig. 3. Computational grid for the governing system of equations.

From the figure, the u, v, and ς components are specially arranged. In more detail, ς and C are placed at the centre of the grid cell (i, j), while u is placed in the position (i+1/2, j) and v is in the position (i, j+1/2) (with i, j = 1, 2, 3…). The width and height of a grid cell is Δx and Δy, respectively. The grid is numbered by the index i (for x directions) from 1 to N and the index j (for y) from 1 to M [21]. The model is calculated by three coupled equations: the Reynolds, continuity, and suspended sediment transport equations. At the first-half step, ς, u, and C are implicitly solved in the x-direction and v is the opposite. For the following half step, ς, v and C are implicitly solved in the y-direction and u is the opposite. The bedload continuity equation is solved alternately after a time step.

In this paper, the hydraulic and sediment transport boundaries are developed as follows.

Regarding the hydraulic model: the upstream boundary is the time-dependent sequence of flow data, Q(t), over the region, while the downstream boundary of the flow will be in the form of the fluctuating water level, ς(t). From the flow sequence Q(t), the program will recalculate the velocity distribution u,v(x, y, t) on the liquid boundary according to the formula assuming the roughness coefficient n is constant at the boundary inlet. Then, the boundary is calculated as follows [22]:

$$u,v=\left[\frac{\dfrac{Q}{\Sigma\left(h_i^{\frac{5}{3}}\right)}h_i^{\frac{5}{3}}}{h_i\Delta x}\right] \quad (7)$$

where

Q=Q(t): the sequence of flow data (m^3/s);

h_i: bottom depth at calculation node (m);

Δx: the distance between two nodes (m).

Furthermore, because the fluctuations of water levels vary from time to time, the moving boundaries problem (flooding and drying fronts), which is based on the work by Zhao, et al. (1994) [16] and Sleigh, et al. (1998) [17], is applied in this model. The study area is classified into grid cells. The depth of each element/cell is monitored and the elements are classified as dry, partially dry, or wet. In more detail, an element is defined as flooded if the water depth of at least three corners of a grid cell is greater than 0.1. An element is dry if the water depth of at least 3 corners of a grid cell is less than 0.1, then, the element is removed from the calculation. An element is partially dry if the water depth at two corners of a grid cell is less than 0.1. These two parameters will regulate when a given cell should be exposed for a flooding or drying check during the simulation.

Figure 4 presents the general framework of the calculation for our coupled model based on the coupling of all the governing equations previously described. Hydrodynamic and sediment transport models were tested with an analytic solution [20].

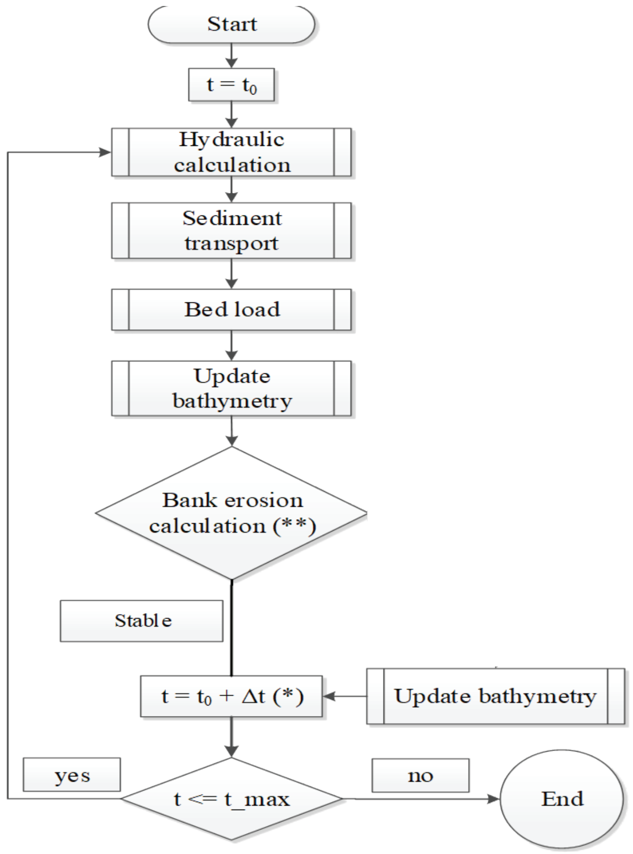

Fig. 4. General computational procedure used in the coupled.

$Q(t)$, alluvial, $C(t)$, and water level, $\varsigma(t)$, of the flood seasons from 1999 to 2006 at the Tan Chau station.

Initial conditions: from $t_0=0$ in the model, the hydraulic module is tied to a static state and the sediment transport module is set to an initial constant basal concentration. If the problem is calculated from a time $t=t_1$, the initial condition is the velocity fields u,v(x, y) and concentration C(x, y) at time t_1 across the computational domain.

Boundary conditions:

(1) Open boundaries: the $Q(t)$, $C(t)$, and $\varsigma(t)$ of the flood seasons from 1999 to 2006 at Tan Chau station (as Fig. 5). The study area has two boundaries whose features are identified based on the correlation functions $f(\varsigma)$, $f(Q)$, and $f(C)$ from the Tan Chau station. Measurement data at the boundaries of the project come from "Research to identify causes, mechanisms and propose feasible technical and economical solutions to reduce erosion, sedimentation for the Mekong river system (2017-2020)", code No. KHCN-TNB.DT/14-19/C10 from 10 am 06/06/2018 to 10 am 13/06/2018. Typical boundary data for 1999 and 2001 are shown in Fig. 5.

(2) Solid wall boundary: hydrodynamics conditions $u_n=0$ and sediment transport conditions $\frac{\partial C}{\partial n_p} = 0$.

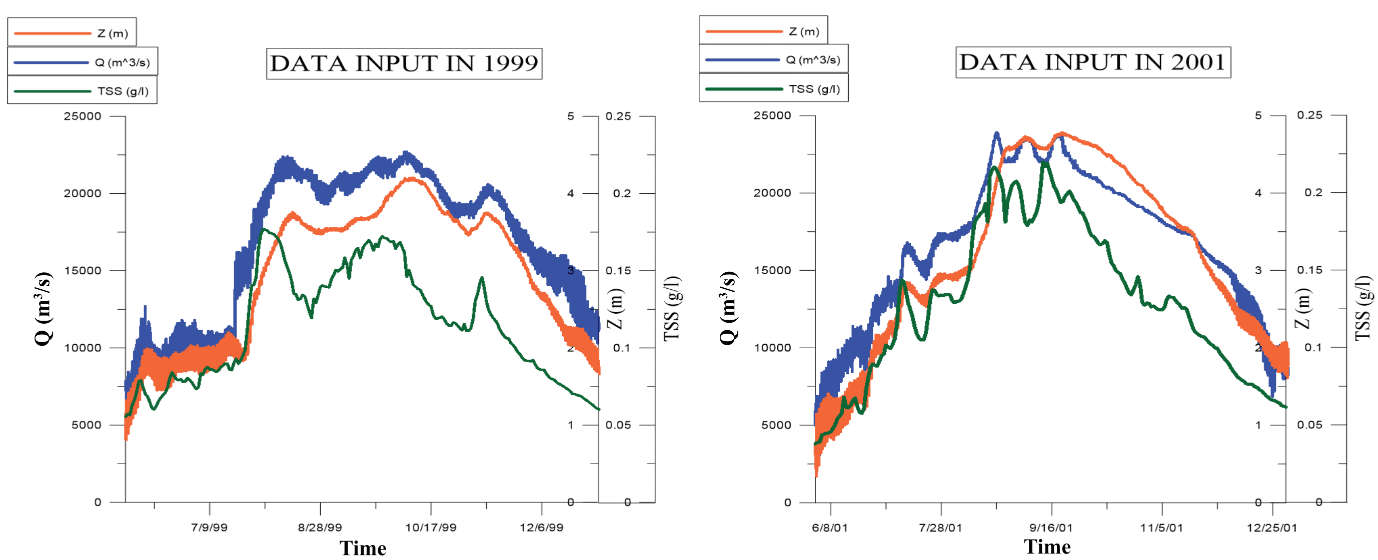

Fig. 5. Input data in 1999 and 2001.

Setup of the model for the study area

Bathymetry: the entire study area is represented by a rectangular mesh of size 981x845 pixels, including the land and riverbed, where $\Delta x=\Delta y=10$ m and the time step $\Delta t=2$ s. At the curve, the size is 492x424 pixels including the land and riverbed. The boundary condition includes the flow,

Model calibration and validation criteria

In order to calibrate and validate the model with a comparison, the Nash-Sutcliffe efficiency coefficient (NSE) and the coefficient of determination (R^2) are used to measure model performance [30-32].

The Nash-Sutcliffe efficiency coefficient (NSE): the NSE ranges between $-\infty$ and 1. A value of NSE=1 indicates a perfect match between observed and predicted results. The general performance ratings for model evaluation are shown in Table 1. NSE is computed as shown in Eq. (8):

$$\mathrm{NSE} = 1 - \left[\frac{\sum_{i=1}^{n}(O_i - P_i)^2}{\sum_{i=1}^{n}(O_i - \bar{O})^2}\right] \quad (8)$$

where

O_j: the ith observation for the constituent being evaluated;

P_i: the ith simulated value for the constituent being evaluated;

$\bar{O}$: the mean of observed data for the constituent being evaluated;

N: is the total number of observations.

Table 1. General performance ratings for model evaluation.

			Range	Optimal value	Performance Rating			
					Very good	*Good*	*Satisfactory*	*Unsatisfactory*
NSE	Flow	Annual	$-\infty$ to 1.0	1.0	>0.75	0.60≤NSE≤0.75	0.50≤NSE≤0.60	≤0.50
		Monthly			>0.85	0.70≤NSE≤0.85	0.55≤NSE≤0.70	≤0.55
		Daily			>0.80	0.70≤NSE≤0.80	0.50≤NSE≤0.70	≤0.50
	Sediment				>0.80	0.70≤NSE≤0.80	0.45≤NSE≤0.70	≤0.45
	General				>0.80	0.60≤NSE≤0.80	0.50≤NSE≤0.60	≤0.50
R2	Flow	Annual	0.0 to 1.0	1.0	>0.75	0.70≤ R^2≤0.75	0.60≤ R^2≤0.70	≤0.60
		Monthly			>0.85	0.80≤ R^2≤0.85	0.70≤ R^2≤0.80	≤0.70
		Daily			>0.85	0.70≤ R^2≤0.85	0.50≤ R^2≤0.70	≤0.50
	Sediment				>0.80	0.65≤ R^2≤0.80	0.40≤ R^2≤0.65	≤0.40
	General				>0.80	0.70≤ R^2≤0.80	0.50≤ R^2≤0.70	≤0.50

The coefficient of determination (R^2)

The coefficient of determination, R^2, ranges between 0 and 1. It describes the portion of the variance in the measured data where higher values indicate less error variance. The general performance ratings for model evaluation using the coefficient of determination is shown in Table 1. R^2 is computed as shown in Eq. (9):

$$R^2 = \left[\frac{\sum_{i=1}^{n}(O_i - \bar{O})(P_i - \bar{P})}{\sqrt{\sum_{i=1}^{n}(O_i - \bar{O})^2}\sqrt{\sum_{i=1}^{n}(P_i - \bar{P})^2}}\right]^2 \quad (9)$$

Results and discussion

The results for the hydraulic model

The verification parameter in the model is the roughness coefficient, which changes inversely with water depth. The results of the calibration show that there was little difference between the simulation results and measurements of the discharge and water level at Tan Chau station for two periods from 5/7/1999 to 30/12/1999 (Fig. 6). The graphical results during calibration indicated an adequate calibration and validation over the range of discharges and water levels. However, the calibration results of water level showed a better match than that of discharge. The NSE values for the discharge and water level calibration reached 0.71 and 0.81, respectively, while the R^2 values were 0.82 and 0.88, respectively. According to Moriasi, et al.'s research (2015) [32], these values indicate that the hydraulic model performance peaked very well. It is believed that if a hydrodynamic model is well calibrated, then the predicted results are close to the actual water movements.

The roughness coefficient was recorded after calibration with a range of 0.055 from 0.005 to 0.06 corresponding to water depths from 41 to 0.1 m. During the experimental process, the n_2 (0.003) corresponding to h^2 (25 m) was found to make the roughness coefficient in the study area more suitable for simulation. If $h_{min}<h_{i,j}<h^2$, Eq. (10) is used to calculate the roughness value at a position i,j, while Eq. (11)

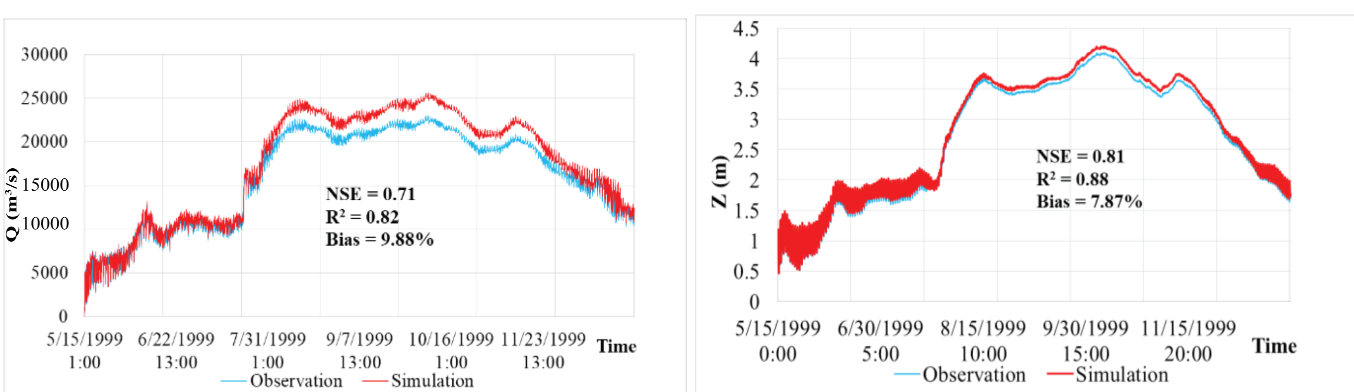

Fig. 6. Calibration results at Tan Chau station from 5/7/1999 to 30/12/1999 for water level (Z) and discharge (Q).

is used when $h_2<h_{i,j}<h_{max}$. These equations are computed as follows:

$$n_{i,j} = \frac{(n_2 - n_{min})(h_{i,j} - h_{min})}{h_2 - h_{min}} + n_{min} \quad (10)$$

$$n_{i,j} = \frac{(n_{max} - n_2)(h_{i,j} - h_2)}{h_{max} - h_2} + n_2 \quad (11)$$

Below is a rough map for the first 500 h starting on 5/15/1999 in Fig. 7. Consequently, the roughness coefficient in the domain is computed according to Eqs. (10) and (11).

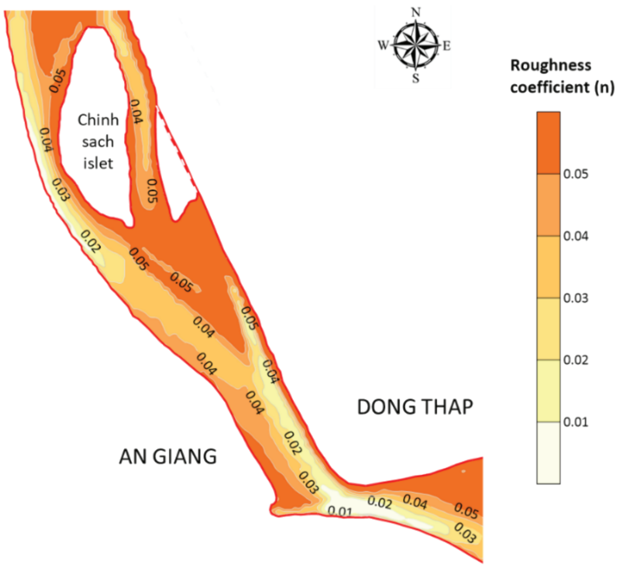

Fig. 7. Roughness coefficient for the study area.

After calibration, the model was validated from 29/06/2001 to 30/12/2001 (flood season). Although the calibration result of the water level showed a better match than discharge (Fig. 8), the evaluation criteria values were satisfactory in terms of both features. The NSE values were 0.71 and 0.81 for discharge and water level, respectively, and the R^2 values were 0.81 and 0.82, respectively. The bias of both the calibration and validation were smaller than 10%.

Calibration and validation results for sediment transport model

Like the hydraulic model, the sediment transport simulation was calibrated and validated for two periods from 5/7/1999 to 30/12/1999 and 29/06/2001 to 30/12/2001. According to the evaluation criteria values, the sediment transport model worked very well in terms of sediment concentration. For calibration and validation, the NSE values were 0.82 and 0.80, respectively, and the R^2 value was 0.91 for both processes. The bias of both calibration and verification was smaller than 10%. Graphical results during calibration and validation at Tan Chau station are shown in Fig. 9.

After calibration and validation, numerous studies have applied bed parameters such as dispersion, critical shear stress for deposition, and acute shear stress for the erosion of bed layers to simulate the processes of sediment transportation, erosion, and deposition [33]. In this study, these parameters were used for calibrating the sediment

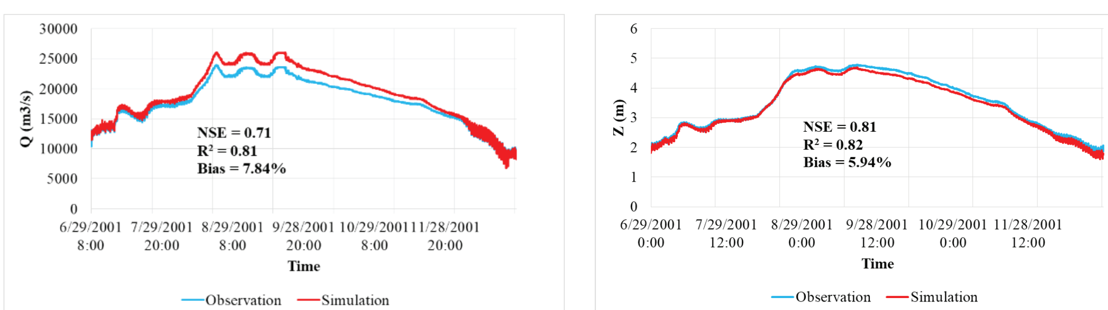

Fig. 8. Observed and simulated data at Tan Chau station from 29/06/2001 to 30/12/2001 for water level (Z) and discharge (Q).

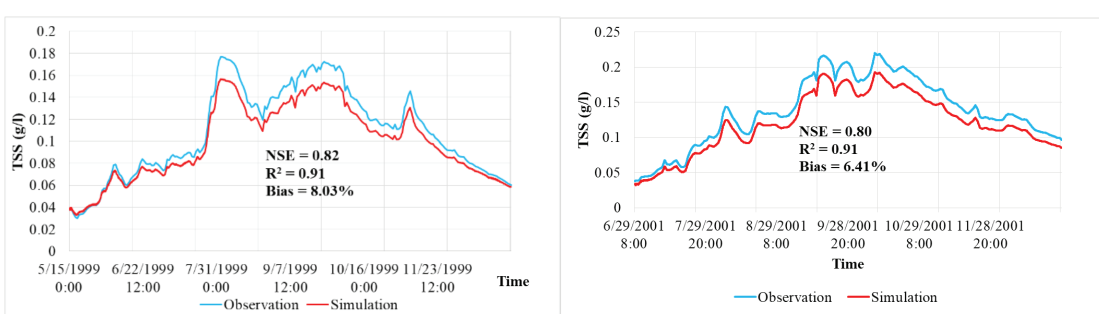

Fig. 9. Observed and simulated TSS data at Tan Chau station for calibration and validation.

simulation and the most relevant parameters in the model are summarized in Table 2.

Table 2. Model parameters.

Parameter	Value
Time step (Δt)	2 s
Mean diameter of particle (D)	0.01 mm
Diameter of particle 90% of the mass of particles present (D_{90})	0.04 mm
Density of particles (ρ_s)	2600 kg/m^3
Kinematic viscosity coefficient (ν)	1.01x10^{-6} m^2/s
Critical shear stress for deposition (τ_d)	0.35 N/m^2
Critical shear stress for erosion (τ_e)	0.04 N/m^2

Simulating bed change of a Tien river segment in Mekong delta from 1999 to 2006

Because the dry season results did not significantly change, we decided to calculate the change in the current study area for the flood seasons from 1999 to 2006. The calculation results of bed changes after each year are extracted and represented by the images shown in Figs. 10 and 11. When applying the moving boundary, the development of mudflats and the loss and formation of islets are calculated.

For example, the Beo islet was an underground islet, with a mesh in the model bathymetry, that eroded from 1999 to 2005 and disappeared in 2006. The model investigated the conditions of the dry/wet cell as described in the methodology. For cells with a depth less than 0.1 m, the model closed the cells and considered them as a dry cell. Then, the simulation results showed the accretion areas over the years. According to the results, the tail of Chinh Sach Islet was deposited over the years including the accretion area. The information is described in more detail in Table 3.

On Dong Thap side, a mudflat area at the downstream site developed from the end of 1999 to 2006. Specifically, the area of the mudflat in 1999 was about 76 hectares and by 2006 the area of the mudflat increased to just over 226 hectares, which is an increase of about 150 hectares compared to 2005, as detailed in Table 3.

Table 3. Increasing mudflat area of simulation.

	2000	2001	2002	2003	2004	2005	2006
A mudflat of Chinh Sach islet tail (m^2)	0.10	0.67	0.16	0.24	0.30	0.14	0.46
A mudflat on Dong Thap province side	1.46	1.01	0.80	0.89	0.76	0.26	0.27

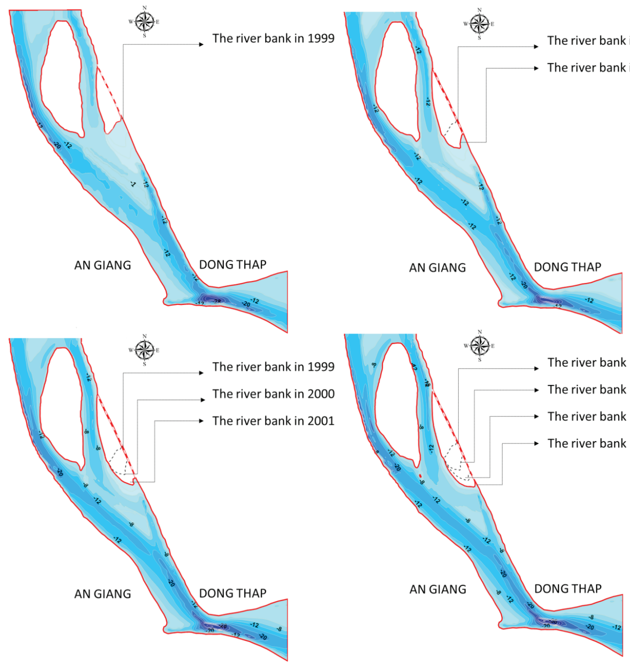

Fig. 10. The bed changes from 1999 to 2002.

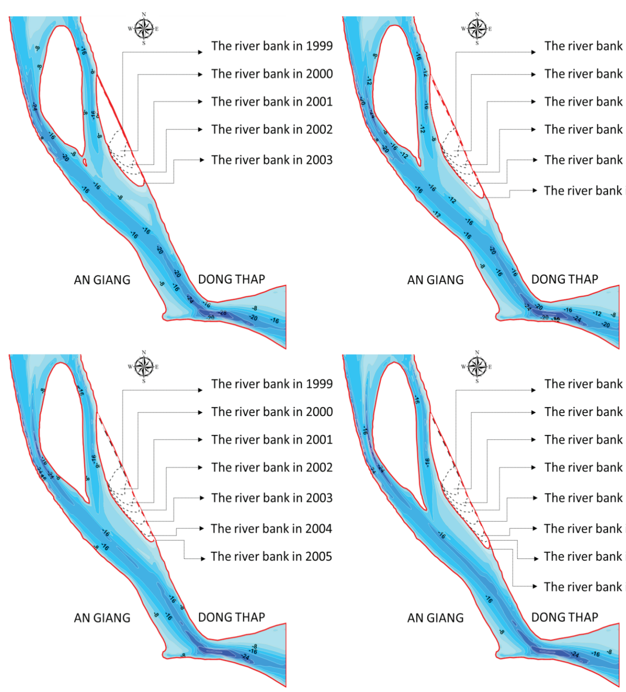

Fig. 11. The bed changes from 2003 to 2006.

The calculation results from the mud flats and Beo islet changes were relatively consistent with the results extracted from Google Earth (GE). The mudflat on the Dong Thap site has grown gradually downstream and the Beo islet has also disappeared in 2006. The tail of the Chinh Sach islet showed gradual expansion downstream (Fig. 12).

Fig. 12. The riverbank from 1999 to 2006 (Source: Google earth).

In the model's study area, the water depth at several cross sections were extracted to record the values each year from 1999 to 2006 at 3 locations denoted cross sections 1, 2, and 3 as described in Fig. 13.

At cross section 1 (Fig. 13) of the model along the bottom left range of the river (on the Dong Thap province side), the bed changes are consistent with the actual bed movements from 1999 to 2006. Specifically, in 1999, the water depth reached an elevation of nearly -18.2 m and gradually accrued to -4.8 m in 2006. The measurement results of the elevation at this area in 2006 was actually -2.1 m. Meanwhile, on the right side of the river (the An Giang province side), there was a gradual erosion trend from -10.8 m in 1999 to -20.9 m in 2006. This trend was also consistent with actual measurements. However, the measurement results showed that the bottom was more eroded and skewed towards the An Giang province. During the data collection, we discovered that there was a sand mine from 2002 to 2004, which made the bed river more eroded in this area compared with the calculation results. It should be noted that the mathematical model in this study did not consider bed change due to sand mining.

In the downstream area, both the Dong Thap and An Giang provinces have built embankments along the river and were not affected by sand mining activities. The simulation results of this downstream area are quite suitable for measurement data. In Fig. 13, there was a variation of the bottom in 2002 where a deep pool was filled with 14 m [34], so the elevation of the deep pool was raised to -28 m (described by dash-dot line in Fig. 13). The deep pool tended to erode again after a period of 4 years from 2003 to 2006. The bed elevation of the deep pool in 2006 was near -38 m while the measurement was actually -36 m at cross section 2 (Fig. 13). At cross-section 3 (Fig. 13), the results do not differ much between simulation and observation. At this position, close to the downstream boundary, the result is satisfactory when applying the characteristic line method. The difference between the simulation and observation was 9.2%.

Conclusions

According to the simulation analyses, we deduce that the HYDIST model well simulates both hydraulic and bed change in the river. For the hydraulic module, the results from the calculated flow and water level models showed high reliability during the process of calibration and validation. The NSE values were 0.71 and 0.81 for discharge and water level, respectively, while the R^2 values were 0.82 and 0.88, respectively. For the sediment transport module, the model performed very well in terms of sediment concentration for calibration and validation, with NSE values of 0.82 and 0.80, respectively, and an R^2 value of 0.91 for both processes. For verification of the model's applicability in a segment of the Tien river, the results were not much different between the simulation and measurement from 1999 to 2006, the percent of difference (BIAS)>10%. The changes of the islets and mudflats were closely modelled to the actual development i.e. the disappearance of Beo and the change in the mudflats on the An Giang side. Furthermore, when extracting the simulation data in some sections, the calculation results were entirely consistent with the actual development. At this position, close to the downstream boundary, the result was still satisfactory when applying the characteristic line method and the difference of comparison between simulation and observation was 9.2%.

However, the bed change module was run without the influence of sand mining in this study. In future studies, sand mining sources will be integrated into the bed load continuity equation.

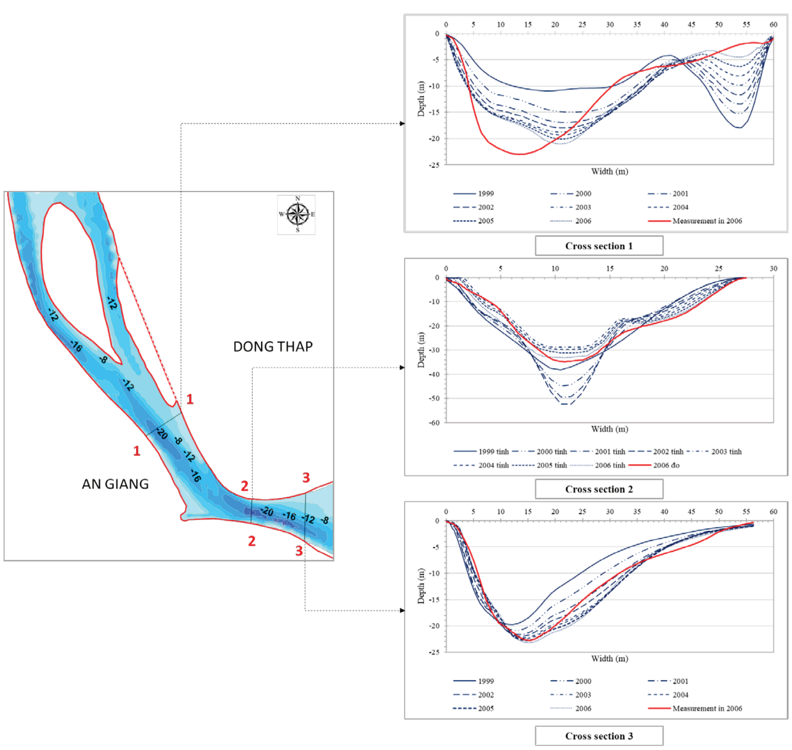

Fig. 13. The water depth at three cross sections.

Nomenclatures

u : depth-averaged horizontal velocity components in x direction (m/s)
v : depth-averaged horizontal velocity components in y direction (m/s)
ς : fluctuation of water surface, compare to "zero" level (m)
H : static depth from the still water surface to the bed (m)
K : friction bed coefficient
A : eddy horizontal viscosity coefficient (m^2/s)
g : acceleration gravity (m/s^2)
C : depth-averaged concentration of suspended load (m^3/m^3)
K_x : dispersion coefficient in Ox direction (m^2/s)
K_y : dispersion coefficient in Oy direction (m^2/s)
H : averaged depth used in the model (H=h+ς) (m)

γ_v : velocity coefficient in the depth; calculated from $\gamma_v = \dfrac{(1-Z)\left[1-\left(\dfrac{a}{H}\right)^{0.2}\right]}{(1.2-Z)\left[1-\left(\dfrac{a}{H}\right)^{1-Z}\right]}$

Z : suspension number and defined after Van Rijn (1993), $Z = \dfrac{\omega_s}{\chi(u_* + 2\omega_s)}$

χ : von Karman constant = 0.4

u_* : bed shear velocity, $u_* = \sqrt{\dfrac{g}{Ch^2}(u^2+v^2)}$

Ch : chezy coefficient, $Ch = 18\log\left(12\dfrac{H}{K_s}\right)$

K_s : bed roughness, $K_s = 3D_{90}$
D_{90} : diameter of particle that is equal to or less than 90% of the mass of particles present
S : standing for erosion and deposition rates (m/s).
M : sediment size-depended coefficient after Van Rijn (1993): 0.00001 ($kg/m^2/s$)
C_b : concentration of bed load (m^3/m^3)
ω_{sm} : particle fall velocity in mixture of water and sediment (m/s), $\omega_{sm} = (1-C)^4\,\omega_s$

ω_s : particle fall velocity, $\omega_s = \dfrac{(\frac{\rho_s}{\rho}-1)gd^2}{18\nu}$

D : mean diameter of particle (m)
ν : kinematic viscosity coefficient (m^2/s)
τ_e : critical bed shear stress for erosion at bottom (N/m^2)
τ_d : critical bed shear stress for deposition at bottom (N/m^2)

τ_b : bed shear stress (N/m^2), $\tau_b = \dfrac{1}{8}\rho f_w V^2$

f_w : friction coefficient of Darcy – Weisbach, calculated from Chezy formula; $f_w = \dfrac{8gn_r^{\,2}}{H^{1/3}}$

ρ : mass density of water (kg/m^3)

ρ_s : density of particles (kg/m^3)

n_r : roughness coefficient

ε_p : void ratio of sediment

D_* : dimensionless particle parameter: $D_* = d_m \left[\frac{g\left(\frac{\rho_s}{\rho} - 1\right)}{v^2} \right]^{\frac{1}{3}}$

T : dimensionless bed shear stress: $T = \left[\frac{u_*^2 - u_{*,cr}^2}{u_{*,cr}^2} \right]$

$u_{*,cr}$: critical depth-averaged flow velocity based on Shields (m/s), $u_{*,cr} = 0.25(\frac{\rho_s}{\rho} - 1)^{\frac{8}{15}} d^{\frac{9}{15}} g^{\frac{8}{15}} v^{-\frac{1}{15}}$

qb : bed load

$$q_b = 0.053((\frac{\rho_s}{\rho} - 1)g)^{0.5} d_m^{1.5} T^{2.1} D_*^{-0.3} \frac{(u, v)}{\sqrt{u^2 + v^2}}$$

ACKNOWLEDGEMENTS

This research was funded by the Institute for Computational Science and Technology, with the topic "Development of bank erosion numerical model basing on HPC in connection with hydraulic model and to apply for some river reaches of the Mekong river", code No. NDT.28.KR/17.

This work was supported by the Domestic Master/PhD Scholarship Programme of Vingroup Innovation Foundation.

COMPETING INTERESTS

The authors declare that there is no conflict of interest regarding the publication of this article.

REFERENCES

[1] W.H. Graf (1984), *Hydraulics of Sediment Transport*, Water Resources Publication, 524pp.

[2] L.C. Van Rijn (1984a), "Sediment transport, part I: bed load transport", *Journal of Hydraulic Engineering*, **110(10)**, pp.1431-1456.

[3] L.C. Van Rijn (1984b), "Sediment transport, part II: suspended load transport", *Journal of Hydraulic Engineering*, **110(11)**, pp.1613-1641.

[4] N. Chien and Z. Wan (1999), *Mechanics of Sediment Transport*, ASCE Press, 913pp.

[5] S.I. Khassaf and S.M. Ressen (2014), "Estimation the quantity of sediment transport upstream of Al-Hafar regulator using different formulas", *International Journal of Scientific & Engineering Research*, **5(7)**, pp.456-466.

[6] S.U. Choi and J. Lee (2015), "Prediction of total sediment load in sand-bed rivers in Korea using lateral distribution method", *Journal of the American Water Resources Association*, **51(1)**, pp.214-225.

[7] T. Falkowski, et al. (2017), "Channel morphology changes and their relationship to valley bottom geology and human interventions; a case study from the Vistula valley in Warsaw, Poland", *Geomorphology*, **297**, pp.100-111.

[8] R.G. Jackson (1975), "Velocity-bed-form-texture patterns of meander bends in the lower Wabash river of Illinois and Indiana", *Geological Society of America Bulletin*, **86(11)**, pp.1511-1522.

[9] J. Sun, L. Binliang, Y. Haiyan (2015), "Development and application of a braided river model with non-uniform sediment transport", *Advances in Water Resources*, **81**, pp.62-74.

[10] S. Peirce, P. Ashmore, P. Leduc (2018), "The variability in the morphological active width: results from physical models of gravel-bed braided rivers", *Earth Surface Processes and Landforms*, **43(11)**, pp.2371-2383.

[11] S. Ikeda, M. Yamasaka, M. Chiyoda (1987), "Bed topography and sorting in bends", *Journal of Hydraulic Engineering*, **113(2)**, pp.190-204.

[12] S. Ikeda, G. Parker (1989), "Sediment transport and sorting at bends", *River Meandering*, **12**, pp.103-125.

[13] Z.L. Wei, L.K. Zhao, X.P. Fu (1997), "Research on mathematical model for sediment in Yellow river", *Journal of Wuhan University Hydraulic & Electric Engineering*, **30(5)**, pp.21-25.

[14] W. Wu (2008), *Computational River Dynamics*, CRC Press, 508pp.

[15] L.X. Luu, S. Egashira, H. Takebayashi (2004), *Investigation of Tan Chau Reach in lower Mekong Using Field Data and Numerical Simulation*, Proceedings of Hydraulic Engineering, DOI: 10.2208/prohe.48.1057.

[16] D.H. Zhao, et al. (1994), "Finite-volume two-dimensional unsteady-flow model for river basins", *Journal of Hydraulic Engineering*, **120(7)**, pp.863-883.

[17] P.A. Sleigh, et al. (1998), "An unstructured finite-volume algorithm for predicting flow in rivers and estuaries", *Computers & Fluids*, **27(4)**, pp.479-508.

[18] P. Brufau, P. García-Navarro, M.E. Vázquez-Cendón (2004), "Zero mass error using unsteady wetting - drying conditions in shallow flows over dry irregular topography", *International Journal for Numerical Methods*, **45(10)**, DOI: 10.1002/fld.729.

[19] X. Liu, A. Mohammadian, J.A.I. Sedano (2014), "A well-balanced 2-D model for dam break flow with wetting and drying", *Journal of Fluid Flow, Heat and Mass Transfer*, **1**, pp.30-37.

[20] N.T. Bay, et al. (2019), "HYDIST model and the approach of solving sediment concentration at open boundaries", *Vietnam Journal of Hydro-Meteorology*, **704**, pp.57-64.

[21] N.T. Bay, et al. (2012), "Numerical investigation on the sediment transport trend of Can Gio coastal area (southern Vietnam)", *Journal of Marine Environmental Engineering*, **9(3)**, pp.191-211.

[22] Y. Zhang (2001), *CCHE2D: Two-Dimensional Hydrodynamic and Sediment Transport Model for Unsteady Open Channel Flows Over Loose Bed*, Technical Report No. NCCHE-TR-2001-1, University of Mississippi, 182pp.

[23] T.P. Hoanh (2014), "Current situation of erosion on Tien river bank running through Dong Thap province in the period of 2009-2013", *Journal of Science*, **58**, pp.161-171.

[24] N.T.D. Thuy, et al. (2019), *Modelling Accresion and Erosion Processes in the Bassac and Mekong Rivers of the Vietnamese Mekong Delta*, International Conference on Asian and Pacific Coasts, pp.1431-1437.

[25] D.N. Khoi, et al. (2020), "Morphological change assessment from intertidal to river-dominated zones using multiple-satellite imagery: a case study of the Vietnamese Mekong delta", *J. Regional Studies in Marine Science*, **34**, DOI: 10.1016/j.rsma.2020.101087.

[26] M. Guidolin, et al. (2013), "Using high performance techniques to accelerate demand-driven hydraulic solvers", *Journal of Hydroinformatics*, **15(1)**, pp.38-54.

[27] E.J. Anthony, et al. (2015), "Linking rapid erosion of the Mekong river delta to human activities", *Scientific Reports*, **5(1)**, pp.1-12.

[28] N.T. Bay and M.Q. Trang (2006), "Mathematical model of cohesive sediment transport in the shallow sea basin", *Journal of Science and Technology Development - Vietnam National University, Ho Chi Minh city*, **9**, pp.31-39.

[29] J. Douglas, Jim (1955), "On the numerical integration of by implicit methods", *Journal of the Society for Industrial and Applied Mathematics*, **3(1)**, pp.42-65.

[30] J.E. Nash and J.V. Sutcliffe (1970), "River flow forecasting through conceptual models part I - a discussion of principles", *Journal of Hydrology*, **10(3)**, pp.282-290.

[31] D.N. Moriasi, et al. (2007), "Model evaluation guidelines for systematic quantification of accuracy in watershed simulations", *Transactions of the ASABE*, **50(3)**, pp.885-900.

[32] D.N. Moriasi, et al. (2015), "Hydrologic and water quality models: performance measures and evaluation criteria", *Transactions of the ASABE*, **58(6)**, pp.1763-1785.

[33] A.J. Mehta, et al. (1989), "Cohesive sediment transport. I: process description", *Journal of Hydraulic Engineering*, **115(8)**, pp.1076-1093.

[34] H.Q. Hai (2011), "Correlation of sedimentation - erosion in Tien and Hau rivers", *Journal of Earth Sciences*, **33(1)**, pp.37-44.

DOI: 10.31276/VJSTE.62(4).60-64

Assessment of phosphorus release from alluvial sediments using single extraction: a case study in Can Gio, Southern Vietnam

Thi Thu Dung Tran[1*], Thanh Thoang Ngo[1], Ngoc Tuyen Nguyen[1], Bich Chau Tran[1], Minh Hoang Truong[2]

[1]*Faculty of Environment, University of Science, Vietnam National University, Ho Chi Minh city*
[2]*Faculty of Geology, University of Science, Vietnam National University, Ho Chi Minh city*

Received 7 August 2020; accepted 30 October 2020

Abstract:

Sediment-water interaction is a complicated process; hence, it is essential to know the potential mobility of an element from sediment to the aquatic environment. In this study, the potential mobility of phosphorus (P) in sediment from Can Gio was investigated. Three single extractions were applied including a mild salt (NH_4Cl), an acid (HCl), and a base (NaOH) each representing different environmental factors during sediment resuspension. Other geochemical parameters were also determined. The total amount of P in the sediments varied from 320.41 mg/kg to 668.22 mg/kg in five sampling sites. The general range of potential mobility of P decreased as follows: P-mild (3.70-13.13 mg/kg) < P-base (36.80-78.53 mg/kg) < P-acid (133.85-380.57 mg/kg). Although P-acid was not easily released to the environment, its relatively high concentration can affect the aquatic environment when the environment becomes acidic.

Keywords: **phosphorus release, sediment, sediment resuspension, single extraction.**

Classification number: **5.1**

Introduction

In natural ecosystems, phosphorus (P) is not only a major nutrient controlling eutrophication but it is also a limiting nutrient in many aquatic systems [1, 2]. Besides aquatic plants and algae, sediment is considered as the main contributor of P to the aquatic system from internal sources [3]. Phosphorus can exist in several forms in sediments with different mobilities, however, not all the fractions of P in sediments are likely to be released and become bioavailable in a water environment [4]. Knowledge of the potential release of P from sediment is useful since it can serve as indicators of the potential of P loading contributions to the water environment [3]. Fractionation of P by sequential extractions are often used to evaluate the potential release as well as the origin of P in the sediment [4, 5]. There are several extraction tests for sediments, including single extractions and sequential extractions, each with different purposes and implications. However, sequential extractions, which are laborious and time consuming, will not be applied in the present study. Single extractions with reagents representing different environmental conditions that the sediments might encounter during resuspension is a fast, simple, and relatively cheap way to assess the potential release of elements from sediments to the water environment [6]. Hence, it is recommended as a useful tool for water managers on a routine basis to calculate the releasable P stock in sediment [4].

Can Gio, a coastal district of Ho Chi Minh city, has a large area covered by a mangrove forest that was designated as a Biosphere Reserve by UNESCO [7]. As home to a tropical mangrove ecosystem, Can Gio is a dynamic transitional coastal ecosystem where natural and anthropogenic impacts are mixed [8]. The major sources of nutrients in this area are the decomposition of organic matter by litter mineralization in the mangrove forest, effluents from aquaculture activities, and municipal sewage [9]. As a transitional ecosystem, mangrove is also considered as a barrier retaining nutrients (N and P) [10]. However, mangrove sediments can also act as a source of nutrients for the water environment due to mineralization [11]. Recently, some work has been done to understand the behaviour of nutrients in the Can Gio mangrove

*Corresponding author: Email: tttdung@hcmus.edu.vn

system. However, their research was focused on evaluating the nutrient status of reforested and natural mangrove stands with different site-specific species [12] or the influence of vegetation, tidal cycles, and seasonality to the dissolved inorganic nutrient concentrations in porewater [9].

The objective of this research is to assess the potential release of P during the resuspension of sediments in the Can Gio area. Moreover, instead of simply using the total P (TP), this study applies the single extraction to provide information about the fractions that compose the P load. By using single extraction, this study aims to prove that single extraction can be a valuable tool for environmental management. This kind of study can provide information about the role of the internal release of P from the sediment, which is helpful to local managers in terms of water quality management since most of the water quality protection policy has put the focus on reducing the external source without considering an internal source from sediment.

Materials and methods

Sampling

The study area is located in Can Gio district, Ho Chi Minh city, Vietnam. Surface sediments (approximately 1 kg each) were collected in the dry season in 2017 (Fig. 1). Sampling sites S1, S2, and S3 were located in a densely populated shrimp farming settlement. On the other hand, sampling sites S4 and S5 were located in the core zone of the mangrove forest. To get a good representation of the system, a sample was composed of 5 sub-samples at each sampling site. After collection, the samples were placed in sealed plastic bags and transported to the University of Science (Ho Chi Minh city, Vietnam) in a cooler box. The samples were air-dried, homogenized in a porcelain mortar, and sieved over a 2 mm mesh sieve.

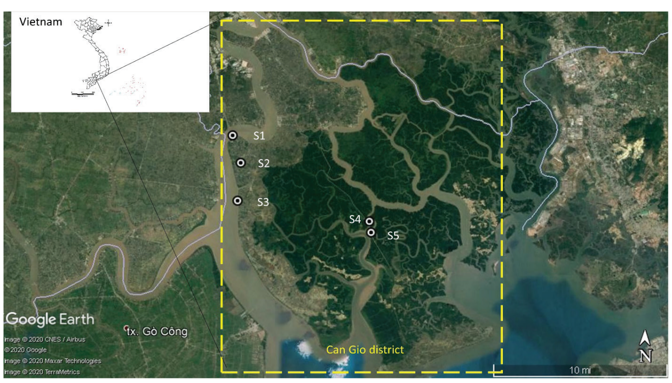

Fig. 1. Map of the sampling sites in the studied area (map was modified based on the satellite image provided by Google Earth, 2020).

General sample characterization

Organic carbon (OC) was inferred from the organic matter determined by the Walkley and Black manual titration method [13]. Grain size distribution was determined by sieving and hydrometer methods [14]. The pH of each sample was measured in water (1:5 ratio w/w). The total elemental (Al, Ca, Fe, K, Mg, P) content of the samples were determined after digestion by the so-called 3 acids digestion method (HNO_3, $HClO_4$, HF). About 0.5 g of dried sediment sample was digested with an acid mixture containing HCl_{cc} (4 ml), HNO_{3cc} (2 ml), and HF_{cc} (2 ml) in a Teflon beaker on a hot plate. After digestion, the residue was dissolved with HCl 2.5 mol/l. The major elements (Al, Ca, Fe, K, Mg) in the digested solutions were analysed with ICP-OES (Perkin Elmer Optima 7300 DV) while P was determined by the molybdate blue method of Murphy and Riley (1962) [15].

Single extraction

Single extraction was carried out by three independent batches with different reagents and conditions. A mild salt (1 M NH_4Cl), an acid (0.5 M HCl), and a base (0.1 M NaOH) [16] were used to assess the three forms of phosphorus existing in the sediment i.e. P-Ca/Mg (apatite P), P-Al/Fe (non-apatite P), and weak bonding P. The original extraction scheme was a sequential protocol and developed by Hieltjes & Lijklema (1980) [17]. However, it was modified to include different independent steps that are not sequential as in [16]. This single extraction was applied in the present study since it is simple and practical [4]. About 1 g of dried sediment was weighed into a centrifuge tube and then 10 ml of 1 M NH_4Cl was added. The sediment was extracted by shaking for 2 h. All the supernatant was collected and another 10 ml of 1 M NH_4Cl was added to the residue. This mixture was shaken by another 2 h. The solution was centrifuged at 3500 rpm for 10 min. The latter and the first solution were mixed together and measured for weak bonding P (P-NH_4Cl). Another 0.1 g portion of the dried sediment was weighed into a centrifuge tube, then 5 ml of 0.5 M HCl was added and the solution was shaken for 24 h. On the following day, the collected supernatant was measured for apatite P (P-HCl). For the base extraction, 10 ml of 0.1 M NaOH was added to 1 g of sediment and shaken for 17 h. The supernatant was measured for non-apatite P (P-NaOH). All the extractions were carried out at room temperature. After each extraction step, the samples were centrifuged (3000 rpm for 10 min) and the phosphorus in the extracts was determined accordingly. All P forms were expressed as the amount of P in milligrams per kilogram of sediment (mg/kg) taking into account the volume of extraction solvent for each extraction.

Quality assurance and quality control

All reagents were of analytical grade. For each sample, duplicate (total element concentrations and single extractions) or triplicate (pH and organic matter) analyses were performed to ensure the analytical precision and reproducibility. Results are displayed as the averages of the replicates. Duplicate blanks were also inserted into each batch.

Results and discussion

Sediment characteristics

General characteristics (fine fraction, pH, organic matter): the average of the fine fraction (FF) (≤63 µm, silt and clay), OC, pH, and elemental concentrations in the sediment are presented in Table 1. Grain size analysis revealed the dominance of fine fraction (>90%) and the values were rather uniform between the sampling sites. The pH values in the sediments indicated an acidic to neutral medium (6.30-7.30). The amount of organic carbon in sediments varied from 2.24 to 3.66% and exhibited slightly higher values in the core zone of the mangrove forest (S4-S5). This could be explained by the high biological productivity in sediments associated with mangrove [18].

Table 1. The average of the fine fraction (FF) (≤63 μm, silt and clay), OC, pH, and elemental concentrations in the sediment.

Parameter	Unit	Site						
		S1	*S2*	*S3*	*S4*	*S5*	*Average S1-S3*	*Average S4-S5*
pH		6.30	6.50	6.37	7.30	7.29	6.39	7.29
OC	%	2.24	2.90	3.30	3.66	3.04	2.81	3.35
FF	%	99.62	98.92	97.90	90.18	97.93	98.81	94.06
Al	g/kg	77.2	79.5	81.2	61.3	50.9	79.3	56.1
Fe	g/kg	43.4	44.8	42.0	39.3	44.9	43.4	42.1
Ca	g/kg	3.8	2.4	2.5	3.5	1.9	2.9	2.7
Mg	g/kg	13.3	11.7	10.9	11.1	8.1	11.9	9.6
TP	mg/kg	668	575	431	645	320	558	483
OC:TP		34	50	77	57	95	53	76

Major element and total phosphorus: among the sampling sites, the concentration of Fe in the sediments did not change much from 39.3 to 44.9 g/kg (Table 1), while the Al concentration varied over a much wider range from 50.9 to 81.2 g/kg. The sediment at sites S1-S3 had a higher content of fine fraction and Al in comparison to S4-S5, which suggests higher content of clay minerals in S1-S3 since Al is considered representative for clay minerals [19]. Data of Al in Can Gio area is rather limited making it difficult to compare. However, Al content was slightly higher than those reported in other studies in the mangrove forests of other countries [1]. Iron content was in the same range of those in other studies conducted in particulate sediments in Can Gio [20] as well as other mangrove forest sediments [1]. Generally, Ca concentrations were very low with a minimum of 1.9 and a maximum of 3.8 g/kg. The concentration of TP in the sediments were moderately different from each other and ranged from 320 to 668 mg/kg (Table 1). Total phosphorus in the sediments was higher than those observed in the previous study carried out in the Can Gio area (87-306 mg/kg) [21] but more or less in a similar range to another study in a mangrove forest in India (360-550 mg/kg) [18]. The higher content of TP in the present study might be attributed to the completed digestion of the samples by using a mixture of HCl_{cc}, HNO_{3cc}, and HF_{cc}. The use of HF is believed to digest minerals associated with a silicate matrix, which is difficult to be digested using other acids and thus results in higher TP [22].

Single extractions

The results from the single extractions are presented in Fig. 2. Apatite P was the main form of P in all the investigated sediments, which ranged from 133.85 to 380.57 mg/kg and thus represented 31 to 62% of their total P pools. Generally, acid-soluble P is considered as apatite P (Ca- and Mg-bound P) [23]. However, a small amount of P fraction that is absorbed into amorphous Fe oxides, FeS, and Fe phyllosilicates is also dissolved during this extraction [24]. The second most important form of P was non-apatite inorganic P. This form ranged from 36.80 to 78.53 mg/kg, thus representing 7 to 14% of the total P pools. Non-apatite P includes P bound to Al, Fe, and Mn (hydr)oxides [3]. Samples having a relatively higher apatite P amounts are expected to have higher pH values while samples having a relatively higher non-apatite P amount are expected to have lower pH values. This is due to the fact that elevated adsorption of P into the Al and Fe (hydr) oxides are observed at lower pH values, whereas precipitation of P with CaCO3 compounds occurs at higher pH values [25]. However, this assumption was not observed in the present study. The lowest form of P was weak bonding P, which only contributed to 1-2% of the total P pool (ranging from 3.70 to 13.13 mg/kg). This fraction of P is considered as loosely bound, labile, or exchangeable P because NH_4Cl is used to extract P adsorbed by exchange sites [17]. However, small amounts of P associated with Al and Fe compounds are also dissolved during this extraction [4].

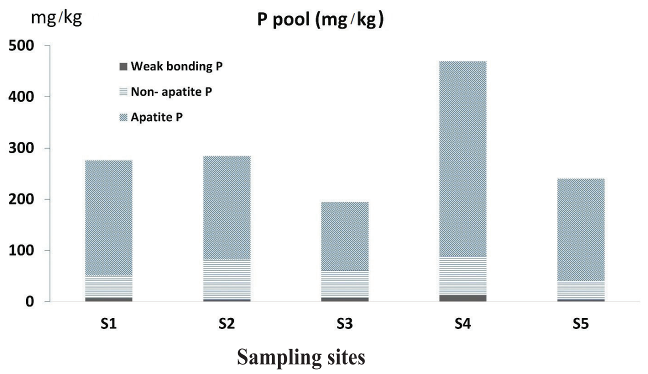

Fig. 2. Concentrations of different P-forms from single extractions.

Environmental implications

Pollution of sediments based on the TP can be classified as no P pollution (TP<500 mg/kg), medium pollution (500 mg/kg<TP<1000 mg/kg), and pollution (TP>1000 mg/kg) [5]. The results indicated that the status of the investigated sediment is from no P pollution to medium pollution.

Based on the relationship between TP and other geochemical characteristics (organic matter or major elements), preliminary information about the potential release and the origination of P in the sediments may be predicted. Reddy and Delaune (2008) [26] concluded that mineralization of organic phosphorus and OC:TP ratio is inversely related. Hence, the lower OC:TP ratio results in the higher potential release of P from organic matter [27]. Among the studied sediments, S1 had the lowest OC:TP and this site is predicted to have the highest mineralization and subsequently highest release of P from organic matter. However, organic phosphorus is known to be very stable and thus requires a long time to be degraded. The OC:TP ratios (by weight) of S2 to S5 (50-95) were higher than the Redfield ratio [28], which indicates that the organic matter is not enriched with phosphorus [27]. Hence, it can be inferred that most of the P in the investigated sediments (except S1) are associated with inorganic compounds. It is reported by Jensen, et al. (1992) [29] that the ratio of total iron to total phosphorus (Fe:TP ratio) in the sediment is an indicator for the release of P into the water environment. Sediments with Fe:TP over 15 (by weight) release relatively less P in anoxic conditions whereas Fe:TP ratios below 10 seem to be unable to retain P [29]. This is due to the fact that the formation of minerals of Fe (II) and P is favoured when there is A high availability of Fe in sediment [30]. The ratio of total iron to total phosphorus (Fe:TP ratio) of the sediments in Can Gio was higher than 15, suggesting a low release of P from iron minerals.

Although the total concentration of P can provide information on the current pollution status and the ratio of TP to other elements in sediments may help to predict P-leaching, they do not allow the assessment of the mobility of P into the water environment. Single extractions may give some information about the mobility of P under changing environmental conditions. To assess the potential release of P as an internal load from sediment to the water environment, two P-pools were characterized as mobile P and non-mobile P. The mobile P was determined by the sum of the weak bonding P, apatite P, and non-apatite P form, which is the P that can be released when external environmental conditions change. The difference between TP and the mobile P represents the non-mobile sediment P pool (Fig. 3). The mobile P forms ranged from 41 to 49% (S1-S3) and 73 to 75% (S4-S5). Hence, it seems likely that mangrove forest sediments are more sensitive to P release. As mentioned above, sediments in S1-S3 had a higher content of clay materials, Fe, and Al, and thus had a better ability to adsorb and retain P than the sediments in S4-S5. Different forms of P are of different significance in terms of environmental meaning [4]. The potential mobility of P increased as follows: weak bonding P < non-apatite P < apatite P. This order agreed well with the findings of other studies [2, 14]. Phosphorus extracted by mild extraction with NH4Cl is known as the most labile P among investigated forms of P. Hence, weak bonding P can be represented by the immediately available P when sediment is resuspended in water. The result obtained from NH4Cl extraction in this study was quite low (1-2%) and similar to Kapanen (2008) [16] who found a low extraction yield of P (1% of the TP) in the sediment samples. This indicated that sediments in Can Gio have a poor leachability of P during resuspension in water.

The concentration of the non-apatite P representing P bound to metals is also used to estimate the available algal P [31]. This form of P is sensitive to changing redox conditions [3]. When the sediment becomes anaerobic, Fe(III) binds lightly with P and is reduced to Fe(II), which is more soluble and can be more readily exchanged with the solution [21]. Therefore, non-apatite P can act as a source of P under anoxic conditions. The concentration of non-apatite P present in the sediment in Can Gio (44-79 mg/kg) was higher than the concentration found in normal sediments in Estonia (11.95-39.43 mg/kg) [16], but in the lower range of sediments in a eutrophic area of Brazil (119-279 mg/kg [3]) and Norway (480-710 mg/kg [30]).

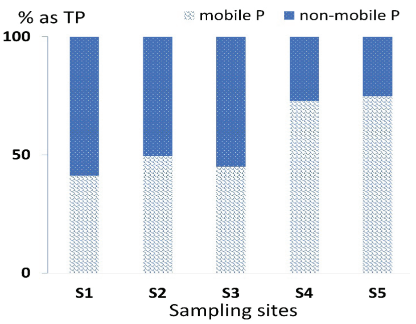

Fig. 3. The relative contributions of mobile and non-mobile forms to the total P pool.

Among the mobile forms, the dominant form of P in Can Gio sediments was apatite P (Fig. 3). This form corresponds to P bound to calcium, including apatite-P and P bound to carbonates [4]. The amounts of apatite P present in the Can Gio sediments (134-381 mg/kg) were similar to the values obtained in other studies (154.23-570.90 mg/kg [16], 260-350 mg/kg [30], 46-366 mg/kg [3]). Apatite-P is observed to be the main form of P in mangrove sediment based on its stability under the redox variations [27]. This form is considered to be non-bioavailable and difficult to release, however, under weakly acidic conditions, it can be partly released [32]. Therefore, the result from the P-HCl extraction is useful to assess the potential mobility of P when the external pH decreases. Results from single extraction indicated that acidification has a more profound impact on P-leaching of sediments in Can Gio compared to changing redox condition because apatite P is much higher than non-apatite P. However, non-apatite P can be mobilized and turn into an internal P source in anoxic conditions [3]. Hence, non-apatite P is also an important pool in terms of the potential release of P from Can Gio sediments due to the fact that most of the sediments in Can Gio are affected by periodic tidal forces and inundation [9]. Therefore, reducing the loading of P by improving the quality of wastewater being discharged into public water ways, as well as avoiding drastic acidification of the sediment, would be helpful in preventing pollution from P release.

Conclusions

The sediments investigated in Can Gio are characterized by low-to-medium P concentrations, which reflects a sediment status ranging from no pollution to medium pollution of P. Single extractions were useful to assess the potential release of P when the external environment changes. Results from the single extractions indicated that the mobile form of P was dominant in the core zone of the mangroves (71-75%), which suggests that these mangrove sediments have the potential to act as a source of phosphorus in the aquatic environment. The mobile-P consisted mainly of apatite P (31-62%), while non-apatite P and weak bonding P only contributed a minor part (1-14%) to the studied sediments. Although apatite P is considered to be non-bioavailable and difficult to release, it may attribute to the permanent pool of P in sediments. Therefore, these fractions are considered as a source for internal P-loading to the water environment.

ACKNOWLEDGEMENTS

This research is funded by Vietnam National University, Ho Chi Minh city (VNU-HCM) under grant number C2020-18-16.

COMPETING INTERESTS

The authors declare that there is no conflict of interest regarding the publication of this article.

REFERENCES

[1] P. Ranjan, A.L. Ramanathan, A. Kumar, R.K. Singhal, D. Datta, M. Venkatesh (2018), "Trace metal distribution, assessment and enrichment in the surface sediments of Sundarban mangrove ecosystem in India and Bangladesh", *Mar. Pollut. Bull.*, **127**, pp.541-547.

[2] B. Gunduz, F. Aydin, I. Aydin, C. Hamamci (2011), "Study of phosphorus distribution in coastal surface sediment by sequential extraction procedure (NE Mediterranean Sea, Antalya-Turkey)", *Microchem. J.*, **98 (1)**, pp.72-76.

[3] H. Cavalcante, F. Araújo, N.P. Noyma, V. Becker (2018), "Phosphorus fractionation in sediments of tropical semiarid reservoirs", *Sci. Total Environ.*, **619(620)**, pp.1022-1029.

[4] C. Wang, Y. Zhang, H. Li, R.J. Morrison (2013), "Sequential extraction procedures for the determination of phosphorus forms in sediment", *Limnology*, **14(2)**, pp.147-157.

[5] L. Cheng, et al. (2019), "A 30-year record of sedimentary phosphorus species in a coastal salt marsh southwest of Hangzhou Bay, China", *Cogent Environ. Sci.*, **5(1)**, pp.1-13.

[6] V. Cappuyns (2012), "A critical evaluation of single extractions from the SMT program to determine trace element mobility in sediments", *Appl. Environ. Soil Sci.*, **2012**, pp.1-15.

[7] V.Q. Tuan and C. Kuenzer (2012), *Can Gio Mangrove Biosphere Reserve Evaluation 2012: Current Status, Dynamics, and Ecosystem Services*, International Union for the Conservation of Nature, IUCN, 109pp.

[8] S. McDonough, W. Gallardo, H. Berg, N.V. Trai, N.Q. Yen (2014), "Wetland ecosystem service values and shrimp aquaculture relationships in Can Gio, Vietnam", *Ecol. Indic.*, **46**, pp.201-213.

[9] P. Taillardat, et al. (2019), "Assessing nutrient dynamics in mangrove porewater and adjacent tidal creek using nitrate dual-stable isotopes: a new approach to challenge the outwelling hypothesis?", *Mar. Chem.*, **214**, DOI: 10.1016/j.marchem.2019.103662.

[10] A. Aschenbroich, et al. (2015), "Spatio-temporal variations in the composition of organic matter in surface sediments of a mangrove receiving shrimp farm effluents (New Caledonia)", *Sci. Total Environ.*, **512-513**, pp.296-307.

[11] T. Dittmar, N. Hertkorn, G. Kattner, R.J. Lara (2006), "Mangroves, a major source of dissolved organic carbon to the oceans", *Global Biogeochem. Cycles*., **20(1)**, pp.1-7.

[12] J.F. Oxmann, Q.H. Pham, L. Schwendenmann, J.M. Stellman, R.J. Lara (2010), "Mangrove reforestation in Vietnam: the effect of sediment physicochemical properties on nutrient cycling", *Plant Soil*, **326(1)**, pp.225-241.

[13] D.W. Nelson and L.E. Sommers (1982), *Total Carbon, Organic Carbon and Organic Matter*, pp.539-579, https://acsess.onlinelibrary.wiley.com/doi/pdf/10.2134/ agronmonogr9.2.2ed.c29.

[14] K.H. Head (1992), *Manual of Soil Laboratory Testing Volume I - Soil Classification and Compaction Tests (2nd edition)*, Pentech Press, 388pp.

[15] J. Murphy and J.P. Riley (1962), "A modified single solution method for the determination of phosphate in natural waters", *Anal. Chim. Acta*, **27**, pp.31-36.

[16] G. Kapanen (2008), "Phosphorus fractionation in lake sediments", *Est. J. Ecol.*, **57(4)**, pp.244-255.

[17] A. Hieltjes and L. Lijklema (1980), "Fractionation of inorganic phosphates in calcareous sediments", *J. Environ. Qual.*, **9**, pp.405-407.

[18] A.L. Ramanathan, R.K. Ranjan, M.B.K. Prasad, R. Chauhan, G. Singh (2010), "Sediment - nutrient dynamics in selected Indian mangrove ecosystems - land use and climate change implications", *International Association of Hydrological Sciences*, **337**, pp.84-92.

[19] B. Rubio, M. Nombela, F. Vilas (2000), "Geochemistry of major and trace elements in sediments of the Ria de Vigo (NW Spain): an assessment of metal pollution", *Mar. Pollut. Bull.*, **40(11)**, pp.968-980.

[20] N. Thanh-nho, E. Strady, T. Nhu-trang, F. David, C. Marchand (2018), "Trace metals partitioning between particulate and dissolved phases along a tropical mangrove estuary (Can Gio, Vietnam)", *Chemosphere*, **196**, pp.311-322.

[21] L.T. Loi (2008), *Effect of Hydrology on Mangrove Ecosystems: Effect of Hydrology on the Structure and Function of Mangrove Ecosystems in the Can Gio Mangrove Biosphere Reserve, Vietnam*, LSU Doctoral Dissertations, 232pp.

[22] J. Ne'mery and J. Garnier (2007), "Origin and fate of phosphorus in the Seine watershed (France): agricultural and hydrographic P budgets", *J. Geophys. Res.*, **112(G03012)**, pp.1-14.

[23] G.M. Pierzynski (2000), *Methods of Phosphorus Analysis for Soils, Sediments, Residuals, and Waters*, Southern Cooperative Series Bulletin No. #396, 110pp.

[24] J. Deborde, C. Marchand, N. Molnar, L. Patrona, T. Meziane (2015), "Concentrations and fractionation of carbon, iron, sulfur, nitrogen and phosphorus in mangrove sediments along an intertidal fradient (semi-arid climate, New Caledonia)", *J. Mar. Sci. Eng.*, **3(1)**, pp.52-72.

[25] J.F. Oxmann and L. Schwendenmann (2015), "Authigenic apatite and octacalcium phosphate formation due to adsorption-precipitation switching across estuarine salinity gradients", *Biogeosciences*, **2(3)**, pp.723-738.

[26] K. Reddy and R. Delaune (2008), *Biogeochemistry of Wetlands: Science and Applications*, CRC Press, 387pp.

[27] M.M. Joseph, C.S.R. Kumar, K.R. Renjith, T.R.G. Kumar, N. Chandramohanakumar (2011), "Phosphorus fractions in the surface sediments of three mangrove systems of southwest coast of India", *Environ. Earth Sci.*, **62(6)**, pp.1209-1218.

[28] R.E. Hecky, P. Campbell, L.L. Hendzel (1993), "The stoichiometry of carbon, nitrogen, and phosphorus in particulate matter of lakes and oceans", *Limnol. Oceanogr.*, **38(4)**, pp.709-724.

[29] H.S. Jensen, P. Kristensen, E. Jeppesen, A. Skytthe (1992), "Iron: phosphorus ratio in surface sediment as an indicator of phosphate release from aerobic sediments in shallow lakes", *Hydrobiologia*, **235**, pp.731-743.

[30] K. Lukawska-Matuszewska, R.D. Vogt, R. Xie (2013), "Phosphorus pools and internal loading in a eutrophic lake with gradients in sediment geochemistry created by land use in the watershed", *Hydrobiologia*, **713(1)**, pp.183-197.

[31] Q.X. Zhou, C.E. Gibson, Y.M. Zhu (2001), "Evaluation of phosphorus bioavailability in sediment of three contrasting lakes in China and the UK", *Chemosphere,* **42**, pp.221-225.

[32] L. Li, L. Liu, S. Wang (2015), "Spatial distribution ofphosphorus fractions in sediment and the potential mobility of phosphorus in Dianchi lake", *Environ. Earth Sci.*, **74**, pp.3721-3731.

Assessing existing surface water supply sources in the Vietnamese Mekong delta: case study of Can Tho, Soc Trang, and Hau Giang provinces

Diep Anh Tuan Dinh*, Thanh Loc Nguyen, Thi Ngoc Phuong Nguyen, Hieu Trung Nguyen

Research Institute for Climate Change, Can Tho University

Received 31 August 2020; accepted 27 November 2020

Abstract:

In the recent past, the quality of surface water for domestic use in the Vietnamese Mekong delta (VMD) has been seriously affected by severe water pollution and intense saltwater intrusion. This study aims to assess existing surface water sources in the provinces of Can Tho, Hau Giang, and Soc Trang. By assessing the existing salinity status to point out areas of low salinity frequency hazards, this work identifies suitable areas through water quality assessments. The results indicated that the Hau river and its tributaries from Ke Sach (in Soc Trang) toward inland has a lower risk of salinity. This indicated that water sources in Ke Sach could be a possible raw water source for water supply treatment plants in Soc Trang. Specifically, water sources including the Hau river's mainstream, Cai Khe canal, Khai Luong canal, and Thom Rom canal in Can Tho city, the Hau river's mainstream, the Mai Dam river in the Hau Giang province, and the Cai Con river, the Hau river's mainstream in Ke Sach, and the Cai Vop and Cai Tram canals in the Soc Trang province, could be exploited for water supply. However, a treatment for pollutants such as BOD_5, COD, TSS, and total coliform in these water sources musts be taken into consideration.

Keywords: **saltwater intrusion, surface water quality assessment, surface water supply.**

Classification number: **5.1**

Introduction

The VMD, home to over 21 million people, is a part of the Mekong delta that covers an area of approximately 3.9 million hectares with a dense maze of canals and rivers [1]. Water plays a significant role in strategies for economic growth for the region in general and specifically for the provinces of Can Tho, Hau Giang, and Soc Trang [2]. Nonetheless, in recent years, the impacts of climate change and sea level rise are serious threats as they cause extreme phenomena such as salinity intrusion and severe droughts [3, 4]. These negative effects on water supply security in the delta creates possible threats to water supply systems. While groundwater is widely used in coastal areas, surface water is still a primary source of water in the provinces. However, the substantial extraction of groundwater for domestic use causes delta-wide subsidence that necessarily restricts excessive groundwater extraction [5, 6], therefore, the probability of switching to surface water needs to be taken into account. Rivers and canals in this region are usually considered as surface water resources for water supply systems. Nevertheless, the degradation of surface water quality due to pollution from anthropogenic activities has also limited the availability of surface water for domestic use in these provinces [7]. Assessing the water quality from the rivers and canals therefore is an important part of identifying acceptable areas for surface water supply abstraction to support water supply management. Currently, most water treatment plants in the VMD experience low capability of desalination followed by expensive construction and operation costs [8, 9]. Meanwhile, salinity is a significant criterion for the selection of water sources. Selected water sources are characterized by low frequency of salinity. Geographic Information System (GIS) software has continually demonstrated very informative spatial analyses in water monitoring research that supports water supply management. This paper aims to evaluate existing salinity and surface water quality in Can Tho, Hau Giang, and Soc Trang provinces, thereby building effective strategies and providing support to water utilities for water supply security in the context of climate change and local human activities.

*Corresponding author: Email: ddatuan@ctu.edu.vn

DOI: 10.31276/VJSTE.62(4).65-70

Methodology

Scope of the study

This study was undertaken in three VMD provinces with low-lying terrain, namely, Can Tho, Hau Giang, and Soc Trang (Fig. 1). Located in the South of Hau river, the study area comprises a relatively dense network of river courses and canals including natural river systems and canals. The 3 selected provinces are characterised by monsoon-dominated seasonal climate divided into the rain season (July-October) and the dry season (December-May). The tidal regime includes two tidal cycles on a daily basis that play an important role in saline water dynamics and water quality [10].

Method of research

This study uses an approach of evaluating surface water quality for water supply to identify areas of low salinity effects and water quality assessment [11]. This approach assesses existing salinity to find out areas with low salinity frequency and thereby evaluate the water quality to select the areas of acceptable condition for exploiting water supply. Research process were described as Fig. 2 as follow:

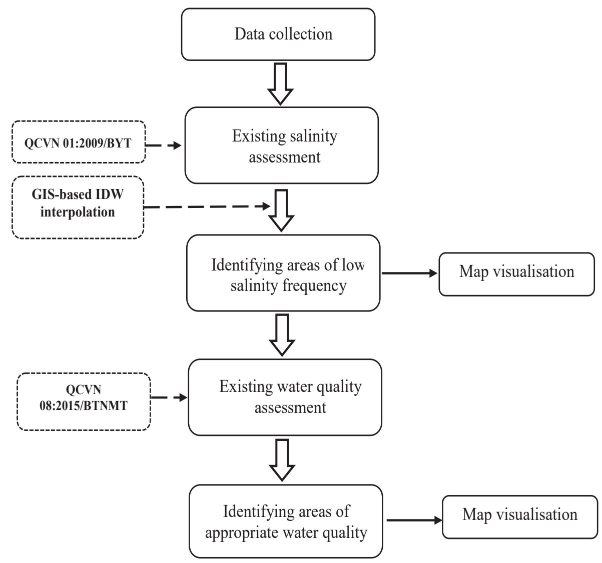

Fig. 2. A flowchart of research steps.

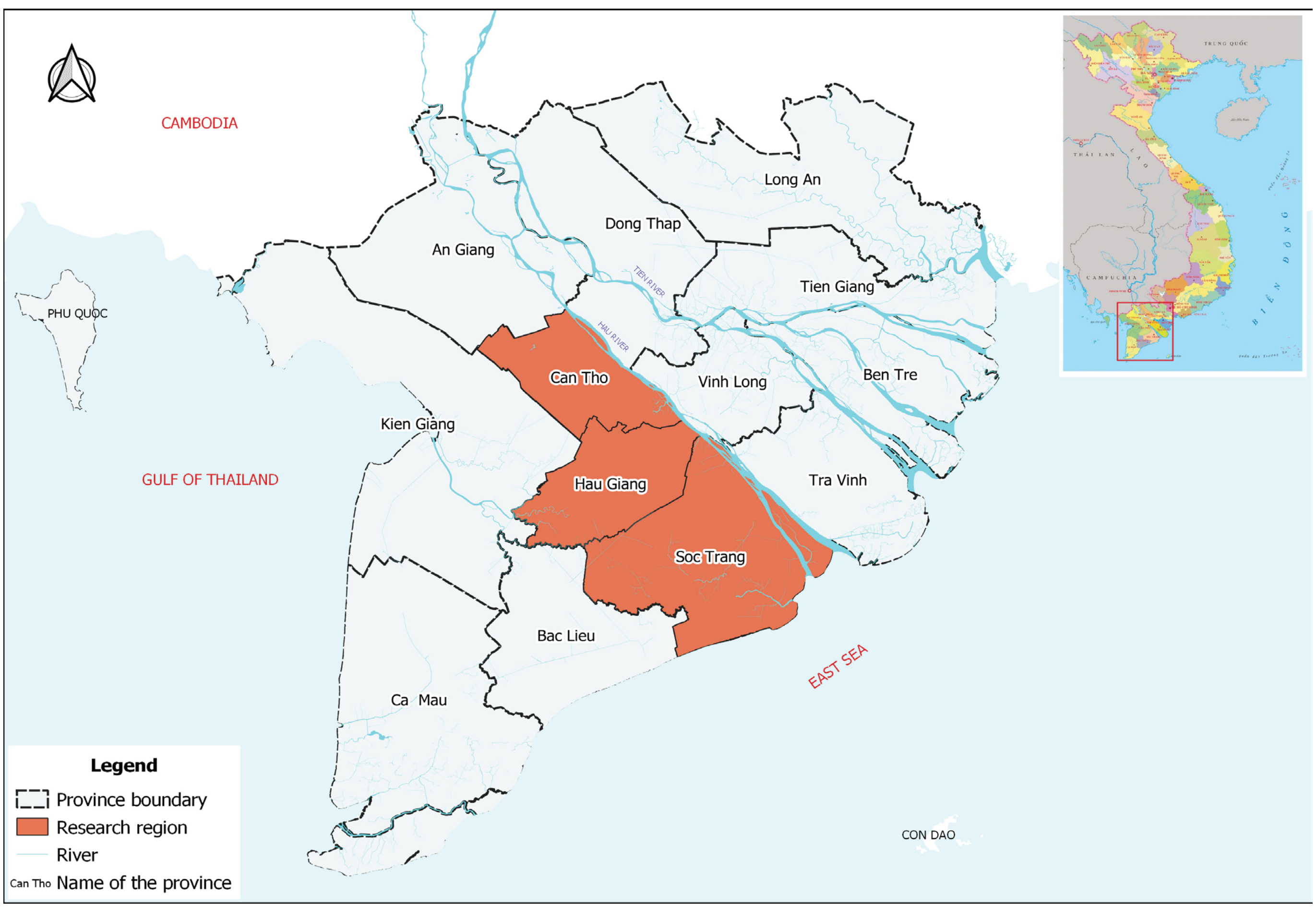

Fig. 1. Map of the study area.

The process consisted of 5 steps. Firstly, the study collected relevant data and performed data analysis (step 1). Then, the collected data of salinity was compared to the National Technical Regulation on the Drinking Water Quality (QCVN 01:2009/BYT). Step 3 involved defining areas that had low salinity effects by GIS-based interpolation. Spatial-analytical tools have increasingly been utilized for spatial assessment on water quality. Particularly, Inverse Distance Weighted (IDW) interpolation is easy implement and is available in almost any GIS-based platform under a wide range of conditions [12]. To create thematic maps, the boundary of the study area was digitised from collected toposheets using QGIS software, a popular Open Source GIS. In step 4, the selected areas of low salinity were then assessed for water pollutants. Statistical analysis, like mean, standard variation, etc., was used to evaluate the collected data. The results were compared to the National Technical Regulation on surface water quality (QCVN 08:2015/BTNMT) to find the areas of acceptable water quality. The precise locations of the monitoring sites were recorded using GPS receivers and were then imported into the GIS platform. This results in areas of appropriate water pollution were visualised on a map in step 5.

Data sources

Monitored salinity data (2015-2019) and monitored surface water quality (2016-2018) were collected from local Departments of Irrigation and Centers for Environmental Monitoring. The monitored surface water quality included parameters: pH, DO, TSS, BOD_5, COD, NH_4-N, NO_2-N, NO_3-N, PO_4-P, total iron, and total coliform. The study then applied statistical analysis to calculate the maximum and minimum values, the total amount, and the frequency of occurrence.

Results and discussion

Assessment of salinity hazard in existing water sources

Assessment of existing salinity data: salinity is considered as a crucial parameter in planning for water exploitation plants since saltwater intrusion severely influences water supply sources in coastal provinces. Based on the results shown in Table 1, salinity in 2016 was somewhat higher than in 2017. According to a report of CGIAR [13], the 2016 drought and salinity intrusion greatly influenced 11 out of the 13 provinces in the MRD causing a lack of freshwater for domestic use and farming activities. Data at monitoring points in the Soc Trang and Hau Giang provinces that reside closer to the sea, more exceeding the permitted salinity according the QCVN 01:2009.

Table 1. Salinity values at monitoring points in the Can Tho, Hau Giang and Soc Trang provinces.

	Monitoring points	Salinity in 2016 (mg/l)	Salinity in 2017 (mg/l)	QCVN 01:2009
Can Tho	Cai Cui	12-**350**	6-120	250-300
Hau Giang	Cay Duong	22-**680**	25-65	250-300
	Ranh Hat	26-**1,305**	15-**756**	250-300
	Mang Ca	19-**1,290**	11-**360**	250-300
	Cho Noi	18-**535**	12-65	250-300
	Ho Thu NB	14-160	15-65	250-300
	Ho Thu TPH	15-**605**	11-50	250-300
	Cau Cai Tu	14-**13,826**	13-50	250-300
	Ho Thu VT	16-**398**	15-20	250-300
	Thuan Hung	19-210	16-120	250-300
Soc Trang	Thanh Thoi Thuan	388-**8,912**	88-**5,669**	250-300
	Tran De	1,772-**13,340**	831-**9,078**	250-300
	Long Phu	167-**10,517**	37-**7,510**	250-300
	Thanh Phu	45-**6,643**	39-**2,796**	250-300
	An Lac Tay	36-**3,820**	36-**1,112**	250-300
	Dai Ngai	111-**6,643**	75-**2,994**	250-300
	Nga Nam	54-**12,344**	65-**8,428**	250-300

Notes: values exceeding the standard are outlined in bold.

Map of frequency of salinity occurrence: as a result of GIS-based spatial interpolation techniques, the frequency of salinity occurrence in all provinces in 2016 was reported more severe than in 2017 (Fig. 3). In the drought of 2016, the study area was severely affected by salinity intrusion. In Hau Giang, saltwater has greatly intruded at some points in Vi Thanh city and the Long My district. Soc Trang, a coastal province, showed high frequency of salinity occurrences at Thanh Thoi Thuan, Tran De, and Long Phu. Can Tho had low salinity frequency although saltwater also occurred in 2016.

In 2017, salinity had generally not affected Can Tho city. Salinity of surface water is characterised by high spatial variability depending on the distance to the sea [14]. A detailed analysis shows that the saltwater intrusion is weaker further inland from the sea where river salinity is lower. The Hau river and its tributaries from the Ke Sach district (Soc Trang) towards the inland were less affected by the salinity compared to other areas. Therefore, it is possible to take raw water in these areas for water supply treatment plants.

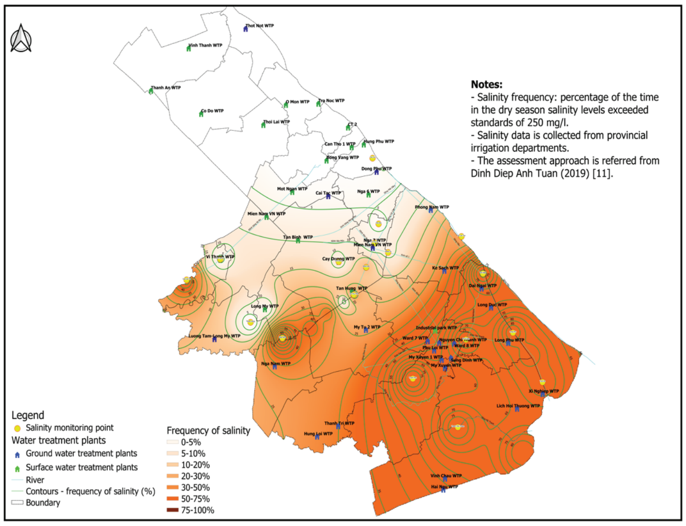

(A) Salinity frequency in 2016 (severe salinity year).

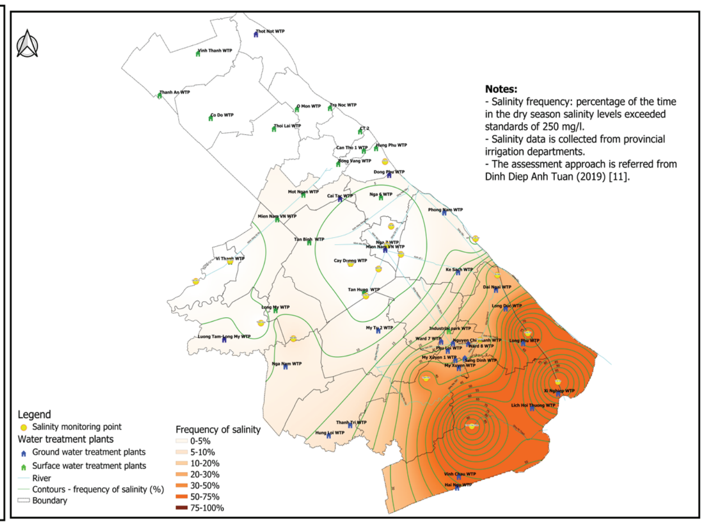

(B) Salinity frequency in 2017 (normal salinity year).

Fig. 3. Severe and normal salinity years in the Can Tho, Hau Giang, and Soc Trang provinces.

Water quality assessment of surface water supply source

Existing surface water supply sources: from the results of selecting areas of low salt frequency, the study then assessed the surface water quality in these areas. A summary of the physical, chemical, and microbiological parameters per province is presented in Table 2.

Table 2. Summary of characteristic of physical, chemical and microbiological of surface water in Can Tho, Hau Giang, and Soc Trang.

Parameters	Can Tho	Hau Giang	Soc Trang	QCVN 08:2015 (level A2)
pH	7.35±0.04	7.11±0.06	6.96±0.13	6.0-8.5
DO (mg/l)	**5.68**±0.16	4.32±0.46	3.11±0.64	5
TSS (mg/l)	**48.70**±6.76	**64.30**±14.98	**95.79**±8.45	30
BOD_5 (mg/l)	**6.01**±0.49	**12.71**±1.46	**8.06**±2.67	6
COD (mg/l)	12.58±1.23	**20.32**±2.35	**27.76**±4.29	15
NH_4-N (mg/l)	0.13±0.02	**0.35**±0.05	**0.82**±0.20	0.3
NO_2-N (mg/l)	0.02±0.004	0.04±0.009	**0.09**±0.03	0.05
NO_3-N (mg/l)	0.86±0.17	0.26±0.04	0.32±0.11	5
PO_4-P (mg/l)	0.07±0.01	**0.22**±0.15	**0.23**±0.009	0.2
Total Fe (mg/l)	0.29±0.04	**2.00**±0.54	**2.25**±0.48	1
Total coliform (MNP/100 ml)	1,982±106	**10,248**±384	**77,548**±1656	5,000

Notes: DO: dissolved oxygen; TSS: total suspended solids; BOD: biochemical oxygen demand; COD: chemical oxygen demand; NH_4-N: ammonium; NO_2-N: nitrite-nitrogen; NO_3-N: nitrate-nitrogen; PO_4-P: phosphate phosphorus; total Fe: total iron. Values exceeding the standard are outlined in bold.

The results in the Table 2 indicated that all provinces had various and different pollutants, but most were generated from TSS, BOD_5, COD, and total coliform. In particular, according to the level A2 standard in QCVN 08:2015/BTNMT, the TSS, DO, and BOD_5 levels at monitoring points in Can Tho city exceeded the standard limit. These results were also similar to the study of V.T.N. Giau, et al. (2019) [15], which indicated that TSS and BOD_5 in Can Tho river were much higher than the standard over the period 2010-2014. In Hau Giang, almost all average pollution parameters were higher than the limit of seriously polluted levels. Pollution from total coliform also reached a seriously polluted level. Both COD and TSS were in the slightly polluted level with the average pollution index exceeding the standard by 150% and 300%, respectively. Similarly, the total coliform, TSS, and BOD_5 were far beyond the standard in Soc Trang. D.D.A. Tuan, et al. (2019) [11] implied that a non-point source, caused by several domestic wastewater and sewage farms, constitutes the major pollution source in the Soc Trang watershed. Consequently, these results may somehow affect water supply intake to surface water treatment plants in all three provinces.

Fig. 4 revealed that the overall frequency of occurrence of water pollutants in Can Tho City was significantly lower than that of the Hau Giang and Soc Trang provinces. On the other hand, both Hau Giang and Soc Trang were in worse situations in terms of the overall frequency. However, the frequency of occurrence of both nitrogen and phosphorus (N and P) in Hau Giang was at the slightly polluted level compared to that of Soc Trang. Excessive anthropogenic N and P input may limit trophic interactions and quality of water sources [16]. The impact of wastewater resources from concentrated populations living along rivers and canals, along with industrial waste, has caused surface water pollution in the region [17].

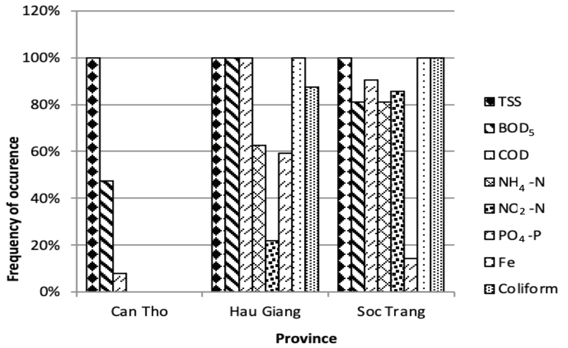

Fig. 4. Frequency of surface water pollutants in Can Tho, Hau Giang, and Soc Trang.

Potential surface water supply sources: as indicated in Fig. 5, the frequency of TSS showed up at almost all the monitoring points in Can Tho city with a substantial level over the given period. The figures of BOD_5 and total coliform experienced high frequencies at monitoring points along the Hau river, especially at the city's core urban districts like Ninh Kieu, Binh Thuy, and Cai Rang, that are shaped by the city's population density and industrial activities. Nevertheless, in general, water sources in Can Tho are still possible for water supply. Conversely, the occurrences of BOD_5, COD, and total coliform pollutants appeared at a high rate in Soc Trang and Hau Giang. Accordingly, to exploit

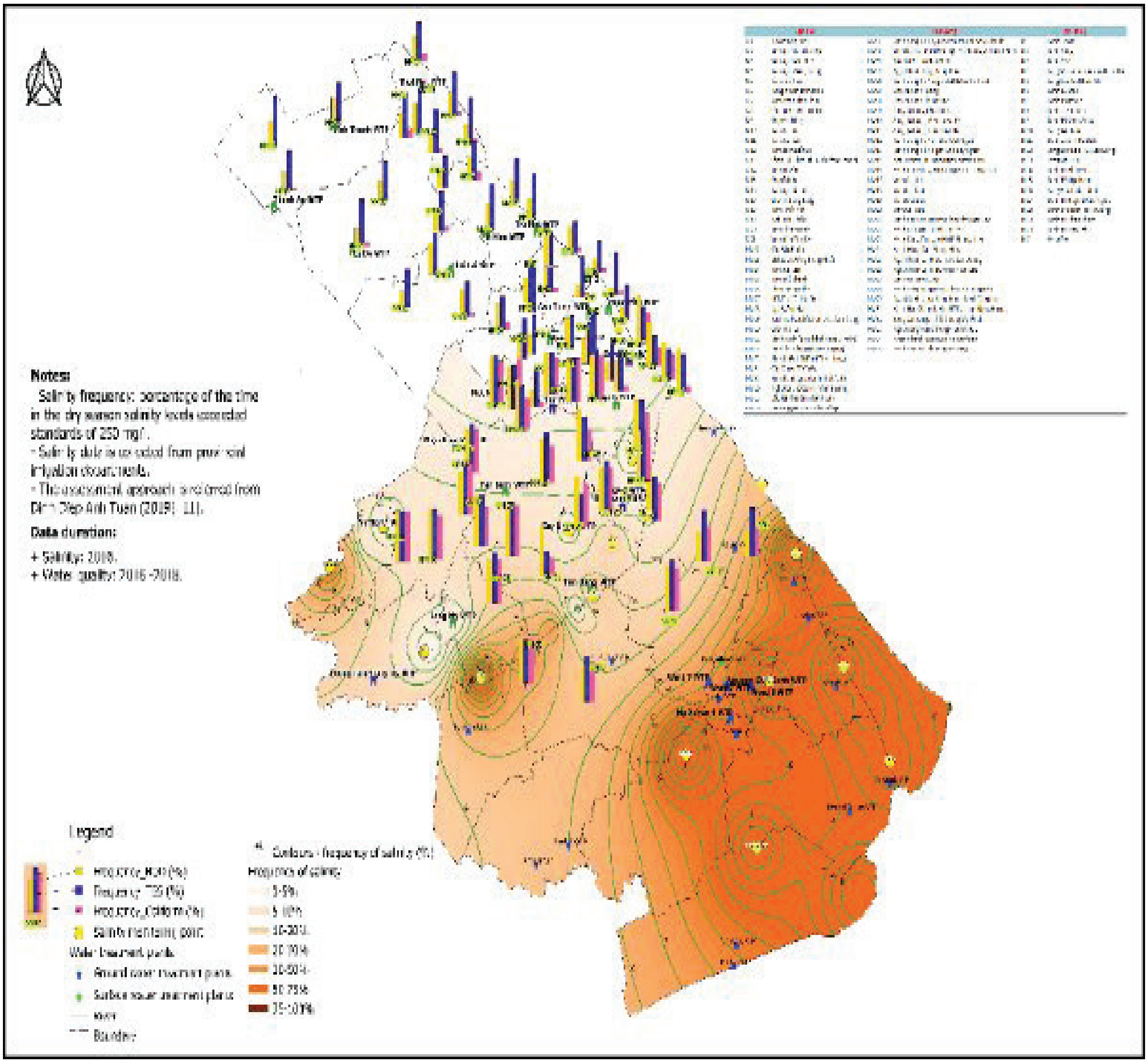

Fig. 5. Frequency of water pollutants and salinity occurrence in Can Tho, Hau Giang, and Soc Trang.

water from these sources, the appropriate preliminary treatment for water supplies must be implemented.

Given the results of surface water quality, the three provinces could exploit water sources from the Hau river and its main tributaries. In detail, surface water sources at sites off the Hau river's mainstream in Can Tho city. In Hau Giang, it is possible for abstracting water for the treatment plants along the Hau river's mainstream, the Mai Dam river, and the Cai Con river. Moreover, the water resources from the Hau river in Ke Sach, and Cai Vop, Cai Tram canal located in Ke Sach, Soc Trang can be considered as a suitable surface water resource for the water treatment plants in Soc Trang as well.

Conclusions

This study used an integrated approach of assessing current salinity to select areas of low saltwater frequency associated with assessing water quality in these areas. This research also applied the IDW technique to interpolate areas of salt influence and generated a GIS-based map to display more robust and informative data.

It is concluded that salinity tends to decline towards inland. Surface water sources in Soc Trang are somehow the worst influenced zone by saltwater intrusion among the three provinces. The Hau river and its tributaries from the Ke Sach district (Soc Trang) towards inland had a lower risk of salinity. This indicated that water sources in Ke Sach could be a possible raw water source for water supply treatment plants in Soc Trang.

The results of this study will contribute to urgently needed decision-making about water quality assessment and the water source selection process in these three provinces. However, further study needs to be implemented to collect the primary data for calibration data.

COMPETING INTERESTS

The authors declare that there is no conflict of interest regarding the publication of this article.

REFERENCES

[1] T. Triet (2016), "Transboundary Mekong river delta (Cambodia and Vietnam)", *The Wetland Book*, pp.1-12, DOI: 10.1007/978-94-007-6173-5_40-1.

[2] T.V. Thang, T.A. Thong, L. Duy (2016), "Water governance for sustainable development: international practices and implications for the Mekong delta region", *Journal of Economic Development*, **24(4)**, pp.99-120, DOI: 10.24311/jed/2017.24.4.6.

[3] D.T. Ha (2014), "Assessing the vulnerability of climate change to rural water supply in the Mekong delta", *Science and Technology Journal of Irrigation and Environment*, **46**, pp.34-40.

[4] R. Jayakumar (2015), "Groundwater level monitoring-importance global groundwater monitoring network", *Journal of Groundwater Science and Engineering*, **3(4)**, pp.295-305.

[5] E.E. Laura, M.G. Steven, A.Z. Howard (2014), "Groundwater extraction, land subsidence and sea-level rise in the Mekong delta, Vietnam", *Environ. Res. Lett.*, **9(8)**, 6pp.

[6] P.S.J. Minderhoud, et al. (2015), "Assessing the potential of the multi-aquifer subsurface of the Mekong delta (Vietnam) for land subsidence due to groundwater extraction", *Proceedings of the International Association of Hydrological Sciences*, **92**, pp.1-4, DOI: 10.5194/piahs-92-1-2015.

[7] R. Chea, G. Grenouillet, S. Lek (2015), "Evidence of water quality degradation in lower Mekong basin revealed by self-organizing map", *PLOS ONE*, **11(1)**, DOI: 10.1371/journal.pone.0145527.

[8] P.G. Youssefa, R.K. AL-Dadaha, S.M. Mahmoud (2014), "Comparative analysis of desalination technologies", *Energy Procedia*, **61**, pp.2604-2607, DOI: 10.1016/j.egypro.2014.12.258.

[9] G. Noreddine, M.M. Thomas, L.A. Gary (2014), "Technical review and evaluation of the economics of water desalination: current and future challenges for better water supply sustainability", *Desalination*, **309**, pp.197-207, DOI: 10.1016/j.desal.2012.10.015.

[10] E. Sepehr, et al. (2019), "Flow division dynamics in the Mekong delta: application of a 1D-2D coupled model", *MDPI*, **11(4)**, 837pp, DOI: https://doi.org/10.3390/w11040837.

[11] D.D.A. Tuan, B.A. Thu, N.H. Trung (2019), "Assessing surface water quality for exploitation and water supply for Soc Trang city", *Can Tho University Journal of Science*, **55(4)**, pp.61-70, DOI: 10.22144/ctu.jvn.2019.096.

[12] J. Li, A.D. Heap (2008), *A Review of Spatial Interpolation Methods for Environmental Scientists*, Geoscience Australia: Record 2008/23, 137pp.

[13] L.S. Sebastian, et al. (2016), *The Drought and Salinity Intrusion in the Mekong River Delta of Vietnam*, Assessment Report, CGIAR Research Centers in Southeast Asia, 51pp.

[14] T.A. Dang, et al. (2019, "Stable isotope characteristics of water resources in the coastal area of the Vietnamese Mekong delta", *Isotopes in Environmental and Health Studies*, **55(6)**, pp.566-587, DOI: 10.1080/10256016.2019.1673746.

[15] V.T.N. Giau, et al. (2019), "Assessment of changes in water quality in Can Tho river in the period of 2010-2014 by calculation of water quality index (WQI)", *Can Tho University Journal of Science*, **55(2)**, pp.105-113.

[16] https://www.frontiersin.org/articles/10.3389/fevo.2017.00070/full.

[17] N.H. Thoi, A.D. Gupta (2001), "Assessment of water resources and salinity intrusion in the Mekong delta", *Water International*, **26(1)**, pp.86-95, DOI: 10.1080/02508060108686889.

DOI: 10.31276/VJSTE.62(4).71-76

The zoning of surface water quality by WQI index in the Tien Giang province, Vietnam

Thi Anh Nguyen[1*], Ngoc Han Bui[2]

[1]*University of Labor and Social Affairs, Ho Chi Minh city, Vietnam*
[2]*Ritsumeikan Asia Pacific University, Japan*

Received 11 August 2020; accepted 10 November 2020

Abstract:

According to Decision No. 711/QD-TCMT of the Ministry of Natural Resources and Environment, the water quality index (WQI) formula has been adjusted toward localisation, particularly, for the Nhue Day and Cau river basins. In this work, the WQI formula was amended by adjusting the weights of the components of surface water quality. This is an advance forward toward enhancing the effectiveness of local environmental management so that local economic development conditions are shaped according to its own potential and in accordance with the natural characteristics and culture of the regions. Based on surface water quality data from 2012 to 2019 in Tien Giang and the theory of fuzzy entropy weighting to identify component weights, this study adjusted the WQI formula in accordance with natural conditions as well as special characteristics of the socio-economic development of Tien Giang. Finally, a zoning map of surface water quality in the province was set up.

Keywords: **Tien Giang province, water quality index, water quality management, zoning water quality, 711/QD-TCMT.**

Classification number: **5.1**

Introduction

Assessment of the surface water quality by an index is widely applied in research in the water sector as well as in environmental management. The water quality index (WQI) formula has many forms based on the researcher(s) and location of the research. For example, it could be the arithmetic mean, average multiplication, or a combination with a weighted or non-weighted set [1]. In Vietnam, the WQI is commonly used and it is considered a good tool for determining water quality [2, 3]. In addition, formula and water quality assessments have been standardised and unified over the whole country through Decision No. 879/QD-TCMT of the General Department of Environment under the Ministry of Natural Resources and Environment.

Table 1. The weight sets of water quality groups and each parameter used in the WQI formula under Decision No. 711/QD-TCMT.

Name of water quality group	Name of water quality parameter	Weight set for group		Weight set for parameter	
		Cau river	*Nhue river*	*Cau river*	*Nhue river*
Group 1 (WQI_a)	TSS	0.30	0.20	0.17	0.12
	Turbidity			0.13	0.08
Group 2 (WQI_b)	DO	0.60	0.65	0.17	0.20
	COD			0.12	0.13
	BOD			0.12	0.12
	$N-NH_4^+$			0.10	0.10
	$P-PO_4^{3-}$			0.09	0.10
Group 3 (WQI_c)	Coliform	0.10	0.15	0.10	0.15

Nowadays, Vietnam has developing economic sections like agriculture, industry, trade service, and tourism that has conformed to the local natural characteristics of all provinces. The common use of the WQI formula is simple but its level of accuracy in a special location is limited. The General Department of Environment recognised and

*Corresponding author: Email: hiyomayopinklove@gmail.com

implemented an initial step with Decision No. 711/QD-TCMT in 2015, which adjusted the weight set of the WQI formula under Decision No. 879/QD-TCMT applied to the specific river basins of the Nhue Day and Cau rivers. Table 1 summarises the weights of the water quality groups and the parameters that were determined to have different importance levels in accordance with natural conditions and key economic sectors in the two river basins.

In this study, the authors used the entropy weighting method combined with fuzzy theory. Particularly, the authors used the combination of entropy weighting with a part of the fuzzy comprehensive evaluation method [2, 4]).

Methods

This research determined the weighted sets of local water quality parameters and groups in the following way:

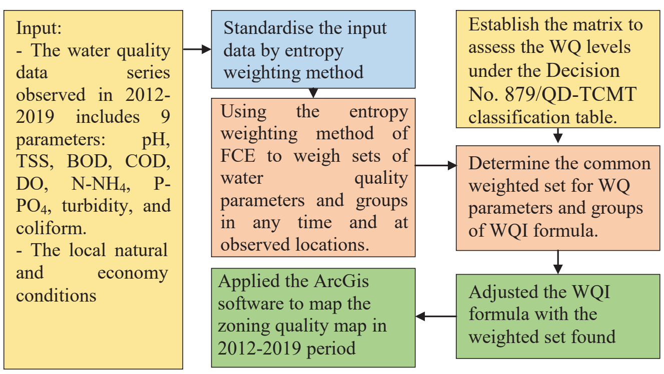

Fig. 1. Flow chart of the research approach.

The current WQI formula for assessing local surface water quality was included in the dataset of the following surface water quality parameters: pH, TSS, turbidity, COD, BOD_5, DO, $N\text{-}NH_4$, $P\text{-}PO_4$, and coliform. Fuzzy theory combined with entropy weighting calculations [3] were used to determine the weighted set of the water quality parameters and groups according to the implementation guidelines of Decision No. 711/QD-TCMT. The determination of the weight set for the formula to assess surface water quality was carried out in the same manner as Fig. 1. In detail:

The first step: standardising the water quality measurement data by entropy.

Prepare the standardised matrix R as follows:

$r_{i,j} = (x_{i,j} - \mathrm{Min}(\Sigma\, x_{i,j}))/(\mathrm{Max}(\Sigma\, x_{i,j}) - \mathrm{Min}(\Sigma\, x_{i,j}))$ for parameters pH and DO (1)

$r_{i,j} = (\mathrm{Max}(\Sigma\, x_{i,j}) - x_{i,j})/(\mathrm{Max}(\Sigma\, x_{i,j}) - \mathrm{Min}(\Sigma\, x_{i,j}))$ for remaining parameters (2)

Determine the value of entropy (H_i):

$$H_i = \frac{1}{lnn}\sum_{j=1}^{n} f_{ij}\ln(ij) \text{ with } f_{i,j} = \frac{r_{ij}}{\sum_{j=1}^{n} r_{ij}}, \quad 0 \le H_i \le 1 \quad (3)$$

$f_{ij} = (1 + r_{ij})/\sum_{j=1}^{n}(1 + r_{ij})$ with $f_{ij} = 0$

Determine the weights of entropy as follows:

$$w_i = (1 - H_i)/(m - \sum_{i=1}^{m} H_i),\ 0 \le w_i \le 1,\ \sum_{i=1}^{m} w_i = 1 \quad (4)$$

The original matrix, X, after standardisation: $x^E_{i,j} = x_{i,j} * (1 - w_i)$ (5)

The second step: applying the surface water quality classification table. Using in the fuzzy comprehensive evaluation [2, 4] for determining the weighted set of the water quality parameters and groups in the WQI formula, the pollution level of water sources were categorised according to five levels. A hierarchy for evaluation factors based on the pollution/water quality classification was developed and is provided in Table 2.

Table 2. Classification of surface water quality [2].

Parameters	Pollution/water quality classification				
	I (No pollution)	*II (Light pollution)*	*III (Medium pollution)*	*IV (Hard pollution)*	*V (Extreme pollution)*
pH	6.5-7.5	6-6.5/7.5-8	5-6/8-9	4.5-5/9-9.5	<4.5/>9.5
% $DO_{Saturated}$	88-112	75-88/112-125	50-75/125-150	20-50/150-200	≤20/≥200
BOD_5	≤4	6	15	25	≥50
$N\text{-}NH_4$	≤0.1	0.2	0.5	1	≥5
$P\text{-}PO_4$	≤0.1	0.2	0.3	0.5	≥6
TSS	≤20	30	50	100	>100
COD	≤10	15	30	50	>80
Coliform	≤2500	5000	7500	10000	>10000
Turbidity	≤5	20	30	70	≥100

The standardised matrix, X, was used to determine the contribution level of the parameters and groups to the CLN from the water quality according to the classification Table 2. Each level of water quality (pollution level) had a series of different contribution levels (weighted sets).

The sequence of the parameters' weighted sets for each year as a weighted set for the new WQI formula according to the conditions was determined. Namely, (1) the standard deviation of the sequence of contributions on a pollution step is minimal; (2) the standard deviation of the series of contributions on a pollution step is average; (3) the standard deviation of the series of contributions on a pollution step is the largest [5, 6]. In general, it is common to choose condition (1) because the size of the actual measured dataset is large and the weighted set of the water quality parameters and groups quickly converge.

Based on the WQI formula of Decision No. 879/QD-TCMT, the new WQI formula is to be adjusted to the form [6, 7]:

$$WQI = \frac{WQI_{pH}}{100}\left(WQI_a^{ra} \times WQI_b^{rb} \times WQI_c^{rc}\right) \quad (6)$$

where:

$WQI_a = h_1\, WQI_{DO} + h_2\, WQI_{BOD_5} + h_3\, WQI_{COD} + h_4\, WQI_{N\text{-}NH_4} + h_5\, WQI_{P\text{-}PO_4}$

$WQI_b = ly_1\, WQI_{TSS} + ly_2\, WQI_{turbidity}$

$WQI_c = s\, WQI_{coliform}$

r_a, r_b, r_c are the weights of groups with $r_a + r_b + r_c = 1$

h_1-h_5; ly_1, ly_2, and s are the parameters' weights with $h_1+h_2+h_3+h_4+h_5=1$; $ly_1+ly_2=1$; $s=1$.

The third step: applying ArcGis software to map water quality zoning of the Tien Giang province of Vietnam over the period 2012-2019.

Therefore, we proposed to adjust the weighted sets of quality parameters and groups in the WQI formula under the guidance of Decision No. 711/QD-TCMT, which was only applied to the assessment of surface water quality in Tien Giang province. Based on the new WQI formula, the map of surface water quality zoning in the Tien Giang province over the 2012-2019 period was created to serve the Tien Giang Provincial Department of Natural Resources and Environment in the management of surface water quality. The results are given below.

Results and discussion

The Tien Giang province is at the end of the Tien river in the Mekong delta. This is a province with similar natural characteristics governed by both the hydrological regime of the Mekong river system and the seashore current. The Tien Giang province is also an agricultural province in the Mekong delta that is predominant in rice cultivation. Therefore, the WQI formula must be suitable to the natural and economic development conditions in the Tien Giang province.

The water quality measurement data set was used for the determination of weighted sets from 2012 to 2019 at the observation locations presented in Fig. 2. The quality datasets were collected including 9 water quality parameters including pH, BOD_5, COD, DO, $N\text{-}NH_4$, $P\text{-}PO_4$, TSS, turbidity, and coliform (Table 3).

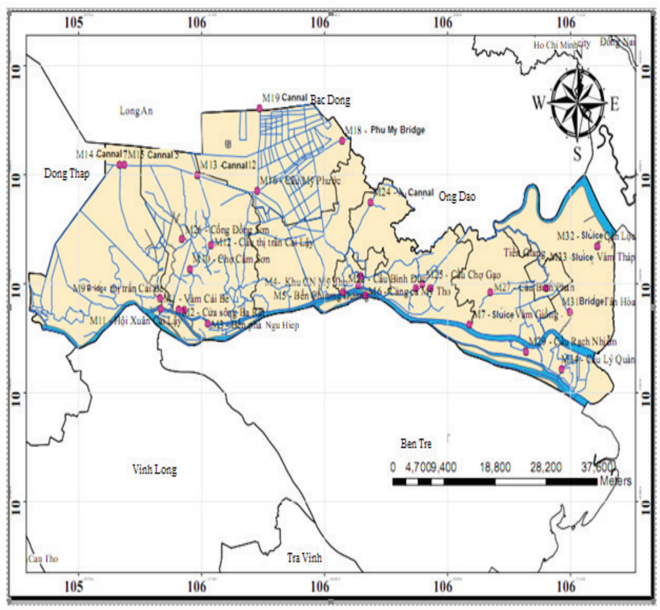

Fig. 2. Administration and observation locations map of Tien Giang.

Source: Department of Natural Resource and Environment of Tien Giang province, 2019.

Table 3. The observation database of water quality (Example on March 2018).

Location - name	°C	pH	DO	TSS	COD	BOD_5	$N\text{-}NH_4^+$	$P\text{-}PO_4^{3-}$	Coliform	Turb
			mg/l	*mg/l*	*mg/l*	*mg/l*	*mg/l*	*mg/l*	*MPN/100 ml*	*NTU*
M1 - Vam Cai Be	28.90	7.30	4.90	3.00	0.00	25.0	0.00	0.00	250	7.10
M2 - Ba Rai river mouth	28.40	6.86	4.22	13.0	5.00	22.0	0.00	0.00	350	6.30
M3 - Ngu Hiep ferry	28.00	6.80	4.25	17.0	7.00	26.0	0.00	0.00	400	7.40
M4 - My Tho industrial zone	29.20	7.07	3.90	9.00	3.00	36.00	0.02	1.24	110	10.3
M5 -Chuong Duong ferry	29.50	7.17	4.26	8.00	3.00	46.00	0.02	0.05	130	13.1
M6 - My Tho fish port	29.50	7.10	4.15	3.00	0.03	44.00	0.02	0.07	170	12.6

Source: Department of Natural Resource and Environment of Tien Giang province, 2019.

Using Eq. 1 through Eq. 5 with input from observed data of water quality in the Tien Giang province from 2012-2019, the final results of the first step is listed in Table 4.

Table 4. The weighted contribution of quality parameters in the determination of water quality level at M1 (observation location) in March 2018.

Parameters		The weighted contribution in each quality level (%)				
Name	*Values*	*1*	*2*	*3*	*4*	*5*
pH	7.23	0.268	0.731	0	0	0
% $DO_{satur.}$	63.92	0	0	0.443	0.556	0
COD	0.03	1	0	0	0	0
BOD_5	24.77	0	0	0.976	0.023	0
TSS	2.97	1	0	0	0	0
$N\text{-}NH_4$	0.02	1	0	0	0	0
$P\text{-}PO_4$	0.03	1	0	0	0	0
Coliform	247.66	1	0	0	0	0
Turbidity	7.08	0.138	0.861	0	0	0

The general weighted sets of the quality groups and parameters used in the new WQI formula were applied to the Tien Giang province and the results are given in Table 4. The final values of the weighted sets, as well as their convergence level, are listed in Tables 5-7 and shown in Figs. 3 and 4.

Table 5. The weighted set of organic quality parameters.

Name	General contribution at each quality level (%)					Weighted set of parameters at each quality level					General values
	1	*2*	*3*	*4*	*5*	*1*	*2*	*3*	*4*	*5*	
% $DO_{Satur.}$	0.00	0.03	0.20	0.34	0.38	0.00	0.07	0.29	0.50	0.52	0.07
COD	0.12	0.12	0.14	0.07	0.04	0.25	0.27	0.20	0.10	0.06	0.27
BOD_5	0.06	0.13	0.20	0.14	0.15	0.12	0.29	0.29	0.20	0.20	0.29
$N\text{-}NH_4$	0.12	0.08	0.11	0.11	0.13	0.25	0.18	0.15	0.15	0.17	0.18
$P\text{-}PO_4$	0.18	0.09	0.04	0.03	0.03	0.37	0.20	0.06	0.05	0.05	0.20

Table 6. The weighted set of physical quality parameters.

Name	General contribution at each quality level (%)					Weighted set of parameters at each quality level					General values
	1	*2*	*3*	*4*	*5*	*1*	*2*	*3*	*4*	*5*	
TSS	0.14	0.12	0.09	0.07	0.05	0.61	0.45	0.49	0.29	0.29	0.49
Turbidity	0.09	0.14	0.10	0.17	0.12	0.39	0.55	0.51	0.71	0.71	0.51

Table 7. The weighted set of quality groups.

Name	Weighted set of groups at each quality level					General values
	1	*2*	*3*	*4*	*5*	
Organic	0.53	0.60	0.77	0.73	0.75	0.53
Physics	0.25	0.35	0.21	0.25	0.17	0.25
Biology	0.22	0.05	0.03	0.02	0.07	0.22

The set of weights in Tables 5-7 did not change much when the number of calculation years was over 5 y. The magnitude of the fluctuation in weight value of the quality parameters and groups are summarised as shown in Figs. 3 and 4.

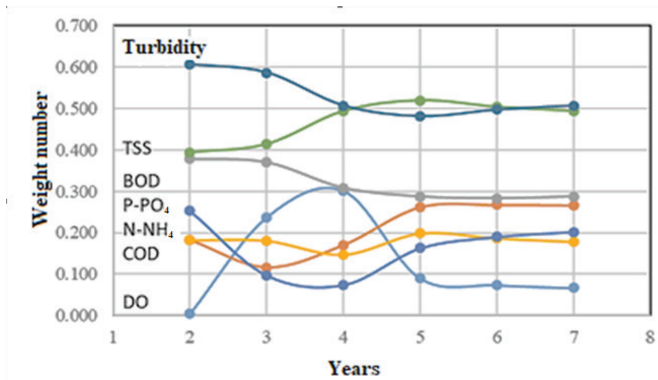

Fig. 3. The magnitude of fluctuation in weight value of quality parameters.

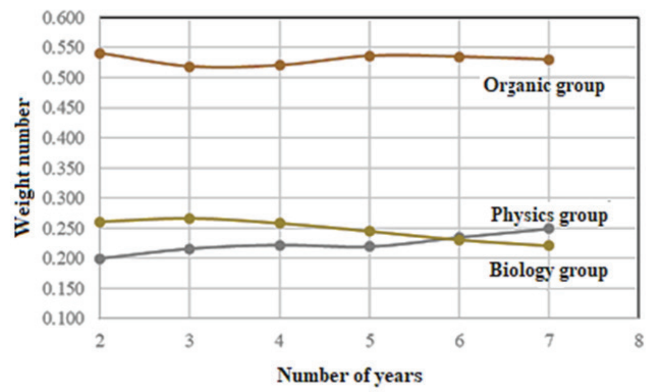

Fig. 4. The magnitude of fluctuation in weight value of quality groups.

Finally, the new WQI formula under Decision No. 711/QD-TCMT guidelines was applied to assess the water quality in Tien Giang province, which is given i Eq. 7.

$$WQI = \frac{WQI_{pH}}{100}\left[(0.07WQI_{DO} + 0.27WQI_{COD} + 0.29WQI_{BOD} + 0.18WQI_{N-NH_4} + 0.20WQI_{P-PO_4})^{0.53}(0.49WQI_{TSS} + 0.51WQI_{DD})^{0.25}WQI_{colif}^{0.22}\right] \quad (7)$$

Eq. 7 showed that the organic group leads and decides the water quality level in Tien Giang due to its highest weight (0.53). This is reasonable because the production structure is inclined toward the discharge of organic substances as agriculture, aquaculture, and urban areas are expended.

Eq. 7 is considered to reflect the development of the local economy as well as express local economic characteristics because the weighted set of water quality parameters determined from the water quality data was observed for a long time [6].

Nowadays, the Mekong river's flow has been reduced due to increasing upstream water use. The evidence for this is expressed by the decreasing flood peak level over time (Fig. 5). This leads to the decline of river and canal waters.

This is one of many reasons pollution is occurring in the inland canal system of Tien Giang.

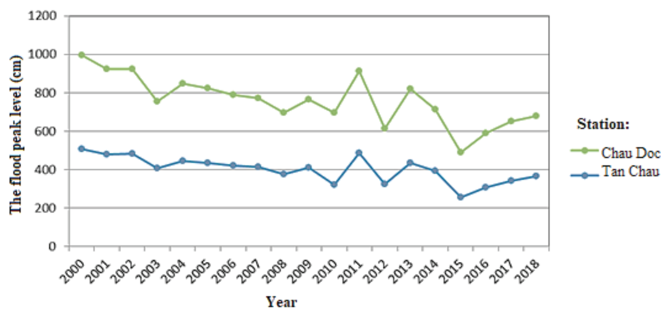

Fig. 5. The flood peak level lines at Tan Chau and Chau Doc upstream stations.

With the new WQI formula, the distribution of water quality in the river and canal system of Tien Giang was mapped from 2012-2019 by ArcGis and is shown in Figs. 6-8.

The water quality level of the river system in Tien Giang depends a lot on upstream flood conditions. A year with medium-to-large upstream floods flowing into Tien Giang comes along with improved water quality in the river system. The areas with low water quality are normally urban locations, agricultural locations, and adjacencies to Ho Chi Minh city (HCMC). The general assessment of water quality over the 2012-2019 period is good water quality in the river system of Tien Giang, except for some areas adjacent to HCMC with a medium pollution level. These areas are industrial parks that support HCMC.

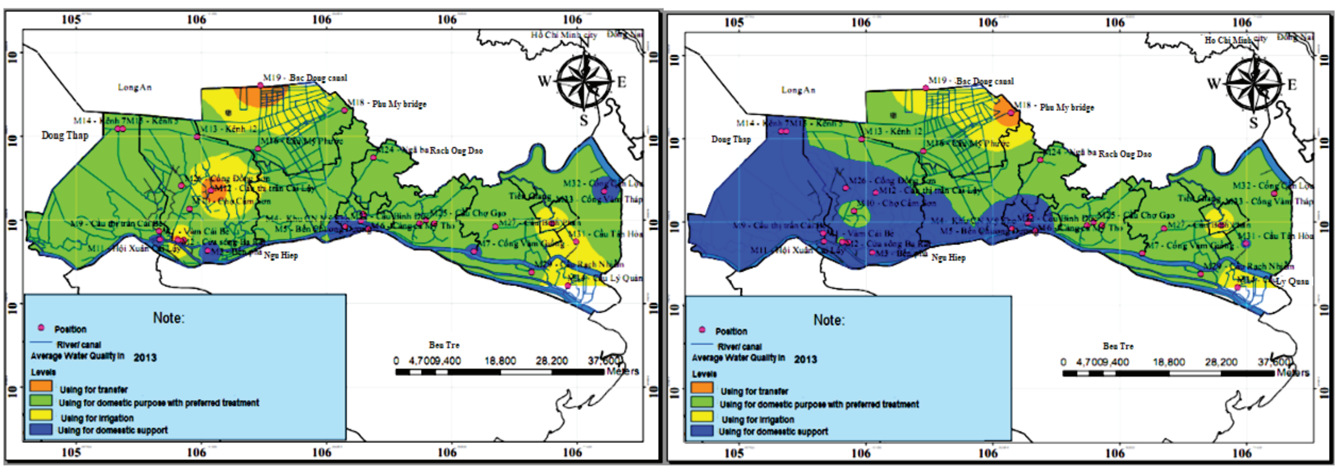

Fig. 6. The water quality distribution for years 2013-2014 with medium flood situation.

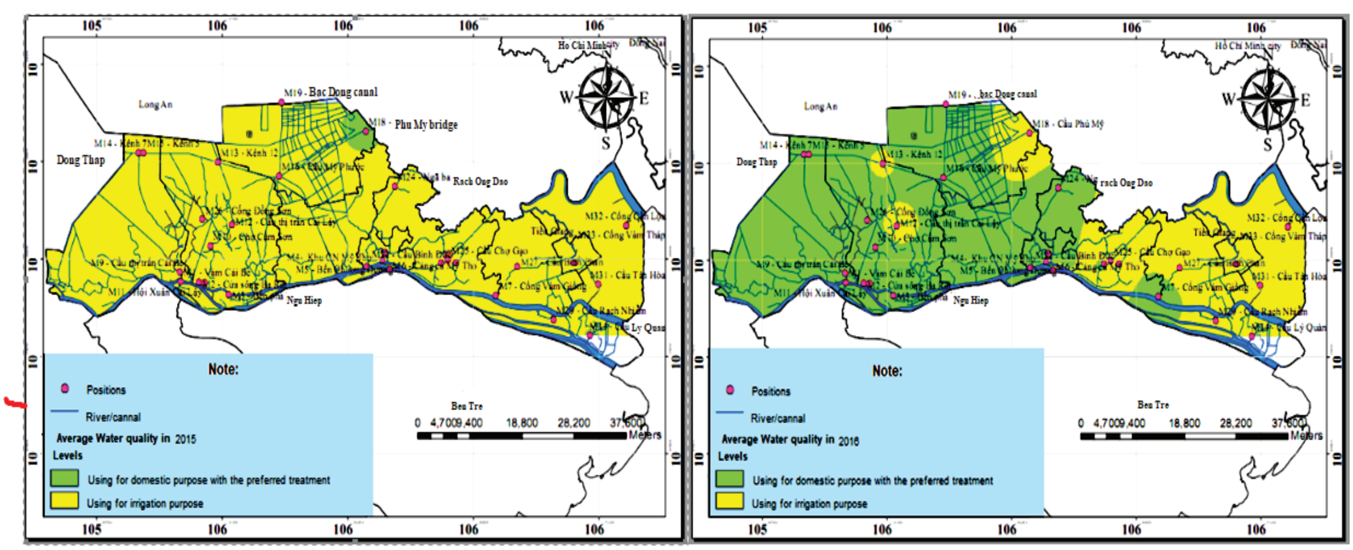

Fig. 7. The water quality distribution for years 2015-2016 with small flood situation.

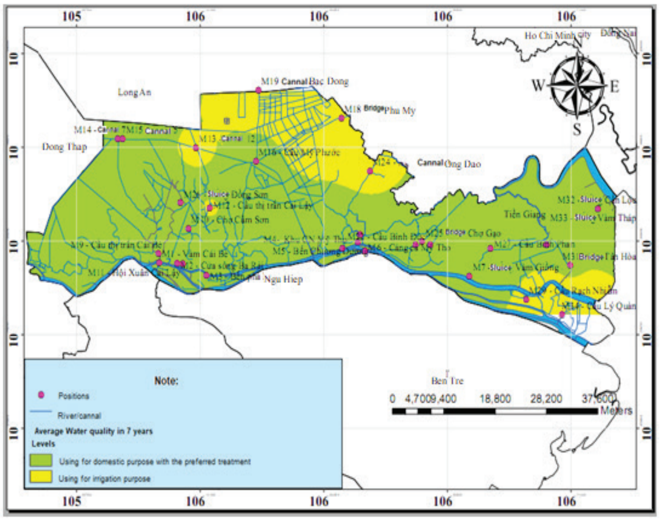

Fig. 8. The water quality distribution from 2012-2019 in Tien Giang.

Conclusions

The results of the surface water quality assessment according to the adjusted formula initially show conformity of the natural conditions and local economic development. However, it is also necessary to emphasise that the weight set of the water quality parameters and groups should be continuously recalculated to give the final formula by extending the number of years of the actual data series.

COMPETING INTERESTS

The authors declare that there is no conflict of interest regarding the publication of this article.

REFERENCES

[1] P.T.M. Hanh (2010), "Development of water quality indices for surface water quality evaluation in Vietnam", *Journal of Environmental Engineering*, **137(4)**, DOI: 10.1061/(ASCE)EE.1943-7870.0000314.

[2] L.D. Che (2013), "Applying the 'fuzzy' comprehensive evaluation method in the model of water quality assessment of Saigon river flowing through Binh Duong province", *Jounal of Environment*, **6**, pp.30-42.

[3] Y. Geng, et al. (2011), "Fuzzy synthetic evaluation of weight water quality", *Environmental Engineering and Management Journal*, **10(10)**, pp.1477-1484.

[4] A. Lermontov, et al. (2009), "River quality analysis using fuzzy water quality index: Ribeira do Iguape river watershed, Brazil", *Ecological Indicators*, **9(6)**, pp.1188-1197.

[5] T.M.U. Nhi (2018), *Assessment the Surface Water Quality on the Main Canals in Vinh Long City*, University of Science - VNU of Ho Chi Minh city.

[6] B.V. Hung (2017), "Application of fuzzy comprehensive evaluation for surface water quality assessment", *The Science and Technology Results Collection 2016*, Southern Institute of Water Resource Research, **12**, pp.92-101.

[7] B.V. Hung, T.M.U. Nhi (2018), "Adjustment of the formula to assess the local surface water quality", *Journal of Agriculture and Development*, **5**, pp.102-113.

Evaluating the impacts of climate change on the hydrology and water resource availability in the 3S river basin of Cambodia, Laos, and Vietnam

Nguyen Thi Thuy Trang[1*], Sangam Shrestha[2], Hiroshi Ishidaira[3], Pham Thi Thao Nhi [1, 4]

[1]*Faculty of Environment, University of Science, Vietnam National University, Ho Chi Minh city, Vietnam*
[2]*Water Engineering and Management, School of Engineering and Technology, Asian Institute of Technology, Thailand*
[3]*Interdisciplinary Centre for River Basin Environment, Graduate Faculty of Interdisciplinary Research, University of Yamanashi, Japan*
[4]*Institute for Computational Science and Technology (ICST), Ho Chi Minh city, Vietnam*

Received 12 August 2020; accepted 10 November 2020

Abstract:

The goal of this study is to examine the responses of hydrology and water resource availability to future climate change in the 3S (Sekong, Sesan, and Srepok) river basin located in the tropical countries of Laos, Vietnam, and Cambodia. The calibrated the Soil and Water Assessment Tool (SWAT) model was used to investigate changes to the hydrological regime and water resources under various climate change scenarios. The climate change scenarios were designed based on an ensemble of 5 GCM simulations (HadGEM2-AO, CanESM2, ISPL-CM5A-LR, CNRM-CM5, and MPI-ESM-MR) for medium emission (RCP4.5) and high emission (RCP8.5) scenarios. The climate of the basin was prognosticated to be warmer and wetter with increased temperature and precipitation in the future. Future climate change causes an increase in stream flow from 29.0 to 45.0%, 2.0 to 8.3%, and 1.2 to 10.6% for the Srepok, Sekong, and Sesan rivers, respectively. Although the discharge is projected to increase in the future, the per capita water availability is projected to decrease to 48.5, 55.1, and 80.2% in the 2090s compared to 2010 for the Srepok, Sekong, and Sesan rivers, respectively, due to population growth. The Sekong and Srepok basins will experience the most serious decline in trend and absolute value of water availability, respectively. The results of this study will be helpful to water resource development, planning, and management under climate change scenarios in the 3S river basin (3SRB).

Keywords: **climate change, SWAT model, transboundary river basin, water resources, 3S (Sekong, Sesan, Srepok) river basin.**

Classification number: **5.1**

Introduction

As emphasised in the IPCC Fifth Assessment Report (AR5), climate change is occurring across nearly all the regions of the world [1]. Climate change can considerably affect the regional hydrology and water resources through changes in hydrological processes, especially in evapotranspiration, soil water, and surface runoff. Furthermore, climate change may include an increased frequency and magnitude of hydro-meteorological extremes, namely droughts and floods [2]. Such hydrological changes will lead to the redistribution of water resources that impact water supply, hydropower, and irrigation on multiple scales. Therefore, discovering ways that water resource systems can be impacted and their respond to climate change scenarios has been the research topic of interest of the IPCC and many other international organizations and research institutions.

Many studies have been conducted to evaluate climate change impacts on regional hydrology and water resources [3-7]. In these studies, the modelling approach is preferred because it is the most suitable for hydrology simulation. The hydrological model is first calibrated against the observed data and then run with future climate scenarios using calibrated hydrological parameters. There are numerous hydrological models that have been developed such as HEC-HMS (Hydrologic Engineering Center - Hydrologic Modelling System), HSPF (Hydrological Simulation Program - FORTRAN), the NAM (Nedbor-Afstromings Model) rainfall and runoff model, and SWAT (Soil and Water Assessment Tool). Among these models, SWAT has been proven to be effective for simulating hydrology in several types of watersheds with various agro-climate conditions around the world (see SWAT database: https://www.card.iastate.edu/ swat_articles/). However, the climate change impact on hydrology and water resources are spatially different depending on the geographic location of the study area. For this reason, it is necessary to quantify the hydrological impact of climate change in specific basins.

*Corresponding author: Email: ngtttrang@hcmus.edu.vn

The Sesan, Sekong, and Srepok rivers form the transboundary 3SRB in the Mekong river, which is shared by three tropical countries namely Cambodia (33%), Laos PDR (29%), and Vietnam (38%), which contribute between 16 and 26% of the Mekong's total annual flow [8]. The 3SRB plays an important role in economic growth and ecosystem services. The biggest paddy field in the Vietnamese Mekong delta is located downstream of the 3SRB, which means that the outflow from the outlet of the 3SRB will impact the water use in the Mekong delta for irrigation or rice growth. This will undoubtedly affect national food security and the export industry. In recent years, the continuous trend of population increases, urbanisation, and industrial development in the upstream of the Sesan and Srepok basins has caused a higher water demand for multiple purposes such as the domestic, agricultural, industrial, and fishery as well as environmental [8-10]. Moreover, as more hydropower dams are constructed in the basin, the streamflow regime and water availability downstream will change accordingly. There is also a problem with the three countries in the trans-boundary basin sharing water benefits and responsibility for water pollution.

Additionally, the 3SRB has been identified as one of the three most vulnerable areas impacted by climate change in the lower Mekong basin [11]. There could be an increase of 3 to 5°C in annual temperature and a 35 to 365 mm increase in annual rainfall, which may result in sudden changes to the habitat of certain livestock, aquatic life, and crops. In economic development and climate change scenarios, the water resource management task becomes more challenging, especially in the transboundary basin, which is associated with the issue of sharing benefits and responsibility. Therefore, a reliable and comprehensive assessment of changes in hydrological characteristics and water resources for the whole basin and each sub-basin under the future climate change perspectives is important for supporting decision-makers and managers in sustainable water resource management and planning. There have been some studies conducted on the 3S basin considering the fish assemblage dynamics affected by a dam [12], the change of riverine nitrate in the periods of 2005-2008 [13], sediment trapped in reservoir alternating by the flow and hydropower regime management [14], and the hydropower production and impact by the seven large proposed dams on water flows [15]. The projection of 3S river discharge change under the impact of future climate has been done using SWAT model by various researches [6, 16-18]. These studies assessed and analysed the change of streamflow for the whole 3S basin but did not consider an analysis of each of the three sub-basins. Meanwhile, each basin has its own socio-economic characteristics that required unique management measures and policies. Therefore, to ensure the demand of each sub-basin, but also to not compromise the development of others, we decided to conduct a study on streamflow change and water availability across the whole 3S basin considering the assessment from each sub-basin.

The main goal of this study is to investigate changes in the hydrology and water resource availability over the whole 3SRB and each sub-basin under various climate change scenarios to support managers in obtaining further wisdom into climate change impacts on water resources and adaptation.

Materials and methods

Study area description (Fig. 1)

Located in the south eastern part of the Mekong basin, the 3SRB comprises an area of 78529 km^2 accounting for 10% of the Mekong basin and contributing to 16-26% of the Mekong's river total flow [8]. The Sekong river originates in the

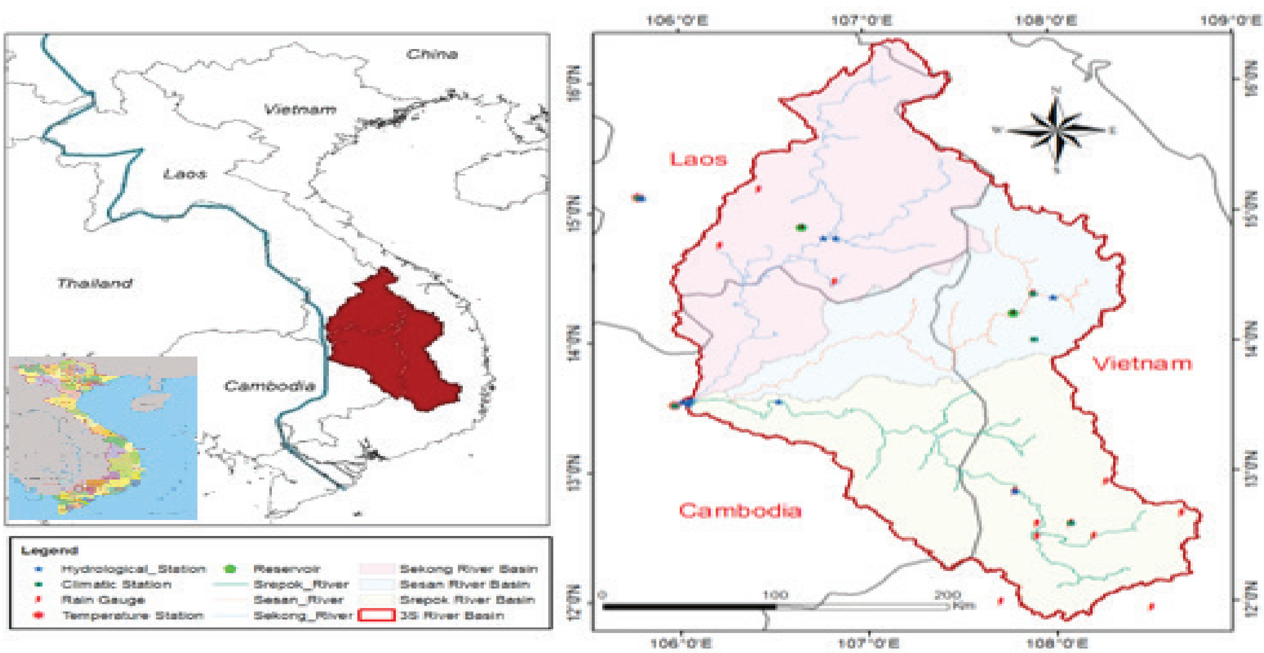

Fig. 1. The locations of 3SRB and hydro-meteorological stations.

Annamite Range in Laos PDR, while the Sesan and Srepok rivers originate in the Central Highlands of Vietnam. The elevation of this region ranges from 80 to 2040 m and runs from south to north and east to west. The area of the basin in Cambodia is flatter than those located in Laos and Vietnam. In the 3SRB, the climate is divided into two distinct seasons of wet (May to October) and dry (November to April). The annual precipitation and temperature over the basin, recorded in the period 1981-2008, were 2080 mm and 22-23°C, respectively. The heavier rainfall intensities occurred in the Highlands of Laos PDR and Vietnam. The annual discharge generated from the whole basin was observed at 2970 m^3/s from 1999 to 2008.

Hydrological simulation

Data requirements and model setup for hydrological simulation: the SWAT model is a semi-distributed, time-continuous, and process-based hydrological model that is widely used for investigating the impacts of climate change on hydrology and water resources at the regional scale, especially southeast Asia [19]. In this work, the authors used SWAT version 2012 that was integrated into an ArcGIS 10.3 interface.

SWAT requires spatial and temporal data as shown in Table 1 to simulate the hydrological processes of the 3SRB. The spatial data, which includes the topography, soil properties, and land use/land cover, were collected from the Mekong River Commission (MRC). Daily discharge data over the period 1994-2008 at nine hydrological stations, the operation data of two reservoirs, and meteorological data over the period 1981-2008 that includes precipitation, temperature, relative humidity, wind speed, and solar radiation were obtained from the MRC and Vietnam's National Hydro-Meteorological Service (NHMF) (see Fig. 1). In addition, population data was collected from the MRC.

Table 1. Required input data for the hydrological simulation in the 3SRB.

Data type	Spatial resolution	Temporal coverage	Sources
Soil map	250x250 m	-	
Land use map	250x250 m	2003	
Digital elevation model (DEM)	250x 50 m	-	MRC
Population	-	2007, 2030, 2060, 2090	
Weather data (precipitation, max and min temperature, relative humidity, solar radiation, and wind speed)		1981-2008	NHMF
Streamflow	-	1994-2008	NHMF
Reservoir	-	1999-2008	MRC

The 3SRB was separated into several sub-basins using the DEM to present the topological characteristics. The DEM at a spatial resolution of 250x250 m provided by the MRC was used in the study. The Hydrologic Response Unit (HRU) represents the smallest geographical area for processing the transport of flow and substances [20], which was generated by the land use/land cover, soil, and slope maps of 250x250 m resolution (Fig. 2). As a result, 133 sub-basins and 1011 HRU determined by the Arc SWAT model represent homogeneity and heterogeneity, respectively.

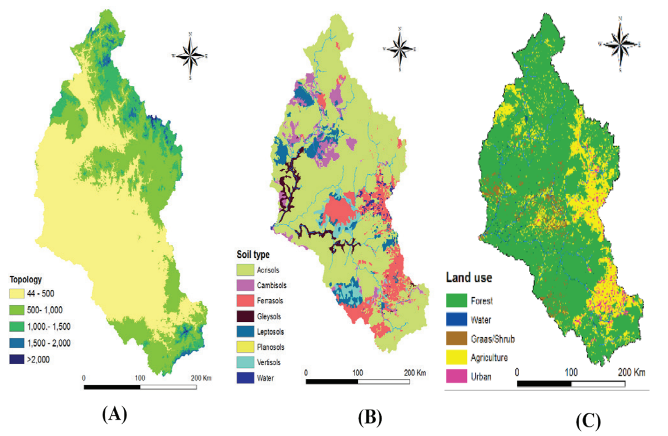

Fig. 2. (A) Topology characteristic, (B) Soil type, and (C) Land use maps of the 3S basin [18].

Calibration, validation, and sensitivity analysis: the daily flow data was observed over nine stations between 1994 and 2008. Since the observation periods of streamflow at eight of the stations were not well distributed across the basin, the calibration and validation of the data may not be conducted at the same station. The flow calibration was processed not only at the basin outlet station, but also the 5 stations that distribute to the 3 sub-basins of Sekong, Sesan, and Srepok. The SWAT-CUP was used to calibrate streamflow for the period between 2005 and 2008 and was validated over 3 time periods: 1994-1999, 2001-2005, and 2006-2008. The calibration and validation periods are presented in Table 2. The SWAT-CUP model built by the "Neprash Corporation and Texas A&M University" was employed to calibrate the model due to its high efficiency and popularity [21] in large-scale watersheds [16] while still considering the uncertainty of input data. There are four procedures of calibration, validation, and uncertainty analysis that are integrated in SWAT-CUP.

There are many parameters related to flow simulation, each with different magnitudes of effect on runoff calculations. Significant changes to non-sensitive factors do not result in a pronounced change in hydrology. Additionally, the calibration of all parameters is very time consuming but it does not generate a remarkably better model for simulation purposes. Therefore, sensitivity analysis was first performed in the SWAT-CUP (SUFI2) to ascertain the parameters that strongly affect the hydrological simulation. The parameter values were determined by sensitivity analysis simulation.

Sensitivity analysis was conducted to determine the influence a set of parameters has on predicting streamflow. Sensitivity was approximated using the relative sensitivity (S):

$$S = \left(\frac{p}{y}\right)\left(\frac{y_2 - y_1}{p_2 - p_1}\right)$$

where p is the particular parameter and y is the simulated value, p_1, p_2 and y_1, y_2 correspond to ±10% of the initial parameter and corresponding simulated flows, respectively [22]. The greater the S value, the more sensitive the simulated flow was to that particular parameter.

The Nash-Sutcliffe efficiency coefficient (NSE), percentage bias (PBIAS), and correlation coefficient (R^2) [18, 19, 21] was applied to examine the model's performance. In general, simulation results can be accepted with NSE ≥0.5.

The R^2 parameter (i.e. correlation coefficient) considers the pattern of the observed and simulated data. Therefore, a high R^2 value may be obtained despite any underestimates or overestimates of the model. The correlation coefficient (R^2) considers the model's ability to explain the dispersion showing in the observed data. Therefore, only the pattern of observed and simulated data is concerned. Thus, underestimation or overestimation of the model in maintaining the hydrograph's pattern will still result in good R^2.

The NSE is used to determine the relative magnitude of the residual variance ("noise") compared to the measured data variance ("importance"). PBIAS measures the consistency of the observed and simulated value. PBIAS measures the average tendency of the model's predicted values to be larger or smaller than their corresponding measured values. The optimal value of PBIAS is 0.0 and low magnitude values indicate accurate model simulations. Positive or negative values indicate model underestimation or overestimation bias, respectively [23].

$$R^2 = \frac{\sum_{k=1}^{m}\left(\left(X_k - \bar{X}\right)\times\left(Y_k - \bar{Y}\right)\right)}{\sqrt{\left(\sum_{k=1}^{m}\left(X_k - \bar{X}\right)^2 \times \sum_{k=1}^{m}\left(Y_k - \bar{Y}\right)^2\right)}} \quad (1)$$

$$E_{NS} = 1 - \left|\frac{\sum_{k=1}^{m}\left(X_k - Y_k\right)^2}{\sum_{k=1}^{m}\left(X_k - \bar{X}\right)}\right| \quad (2)$$

$$PBIAS = \frac{\sum_{k=1}^{m}\left(X_k - Y_k\right)}{\sum_{k=1}^{m}\left(X_k\right)} \times 100 \quad (3)$$

where X_k is observed data at time i, $\bar{X}$ is average value of observed data, Y_k is simulated data at time i, $\bar{Y}$ is average value of simulated data, and m is number of data points.

Table 2. Selected stations and time periods used for streamflow calibration and validation in 3 sub-basins.

Sub-basin	Station	Calibration	Validation
Sekong	Chantangoy, Attopeu, Ban Veunkhene	2000-2005	1994-1999/2001-2005
Sesan	Ban Kamphun, Kontum	2000-2005	1994-1999
Srepok	Lumphat, Ban Don	2000-2005	2006-2008/1994-1999
3S	Outlet	2000-2005	2006-2008

Climate change scenarios

The perturbation method was applied to correct the discrepancy between the measured and ensembles of data for 5 GCM simulations (HadGEN2-AO, CanESM2, ISPL-CM5A-LR, CNRM-CM5, and MP-ESM-MR) (Table 3). Perturbation facilitates the production of huge reasonable climate scenarios in a number of GCMs quickly leading to the popularity of its use in numerous hydrological studies [22-25]. The principles generate a future climate dataset to specify the factors and difference between the observed and simulated value in the GCM variables. Consequently, different factors will be assigned to the regional historical data such as daily precipitation and maximum and minimum temperatures to generate the future data set. The basic assumptions of the perturbation method are: (1) the baseline and simulated periods have same GCM biases; and (2) the similar values of temporal change (daily to inter-annual) for the observed climate variables are applied to both the baseline and projected periods.

$$\text{Temperature: } CF_m = T'^{GCMfut}_m - T'^{GCMref}_m, \quad T'^{fut}_{k,m} = T^{obs}_{m,k} + CF_m \quad (4)$$

$$\text{Precipitation: } CF_k = \frac{P'^{GCMfut}_k}{P'^{GCMref}_k}, \quad P'^{fut}_{k,m} = P^{obs}_{m,k} * CF_m \quad (5)$$

where CF_m is the monthly mean change factor at month *m;* T'^{GCMfut}_m and T'^{GCMref}_m are the GCM-simulated temperature for the future period and the reference period, respectively, at month *m*; $T'^{fut}_{m,k}$ and $T^{obs}_{k,m}$ are the future and observed temperature, respectively, at day *k* and month *m*; P'^{GCMfut}_m and P'^{GCMref}_m are the GCM-simulated precipitation for future and reference period, respectively, at month *m*; $P'^{fut}_{k,m}$ and $P^{obs}_{k,m}$ are the future and observed precipitation, respectively, at day *k* and month *m*.

Table 3. 5 GCMs used in this study.

Model name	Scenarios	Resolution (long. x lat.)	Institution	Country used GCMs
CanES2	RCP4.5 RCP8.5	2.8°x2.8°	Canadian Centre for Climate Modelling and Analysis, Canada (http://www.cccma.ec.gc.ca/data/cgcm4/CanESM2/index.shtml)	Malaysia
CNRM-CM5	RCP4.5 RCP8.5	1.4°x1.4°	Centre national de Recherches Meteorologiques, France (http://www.cnrm-game-meteo.fr/?lang=fr)	Vietnam
HadGEM2-AO	RCP2.6 RCP4.5 RCP6.0 RCP8.5	1.9°x1.25°	Hadley Centre, UKMO (http://www.metoffice.gov.uk)	South Korea
IPSL-CM5A-LR	RCP2.6 RCP4.5 RCP6.0 RCP8.5	3.75°x1.9°	Institute Pierre-Simon Laplace, France (https://www.ipsl.fr/en/)	Malaysia
MPI-ESM-MR	RCP2.6 RCP4.5 RCP8.5	1.9°x1.9°	Max Planck Institute for Meteorology (http://www.mpimet.mpg.de/en/science/models/mpi-esm.html)	Thailand

Results and discussion

Performance of the SWAT model

The key parameters controlling the basin's hydrology were found to be CN2, SOL_K, soil depth SOL_Z, CANMX, ALPHA_BF, GW_DELAY, CH_K2, SOL_ALB, CH_N2, and SLSUBBSN which were the results from the parameter sensitivity analysis of a previous study [18].

For the feasibility of using simulated values for future flow projections, the statistical coefficients of R^2 and PBIAS were calculated as in a previous study [18]. Almost all values of R^2 and NSE were greater than 0.6 and the range of PBIAS was ±25%. The model performs flow simulation at the 3SRB outlet determined by the highest value of R^2 and NSE and the lowest PBIAS values. As elaborated in Table 4 [26], the calibrated SWAT model would be acceptable for discharge simulation in 3S.

Table 4. The statistic for the observed and simulated daily flow calibration and validation periods.

Sub-basin		Sekong	Sesan	Srepok	3S
Calibration	R^2	0.56	0.6	0.5-0.74	0.72
	NSE	0.49	0.36	0.54-0.65	0.72
	PBIAS	-9.36	-9.56	-8.3- -6.9	8.21
Validation	R^2	0.59-0.80	0.58-0.68	0.58-0.77	0.68
	NSE	0.65-0.80	0.60-0.73	0.57-0.8	0.68
	PBIAS	1.61-8.01	-0.82-24.11	-3.52- -0.83	-2.86

The streamflow peak occurring in the months of August and September did not fit well and was mostly underestimated at 5 stations despite of the good fit between observed and expected data (Fig. 3). Missing and undistributed rainfall gauges, unpresented local rainfall storms, or the curve number (CN2) employed to simulate surface runoff may have caused the mismatch. The CN2 method assumes a unique relationship between cumulative rainfall and runoff for the same antecedent moisture conditions generated from the study conducted at a basin located in the US [27-29]. Nonetheless, this study aimed to assess the water resources but not predicting flood. Therefore, the peak flow mismatch was not significantly more important than the total flow or mean annual water balance shown in Table 5. The difference between the average annual observed value and simulated value was less than 10% for 5 monitoring stations in the calibration period, which indicated a good match between the historical and the model's simulated flow.

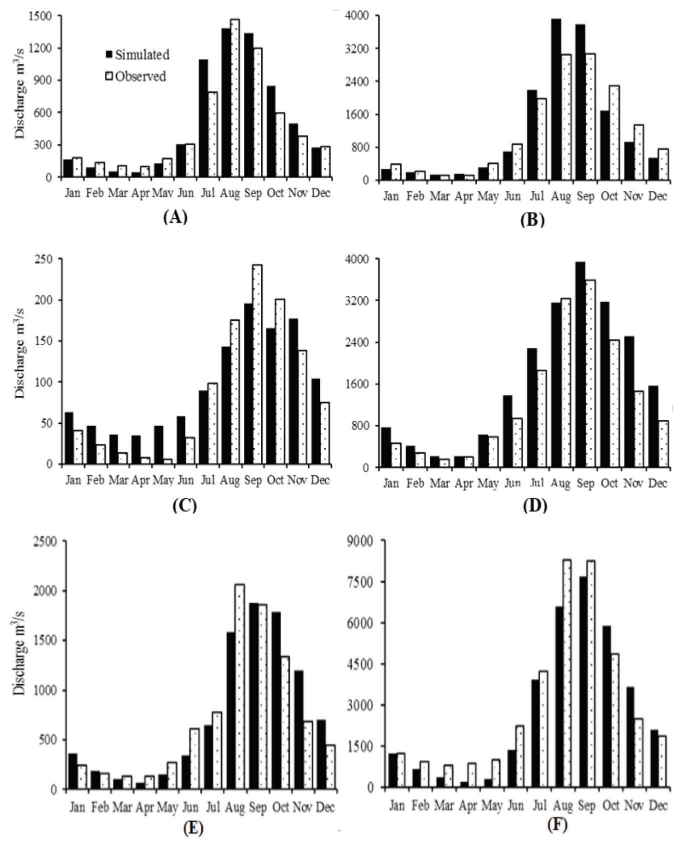

Fig. 3. Comparison of the observed and expected discharge for calibration and validation in the 3S basin and 3 sub-basins at (A) Attapeu (Sekong basin); (B) Chantangoy (Sekong basin outlet); (C) Kontum (Sesan basin); (D) B. Kamphun (Sesan basin outlet); (E) Lumphat (Srepok basin outlet); and (F) 3S basin outlet.

Table 5. The average annual water balance in the calibration and validation periods.

Station	Annual mean flow(m^3/s)					
	Calibration			*Validation*		
	Observed	*Expected*	*Difference (%)*	*Observed*	*Expected*	*Difference (%)*
Attapeu	477.02	521.65	9.36			
Kontum	91	98	7.69	102.36	77.4	-24.38
Bandon	267.50	289.70	8.30	308.02	333.67	8.33
Lumphat	733.67	758.9	3.44	722.92	743.54	2.85
Outlet	3014	2850	-5.44	2737	2688	-1.79

Future climate of temperature and rainfall

Temperature and precipitation indicate climate change magnitude, which directly affects the focal water resources. These prognostic variables changed for different periods along with radiative forcing [18]. The change in average monthly temperature over the 2030s, 2060s, and 2090s decades under the RCP4.5 and RCP8.5 scenarios is provided in Fig. 4. The temperature was found to continually increase under both RCPs, which spanned 3 periods every month. An increase in temperature was indicated from 0.4 to 0.99°C, 1.22 to 1.72°C, and 1.51 to 2.05°C in RCP4.5 and from 0.67 to 1.25°C for the 2030s, 2.04 to 2.59°C for the 2060s, and 3.26 to 4.01°C for the 2090s. The temperature increases in RCP8.5 was approximately 1.2 to 2 times greater than RCP4.5 across the 3 time periods. The highest change occurred in January for the 2030s and 2060s and in April for the 2090s in both RCP4.5 and RCP8.5. The magnitude of the change in temperature is associated with time and radiative forcing. The most substantial increase will occur in the RCP8.5 scenarios in the late twentieth century.

There is an obviously fluctuation in the average monthly precipitation for the 2030s, 2060s, and 2090s in the 3S basin for both the RCP4.5 and RCP8.5 scenarios related to the base years illustrated in Fig. 5. The changes in monthly rainfall fluctuated according to time and radiative forcing scenarios. Compared to the baseline, the average monthly precipitation changed from -7.1 to 18.9%, -2 to 10.8%, and -14.5 to 15.9% under RCP4.5 for the 2030s, 2060s, and 2090s, respectively, and from -18.4 to 21.9%, -16.3 to 17.2%, and -33.9 to 15.8% under RCP8.5 for the 2030s, 2060s, and 2090s, respectively. However, the most substantial decrease occurred in March in all cases. Generally, monthly rainfall is expected to increase during the 3 periods for the RCP 4.5 scenario in the wet season months (May to October) with fluctuations during the dry season months. Meanwhile, a major decline occurred in the period of February to April and at the beginning of the wet season (May) for the RCP 8.5 scenario (Fig. 5B). The precipitation had higher fluctuations under RCP8.5 due to the most severe increases and decreases occurring in the 2060s and 2090s.

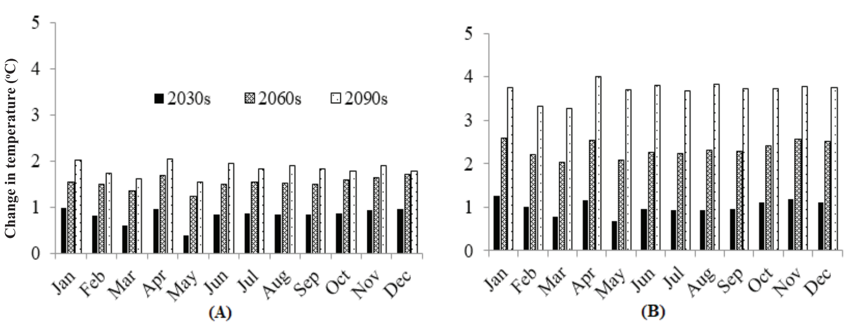

Fig. 4. Changes in monthly average temperature under (A) RCP4.5 and (B) RCP8.5 for the 2030s, 2060s, and 2090s compared to the baseline.

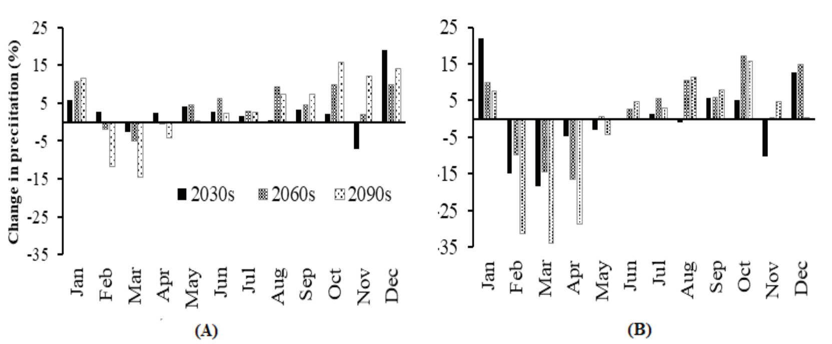

Fig. 5. Changes in monthly average precipitation under (A) RCP4.5 and (B) RCP8.5 for the 2030s, 2060s, and 2090s compared to the baseline.

Climate change impact on hydrology and water resources for the 3SRB

The relative change of average monthly streamflow under the climate change scenarios are presented in Fig. 6. The average monthly streamflow is projected to rise during the wet season and fall in dry season during all 3 decades for both RCP scenarios. Reductions in streamflow were detected from January to April for RCP4.5 and January to May for RCP8.5 for all 3 examined decades. The highest growth in streamflow occurred in June by 79% (2060s) for RCP4.5 and by 95% (2030s) for RCP8.5. The largest reductions in precipitation occurred in March at -66% (2030s) for RCP4.5 and in April at -79% (2090s) for RCP8.5. The increase in streamflow can be explained by increases in precipitation. The simulation results showed a reduction in runoff during the dry season under RCPs 4.5 despite the increase in precipitation. This may be explained by the combined impact of evaporation and precipitation on streamflow. The temperature during the dry season is predicted to increase more than in the wet season (Fig. 4), which leads to greater evaporation. In addition, the increase in precipitation during the dry season is not significant compared to that of the wet season. The river flow change is marginal in terms of absolute value but significant in term of relative value to the dry season.

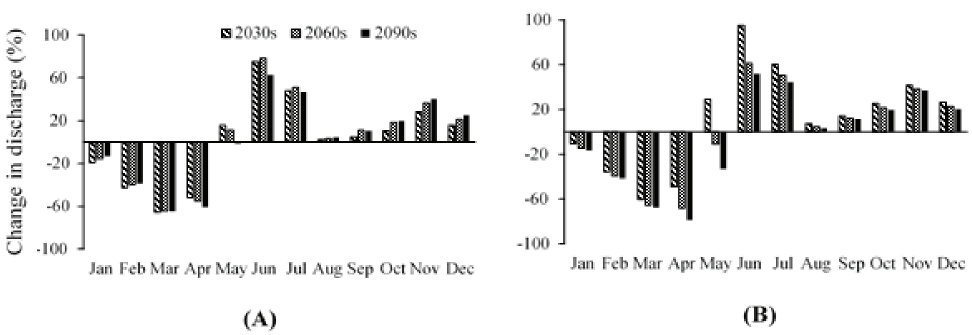

Fig. 6. Changes in monthly discharge in 3SRB under (A) RCP4.5 and (B) RCP8.5 for the 2030s, 2060s, and 2090s compared to the baseline.

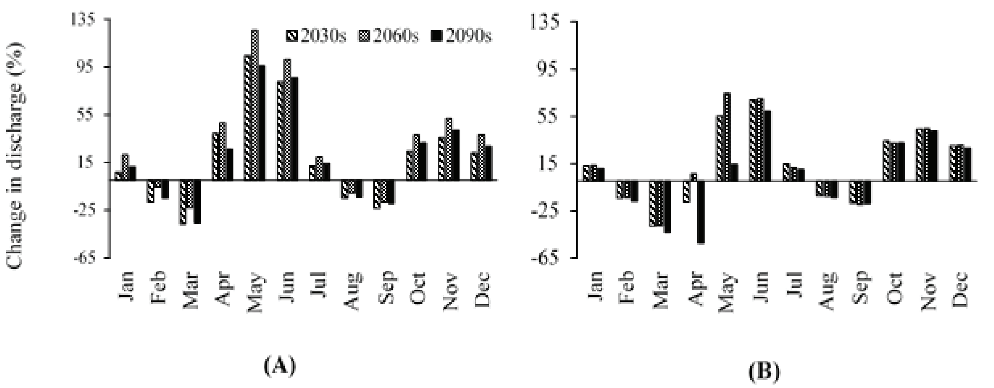

Fig. 7. Changes in monthly river discharge under (A) RCP4.5 and (B) RCP8.5 for the 2030s, 2060s, and 2090s relative to the baseline in the Sekong river basin.

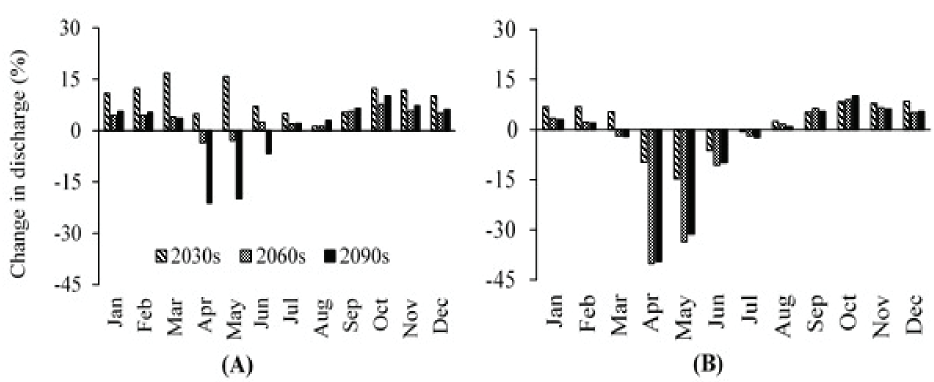

Fig. 8. Changes in monthly river discharge under (A) RCP4.5 and (B) RCP8.5 for the 2030s, 2060s, and 2090s relative to the baseline in the Sesan river basin.

Impact of climate change on hydrology and water resources for the 3SRB

The climatic, geographical, and social characteristics of the 3SRB are obviously different. Therefore, the assessment of climate change impact on each of the 3 sub-basins is essential to the launch of an appropriately tailored plan and mitigation measures for each sub-basin.

There was an average increase of flow by 6.1 and 3.2 % in Sekong, 5.9 and 2.7% in Sesan, and 35.9 and 32.1% for Srepok under RCP 4.5 and RCP 8.5 scenarios, respectively. However, the change in monthly flow of the 3 rivers varies as illustrated in Figs. 7-9. It can be seen that the pattern of monthly flow changes varies for all 3 sub-basins as well as over the different climate change scenarios. The projected simulated annual flow was analysed for the 3 sub-basins. Considering the monthly flow, a decrease was detected at the end of the dry season and in the middle of the wet season for the Sekong and Srepok basins (Figs. 7 and 9). Meanwhile, a decrease in monthly flow occurred from the end of the dry season to the beginning of the wet season in the Sesan river basin as shown in Fig. 8. The Sekong basin will experience the most severe decline and the highest increase in monthly flow during April and May, respectively. The extent of the change is more substantial for the Sekong and Srepok basins.

The relative monthly discharge increase was projected to be the highest in Srepok followed by the Sekong and Sesan river basins. The highest increase observed under RCP8.5 was 120% at the Srepok river basin in November (2060s). The highest increase observed under RCP4.5 was 125% at the Sekong river in May(2060s) and for 16.8% in March (2030s) at the Sesan river basin. The discharge in April increased under RCP4.5 and vice versa for the RCP8.5 at the Sekong river as shown in Fig. 7. The difference in flow between RCP4.5 and RCP8.5 is significant during the wet season for all 3 sub-basins.

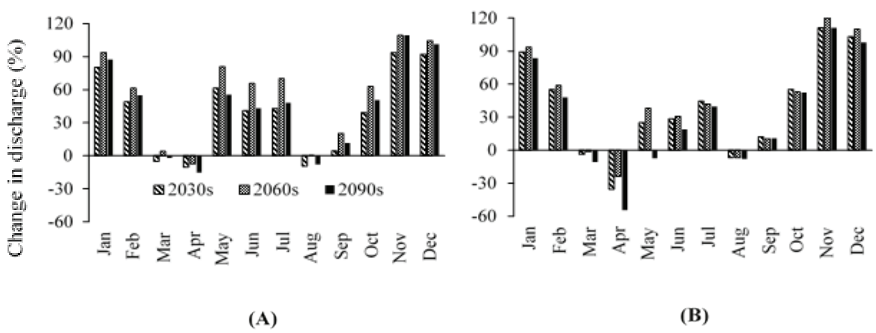

Fig. 9. Changes in monthly river discharge under (A) RCP4.5 and (B) RCP8.5 for the 2030s, 2060s, and 2090s relative to the baseline in the Srepok river basin.

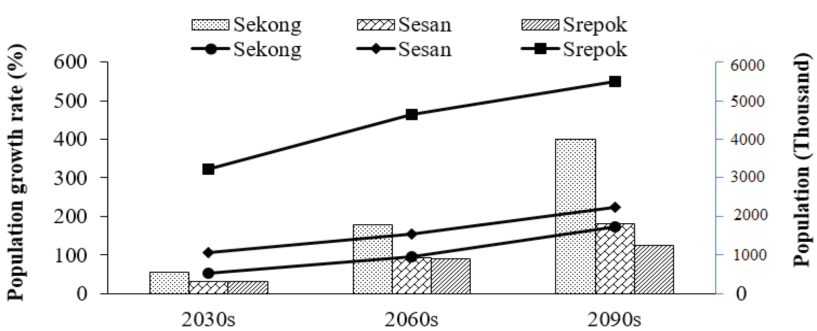

Fig. 10. Population growth rate (bar chart) and population (line) in the 3SRB over 3 decades: the 2030s, 2060s, and 2090s when compared to 2007.

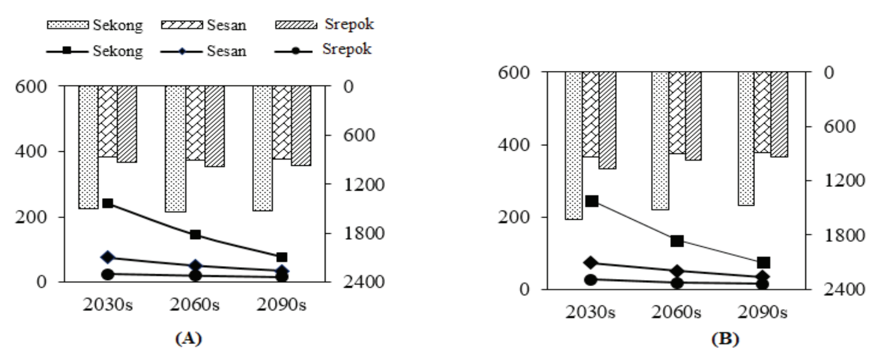

Fig. 11. Average annual flow (bar chart) and water availability (line) in the Sekong, Sesan, and Srepok sub-basins under climate change scenarios of (A) RCP4.5 and (B) RCP 8.5 with respect to the baseline.

Water availability response to climate scenarios and population growth

The population and growth rates of the 3 sub-basins were calculated based on the current and projected population density provided by MRC. These are depicted for 3 time periods, in both a line graph and bar chart, as shown in Fig. 10. In general, the population in the Srepok basin is higher than that of the Sekong and Sesan sub-basins by about 6 and 3 times, respectively, despite Srepok being the second largest in the 3S basin. The highest population is associated with the greatest urbanisation and industrialisation, which implies extended water consumption. The Srepok basin's population is predicted to increase from 2.4 million in 2007 to 3.2, 4.6, and 5.5 million people in the 2030s, 2060s, and 2090s, respectively. However, the increasing population rate in the Sekong basin is the highest at 55.8, 179.7, and 399% for the 2030s, 2060s, and 2090s, respectively. The population is projected to increase by 4, 1.8, and 1.25 times in the 2090s compared to that in 2007 at the Sekong, Sesan, and Srepok sub-basins, respectively. The rapid population increase in the Sekong basin will impose a burden on the water resources.

The annual flow and water availability at each of the 3 sub-basins is presented in Fig. 11 (A) and (B) by a bar chart and line chart, respectively. The results showed an increase in future discharge that underscores both emission scenarios across the 3 examined decades for all 3 sub-basins. In contrast, the sub-basin-specific water availability will have a decreasing trend throughout the century resulting from steady population growth whereas the Sekong river basin is expected to experience a dramatic decrease of 79.3%. The Sesan and Srepok basins may exhibit a consistent decline of 63.3% and 41.6%, respectively, at the end of this century. It can be seen that the declining trend is more severe in the Sekong basin compared to the two other basins. However, the absolute value of water availability in the Srepok basin is the lowest with 15.1 m^3/cap/day compared to 75.7 and 34.7 m^3/cap/day in the Sekong and Srepok, respectively, at the end of the twentieth century.

Discussion

Flood and drought induced from river discharge are the main natural water-related disasters that occur in the lower Mekong basin. Flood and drought is a primary disaster in terms of number of lives lost and number of people affected per disaster, respectively [30]. The risks resulting from these disasters, combined with socioeconomic development, leads to a serious water scarcity issue. Therefore, projecting alternative future hydrological regime scenarios is necessary to the advisement of the appropriate solutions for the adaptation and mitigation of water resources issues.

Under the two climate change scenarios employed in this work, the annual flow is predicted to increase for all the periods studied, namely, the 2030s, 2060s, and 2090s. This result is consistent with the finding from previous studies of 3S and the lower Mekong basin [31-33]. The results show a substantial decrease in flow during the dry season (January to April) under RCP 8.5, which would lead to a serious drought situation. Moreover, the dry season duration would extent to May over a long time period under the RCP 8.5 scenario.

The projected simulated annual flow was analysed for the 3 sub-basins, namely, Sekong, Sesan, and Srepok. The flow changes in the Sesan basin was examined and the projected annual flow was found to increase under all scenarios, especially in the peak month of September, which is similar to the results of [33]. The Srepok annual flow was projected to increase by about 33.9% under climate change impacts. A slight increase of about 3% over long periods was also found in a study by L.A. Ngo, et al. 2018 [34]. The different increasing amounts were explained by the uncertainty in using different climate change GCM models, a land use change map, and the period and station of the meteorological input data. However, our findings are totally different from the results of [30, 35]. In those works, the authors noticed that the annual flow decreased in the perspective of future climate change. This mismatch is explained by the different climate change scenarios used and water shed delineation. Furthermore, those two studies consider the Srepok basin, located in Vietnam only, to be half of the Srepok basin as defined in this study.

The remarkable finding here is the peak month of flow increase, September, and a decline in the trough month (April) for all 3 sub-basins, which exacerbates the severity of water shortages and floods. Together with the continuous increase of water demand induced by the growth of population, water scarcity during the dry month is much more serious. To mitigate the drought hazard, a water storage reservoir should be constructed and water should be reused and recycled.

Flood severity and related hazards increase as a result of the increase in streamflow during the peak month. The flood plain and damages could be mitigated by building embankments and levees to protect residential areas. Early and exact flood forecasting systems are very important and necessary to reduce damage. Effective hydropower dams and reservoir operations are measures considered to mitigate drought and flood magnitudes.

This study simulates and projects hydrology regimes in very large watersheds that lack meteorological data stations in regions like Laos and Cambodia. Therefore, hydrological monitoring systems can be improved by adding hydrological observation stations at borders between the two countries. Such observations could reveal inflow and outflow to respective downstream countries thereby showing the extent of the water resources used by each.

Conclusions

This study presents a quantitative evaluation of climate change and the future demographic impact on hydrological regimes and water resources along the transboundary basin of the 3SRB using the SWAT model integrated with ArcGIS, i.e. the SWAT-CUP.

The findings of this study show that the future climate is expected to be warmer with an increase in temperature and annual precipitation ranging between 10 and 21% over the entire 3SRB. As expected, the relative increase in river discharge reaches 20.9% for the 2060s under RCP8.5. However, the discharge is projected to decrease during the dry season. The important point here is that the streamflow increased in the peak flow month and decreased in the trough flow month for all scenarios leads to exacerbation of the severity of water shortages and floods.

The hydrological response to future climate perspectives varies between sub-basins in terms of magnitude and pattern. In general, the annual flow will increase for all 3 sub-basins under both climate scenarios and over 3 examined time periods. For most of the cases, the river discharge decreases at the end of dry season for the 3SRB, which exacerbates the severity of drought. The increase of flow in the 3SRB occurs in the peak flow month, which is a significant implication for the requisite flood management strategy.

The water availability, as determined by river flow and population characteristics, is anticipated to continuously decline throughout the century for all 3 sub-basins. The decreasing magnitude in the Srepok basin is the smallest among the 3 sub-basins. However, the Srepok river basin has the lowest water availability over all time periods and scenarios. If the decreasing trend continues for the Srepok river basin, water shortage is inevitable. Besides, water availability in the Sekong river basin will experience a dramatic decreasing trend. Therefore, these points should be taken into account in future basin planning for societal development and water supply.

The outcome of this study has significant implications that support policymakers in decision making in unique and appropriate water resource management for the entire 3SRB, and each separate sub-basin, in a sustainable and environmental manner.

ACKNOWLEDGEMENTS

The authors would like to thank the greater Mekong Sub-region for providing the funds required for this research. Similarly, the authors would also like to acknowledge the MRC for providing data and the Center of Water Management and Climate Change, Vietnam National University, and the scholarship of the Ministry of Education, Culture, Sports, Science, and Technology, Japan for facilitating this research.

COMPETING INTERESTS

The authors declare that there is no conflict of interest regarding the publication of this article.

REFERENCES

[1] Intergovernmental Panel on Climate Change (2013), *Climate Change 2013, the Physical Science Basis*, Cambridge University Press, 1535pp.

[2] J.M. Kirby, M. Mainuddin, F. Mpelasoka, M.D. Ahmad, W. Palash, M.E. Quadir, S.M. Shah-Newaz, M.M. Hossain (2016), "The impact of climate change on regional water balances in Bangladesh", *Clim. Change*, **135(3-4)**, pp.481-491.

[3] J.M. Kirby, J. Connor, M.D. Ahmad, L. Gao, M. Mainuddin (2014), "Climate change and environmental water reallocation in the Murray-Darling basin: impacts on flows, diversions and economic returns to irrigation", *J. Hydrol.*, **518**, pp.120-129.

[4] A.R. Fonseca, J.A. Santos (2019), "Predicting hydrologic flows under climate change: The Tâmega basin as an analog for the Mediterranean region", *Sci. Total Environ.*, **668**, pp.1013-1024, DOI: 10.1016/j.scitotenv.2019.01.435.

[5] C. Luo, Z. Li, H. Liu, H. Li, R. Wan, J. Pan, X. Chen (2020), "Differences in the responses of flow and nutrient load to isolated and coupled future climate and land use changes", *J. Environ. Manage.*, **256**, p109918, DOI: 10.1016/j.jenvman.2019.109918.

[6] B. Shrestha, T.A. Cochrane, B.S. Caruso, M.E. Arias, T. Piman (2016), "Uncertainty in flow and sediment projections due to future climate scenarios for the 3S rivers in the Mekong basin", *J. Hydrol.*, **540**, pp.1088-1104, DOI: 10.1016/j.jhydrol.2016.07.019.

[7] J.L. Swirepik, I.C. Burns, F.J. Dyer, I.A. Neave, M.G. O'Brien, G.M. Pryde, R.M. Thompson (2016), "Establishing environmental water requirements for the Murray-Darling basin, Australia's largest developed river system", *River Res. Appl.*, **32(6)**, pp.1153-1165, DOI: 10.1002/rra.2975.

[8] D. Constable (2015), *The Sesan and Srepok River Basins*, IUCN Asia Regional Office, Thailand, 56pp.

[9] N.T.N. Quyen, N.D. Liem, N.K. Loi (2014), "Effect of land use change on water discharge in Srepok watershed, Central Highland, Vietnam", *Int. Soil Water Conserv. Res.*, **2(3)**, pp.74-86, DOI: 10.1016/S2095-6339(15)30025-3.

[10] Asian Development Bank (2010), *Sesan, Srepok, and Sekong River Basins Development Study in Kingdom of Cambodia, Lao People's Democratic Republic, and Socialist Republic of Vietnam*, project number: 40082-012.

[11] P. Hartman, K. Carlucci (2014), *Climate Change Impact and Adaptation Study for the Lower Mekong Basin: Key Final Results*, USAID Mekong ARCC Climate Study, Bangkok, Thailand.

[12] P.B. Ngor, P. Legendre, T. Oberdorff, S. Lek (2018), "Flow alterations by dams shaped fish assemblage dynamics in the complex Mekong-3S river system", *Ecol. Indic.*, **88**, pp.103-114, DOI: 10.1016/j.ecolind.2018.01.023.

[13] C. Oeurng, T.A. Cochrane, M.E. Arias, B. Shrestha, T. Piman (2016), "Assessment of changes in riverine nitrate in the Sesan, Srepok and Sekong tributaries of the lower Mekong river basin", *J. Hydrol. Reg. Stud.*, **8**, pp.95-111.

[14] T.B. Wild, D.P. Loucks (2014), "Managing flow, sediment, and hydropower regimes in the Srepok, Sesan, and Sekong rivers of the Mekong basin", *Water Resour. Res.*, **50(6)**, pp.5141-5157.

[15] T. Piman, T.A. Cochrane, M.E. Arias, A. Green, N. Dat (2012), "Assessment of flow changes from hydropower development and operations in Sekong, Sesan, and Srepok rivers of the Mekong basin", *J. Water Resour. Plan. Manag.*, **139(6)**, pp.723-732.

[16] B. Shrestha, T.A. Cochrane, B.S. Caruso, M.E. Arias (2018), "Land use change uncertainty impacts on streamflow and sediment projections in areas undergoing rapid development: a case study in the Mekong basin", *L. Degrad. Dev.*, **29(3)**, pp.835-848.

[17] D.N. Khoi, L.V. Thang (2017), "Climate change impacts on streamflow and non-point source pollutant loads in the 3S rivers of the Mekong basin", *Water Environ. J.*, **31(3)**, pp.401-409.

[18] N.T.T. Trang, S. Shrestha, M. Shrestha, A. Datta, A. Kawasaki (2017), "Evaluating the impacts of climate and land-use change on the hydrology and nutrient yield in a transboundary river basin: a case study in the 3S river basin (Sekong, Sesan, and Srepok)", *Sci. Total Environ.*, **576**, pp.586-598.

[19] M.L. Tan, A.L. Ibrahim, Z. Yusop, Z. Duan, L. Ling (2015), "Impacts of land-use and climate variability on hydrological components in the Johor river basin, Malaysia", *Hydrol. Sci. J.*, **60(5)**, pp.873-889.

[20] K.C. Abbaspour (2012), *SWAT-CUP 2012: SWAT Calibration and Uncertainty Programs-A User Manual*, Swiss Federal Institute of Aquatic Science and Technology, Switzerland.

[21] C. Maringanti, I. Chaubey, M. Arabi, B. Engel (2011), "Application of a multi-objective optimization method to provide least cost alternatives for NPS pollution control", *Environ. Manage.*, **48(3)**, pp.448-461.

[22] L.D. James, S. Burges (1982), "Selection, calibration, and testing of hydrologic models", *Hydrologic Modeling of Small Watersheds, American Society of Agricultural Engineers, Hydrologic Modeling Monograph*, American Society of Agricultural Engineers.

[23] V.H. Gupta, S. Soroosh, Y.P. Ogou (1999), "Status of automatic calibration for hydrologic models: comparison with multilevel expert calibration", *J. Hydrol. Eng.*, **4(2)**, pp.135-143.

[24] S. Akhavan, J. Abedi-Koupai, S.-F. Mousavi, M. Afyuni, S.-S. Eslamian, K.C. Abbaspour (2010), "Application of SWAT model to investigate nitrate leaching in Hamadan-Bahar Watershed, Iran", *Agric. Ecosyst. Environ.*, **139(4)**, pp.675-688, DOI: 10.1016/j.agee.2010.10.015.

[25] M. Faramarzi, K.C. Abbaspour, R. Schulin, H. Yang (2009), "Modelling blue and green water resources availability in Iran", *Hydrol. Process.*, **23(3)**, pp.486-501, DOI: 10.1002/hyp.7160.

[26] D.N. Moriasi, J.G. Arnold, M.W. Van Liew, R.L. Bingner, R.D. Harmel, T.L. Veith (2007), "Model evaluation guidelines for systematic quantification of accuracy in watershed simulations", *Trans. ASABE*, **50(3)**, pp.885-900, DOI: 10.13031/2013.23153.

[27] H.H. Nguyen, F. Recknagel, W. Meyer, J. Frizenschaf, H. Ying, M.S. Gibbs (2019), "Comparison of the alternative models SOURCE and SWAT for predicting catchment streamflow, sediment and nutrient loads under the effect of land use changes", *Sci. Total Environ.*, **662**, pp.254-265, DOI: 10.1016/j.scitotenv.2019.01.286.

[28] Q. Hong, Z. Sun, L. Chen, R. Liu, Z. Shen (2012), "Small-scale watershed extended method for non-point source pollution estimation in part of the 3 Gorges reservoir region", *Int. J. Environ. Sci. Technol.*, **9(4)**, pp.595-604.

[29] V.H. Gupta, H. Kling, K.K. Yilmaz, G.F. Martinez (2009), "Decomposition of the mean squared error and NSE performance criteria: implications for improving hydrological modelling", *J. Hydrol.*, **377(1)**, pp.80-91.

[30] Mekong River Commission (2012), *The Impact & Management of Floods & Droughts in the Lower Mekong Basin & the Implications of Possible Climate Change*, Working Paper (2011-2015), 112pp.

[31] T. Piman, T. Lennaerts, P. Southalack (2013), "Assessment of hydrological changes in the lower Mekong basin from basin-wide development scenarios", *Hydrol. Process.*, **27(15)**, pp.2115-2125.

[32] L.P. Hoang, et al. (2019), "The Mekong's future flows under multiple drivers: how climate change, hydropower developments and irrigation expansions drive hydrological changes", *Sci. Total Environ.*, **649**, pp.601-609, DOI: 10.1016/j.scitotenv.2018.08.160.

[33] S.V. Raghavan, M.T. Vu, S.-Y. Liong (2012), "Assessment of future stream flow over the Sesan catchment of the lower Mekong basin in Vietnam", *Hydrol. Process.*, **26(24)**, pp.3661-3668, DOI: 10.1002/hyp.8452.

[34] L.A. Ngo, I. Masih, Y. Jiang, W. Douven (2018), "Impact of reservoir operation and climate change on the hydrological regime of the Sesan and Srepok rivers in thelower Mekong basin", *Clim. Change*, **149(1)**, pp.107-119.

[35] L.P. Hoang, H. Lauri, M. Kummu, J. Koponen, M.T.H van Vliet, I. Supit, R. Leemans, P. Kabat, F. Ludwig (2016), "Mekong river flow and hydrological extremes under climate change", *Hydrol. Earth Syst. Sci.*, **20(7)**, pp.3027-3041.

DOI: 10.31276/VJSTE.62(4).87-94

Application of remote sensing in evaluating the PM_{10} concentration in Ho Chi Minh city

Tran Huynh Duy[1], Duong Thi Thuy Nga[2*]

[1]*University of Science, Vietnam National University, Ho Chi Minh city*
[2]*Ho Chi Minh city University of Natural Resources and Environment*

Received 12 August 2020; accepted 9 November 2020

Abstract:

Nowadays, air pollution is a serious problem for the entire world, but especially in developing countries like Vietnam. For monitoring and managing air quality, scientists have successfully used different technologies such as predictive models, interpolation, and monitoring, however; these methods require a large amount of input data to simulate. Further, the results from spatial simulations are not detailed and have deviations from reality due to factors such as terrain changes, wind direction, and rainfall. Based on the physical index extracted from remote sensing images like radiation and reflection values, the aerosol optical depth (AOD) can be extracted. In this work, a regression equation is constructed and the correlation between the extracted AOD and measured PM_{10} concentration is found. The results show that PM_{10} and AOD are best correlated with a non-linear regression equation. This work also shows that the concentration of PM_{10} in Ho Chi Minh city is distributed mainly along the outskirts of the city, which has many highways, industrial parks, factories, and enterprises.

Keywords: **AOD, Ho Chi Minh city, Landsat, PM_{10}.**

Classification number: **5.1**

Introduction

In recent years, countries around the world, along with Vietnam in particular, have been developing, urbanising, and modernising. What has followed is the emergence of many factories and means of transportation. As a result, the emission of dust and pollutants into the environment are increasing.

The National Environmental Status Report 2016 advises that most major cities in Vietnam are facing increasing air pollution [1]. Pollution levels among cities vary widely depending on urban size, population density, traffic density, and construction speed. As for dust pollution, data observed from 2012 to 2016 showed that dust pollution levels in urban areas are high with no sign of reduction over the last 5 years. For PM_{10} and $PM_{2.5}$ dust alone, the measured values at many traffic stations are higher than the annual average threshold, which was mentioned in QCVN 05:2013/BTNMT. According to the 2015 WHO Report, there are 6 diseases related to the respiratory tract that are caused by air pollution and these 6 are among the top 10 diseases with the highest mortality rates in Vietnam. In Vietnam, respiratory diseases are also one of the 5 most prevalent groups of acquired diseases [2, 3].

In order to prevent and minimise the level of pollution, the country has been the subject of a lot of studies that evaluate the air pollution level using the AQI index that is made up of the concentration of pollutant gases of CO_2, VOCs, and NO_x in many urban areas. Nevertheless, these studies only focus on processing data available from ground observation stations for simulation and prediction. These results have some deviations from reality due to the influence of many different factors such as the density of monitoring stations, the terrain where the stations are located, etc. In addition, some studies use modelling but are limited due to the need for a large enough input data source to get simulation results.

Because of these shortcomings, remote sensing is put into use. Remote sensing images show topographical and

*Corresponding author: Email: ngadtt@gmail.com

spatial information of the study area through pixels. Each pixel represents a monitoring station and the concentration of PM_{10} in the area will be more detailed compared to data taken by monitoring stations on the ground. At that time, each pixel will have a specific concentration value, which can show us a general view and clearer distribution of the fine dust in Ho Chi Minh city.

Up to now, Vietnam has had only a few studies using remote sensing technology for monitoring air pollution concentrations in the region. Tran Thi Van, et al. (2014) [4] with the study "Remote sensing aerosol optical thickness (AOT) simulating PM_{10} in Ho Chi Minh city area" used satellite images from Landsat 7 to develop the AOD index in 2003 based on "a clean image" from 1996. Then, the study had given the correlation equation between the real measured AOD and PM_{10}. A similar study was conducted by Nguyen Nhu Hung, et al. (2018) [5] in the Hanoi area titled "Model to determine PM_{10} in Hanoi area using Landsat 8 OLI satellite image data and visual data". Both studies provided a PM_{10} simulation map in two areas at the time of the study, but only at the correlation assessment at the 1-year level. With the same method, this study, which used correlation equations of 1 year for different years of the same period (same February of all years), showed the feasibility of applying remote sensing in simulating air pollution in the area.

Materials and methods

The basic principle of remote sensing technology is based on the reflection and radiation energy of the electromagnetic waves of objects. Different observations on objects will have different reflections at different electromagnetic wavelengths.

Spectral reflection of natural objects

Different observation objects will have various reflection characteristics for different electromagnetic wavelengths. It can be seen in some typical objects, for example, water reflection mainly ranges around 0.4-0.7 μm and is strongly reflected in the blue wavelength (0.4-0.5 μm) and green (0.5-0.6 μm) regions or soil objects whose reflection increases gradually with wavelength. Based on this characteristic, data can be extracted using remote sensing images [6] (Fig. 1).

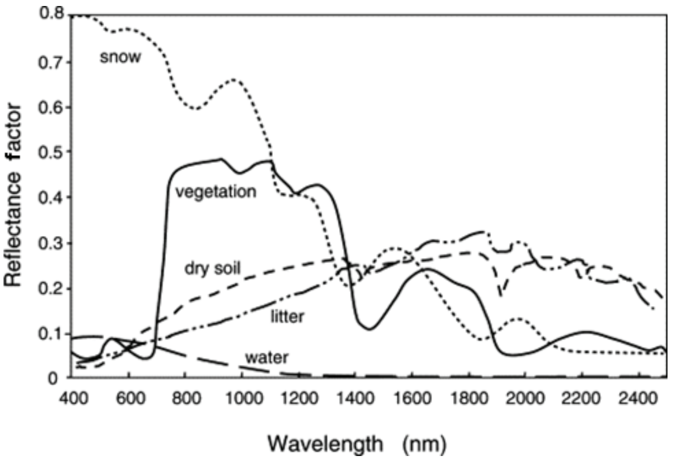

Fig. 1. Spectral reflection of common objects [6].

There are many ways to extract information from remote sensing images in the reflectance spectrum such as visual interpretation or digital image processing. The basis for visual interpretation is direct reading signs. Digital image processing aims to extract information with the help of a computer and is based on the digital signals of pixels. Both methods have different advantages and disadvantages and are applied depending on the purpose.

AOD/AOT

Aerosols are a collection of suspended substances dispersed in air. Aerosols can be in solid or liquid form or in the form of a colloid, which is relatively durable but difficult to deposit. An aerosol system consists of a particle and the air mass containing it. Aerosols can be produced through mechanical decomposition on land or sea (such as sea dust) and by chemical reactions that take place in the atmosphere (such as converting SO_2 to H_2SO_4 in the atmosphere). Moreover, they are also discharged directly into the atmosphere through human daily activities. Natural aerosols include fog, forest secretions, and geysers [7].

When solar radiation enters the atmosphere, some will be lost due to absorption and scattering of material components in the atmosphere, which includes aerosols. To characterise the attenuation of the solar radiation when absorbed and scattered by aerosols, the AOD/AOT is used. According to previous studies, to estimate atmospheric depletion, the moon was used as a source of radiation to calculate the atmospheric emission by the function:

$$T = e^{\frac{-\beta l}{\cos\theta}} \quad (1)$$

where T is the atmospheric transmittance, β is the optical index of the surveyed material, l is the atmospheric thickness, and θ is the angle of the main projection ray measured from the zenith [8]. The transmittance of the atmosphere ranges from 0 to 1, where 0 corresponds to a completely opaque atmosphere and 1 corresponds to a completely transparent atmosphere. According to the functions, the optical thickness (OT) is inversely proportional to atmospheric emission. A large OT means transmittance through the atmosphere is low and OT also has a value ranging from 0 to 1. However, a 0 value for OT corresponds to a completely transparent atmosphere while a value of 1 corresponds to an atmosphere that is completely opaque.

Implementation steps and research methods (Fig. 2)

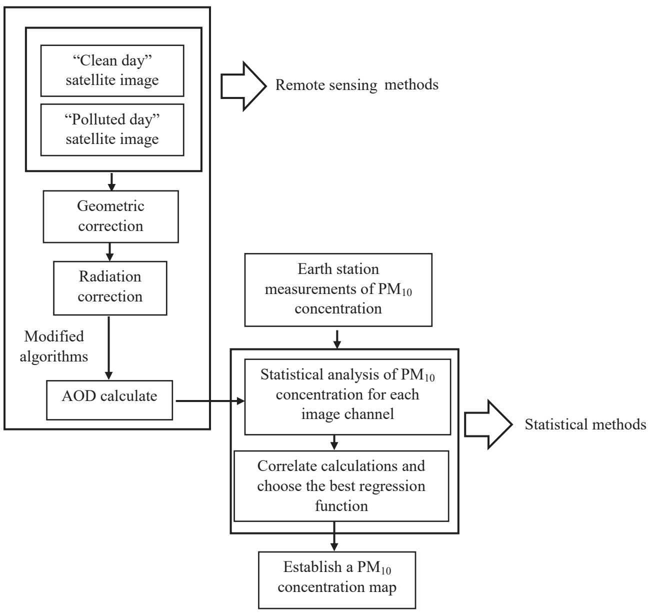

Fig. 2. Implementation steps and research methods [8].

Geometric correction

Before analysis and interpretation, satellite images must be corrected geometrically to limit position errors and terrain differences, which makes it easier to analyse and detect changes. In addition, geometric corrections are also carried out to eliminate distortions during photography and to return images to standard coordinates so that they can be integrated with other data sources. To perform the geometric correction, the authors select ground control points (GCPs). The coordinate parameters are included in the least-squares regression analysis to determine the coefficients of the conversion equation between images and map coordinates. After the conversion equation, the sample redistribution process is performed to determine the pixel values included in the corrected image. The interpolation methods that are applied in the re-division process are interpolation and tertiary interpolation. In order to retain the spatial and radiation quality of the image, the nearest neighbour interpolation method is used over the whole course of image processing.

Radiation correction [9-13]

Conversion to radiation values: this study uses remote sensing images from Landsat 5 TM (used as "clean day" images) and Landsat 8 (for the time of observation).

For the Landsat 5 TM:

$$L_\lambda = A \times (DN - Q_{min}) + B \quad (2)$$

where L_λ is the radiation value on the satellite ($Wm^{-2}\mu m^{-1}$), Q_{min} is the minimum quantitative reflection value on the pixel (Q_{min}=1), B is the minimum reflectance value, DN is the reflection value per pixel, and A is the value calculated by the following equation:

$$A = \frac{(L_{max} - L_{min})}{(Q_{max} - Q_{min})} \quad (3)$$

with L_{max} and L_{min} are the largest and smallest reflected values, respectively, and Q_{max} and Q_{min} are the largest (255) and smallest (1) quantised reflection values on the pixel cell, respectively.

For the Landsat 8 OLI:

$$L_\lambda = M_L \times DN + A_L \quad (4)$$

where M_L and A_L values are radiation multipliers and additions calculated for each channel, respectively.

The values L_{max} and L_{min}, Q_{max} and Q_{min}, and M_L and A_L are taken from an MTL file attached in the remote sensing image file when downloaded.

Conversion to reflection values: for the Landsat 5 TM:

$$\rho_p = \frac{\pi \times L_\lambda \times d^2}{ESUN_\lambda \times \cos\theta_s} \quad (5)$$

where ρ_p is the reflection value on the satellite corresponding with wavelength λ, L_λ is the radiation value on the satellite with unit $Wm^{-2}.\mu m^{-1}$, $ESUN_\lambda$ is the average lighting of the upper atmosphere from the Sun ($Wm^{-2}.Mm^{-1}$), θ_s is the angle of the sun's peak and the complementary angle of the Sun's elevation (θ_s = radians (90° - the angle of the Sun)) and *d* is the distance between Earth and Sun in astronomical units and calculated using Smith's equation (Eq. 6):

$$d = (1 - 0.01672 * \cos(\text{radians}(0.9856 * (\text{Julian Day} - 4)))) \quad (6)$$

with the Landsat 8 OLI, the reflectance value is calculated as the surface reflectance value with Eq. 7:

$$\rho = \frac{\pi * (L_\lambda - L_P) * d^2}{T_V * \{(ESUN_\lambda * \cos\theta_{SZ} * T_Z) + E_{down}\}} \quad (7)$$

with T_v and T_z being a function of transmitting atmospheric radiation from the Earth's surface to the receiver and from the Sun to the Earth, respectively, $ESUN_\lambda$ is the average lighting of the upper atmosphere from the Sun ($Wm^{-2}Mm^{-1}$), E_{down} is the spectral radiation going to the object's terrain surface, *d* is the distance between the Earth and the Sun and L_p is the line radiation calculated by the following Eq. 8:

$$L_P = L_{min} - 0.01 * \frac{T_V * \{(ESUN_\lambda * \cos\theta_{SZ} * T_Z) + E_{down}\}}{\pi * d^2} \quad (8)$$

Based on the DOS method, the determination of T_V, T_Z, and E_{down} parameters which divided into many different methods (DOS1, DOS2, DOS3, DOS4) having different accuracy. In this study, the authors use DOS1, in which the parameters were determined by Moran and his team as T_V=1; T_Z=1; and E_{down} = 0. At this time Eq. 7 will become:

$$\rho = \frac{\pi * (L_\lambda - L_P) * d^2}{ESUN_\lambda * \cos\theta_{SZ}} \quad (9)$$

with L_p is calculated by Eq. 10:

$$L_P = L_{min} - 0.01 * \frac{ESUN_\lambda * \cos\theta_{SZ}}{\pi * d^2} \quad (10)$$

The algorithm calculates AOD

"Blur" effect: after radiation correction, the authors have an image showing the reflection value of the objects. Based on the results of the reflection, the authors proceed to extract AOD by the method of N. Sifakis and P-Y. Deschamps (1992) [14]. The team used 2 remote sensing images, one in completely clean air (used as a "reference image") and the other in polluted air for the survey. According to the previous study, surface radiation is a space-dependent variable and is not time based, so using differential textural analysis (DTA), the team extracted the approximate value of AOD [14].

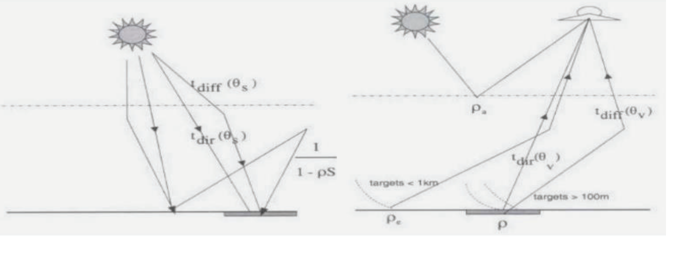

Fig. 3. Different components of total radiation transmitted up and down [14].

In the visible light spectrum of electromagnetic waves, the scattering of shortwave radiation is mostly caused by particulate matter in the atmosphere that causes a decrease in the contrast and distortion of the spectral feedback pattern in the remote sensing image (Fig. 3). This is called the "blurring" effect, which can be estimated using the optical depth (OD) derived from the basic equation of the apparent reflection from a satellite. For research objects in a large space (with a radius within 1 km) and homogeneity between different objects, the authors have the equation of "clear" reflection as follows:

$$\rho^* = \rho \frac{T(\theta_s)T(\theta_v)}{1-\rho S} + \rho_a \quad (11)$$

where ρ^*, ρ, and ρ_a are "clear" reflections in satellites, surface reflections, and atmospheric reflections, respectively. S is the spherical reflectance of the atmosphere defined as the ratio of scattering to total attenuation of radiation, θs and θv are the Sun's zenith angles and their zenith angles, respectively. $T(\theta_s)$ is the total transmission function on the "downlink", it can be analysed as the sum of $t_{dir}(\theta_s)$ and $t_{diff}(\theta_s)$ including direct and diffusion transfer functions. $T(\theta_v)$ is the total transmission function on the uplink and it can be analysed as the sum of $t_{dir}(\theta_v)$ and $t_{diff}(\theta_v)$ including direct and diffusion transfer functions. According to Eq. 11, the authors obtain information about optical thickness as a function of ρ_a with $\rho \approx 0$. However, for research areas having small diameters (<100 m), the authors need to consider the proximity effect and Eq. 1 needs to consider the average reflection of the surrounding objects (ρ_e). Then Eq. 11 will become:

$$\rho^* = \rho \frac{T(\theta_s)t_{dir}(\theta_v)}{1-\rho_e S} + \rho_e\, \rho \frac{T(\theta_s)t_{diff}(\theta_v)}{1-\rho_e S} + \rho_a \quad (12)$$

According to the authors, standard deviation is an indicator of similar contrast as seen on satellite images. So N. Sifakis and P-Y. Deschamps (1992) [14] have given the correlation equation between the standard deviation of the "clear" ($\sigma(\rho^*)$) reflectance and the standard deviation of the true reflectance ($\sigma(\rho)$) based on Eq. 12. The authors took a random set of adjacent pixel cells and found that the change of ($\sigma(\rho^*)$) is only affected by the standard deviation of the actual reflection at the surface ($\sigma(\rho)$). Therefore, the authors obtained the following correlation equation:

$$\sigma(\rho^*) = \sigma(\rho) \frac{T(\theta_s)t_{dir}(\theta_v)}{1-\rho S} \quad (13)$$

Appling the Lambert - Bouguer transmission law to the transmission function $t_{dir}(\theta_v)$, the authors calibrate it to the angle θ_v and the following equation is found:

$$\sigma(\rho^*) = \sigma(\rho) \frac{T(\theta_s)e^{-\tau/\cos(\theta_v)}}{1-\rho S} \quad (14)$$

According to Eq. 14, $-\tau/\cos(\theta_v)$ can be seen as AOD, which is calibrated to the Sun's angle.

Pixel: as mentioned above, following by the method of N. Sifakis and P-Y. Deschamps (1992) [14], the authors divide the study area into random pixel cells to calculate the reflectance standard deviation of the area.

AOD calculation: based on Eq. 14, the authors can calculate the standard deviation of the clean day and pollution day. Then, they take the equation for the clean day and divide by the pollution day, which yields the following equation:

$$\frac{\sigma_1(\rho^*)}{\sigma_2(\rho^*)} = \exp((-\tau_1/\cos(\theta_{v1}) + (-\tau_2/\cos(\theta_{v2})) \quad (15)$$

Landsat-8/OLI has zero viewing angles or zenith views at the center of the image. The maximum value of the view at the edges of the frame is 7.4960 calculated from the height of Landsat 8 satellite (703 km) and the width of 185 km. Hence the viewing angle range is from 0-7.4960 for any satellite image. For the Landsat 5 TM of the clean day image, the authors calculated the same zenith view from which the authors see that the clean day image angle ranged from 0-7.3950. Because the angle of view is small, the authors can assume that cos (θ_{v1}) ≈ cos (θ_{v2}) ≈ 1 and an error of ≈ 0.4%:

$$\frac{\sigma_1(\rho^*)}{\sigma_2(\rho^*)} = \exp(-\tau_1 - \tau_2) \quad (16)$$

with τ_1 and τ_2 is the atmospheric depth in the clean day and the pollution day, respectively. Based on Eq. 16, the authors calculate the AOD difference between the clean day and the pollution day as:

$$\Delta\tau = \tau_2 - \tau_1 = \ln[\frac{\sigma_1(\rho)}{\sigma_2(\rho)}] \quad (17)$$

In Eq. 17, the AOD is equal to the difference of optical depth in the clean and polluted images. However, for "clean days", the atmosphere is assumed to be completely "transparent" so it is possible to indicate that the optical depth on a clean day is approximately zero ($\tau_1 \approx 0$). So, from Eq. 17, the authors obtain the following equation:

$$\Delta\tau = \tau_2 = \ln[\frac{\sigma_1(\rho)}{\sigma_2(\rho)}] \quad (18)$$

The optical depth difference of the clean day and pollution day is also the optical depth of the pollution day and is determined by Eq. 18 [14-16].

Results

Correlation and regression analysis between real AOD and PM_{10}

Like most of the other studies on AOD determination as well as PM_{10} concentration distribution by remote sensing, this study conducted AOD surveys mainly on 4 spectral channels: the blue spectrum channel (0.450-0.515 µm), green spectrum channel (0.525-0.600 µm), red spectrum (0.630-0.680 µm), and near-infrared channel (0.845-0.885 µm). Table 1 shows the results obtained when extracting AOD from the 4 image channels.

Table 1. AOD extract results from 4 channels Landsat image.

Stations	PM_{10} concentration (µg/m^3)	AOD in 28th Feb, 2017			
		Blue	*Green*	*Red*	*Near-infrared*
Zoo	66.4	-1.08318	-2.59237	-1.09258	-1.75548
Binh Chanh	138.5	-3.06638	-2.13509	-4.91728	-2.47673
DOSTE	112	-1.20462	-2.30867	-1.60878	-1.7548
Hong Bang	74.7	-2.04362	-3.58543	-2.67132	-1.14265
Thong Nhat Hospital	87	-2.04362	-3.78751	-1.92392	-2.33622
Tan Son Hoa	96.4	-1.99765	-3.91204	-2.05347	-1.45789
District 2	65	Noise	Noise	Noise	-2.67964

According to these results, the authors established scatter plots with AOD extracted as an independent variable (x) and the actual PM_{10} concentration as the dependent variable (y). Then, a regression equations was found and the results are given in Figs. 4-7.

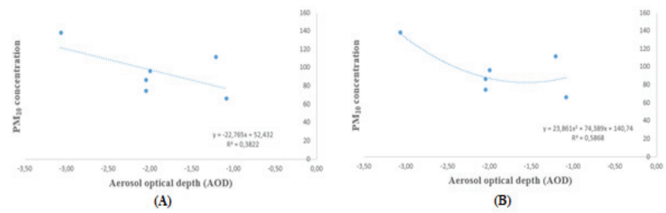

Fig. 4. The correlation between PM_{10} and AOD in the blue channel. (A) linear regression; **(B)** non-linear regression.

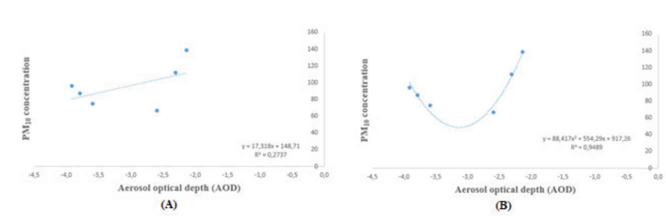

Fig. 5. The correlation between PM_{10} and AOD in the green channel. (A) linear regression; **(B)** non-linear regression.

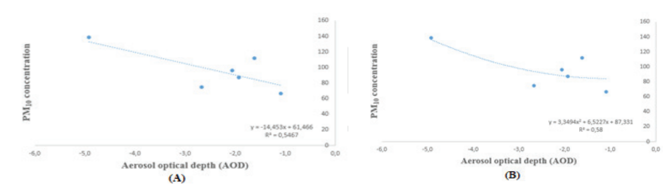

Fig. 6. The correlation between PM_{10} and AOD in the red channel. (A) linear regression; **(B)** non-linear regression.

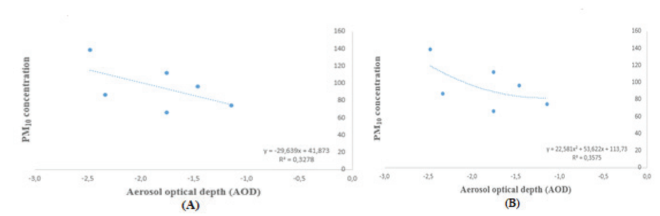

Fig. 7. The correlation between PM_{10} and AOD in the near-infrared channel. (A) linear regression; **(B)** non-linear regression.

Table 2. Regression analysis results among 4 image channels.

		Blue	Green	Red	Near-infrared
Linear regression equation	Equation	y=-22.8x + 52.4	y=17.3x + 148.7	y=-14.5x + 61.5	y=-8.1x + 75.6
	Correlation coefficients	R^2=0.3822	R^2=0.0223	R^2=0.5467	R^2=0.0299
Non-linear regression equation	Equation	y=23.8 x^2 +74.4x + 140.7	y=83.4x^2 +554.3x + 917.3	y=3.3 x^2 +6.5x+ 87.3	y=-32.9 x^2 - 135.9x - 38.9
	Correlation coefficients	R^2=0.5868	R^2=0.9489	R^2=0.58	R^2=0.1151

Through the analysis of the results (Table 2), the authors found that the non-linear regression equation of the blue spectrum channel gives the best correlation results between the two parameters (with R^2=0.9489). Therefore, the authors use non-linear regression between AOD and PM_{10} on the green channel [17].

Evaluation of the error between the actual measured dust concentration and the calculated dust concentration (Table 3)

Table 3. Assessment of the error between the actual measured concentration and the simulated concentration.

Station	Calculated PM_{10} concentration (µg/m^3)	Measured PM_{10} concentration (µg/m^3)	Absolute error
Zoo	66.4	41.9	24.5
Binh Chanh	138.5	124.1	14.4
DOSTE	112	102.2	9.8
Hong Bang	74.7	61.3	13.4
Thong Nhat Hospital	87	82.6	4.4
Tan Son Hoa	96.4	94.1	2.3
Error RMSE	13.5883		

Dust distribution map of Ho Chi Minh city area

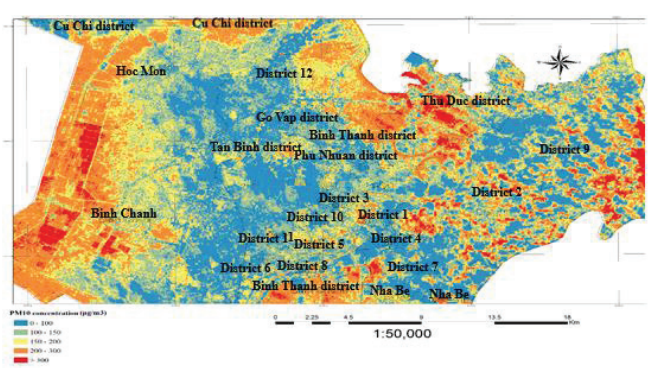

Fig. 8. Spatial concentration of PM_{10} in Ho Chi Minh city in February 28th, 2017.

The spatial concentration of the PM_{10} map was established in Ho Chi Minh city (Fig. 8). The map shows the concentration of dust in the area at 10 am, which is the time that vehicles and factories being operating. At this time, trucks are also allowed to run in the downtown area.

It can be seen that the PM_{10} concentration is highest, at over 300 µg/m^3, in districts with high traffic density and a concentration of many industrial parks such as Binh Chanh, Thu Duc, and district 9. Typically, in the area around the Thu Duc district, there are up to 150 factories with large production scale and thousands of small factories. Similarly, in the area around the Binh Chanh district, not only are there two large industrial parks Ho Chi Minh city, the Vinh Loc and Le Minh Xuan industrial parks, there are also many key roads such as the national highway 1A. High traffic volume also contributes to the high amount of dust and smoke in the Binh Chanh district compared to other areas.

In addition, Fig. 9 shows that PM_{10} concentration is distributed mainly in the western areas of the Hoc Mon and Binh Chanh districts and then disperses to surrounding areas. It can be understood that the process of dispersing suspended matter in the air is still influenced by the wind, but the inner city has a large surface roughness due to many high-rise buildings. So, a monsoon does not affect much in the inner city, only a "whirlwind" does. The characteristic of this wind is to blow along many directions under the influence of the moving flow of vehicles as well as the processes of heat emission from human activities.

In order to consider changes in PM_{10} concentration over time, the authors use the correlation equation obtained over a number of years between 2009-2019. The years selected for the analysis are selected according to the following criteria: photos are available in February each year; selected images with little cloud cover; in the period of 10 years between 2009-2019.

Based on the above criteria, the authors choose 4 years including February 11th, 2010, February 9th, 2015, February 28th, 2016, and February 17th, 2018. The authors obtained the research results shown in Fig. 9.

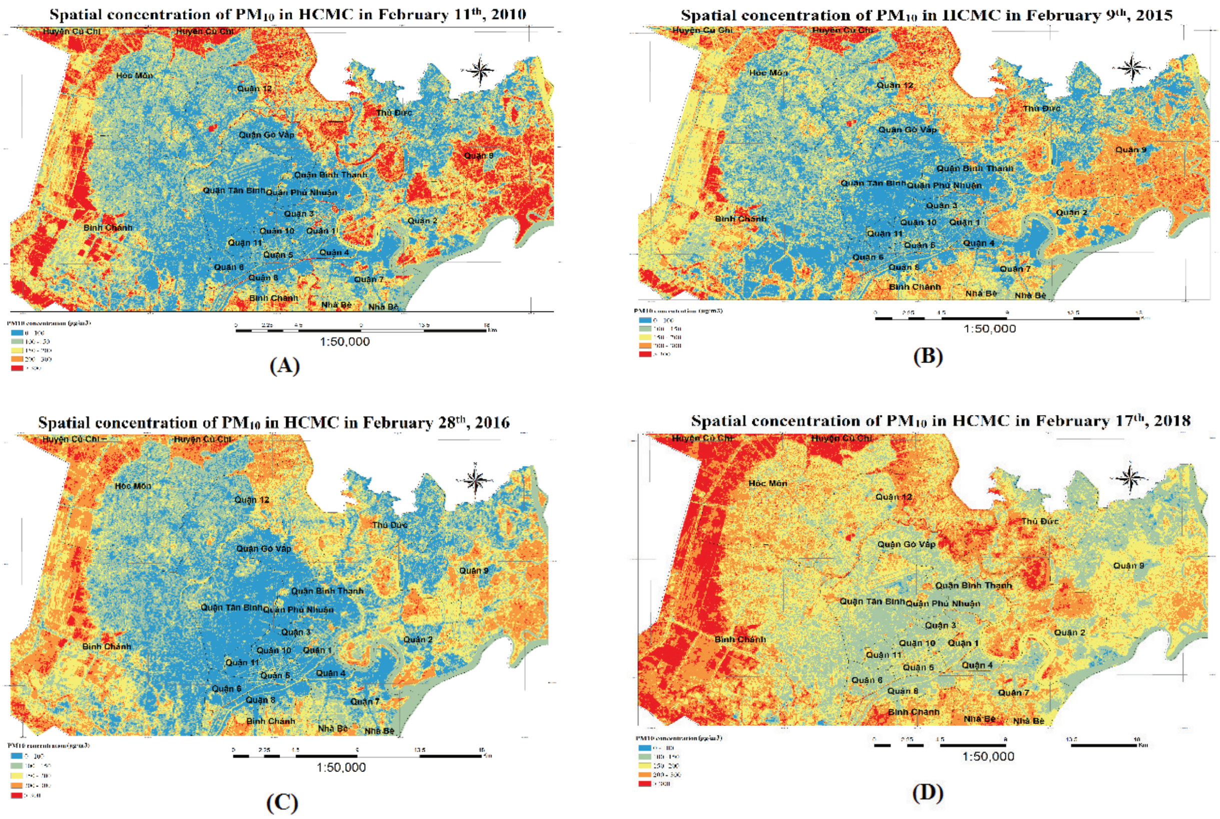

Fig. 9. Spatial concentration of PM_{10} in Ho Chi Minh city in (A) February 11th, 2010; (B) February 9th, 2015; (C) February 28th, 2016; (D) February 17th, 2018.

The results show that PM_{10} concentration in Ho Chi Minh city has increased over time (2010>2016>2015>2017>2018) and there is a fluctuation in concentration across the region. It can be seen that dust movements in the study area fluctuate equally over the years and the highest PM_{10} concentration is in the suburbs of the city. In central Ho Chi Minh city, PM_{10} concentrations increase over the years, especially along major regional roads. In addition, PM_{10} concentration increased sharply in the area of Binh Chanh, Thu Duc, and district 2 due to the strong development of industrial activities. Over time, large and small production factories and industrial zones are growing more and more. Consequently, the transport and transportation activities on route 2 of this area also increased. Particularly in district 2, there is the Cat Lat port that is adjacent to the Hanoi highway with dense traffic between these two areas.

Conclusions

The objective of the study is to use PM_{10} monitoring data in real time together with satellite image data analysis to give an equation showing the relationship between AOD and actual measured PM_{10} concentration. The final result provides an overview of the distribution of pollution concentration in the study area and dust concentration mainly in areas with high traffic density and dense industrial areas like the Binh Chanh,Thu Duc districts, and district 2 with dust concentrations of >300 $\mu g/m^3$. In the remaining areas, the dust concentration is uneven in the range of 50-200 $\mu g/m^3$. At the same time, this work also helps to increase reliability in the application of remote sensing methods for air quality monitoring. Compared to ground monitoring methods, the authors of this work only know the environmental status at the measured location so a wide area cannot be assessed. With the modelling method, the results are also limited due to rather complex input requirements (meteorology, emission sources, etc.). Therefore, using remote sensing technology to create pollution maps for environmental management will bring more efficiency.

Currently, the monitoring stations in the area of Ho Chi Minh city are mainly located in urban areas, so the assessment of air quality is still limited. However, the construction of additional monitoring stations is quite costly, so the assessment of air quality by satellite images is more economical thanks to the advantages of being able to obtain large-scale data together. With the treatment and calculation methods that have been tested in many studies around the world over the years, the remote sensing method can be added as a useful tool for monitoring and evaluating air pollution in the city.

COMPETING INTERESTS

The authors declare that there is no conflict of interest regarding the publication of this article.

REFERENCES

[1] Ministry of Natural Resources and Environment (2016), *National Environmental Status Report 2016: Urban Environment*, Vietnam Publishing House of Natural Resources, Environment and Cartography, **2**, pp.25-45, in Vietnamese.

[2] https://www.who.int/docs/default-source/gho-documents/health-in-2015-mdgs-to-sdgs/health-in-2015-from-mdgs-to-sdgs.pdf?sfvrsn=8ba61059_2.

[3] https://www.who.int/docs/default-source/gho-documents/world-health-statistic-reports/world-heatlth-statistics-2016.pdf.

[4] Tran Thi Van, et al. (2014), "Remote sensing optical thickness aerosol simulation of PM_{10} distribution in urban areas of Ho Chi Minh city", *VNU Journal of Science*, **30(2)**, pp.52-62.

[5] Nguyen Nhu Hung, et al. (2018), "Model to determine PM_{10} dust in Hanoi area using Landsat 8 OLI satellite image data and visual data", *VNU Journal of Science*, **34(1)**, pp.23-36, in Vietnamese.

[6] A.R. Huete (2004), "Remote sensing for environmental monitoring", *Environmental Monitoring and Characterization*, pp.183-206.

[7] S.K. Satheesh (2002), "Aerosol and climate", *Resonance - Journal of Science Education*, **7(4)**, pp.48-59.

[8] K. Omari, et al. (2019), "Aerosol optical depth retrieval over the city of Abu Dhabi, United Arab Emirates (UAE) using Landsat-8 OLI images", *Atmospheric Pollution Research,* **10(4)**, pp.1075-1083.

[9] Tran Thi Van, et al. (2012). "Study the possibility of detecting dust pollution in urban areas by remote sensing technology", *Science and Technology Development Journal*, **15(M2-2012)**, pp.33-47, in Vietnamese.

[10] L. Sun, et al. (2016), "Aerosol optical depth retrieval over bright areas using Landsat 8 OLI images", *Remote Sensing*, **8(1)**, 23pp.

[11] N. Othman, et al. (2010), "Estimating particulate matter concentration over arid region using satellite remote sensing: a case study in Makkah, Saudi Arabia", *Modern Applied Science*, **4(11)**, pp.131-142.

[12] K. Zanter (2015), "Conversion of DNs to physical units", *Landsat 8 Data Users Handbook 1st version*, U.S Geological Survey, pp.61-65.

[13] K. Zanter (2019), "IGS Landsat data archives", *Landsat 7 Data Users Handbook*, U.S Geological Survey, pp.107-127.

[14] N. Sifakis, P-Y. Deschamps (1992), "Mapping of air pollution using SPOT satellite data", *Photogrammetric Engineering and Remote Sensing*, **58(10)**, pp.1433-1437.

[15] A. Retalis, et al. (1999), "Assessment of the distribution of aerosols in the area of Athens with the use of Landsat thematic mapper data", *Int. J. Remote Sensing*, **20(5)**, pp.939-945.

[16] W.E.K. Middleton (1961), *Pierre Bouguer's Optical Treatise on Gradation of Light*, University of Toronto Press, 265pp.

[17] Nguyen Tran Que, Vu Manh Ha (2008), *Textbook of Economic Statistics*, Hanoi National University Publishing House, 208pp, in Vietnamese.

Table of contents in 2020

Vietnam Journal of Science, Technology and Engineering (VJSTE): Manuscript Template

General Instructions on using this template and submitting a manuscript to VJSTE: Thank you for preparing a manuscript for submission to VJSTE. Using this template, or following the guidelines below, will help us in processing your paper. Our goal is to be able to identify each section of your manuscript so that we can accurately record the title, authors, abstract, etc. and also be able to enrich it by including reference links and an accurate layout.

You can submit your paper at http://vietnamscience.vn

So that we can identify the parts of your paper, and even if you do not use our template, please begin each section with the specific key words listed below. Please do not use paragraph breaks in the title, author list, or abstract.

Title

Authors

Affiliations

Abstract

One Sentence Summary

Main Text

Acknowledgements

References

Several of these headings are optional, for example, not all papers will include a one-sentence summary, figures or tables.

Please use the .docx format (all version after Word 2007).

More specific formatting instructions are provided in the actual template, which follows.

Title: How to Format a Science Paper (replace with your real title)

Authors: The author list should be one single paragraph (no breaks). Authors should be listed by first name or initial followed by last name and separated by commas. Use superscript numbers to link affiliations, and symbols *†‡ for author notes. For example, X. Jones[1]*, P. Smith[1,2]

Affiliations:

[1]Affiliations should be preceded by superscript numbers corresponding to the author list, and each affiliation should end with a period.

[2]Each affiliation should be a separate paragraph.

*Correspondence to: include the email addresses or telephone number of the corresponding author(s). Please use the asterisk (*) symbol for the corresponding author information.

Abstract: The abstract should be about 100-150 words, and organized in this structure: An opening sentence that sets the question that you address and is comprehensible to the general reader, background content specific to this study, results, and a concluding sentence. It should be one paragraph only.

One Sentence Summary: A brief summary of the main result of your paper, without excessive jargon and less than 150 characters.

Main Text: In general, this should include a brief (1-2 paragraph) introduction, followed by a statement of the specific scope of the study, followed by results and then interpretations. Please avoid statements of future work or claims of priority, and avoid repeating the conclusions at the end.

All of the Figures and Tables should be cited in order (which should be cited as, for example, figure S1, and table S1). You can include page breaks if you would like to place the figures within the text.

Subheads: These can be included in Research Articles or Reviews and should be brief.

Equations can be included. We do not recommend using the native Word 2007, 2008, 2010 or 2011 equation editor. This can in some cases produce less reliable MathML, the online markup language we use, which may result in display errors. Instead, use the legacy equation editor in word (Insert menu; select insert object; select word equation) or use Mathtype (recommended). If you enter equations in simple LaTeX, check that they will convert accurately (Word 2007 and higher can convert simple LaTeX equations).

Fig. #: (Begin each figure caption with a label, "**Fig. 1.**" for example, as a new paragraph.).

Fig. 1. The figure caption should begin with an overall descriptive statement of the figure followed by additional text. They should be immediately after each figure. Figure parts are indicated with capital letters (**A**). If you prefer, you can place both the actual figures and captions logically through the text near where they are cited rather than at the end of the file (but not both). If a paragraph in the main text begins with the name of a figure, write out "Figure" in full (e.g., <para>"Figure 1 shows….").

Fig. 2. You can place graphics above each equation as part of this file.

Table #: (Begin each table caption with a label "**Table 1.**", etc.) as a new paragraph.

Table 1. Start this caption with a short description of your table. Format tables using the Word Table commands and structures. Do not create tables using spaces or tabs characters.

Acknowledgments: The acknowledgments should include a statement about where the data reported in the paper are presented, archived, or available. If in an archive, include the accession number or a placeholder for it. Please also include relevant funding information such as grant numbers and funding agencies. You can also include a statement of author contributions here. The acknowledgements can be multiple paragraphs.

References:

References should be cited in bracket with a number [1]. Multiple reference citations are separated by commas [2, 3] or if a series, dashes [4-6].

References are listed in numerical order, and in the same order in which they are cited in text. The reference list should include all and only those references you have cited in the text. The reference list appears at the end of the paper.

Please include the above heading "References".

Please do not mix in references with explanatory notes.

The reference consist of: Family name(s) and initials of all authors (year of publication), "Titles of journal articles" (optional), *Title of journal, book or other publication*, **volume(number)**, page numbers.

Example of a reference list:

[1] T. Binzoni, T.S. Leung, D. Boggett, D.T. Delpy (2002), "A new near infrared laser-Doppler flowmeter for deep tissue perfusion monitoring", *MAGMA*, **14,** pp.74-75.

[2] T. Binzoni, T.S. Leung, D. Boggett, D.T. Delpy (2003), "Non-invasive laser Doppler perfusion measurements of large tissue volumes and human skeletal muscle blood RMS velocity", *Phys. Med. Biol.*, **48(1)**, pp.2527-2549.

ISSN 2525-2461

Vietnam Journal of Science, Technology and Engineering

DECEMBER 2020 • VOLUME 62 NUMBER 4

EDITORIAL OFFICE

113 Tran Duy Hung Str., Cau Giay Dist., Hanoi
Tel: (84.24) 39436793; Fax: (84.24) 39436794
Email: khcnvn@most.gov.vn
Website: vietnamscience.vn

PUBLICATION LICENCE

No.1153/GP-BTTTT 26th July 2011
No.2528/GP-BTTTT 26th December 2012
No.592/GP-BTTTT 28th December 2016